CRANFIELD UNIVERSITY

Salwan David Saddawi

Multi-Objective Computational Engineering Design Optimisation for Micro-Combustor Devices

School of Engineering
Department of Power and Propulsion

Ph.D.
Academic Year: 2012 – 2013

Principal supervisor: Professor A.M. Savill
Co-supervisor: Dr T. Kipouros
March 2013

CRANFIELD UNIVERSITY

School of Engineering
Department of Power and Propulsion

Ph.D.

Academic Year 2012 – 2013

Salwan David Saddawi

Multi-Objective Computational Engineering Design Optimisation for Micro-Combustor Devices

Principal supervisor: Professor A.M. Savill
Co-supervisor: Dr T. Kipouros
March 2013

This thesis is submitted in partial fulfilment of the requirements for the degree of *Doctor of Philosophy*

I would like to dedicate this work to my family,
particularly to my beloved grandfather
Mr R.G. Nashi,
who was a great man and a brilliant teacher.

S.D. Saddawi
16/March/2013

Abstract

This thesis describes the development of a multi-objective automated optimisation system to be used for the design optimisation of micro-scale combustion devices. The developed system described within integrates a commercial computational fluid dynamics package and a multi-objective variant of the Tabu Search optimisation algorithm for continuous problems, which is a heuristic optimisation technique that exhibits local search characteristics.

Recent advances in micro-fabrication techniques have resulted in increasing interest from industry and academia to investigate the possibility of replacing the current conventional power supply "battery" with a miniaturised combustion power generation system based on micro-electro-mechanical systems (MEMS) technology. The microcombustor is one of the crucial components of such a power system. The aim is to improve the main micro-scale combustor design characteristics and to satisfy manufacturability considerations from the very beginning of the whole design process.

The main combustor design requirements, challenges and design parameters that influence the device performance at a micro-scale were first defined. Within the optimisation design cycle a robust parameterisation scheme, the geometry and numerical grid representations were implemented. These were achieved by incorporating the knowledge gained from the parametric design study by understanding the design space in depth and identifying issues and their solutions during this design study such as geometry overlapping and mesh refinement.

The developed optimisation system performance was tested in two cases. The results demonstrated that the multi-objective variant of the Tabu Search algorithm is capable of finding optimum designs by navigating through a complex, highly constrained and nonlinear response of the design space to the objective space of a microcombustor. The first case was a simple combustor configuration (baseline design) using a premixed hydrogen-air strategy and implementing 16 design parameters and two design constraints, and the second case was a thermally improved design using a micro-cooling channel and a non-premixed configuration, where eight design parameters and five design constraints are used. Also, an investigation into the use of alternative fuels to the

hydrogen was carried out and a map was constructed describing the hydrocarbon fuels' efficiencies and feasible operating spaces using a specific design configuration.

A method was suggested to design a bell-like shape to describe the divergent section of the convergent-divergent nozzle of a microthruster based on the numerical calculations at sea-level. The thrust force achieved at sea-level and design exit Mach number of 2.0 for two different settings were 47 – 139 mN. A 172 mN of thrust was also achieved when the device was configured to operate in a vacuum. The predicted value of the Mach number at the nozzle exit from the proposed numerical design method appeared to approach the ideal design value based on the one-dimensional compressible flow theory within 5 – 10 % over a range of design exit Mach number of 2.0 – 2.4. These values of thrust suggested the possibility of deploying such a device as a propulsion system on-board current large spacecrafts for attitude control and station keeping.

Finally, a number of recommendations for further research and development in the area of micro-combustion for power and propulsion applications are made.

Acknowledgments

I wish to take this opportunity to express my gratitude and thanks to Professor A.M. Savill for his direction, guidance and for being a great supervisor and listener during the development of this research. I also would like to thank my advisor Dr Timos Kipouros for his help, continuous encouragement and his valuable time and advises.

I would like to thank Dr Jeff Alcock, Dr Usama Attia and Mr Daniele Annicchiarico for the useful information and discussions over manufacturability issues and design configuration. Dr Les Oswald, the high performance computing manager and his successor Mr Andy Gittings for their much needed technical support throughout the entire project. Also, I thank the Power and Propulsion administrative staff, Gill and Nicola for their helps with admin matters.

I would also thank all my colleagues in the Power and Propulsion Sciences Group without exceptions for the discussions, advices and laughter we had.

I wish to thank all my friends outside the University specially Deena, Munaf, Basil and Khaldoon for their continuous encouragement, moral support and their help.

Special thanks go to Professor T.T. Al-Shemmeri for his invaluable advice to be involved in such a research project and his help when needed.

I am also grateful to Louise Woodland for her involvement in editing the text of this work.

Finally, I gratefully acknowledge the support of the Engineering and Physical Sciences Research Council (EPSRC) DTA/DTG Standard Research Studentship Grant.

Contents

List of Figures

List of Tables

Nomenclature

Roman

A	Area (m^2) or Pre-exponential factor – Eq.(1-3)
a, b	Arrhenius exponents
Da	Damköhler number
d_h	Hydraulic diameter (m)
E_a	Reaction activation energy (kcal/mol)
F	Thrust (N)
F_{12}	Shape factor - Eq.(5-12)
g	Gravitational acceleration constant (9.81 m/s^2)
h	Heat transfer coefficient ($W/m^2.K$)
H_2mass	Hydrogen consumption (kg/s)
I_{sp}	Specific impulse (s)
L	Length (m)
M	Mach number
$\dot{m}$	Mass flow rate (kg/s)
P	Pressure (Pa)
Q_{loss}	Heat loss from combustor walls (W)
R	Gas constant (8.3144 J/mol.K)
T	Temperature (K)
V	Velocity (m/s)
Y	Reactant mass fraction

Greek

γ	Specific heat ratio
ε	Radiation emissivity (assumed to be 0.8)
η	Overall combustor efficiency (%)
λ	Thermal conductivity (W/m.K)
ν	Prandtl-Meyer angle (degree)
σ	Stefan-Boltzmann constant – (5.67×10^{-8} $W/m^2.K^4$)
τ	Time (s)
φ	Equivalence ratio

Subscripts

a	Ambient
atm	Atmosphere
datum	Baseline design
conv	Convective
ex	Exit
f	Flame
H_2	Hydrogen
max	Maximum
min	Minimum
N_2	Nitrogen
O_2	Oxygen
o	Stagnation
rad	Radiative
s	Solid
st	Stoichiometric
t	Total
th	Throat section of a CD-nozzle
u	Unburned
v	Vacuum
w	Wall

Acronym

ACS	Attitude Control System
AFR_{st}	Air-fuel ratio at stoichiometry
CD-nozzle	Convergent-Divergent nozzle
CFD	Computational Fluid Dynamics
CPU	Central processing unit
DeMn	Design exit Mach number
DSMC	Direct Simulation Monte Carlo
ER	Equivalence ratio
FEA	Finite element analysis
HHV	High heating value
i_local	Optimisation iteration counter
LHV	Low heating value
MEMS	Micro-Electro-Mechanical System
MFER	Maximum fuel energy release
MFR	Mass flow rate
MOTS	Multi-objective Tabu Search
NASA	National Aeronautics and Space Administration
Nu	Nusselt number
N-S	Navier-Stokes
Re	Reynolds number
UHCmf	Unburned hydrocarbon’s mass fraction

Chapter 1
Introduction

1.1 Background

There is an increasing demand for miniaturized power and propulsion supply systems to be employed in small electronic devices such as portable computers, micro mobile robots, micro satellites (electronics and communication), unmanned micro aerial vehicles (μ-UAV) and aerospace micro-thrusters (Propulsion). It is necessary therefore to explore alternatives to the conventional batteries currently used in such devices, and to develop new propulsion technology.

The current power supply for such systems is restricted by a low power capability. Jejurkar and Mishra (2009) have stated that modern lithium ion batteries provide only 1.2 MJ/kg, whereas the hydrocarbon fuels provide an energy storage capacity of 45 MJ/kg. Also, they require a lengthy re-charging time, have short life span, future environmental consequences (end of life) and are relatively large compared to the overall size of the device.

The possibility of using a micro gas turbine engine for power and propulsion applications was first reported by Epstein et al. (1997). This engine could be fabricated from silicon-based materials using MicroElectroMechanical Systems (MEMS) manufacturing technology, an offspring of the semiconductor chip fabrication technology. This microengine could provide a viable approach to tackle all these challenges, and hence has been experimentally investigated in the recent past by other scientists, and now in the current work from a computational design perspective. Such devices are characterised by sustaining high power density, small volume and lightweight.

One of the primary components is the micro-scale combustor, where the chemical energy of the fuel is converted to thermal energy. This can then be used to drive a micro-scale gas turbine engine, in order to produce power or thrust or even to be used directly in heating applications.

Since the advances in micro-fabrication techniques, the MEMS and in particular the micro-gas turbine combustor has received substantial attention in the field of design (Groshenry, 1995), fabrication (Mehra et al., 1999), experimental (Tzeng, 1997) and

numerical simulation (Raimondeau et al., 2002). These studies uncovered the possibility to sustain stable combustion inside the micro-combustor chamber, which produces ten times higher power density than the current best lithium battery. However, there are additional design challenges that appear over conventional combustors, such as achieving high power density and efficiency; sufficient residence time for a complete combustion; maximum limits to the exit temperature of the burned gases and structure material temperatures; prevention of spontaneous ignition; managing thermal losses and recirculation zones. These design challenges will be discussed in the next section.

1.2 Microcombustor design requirements

Conventional gas turbine combustor design should meet some fundamental requirements as stated by Mattingly (1996) and Rogero (2003) these are:

- **Complete combustion and high efficiency**
  Maximum combustion efficiency and complete combustion so that all the chemical energy of a fuel is converted into fluid thermal and kinetic energy.
- **Minimum total pressure loss**
  Design of minimum pressure loss should be within the combustor to allow maximum performance of the gas turbine.
- **Flame stability and Fluctuation**
  A combustor should be able to operate within a wide range of pressures, equivalence ratios, and velocities and should be free of combustion instabilities and no possibility of flame quenching or blowout.
- **Re-light**
  The combustor should be able to re-light reliably at a given altitude, ground start and during transients.
- **Pollutant emissions**: The pollutant emissions of a combustor should be minimum, where the pollutant can be either particulates, NOx, CO, UHC, Soot, Smoke or SOx, generated by the combustion process.
- **Cost:** Minimum design, manufacturing and maintenance costs
- **Durability:** The life of the combustor should be compatible with the mission of the gas turbine engine, structure integrity and thermal design cycle.

Other design constraints on the conventional combustor from the gas turbine due to its technology and operating conditions, size and shape are:

- Mass flow rate design range
- Combustor length which is dictated by the compressor-turbine shaft length
- Turbine entry temperature (TET) which is fixed by the thermal cycle requirement and in turn is limited by turbine blades material and cooling technique
- Exit temperature profile which ensures the turbine blades expected life cycles. Finally,
- Combustor inlet pressure and temperature.

Similar design requirements, performances and constraints are expected for micro-scale combustors, however the reduction in size compared to conventional combustors creates new design challenges such as inadequate residence time for a complete combustion and excessive heat loss of the combustor chamber which lowers the reaction temperature and increases chemical reaction time. Finally, the requirement of operating at elevated combustion temperature adds further constraint and complexity to the type of material used and design manufacturability respectively. These design challenges shall be discussed next.

1.3 Microcombustor design challenges

The functionality and performance requirements of a micro-scale combustion device are similar to that of a conventional gas turbine combustor, where fuel reacts with an oxidiser under specific mixture, pressure and temperature conditions, to form products and release heat. The main design difference between a micro and a large combustor is the reduction in total volume. Waitz et al. (1998) reported that a conceptual microcombustor design with a pressure ratio of 4.5:1 has a reduction in size by a factor of 100 and by over six orders of magnitude in volume in comparison to a typical gas turbine combustor with a pressure ratio of 30:1. A high power density can be achieved using a micro-scale combustor. This is based on the fact that a highly efficient combustion process is required within the small chamber volume of a microcombustor operating at high mass flow rate, where all the fuel energy released is expected to be transferred into a fluid thermal and kinetic energy during the combustion process. Thus

the design performance of a microcombustor is limited by the chemical reaction time constraints of the fuel (Mehra, 2000), and the microcombustor must operate at a larger Damköhler number than unity.

However, there are two main design challenges facing the microcombustor designer and these are: operational and geometrical issues. A detailed discussion of those challenges shall be presented next.

1.3.1 Operational design considerations

1.3.1.1 Damköhler number

For complete combustion process, hence high chemical efficiency in a micro scale combustor, the Damköhler number should be greater than one. The Damköhler number is defined as the ratio of flow residence time to chemical reaction time

$$\mathrm{Da} = \frac{\tau_{\mathrm{residence}}}{\tau_{\mathrm{chemical}}} \tag{1-1}$$

- ***Flow residence time***

Insufficient residence time in any combustion chamber leads to incomplete combustion which reduces the total device efficiency and increases flame instability and/or flame blowouts. (Waitz et al., 1998) have reported that their MIT (Massachusetts Institute of Technology) micro gas turbine combustor was highly constrained by insufficient residence time which is defined as:

$$\tau_{residence} = \frac{\mathrm{Volume}}{\mathrm{Volumatic\ flow\ rate}} = \frac{\mathrm{V} * \rho}{\dot{m}} \tag{1-2}$$

Hence, increasing the effective volume of the microchamber or operating pressure, and decreasing mass flow rate will increase residence time.

- ***Chemical reaction time***

Another factor that influences the Damköhler number is the chemical reaction time, which is described by the Arrhenius expression by Mehra et al. (1999) as:

$$\tau_{chemical} = \frac{[\mathrm{Fuel}]_{\mathrm{initial}}}{\mathrm{A}\,[\mathrm{Fuel}]^{\mathrm{a}}\,[\mathrm{Oxidiser}]^{\mathrm{b}}\,\mathrm{e}^{-(\mathrm{E_a}/\mathrm{RT_f})}} \tag{1-3}$$

From the above, it can be seen that the reaction time is a function of species concentration (Fuel and Oxidiser), activation energy (E_a) and initial mixture temperature ($T_{initial}$).

1.3.1.2 Mass flow rate

Micro gas turbine combustor power density and efficiency are the most important design metrics of interest. Theoretically the power density is directly proportional to the mass flow rate per combustor chamber volume at a given equivalence ratio; thus it is proportional to the ratio of fuel-oxidiser mixture density to the residence time at a given Damköhler number (Spadaccini et al., 2002a).

$$\text{Power density } \alpha \frac{\dot{m}}{V} \alpha \frac{\rho}{\tau_{residence}} \alpha \frac{\rho}{Da * \tau_{chemical}} \quad (1\text{-}4)$$

Therefore, high power density can be achieved by increasing the mass flow rate of the reactants, but this then restricts the flow residence time for a given chamber volume.
On the other hand, to increase the power density of a microcombustor at a given Damköhler number and operating pressure and thus density, the chemical reaction time must be reduced; this in turn requires the increase in residence time to guarantee a complete combustion. This clearly identifies one of the trades-off and design constraints that determine the functionality of the combustor device.

1.3.1.3 Exit temperature of the combustion products

A micro-scale combustor is an integral part in a micro gas turbine engine, hence the exit temperature from the combustor chamber should be considered as a design constraint for the following reasons: firstly, the exit temperature should be of a value which is less than the gas turbine blades operating temperature; otherwise the micro gas turbine blades suffer from a premature mechanical failure. Secondly, the combustor exit temperature which is the turbine inlet temperature should be of a value to close the thermal cycle of the microengine. Tuccillo and Cameretti (2005) have reported the requirement of an exit combustor temperature of 1223 K for a micro gas turbine of the 100 kW range in order to close the thermal cycle of the design considered.

1.3.1.4 Spontaneous ignition temperature

Hydrogen-air mixture which is the main fuel-oxidiser considered in this research project, has an auto-ignition temperature of 858 K at 1 atm, as stated by Glassman (2008), which is a very important design constraint. The reactants mixture should always have a temperature below the auto-ignition temperature to prevent premature combustion occurring before the combustor chamber; such as in the vicinity of initial micro-cooling channel.

1.3.1.5 Structure material temperature

The maximum operating temperature of the material used in such a design is also a crucial factor. Hence, the maximum material operating temperature is one of the key design constraints. In this research, all proposed combustion devices are designed from stainless steel type 316L and in order to assure the structural integrity of those devices in a real-world applications, this temperature is limited to 1000 K (Attia, 2011).
Spadaccini et al. (2002a) have reported that in the MIT microcombustor, the wall temperature of their silicon material was limited to 950 K. In some geometry configurations, like the MIT one, higher power density can be achieved for a short time, but design failures occur when this constraint is not satisfied.

1.3.2 Geometrical considerations

1.3.2.1 Surface area to volume ratio

Surface area to volume ratio is smaller in a conventional “macro-combustor” than a micro-scale combustor (in a macro-combustor the ratio is typically ~4 and in a micro-combustor ~200 – (Jejurkar and Mishra, 2009). This ratio is of great importance when designing a micro-scale combustor. Waitz et al. (1998) have stated that the energy loss to the surrounding environment as a result of heat transfer from the outside walls of the combustion chamber in a conventional gas turbine is typically neglected. On the contrary, one of the conclusions obtained by Cao and Xu (2007) from their experimental work performed in a stainless steel based micro-annular combustor with a chamber height of 2 mm burning hydrogen gas with air was: the heat lost to the environment from the chamber walls is calculated to be 70 % of the total thermal power generated by the combustion.

Waitz et al. (1998) expressed the ratio of heat losses from a combustor surface to total heat generated in the combustion process as

$$\frac{\mathrm{Q_{lost}}}{\mathrm{Q_{generated}}} = \frac{\mathrm{A\ h\ (T_a - T_w)}}{\mathrm{V\ Q}} \tag{1-5}$$

Where: A is wall surface area, h is heat transfer coefficient, V is volume and Q is energy generated per unit volume in the combustion process. Due to the dependence of Nusselt number on Reynolds number (Nu α $Re^{0.8}$) which varies between the fluid regimes. As a result, the convective heat transfer coefficient is inversely proportional to ($d_h^{1.2}$).

From the above, Tzeng (1997) has stated that if the fluid and chamber wall temperatures are assumed to be the same, then the ratio of the heat lost to that generated during the combustion process the would scale with the hydraulic diameter

$$\frac{Q_{lost}}{Q_{generated}} \alpha \frac{1}{d_h^{1.2}} \tag{1-6}$$

Heat loss through chamber walls to the surrounding environment causes a drop in combustor overall efficiency, reduces reaction temperature and in some cases could cause flame quenching (Spadaccini, 2004).

1.3.2.2 Recirculation zone

Another important factor in the design of a micro-scale combustor is the creation of recirculation zones inside the chamber. These zones cause some of the combustion products which have higher temperatures than the reactants to re-circulate and to continually ignite the unburned mixture. This increases the operating range and is a source of flame stabilisation. The design of a larger recirculation zone can have a negative impact on the combustor efficiency, as it reduces the effective chamber volume and residence time hence, decreases the efficiency of the device (Mehra et al., 2000). A sudden expansion in the flow path of reactants mixture at the entrance to the chamber after the flame holder is one method to achieve such recirculation (Glassman, 1987).

1.3.2.3 Micro-cooling channel

Energy loss to the surrounding environment by means of natural convection and radiation from the outside walls of a micro-scale combustion chamber reduces the combustor performance by lowering the reaction temperatures, increasing chemical reaction time, and hence reducing the Damköhler number, (Mehra et al., 2000; Shan et al., 2005). Therefore, an effective measure to reduce the heat loss to the environment is the addition of a micro-cooling channel (Cooling jacket) into the design as previously suggested in literature such as in Mehra et al. (2000). This channel is located between the chamber cavity and the chamber outside walls. It is an important factor to be considered in such a design as it has the following benefits: firstly, acting as a thermal insulator, reducing energy loss to the surrounding area and also the structure temperature. Secondly, it can be considered a "better" heat management design as this channel recovers the heat loss of the chamber and preheats the incoming fresh gases before entering the microchamber which reduces the reaction time.

Another form of a micro-channel is the one deployed in the design of a heat recirculating burner (HRB) – the Swiss Roll burner which was examined theoretically by Weinberg et al. (2002) and Ronney (2003) and experimentally by Sitzki et al. (2001).

1.3.2.4 Inlet port profile and manufacturability

The micro-combustor device manufacturing feasibility is considered from the very beginning of the design process. Following an in-house micro powder injection moulding (μ-PIM) process based on a lost-core approach, which is a novel technique used for the first time and described in detail in Appendix A, it has been suggested by (Attia, 2011) to replace the conventional circular inlet port shape with a slit type inlet of a minimum radius of 100 μm. This measure is implemented due to the limitations associated with the current fabrication technique. These include the minimum feature dimensions and maximum aspect ratio of the polyoxymethylene polymer (POM) core. This core represents the microcombustor cavity as well as the combustor inlet and the outlet (Attia et al., 2009). The implementation of a non-conventional design inlet shape (slit) highlights another design constraint for such a device, due to the reason mentioned above.

1.4 Type of fuel to be used

As the volume of a conventional combustor diminishes to micro-scale size and a complete combustion and a high efficiency conversion of a fuel into fluid thermal and kinetic energy become necessary to achieve high energy density at lowest pollutant emissions possible, therefore hydrogen as a primary fuel was considered as the best candidate for a microcombustor operating within a micro gas turbine engine for power generation and propulsion applications. Table 1-1 compared the fuel properties of the hydrogen with their counterpart of methane in air and at STP. It can be seen that the hydrogen is superior in all combustion properties to that of the hydrocarbon fuel and most importantly has a greater heating value and wider flammability limits. Therefore, it is possible to implement a lean hydrogen-air mixture strategy to achieve an exit combustor temperature in excess of 1600 K at an equivalence ratio of 0.34 and no heat loss (Tzeng, 1997).

This also illustrates the need of near stoichiometric reaction and dilution zones which reduces the microcombustor design and manufacturing complexities. Hydrocarbons such as propane (C_3H_8), ethane (C_2H_6) and butane (C_4H_{10}) were also numerically tested as alternative fuels to hydrogen in this research project.

Hydrocarbon results, the impact on microcombustor performances and design recommendations can be found in chapter 6 - case study 3.

Table 1-1: Fuel properties comparison, hydrogen vs. methane

Hydrogen data (Winter, 1990) and methane data (Baukal, 2001) unless otherwise stated

Fuel property in air at STP	Hydrogen–air	Methane–air
High heating value (MJ/kg)	140	55.48
Autoignition temperature (K)	858	873*
Laminar flame velocity (cm/s)	300	33.5
Minimum ignition energy (mJ)	0.03	0.29
Flammability limits (% by volume)	4 – 75 **	5 – 15
Stoichiometric adiabatic flame temperature (K)	2318 **	2191

* (Robinson and Smith, 1984), ** (Glassman, 2008)

1.5 A review of the previous investigations

1.5.1 Combustion investigation

When a conventional combustor is miniaturised to a millimetre scale, which means a reduction in the overall volume of the device, then the surface area-to-volume ratio of the new combustor becomes very large. This results in the increase in the heat loss of the chamber to the surrounding area during the combustion process due to the increased coupling between the flame (chemical) and the combustor structure (thermal). Heat loss of a microcombustion chamber lowers the reaction temperature, increases chemical reaction time and may result in global flame extinction or flame quenching.

In 1816, Sir Humphrey Davy studied flame quenching when he was investigating the frequent firedamp explosions in coal mines in the North of England. He was able to demonstrate that flames could not propagate through a fine wire-gauze with a quenching gap of the order of 1 mm. This finding led to his invention of a safety lamp for use in flammable environments such as coal mines, known as “the Davy lamp” (Davy, 1816; Davy, 1817).

Another experimental work aiming to characterise the quenching of flame for a narrow cylindrical passage was carried out by Ono and Wakuri (1977) using stoichiometric mixture of methane-air and propane-air. The apparatus consisted of two combustion chambers connected to each other through a quenching block with a single narrow cylindrical port. Different port diameters and height were used experimentally ranging 1.5 – 3.5 mm and 5 – 40 mm respectively. The experimental results showed one point where the lower and the upper flame speed limits met with the decrease in port diameter, which is the critical passage diameter below which no combustion has taken place in the upper chamber. But the exact quenching diameter could not be defined.

Vosen et al. (1984) have carried out experimental measurements during premixed-methane-air combustion quenching of the unsteady heat transfer from the flame to the chamber wall over an equivalence ratio ranging 0.7 – 1.2 and near atmospheric pressure. Those measurements showed that flame quenching occurs when the ratio of the heat dissipated to that generated is greater than 0.29 at mixture equivalence ratio of 1.0. Furthermore, this ratio was equal to 0.351 and 0.35 for ethylene-air and propane-air at stoichiometric reactions respectively (Huang et al., 1986).

In order to overcome quenching of flames in millimetre-scale combustors, thermochemical techniques can be deployed (Fernandez-Pello, 2002) such as operating with adiabatic combustor walls or high temperature walls (near combustion temperature) using in this case materials with high temperature resistance such as ceramics. Moreover, combustor surface coatings can reduce the excessive heat losses and therefore prevent flame quenching. Finally, the implementation of "excess enthalpy" design in millimetre-scale combustor. The latter was investigated first by Weinberg and co-workers (Takeno et al., 1981), the concept by which the enthalpy of the products is used to preheat the incoming reactants mixture in what is known as a *Swiss Roll burner*. This configuration has led to a sustained combustion below the normal flammability limit of the fuel-oxidiser mixture. The increase in wall temperature due to the strong thermal coupling between the flame and the chamber walls reduces the ignition time; this may result in weak flames or flameless combustion (Ju and Maruta, 2011).

Zamashchikov (1995) has demonstrated experimentally that the flame can be stabilised inside a thin-walled tube with an inner diameter of 2.5 mm which is less than the critical of 3.5 mm for stoichiometric methane-air mixture at certain flow rates by heating up of the tube walls.

The flammability limits of hydrogen-air reaction mixtures in a millimetre-scale tube were mapped out experimentally by Tzeng (1997). The tube is similar to a Bunsen burner with a downstream diameter of 2.8 mm after the step flame holder. The flame was stabilised within the tube using an external heating source to raise the tube wall temperature. Also, it was observed that the flame location inside the tube was influenced by the location of the external heat supplied.

Mehra et al. (2000) have carried out experimental testing on a microcombustor measured in millimetres 21 x 21 x 3.8, which was designed for a silicon microengine. The results showed that the combustion of hydrogen-air over a range of mass flow rate and equivalence ratio in a chamber volume of 195 mm^3 and atmospheric pressure can be stabilised inside the combustion chamber with exit gas temperatures in excess of 1600 K and overall efficiencies as high as 95 %. The combustor design incorporated a micro-cooling channel (cooling jacket) in order to reduce the heat loss of the chamber to the

surrounding environment and to preheat the incoming reactant mixture flowing inside this channel based on the excess enthalpy combustors discussed above.

Isomura et al. (2005) studied a microcombustor with a diameter of 15 mm for a micro gas turbine engine. In order to achieve an output power of 100 W, it was calculated that the required combustor inlet and outlet temperatures and pressure are 444 K at 304 kPa and 1323 K at 279 kPa respectively, using hydrogen-air at an equivalence ratio of unity. The initial calculations also suggested that the heat loss to heat release ratio is expected to be about 5%. The designed micro-combustor was validated experimentally but no information about the device performance is reported.

Yahagi et al. (2007) investigated experimentally the flame stability in a micro can combustor of 120 mm in length and 36 mm in diameter with a baffle plate. The fuel was introduced from a central nozzle of the baffle and the air from multiple holes located radially. It was concluded that the use of a baffle plate at a low Reynolds number flow enhances the fuel-air mixing by creating three-dimensional flow recirculation zones inside the combustion chamber.

Li et al. (2009a) studied experimentally the effect of the wall temperature and radiation heat flux of a series of cylindrical microcombustors with a diameter of 2 mm by varying the length, the equivalence ratio and the flow velocity using hydrogen-air mixture. The combustor design also includes a backward-facing step for flame stabilisation. They identified that when the length of the combustor increases, the operating range of the flow for a stable combustion decreases. Also, they observed that a wider operating range of velocity is achieved when the equivalence ratio is increased from 0.6 to 1.0. Furthermore, they investigated the effect of the backward-facing step size on radiation in a separate case (Li et al., 2009b) and they concluded that when the step height to the chamber diameter ratio increases the radiation from the external wall decreases.

Butler et al. (2009) carried out experimental tests for hydrogen diffusion flame quenching and blow-off limits using four different burners, with diameters as small as 8 μm. Most notably, the weakest hydrogen flame was observed from a diameter of 0.152 mm which was generated with a hypodermic needle at 3.9 μg/s of fuel mass flow rate and 0.46 W of heat release.

Excess enthalpy design strategy represented by the implementation of a micro-cooling channel into a micro-scale combustor design which is similar to that of Mehra et al.

(2000) is employed in this research work starting from case study 2 in chapter 6 onwards.

1.5.2 Combustion numerical investigation

In the past, microcombustion and its associated issues were not only investigated experimentally, as reviewed in the previous subsection, but also was extended to involve numerical simulations following the advances in modern computational power and the wide varieties of commercial software available in the public domain. At the initial design and development of a microcombustor, the performance of a combustor, combustion phenomena, fluid dynamics, thermal fluid-solid interaction and device structural integrity have to be studied. Within such a millimetre-scale, the available experimental measurements are limited only to the temperature of the external parts of a combustor such as external structure walls and device outlet, also the pressure drop across a chamber. Within this context, numerical modelling provides an insight into the flow and structure internal behaviour such as fluid flow pattern and properties, internal temperature distribution, flame stabilisation and identification of the possible flame location, structure behaviour and thermal hot-spot,… etc, which is not possible with any small measurement tool currently available. Therefore, product design cycle time and cost are reduced.

Waitz et al. (1998) have studied the combusting flow behaviour inside a microcombustor numerically. A 2D numerical model was used for this purpose. A Navier-Stokes solver integrating finite rate chemistry kinetics model was used which consisted of nine species and 18 chemical reaction mechanisms of a hydrogen-air mixture at an inlet temperature of 450 K, mass flow rate of 0.045 g/s, equivalence ratio of 0.4 and at atmospheric pressure. The numerical results suggested that there is enough residence time to achieve a complete combustion within the small cavity of the tested chamber which was then verified by the results obtained in the experiments.

Spadaccini et al. (2002a) have numerically investigated the temperature profile within a micro-scale combustor which was designed to be compatible for use in the MIT silicon microengine. Hydrogen – air reaction mechanism was modelled with nine species and 20 reaction steps and different inlet-to-chamber geometries. The numerical simulation considered the fluid dynamics and the reaction modelling only, neglecting the heat transfer between the fluid and the solid domains. Therefore, the results showed an over-

prediction of the flame temperature and the device performance due to an accounted heat loss to the surrounding area of the microchamber walls.

Hua et al. (2005b) have studied the combustion of premixed hydrogen–air mixture in a microchamber with various dimensions from millimetres down to micron with the same geometry aspect ratio. Nine species and 19 reversible reactions were modelled to represent the combustion kinetics with a variety of heat transfer scenarios such as adiabatic and non-adiabatic conditions. They concluded that the microcombustor performance is significantly affected by the thermal boundary conditions and the combination of increasing the surface-area-to-volume ratio and larger heat loss of the chamber may result in flame quenching.

The latter authors then investigated the combustion numerically (Hua et al., 2005a) using the same reaction library from the previous study, the microcombustor of Spadaccini et al. (2002a) under the same applied boundary conditions but they accounted for the convective and the conductive heat losses of the chamber with the aim of understanding the effect of different operating conditions, i.e. by applying different mass flow rates and equivalence ratios on flame stabilisation and the characteristics of combustion.

Wang et al. (2006) analysed numerically the combustion characteristics under different design mass flow rates. They introduced a hairpin-shape channel, an extension to the length of the original micro-cooling channel design of a six-wafer microcombustor by Mehra et al. (2000). 3D CFD simulation was used which includes the heat loss calculation of the chamber using nine species and 19 reversible reactions of H_2-O_2. The authors claimed that combustion can be sustained in a wider operating mass flow rate range. However, the implications of the required additional wafer layer, which increases the manufacturing complexity and cost, and importantly increases the device external surface area are that it therefore reduces the overall efficiency of the combustor and were not discussed in this study.

Daou and Matalon (2002) have studied the influence of the heat losses, the channel width, and the main flow velocity on the flame propagation in 2D channel. A diffusive-thermal combustion model was based on the Arrhenius-type expression. Two possible modes of extinction were discussed: partial flame extinction near wider channel walls and total flame extinction in narrow channel, the latter occurred from excessive heat

losses of the channel walls. They also concluded that the heat loss magnitude is proportional to the square of the channel's width and when the burning rate is ~ $0.6S_L$ (S_L: Laminar flame speed) the flame extinction occurs. These numerical findings were verified by the classical results of 1D flame calculations.

Kuo and Ronney (2007) studied a spiral counterflow heat recirculating combustor (Swiss Roll combustor) numerically over a range of ($2 < Re < 5000$). A 2D numerical simulation includes a single-step reaction modelling of a propane-air mixture and heat loss calculations (surface-to-surface radiative heat transfer and heat conduction within the structure). A simplified heat model in the third dimension was also considered. They have concluded that the radiative transfer and wall heat conduction have significant effects on the performance of a Swiss Roll combustor at low Re. Also, a compromise material in terms of the thermal conductivity is required. A high thermal conductivity structure results in the increase in heat loss and possibly also flame extinction. The use of a lower conductivity material affects the heat recirculating from the products to the reactants and this narrows the operating flammability limits of the device.

Norton and Vlachos (2003, 2004) investigated numerically the effects of wall conductivity and thickness, external heat losses, operating conditions and microcombustor dimensions on combustion behaviour and flame stability. The 2D numerical model consisted of two infinitely wide parallel plates which were 1 cm long and less than 1mm apart. The results suggested that the flame stability depends on the thermal conductivity of the wall material. Two flame extinction mechanisms were identified, low wall thermal conductivity material, which limits the preheating effects of the reactants upstream and high thermal conductivity which leads to excessive heat losses and global extinction. Moreover, higher mass flow rate decreases the heat transfer from the fluid to the structure and possible flame blowout on the other hand, the heat generated to sustain combustion becomes too small compared to heat losses which causes flame instability at low mass flow rate.

Raimondeau et al. (2002) investigated the propagation of flame in micro channels. A two-dimensional model with detailed transport and gas chemistry of methane-air reactions (16 species and 46 reactions) is used. It concluded that radial temperature gradients of a small channel diameter at the wall are negligible. Also, radical quenching

and heat loss near the chamber inlet are key issues in managing flame propagation in micro channels.

Woodfield et al. (2003) investigated numerically a method of enhancing a laminar flow mixing at low Re of 100 using a baffle plate in a micro-can combustor. The fuel and the oxidiser were injected axially from a central and multiple radially distributed holes respectively. The numerical results showed that significant improvement to mixing is achieved compared with the co-axial jet problem (without baffle). The authors also claimed that the mixing performance was found to be sensitive to minor changes in the design configuration of the baffle plate.

Kaisare and Vlachos (2007) studied the effect of reactor dimensions and operating conditions on thermal quenching with the aim of finding answers to whether there is an optimal channel length, structure thickness and reactor size that enhances flame stability. The numerical simulation results of a single-step propane-air mixture showed that when operating near extinction limit a shorter reactor is required in order to reduce the heat loss to the surroundings. A flame can be sustained at a higher inlet velocity using a thicker reactor wall of lower thermal conductivity. Finally, the reactor height has a substantial effect on flame quenching limits that is fuel dependent.

Iki et al. (2008) evaluated the numerical simulation results with their counterpart of the experiment for a small annular combustor which is part of a micro gas turbine engine. Then they carried out an optimisation investigation using CFD modelling with the aim to improve the overall efficiency of the micro engine by modifying the size and the position of the cooling air inlet holes following a trial and error approach. Some modifications improved the efficiency and the pattern factor at the combustor exit plane.

Li et al. (2009c) investigated the effects of the size and geometry of a methane-air premixed combustion in non-adiabatic microcombustors with a chamber length of 12 mm and a stainless steel wall of 0.2 mm. A two-dimensional numerical model was constructed and a reaction library of 16 species and 25 reversible reactions were used. The results demonstrated that a chamber with a diameter of 2 mm produces a higher flame temperature than that of 1 mm at a specific flow velocity range. Also, a higher flame temperature was obtained from a 2D planar chamber in comparison to a cylindrical type configuration with the same hydraulic diameter over the tested inlet velocity range.

Shabanian et al. (2010) studied the effect of various boundary conditions of the hydrogen-air mixture in a cylindrical microchamber on flame stabilisation. A three-dimensional numerical model, nine species and 19 chemical reactions and a non-adiabatic wall condition were considered. The numerical results demonstrated a significant effect of the wall's thermal conductivity on flame stabilisation. Also, high heat loss of the chamber external wall, small chamber diameter and high mass flow rate may lead to flame quenching.

Jejurkar and Mishra (2010) designed and studied numerically a simple annular non-adiabatic microcombustor using the stoichiometric ratio of a hydrogen-air mixture and a single-step reaction model. A hollow tube filled with nitrogen positioned axially at the centre of the device is used as an alternative to a catalytic action or a flame holder in order to stabilise the flame inside the chamber. The hollow tube wall and the nitrogen gas acted together as a heat source during the combustor warm-up which resulted in a stable combustion despite the total heat loss at the external wall of the combustor. Furthermore, the authors also studied the effect of applying different inlet mixture temperatures ranging 300 – 700 K (Jejurkar and Mishra, 2011). By using the above mentioned method, the numerical results showed that the combustion could be self-sustained at lower inlet temperatures.

In summary, early works suggested that a flame cannot be sustained inside a cavity with a quenching gap of the order of 1 mm. This dimension depends on material properties and type of combustible fuel employed. In order to overcome quenching of flames in millimetre-scale combustors, thermochemical techniques were suggested such as operating with high temperature chamber wall; using high temperature resistance material, such as ceramic; and the implementation of excess enthalpy approach in what is known as the Swiss Roll Burner configuration.

Recent advances in micro fabrication techniques have demonstrated that a flame can be stabilised within a chamber cavity of less than 100 mm^3 using pre-mixed of hydrogen-air, which resulted in a flow exit temperature in excess of 1800 K.

From the above summary, and the literature survey regarding combustor optimisation carried out in section 4.3, it was clear that automated numerical optimisation (and in particular multi-objective approach to this) had yet been performed in such real-world devices and therefore this was the focus of the current work.

1.6 The aim of the present work

The main aim of this project was to achieve multi-objective design optimisation, considering manufacturing constraints at outset. The implementation of an automated optimisation design system at the final stage of the product development cycle significantly reduces the workload undertaken by a human designer with respect to the product's performance improvement thus, increasing profitability. The designer monitors the optimisation process rather than getting involved in it. This allows the focus on the technical aspects of the design or even undertaking new projects.

The proof of concept and the confidence gained using such an automated system in the design of a real-world application represented by a micro-scale combustor device came from the works of Jaeggi et al. (2008) and D'souza (2008).

The present work has the following intentions. Firstly, to improve a micro-scale combustor's main design characteristics; device efficiency and fuel consumption for simple and then complex geometry configurations using a multi-objective design optimisation technique. In addition, different hydrocarbon fuels to be tested numerically as alternative fuels to hydrogen which is selected to be the prime fuel in microcombustion power and propulsion applications. Engineering maps of the individual fuel that define a combustor operating limits (flame stability and extinction), its efficiency and design recommendations are expected.

The proposed optimisation system to optimise a micro-scale combustor consists of integrating a parameterisation scheme, geometry and numerical grid representation tool, a well-known commercial CFD solver and finally an optimiser algorithm represented by the Tabu Search, in which all system components run harmoniously in an automated manner.

Secondly, to develop a 3D CFD based numerical approach to be used as a tool in the design of a micro-scale bi-propellant propulsion system, where the convergent-divergent nozzle will be integrated to an optimum combustor design configuration achieved from the previous task.

1.7 Thesis organisation

This chapter introduces the motivation behind the design of micro-scale combustion devices, the set of design requirements and the main design challenges facing the designer. It provides the reasons for choosing the hydrogen gas as a fuel for this kind of application. Also, discusses previous investigations in combustion experimentally and numerically. Finally, it outlines the targets and methodologies to be achieved in this research investigation.

Chapter two describes the conventional optimisation design process undertaken by the human designer and the automated integrated design optimisation system developed in this research project. Also, outlines the difference between the two approaches and highlights the possible benefits gained.

Chapter three presents the initial microcombustor design configuration, parameterisation technique and numerical grid representation which includes grid optimisation study and a map of the influential grid parameters as a function of the microcombustor geometry features adopted within the optimisation algorithm.

Chapter four introduces optimisation and past contributions in this field specifically in combustion. Also, presents the multi-objective Tabu Search algorithm, algorithm overview and briefly discusses the main algorithm search features and implementation.

Chapter five describes the objective function, evaluation and constraints. Also, presents the parametric design study, the strategy undertaken and discusses the step size effects of the individual parameter on the objective design target. Finally, defines and discusses the multi-objective Tabu Search parameters settings.

Chapter six represents the results of two case studies obtained from the integration of the multi-objective Tabu Search algorithm with a well-known computational fluid dynamic package in an automated manner. The first case represented a simple microcombustor configuration, where a single and then multi-objective optimisation investigations were carried out. A microcombustor with a complex geometry was optimised in the second case where the benefit of adding a micro-cooling channel into the design was firstly recognised in a separate investigation. The final case study was specifically intended to replace the hydrogen with a hydrocarbon fuel and study the

effects numerically on the combustion and combustor performance inside the micro-scale combustor.

Chapter seven introduces the design of a microthruster to be utilised on-board a spacecraft as a propulsion system for attitude control and station keeping applications. Bi-propellant microthruster type using hydrogen gas as fuel and air as an oxidiser will be examined in depth, based on a previously developed microcombustor design through the multi-objective optimisation work achieved in chapter six-case study 2.

Chapter eight presents this thesis' conclusions and future work recommendations.

Chapter 2

Description of the integrated design optimisation system

This chapter describes the conventional optimisation design process undertaken by the human designer and the automated integrated design optimisation system developed in this research project with the aim of improving the main combustor design characteristics, the device efficiency and the fuel consumption. Also, this chapter outlines the difference between the two approaches and highlights the possible benefits gained.

2.1 Computational Engineering Design

Optimisation in engineering is defined as a process undertaken at the final stage of product development cycle in order to improve the performance of the most critical design aspects while satisfying all design constraints and to finely tune the parameters that describe and define the design problem, and in extent to enhance the overall design. The computational design process is highly demanding in computational time and information storage capacity. The advance developments in micro-electronic components such as the advance in power semiconductors in recent years have improved the performance and the storage capacity of modern computers dramatically. Thus, it is reasonably possible to perform such a process in terms of wall-clock time and computation cost on real-world applications in a time demanding environment.

The advances in computer technologies, the availability of CAD, CFD packages and the optimisation algorithms, offers the designer the opportunity to integrate all these tools to perform a design optimisation. The modern conventional design cycle in a simplistic presentation is shown in Figure 2-1. The design engineer is involved throughout the design process by updating the geometry, generating the required numerical grid, setting up the numerical problem, interpreting the CFD results and finally, using her/his expertise and judgement at each finished cycle on whether the final design fulfils the design intention and meets requirements.

A simple integrated design optimisation system shown in Figure 2-2 outlines the additional stages in comparison to the conventional design cycle, and they are:

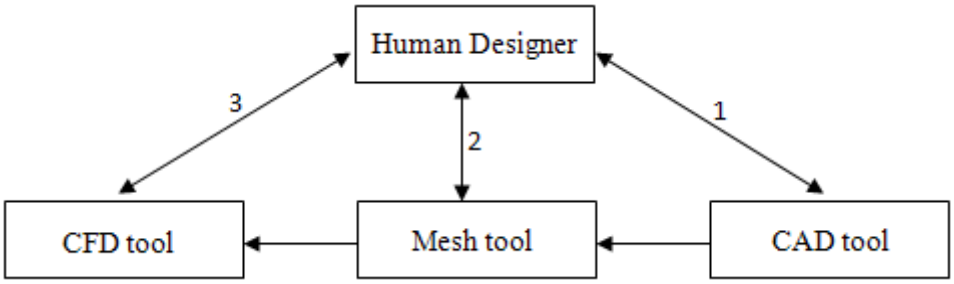

Figure 2-1: Simple modern conventional design cycle

Geometry parameterisation and the introduction of an optimiser algorithm.

Parameterisation (Parametric geometry) is an essential stage in multi-objective optimisation problem which will be discussed in detail in the following chapter whereas, it is not necessary to be implemented in the conventional design approach although it will reduce design time and cost for a complex geometry with many design parameters such as aerofoil, compressor and turbine blades, etc.

The implementation of an automated optimisation design system at the final stage of product development cycle reduces significantly the workload undertaken by the human designer with respect to the product's performance improvement thus, increasing profitability. The designer monitors the optimisation process rather than getting involved in it. This allows the focus on other product development aspects or even undertaking new projects. The human designer can intervene at any time during the optimisation process by tuning the critical optimisation parameters and also directing the optimisation search to achieve the desired performance. Human designer decision making comes at the end of this process to select the most suitable optimum design found from the Pareto optimal set. Finally, the optimum design parameters vector which corresponds to the optimum design found will be manually processed by the designer i.e. creating the geometry, numerical grid and carrying out CFD calculations in order to investigate and evaluate the reliability and the accuracy of the final product meeting all design criteria before the product sign off process begins.

The micro combustor development and testing carried out by a group of researchers at the MIT (Spadaccini et al., 2002a) investigated the mixing length requirement by considering a set of three different fuel inlet ports. The same researchers also investigated two combustor flame holder configurations; a number of hydrocarbon fuels; and two combustion chamber designs.

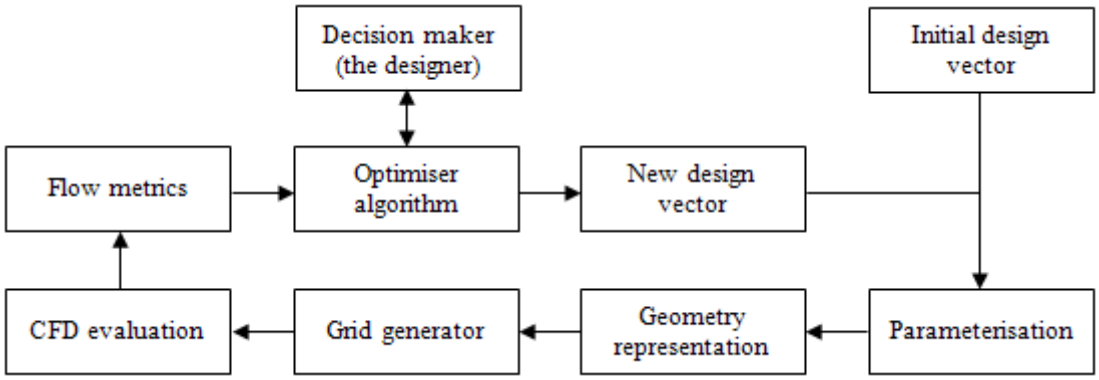

Figure 2-2: A simple integrated design optimisation cycle

During the initial phase of a microcombustor development for a micro machined gas turbine for power generation at the Tohoku University, an empirical model was used to evaluate the effect of the heat loss to the heat release and from that a chamber diameter was selected (Isomura et al., 2005).

The development of a microcombustion chamber with a hair-pin micro channel carried out by Wang et al. (2006) based on 3D CFD simulation for the analysis of different selected micro chamber design.

From the above and other related literature it would appear that no formal design procedures have been applied to such devices prior to the current investigation.

2.2 Development of the design system components

As the current investigation deals with a real-world component design, a single objective approach does not adequately represent the optimal for the whole design spectrum considerations. Usually, there are many design conflicts and trade-offs involving minimising or maximising more than one objective function that reflects the overall performance and behaviour of an engineering component, such as minimising the fuel consumption and maximising the efficiency in the design of micro-combustors.

The multi-objective integrated optimisation system represented by the flowchart is shown in Figure 2-3. This system was specifically developed for the optimisation of a micro-scale combustor but can also be modified with ease to consider different applications such as in the work of Kipouros (2006), D'souza (2008) and Trapani et al. (2012).

The main three stages are:

1. Parameterisation, geometry representation and numerical grid generation using ICEMCFD software
2. Numerical problem setup by applying the relevant boundary conditions, CFD calculations and then post processing the CFD solution to obtain the flow metrics results of interest using ANSYS CFX, and finally
3. The evaluation of the new objective function value against the initial design value then, generating new design vector (new candidate design) by the implementation of MOTS algorithm.

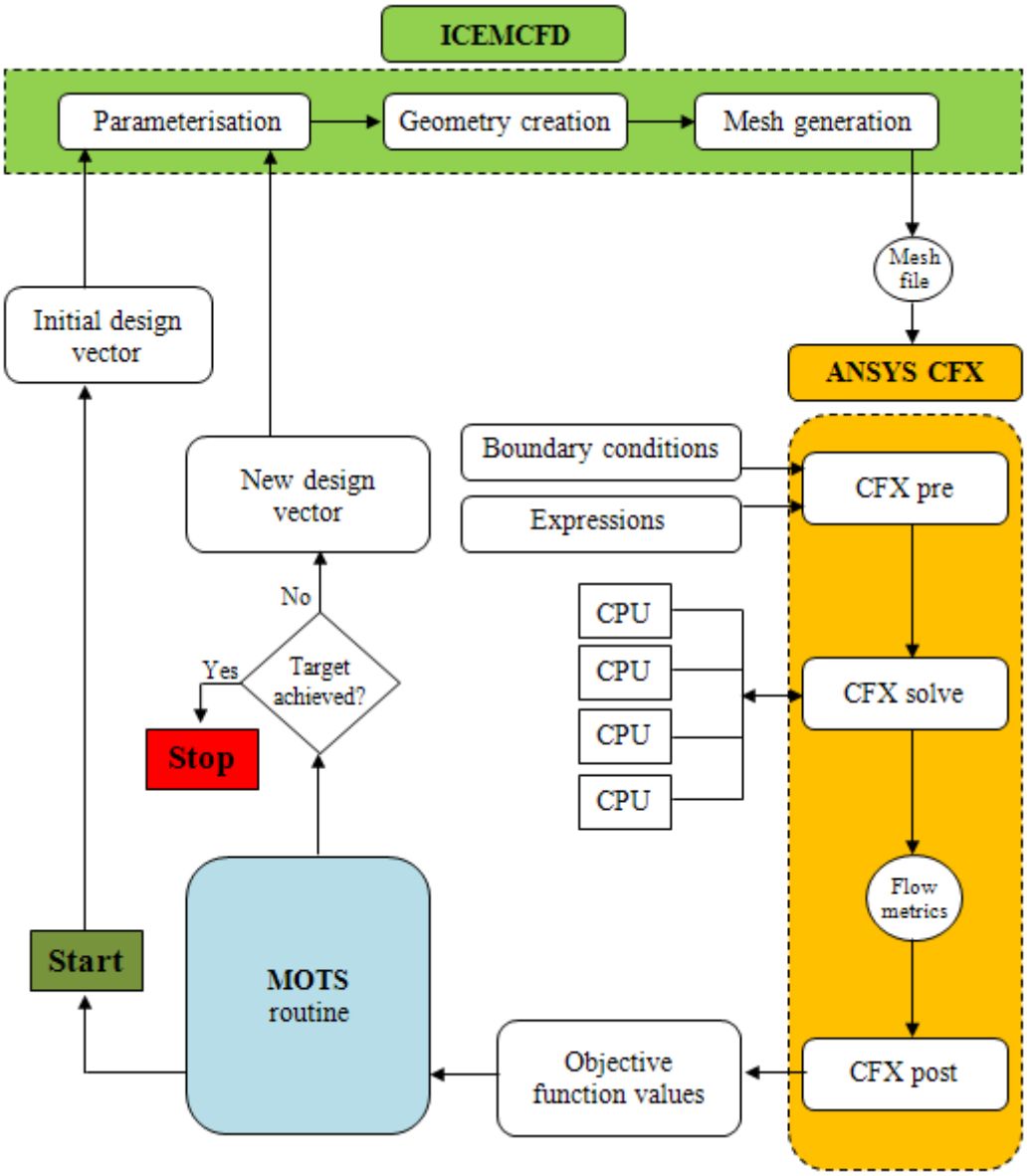

Figure 2-3: Multi-objective integrated optimisation system structure

The optimisation process starts from the initial design vector, which represents the datum design. This vector contains the geometrical and the operational design parameter values which are passed to the relevant tool for example, the geometrical parameters are passed to ICEMCFD in stage 1 herein, there are three design steps, the geometry parameterisation and creation and finally, the grid generation. All these steps are carried out by creating a reliable and robust script file which mimics the modelling steps undertaken to generate the datum design geometry and then the numerical grid. One of the important aspects of this script is the ability of producing the same design quality expected as for the initial design in terms of geometry and grid generation throughout the optimisation process. All tools implemented within the optimisation system in stage 1 and 2 must be capable of generating readable script files which will be managed by the optimiser algorithm. This is an important characteristic to build an integrated automated optimisation system.

In order to reduce the optimisation cost at the early stages of system development and testing, the numerical grid size varied from 90,000 to 350,000 approximately depending on two geometrical parameter values, the device total radius and the chamber total height. Thus a set of rules were created and was eventually managed by the TS algorithm. The numerical grid type, a grid optimisation study and a detail of the set of rules implemented are discussed in the next chapter.

After the generation of the grid file which is the product of stage 1, this file is passed to the CFD calculation tool named ANSYS CFX. Within this stage, there are three main steps starting with CFXpre, where the following are defined: the domain's definitions, the activation of flow equations of interest, all boundary conditions and problem setup. These include all constant values such as the ambient temperature and domain reference pressure, the operational design parameters from the design vector (MFR and ER), which define the chemical reaction and the involved reactants properties and finally all mathematical expressions which describe the heat transfer, radiation, device efficiency and reactants species mass fractions calculations. The second step is CFXsolve where the 3D Navier-Stokes, flow and reaction modelling equations are solved. The time required to obtain convergence simulation results at this step depends mainly on the grid size, the fluid regime (laminar or turbulent) and in this research project on the number of the chemical reaction equations deployed. The CFD results achieved in an iterative

manner, which is the most time consuming in the whole optimisation process. Benefiting from the parallelisation capability provided by this tool therefore, it is possible to solve these equations using more than one CPU, in fact four were used.

The end of the solver run signals the start of the third step where the simulation results are pre-processed through CFDpost tool and the values of the flow metrics results of interest are exported as a text file ready to be accessed by the optimiser algorithm. The evaluation of the objective function(s) hence, directing the optimisation search to find a better design performance depend on the results obtained from the CFD calculations. Even though a well-known commercial code was used in this project and previous rigorous testing and validation were carried out by the code's developer and in literature, it was important to validate its performance within a micro-scale design. This investigation was achieved through three test cases detailed in Appendix B where the CFX code performance was compared with other known commercial code. The results obtained in comparison were satisfactory in the context of micro-scale combustion.

The final stage in the optimisation system is the optimisation routine where the objective functions values obtained from the CFD simulation are compared with the initial design values. As a result, a new design vector is generated (new candidate design) followed by the steps outlined in stage 1 and 2, this process will continue until certain criteria are met.

In the multi-objective design study, the results are a set of optimal designs (Pareto optimal set) in which there are more than one optimum design satisfying one or more design objectives and the selection of the final design is left to the human designer.

In order to reduce the optimisation cost by reducing wall-clock run time, the optimisation system can be parallelised by means of functional decomposition using protocol of the Message Passing Interface (MPI) (Kipouros, 2006). In this research project, system parallelisation was not deployed at the initial development and testing of the system in the optimisation of a micro-scale combustor (chapter 6 - case study 1). However, it was used in Case study 2 where the optimisation was run on a three-node parallel PC cluster with four CPUs per node.

2.3 Chapter summary

This chapter described the conventional design cycle and the involvement of the human designer in all design aspects throughout the design process. Also, it presented the automated integrated design optimisation system developed for a real-world application represented by a micro-scale combustion device with the aim of improving main design characteristics; device efficiency and fuel consumption. The automated system main stages were also described.

Chapter 3

Geometry, parameterisation and numerical grid representation

This chapter presents the initial microcombustor design configuration, parameterisation and numerical grid representation. It is designated to target the following:

- To describe the datum geometry, its main design features, type of fuel, material and sizing.
- To detail the geometry and the most significant operational parameters used within the optimisation process. Also, to describe the parameterisation methodology followed and briefly present some of the rules applied in order to avoid the possibility of geometry features overlapping during the optimisation investigation. And finally,
- To represent the numerical grid configuration, then performed a grid optimisation study and finally, produce a map of the influential grid parameters as a function of the microcombustor geometry features adopted within the optimisation algorithm.

3.1 Description of the microcombustor geometry configuration

The baseline geometry of the microcombustor used in this work is based on the tested prototype proposed by the MIT research group for their micro gas turbine engine. The design is referred to as the 3-stack combustor (Mehra, 2000), which was similar to the micro steel combustor used by Waitz et al. (1998). The 3-stack silicon microcombustor was proven experimentally to be able to sustain a flame within the specified geometry; inner and outer chamber diameters of 5 and 10 mm respectively, a chamber and a device total height of 1.0 and 3.8 mm respectively. This in turn would result in a chamber volume of 66 mm^3. Also, for experimental testing purposes, it was possible to operate the device using non-premixed or premixed lean fuel configurations. A 2D schematic cross section of half of the 3-stack combustor by the MIT (Top) and a 3D cut away of the baseline microcombustor design implemented in this work (Bottom) are presented in Figure 3-1.

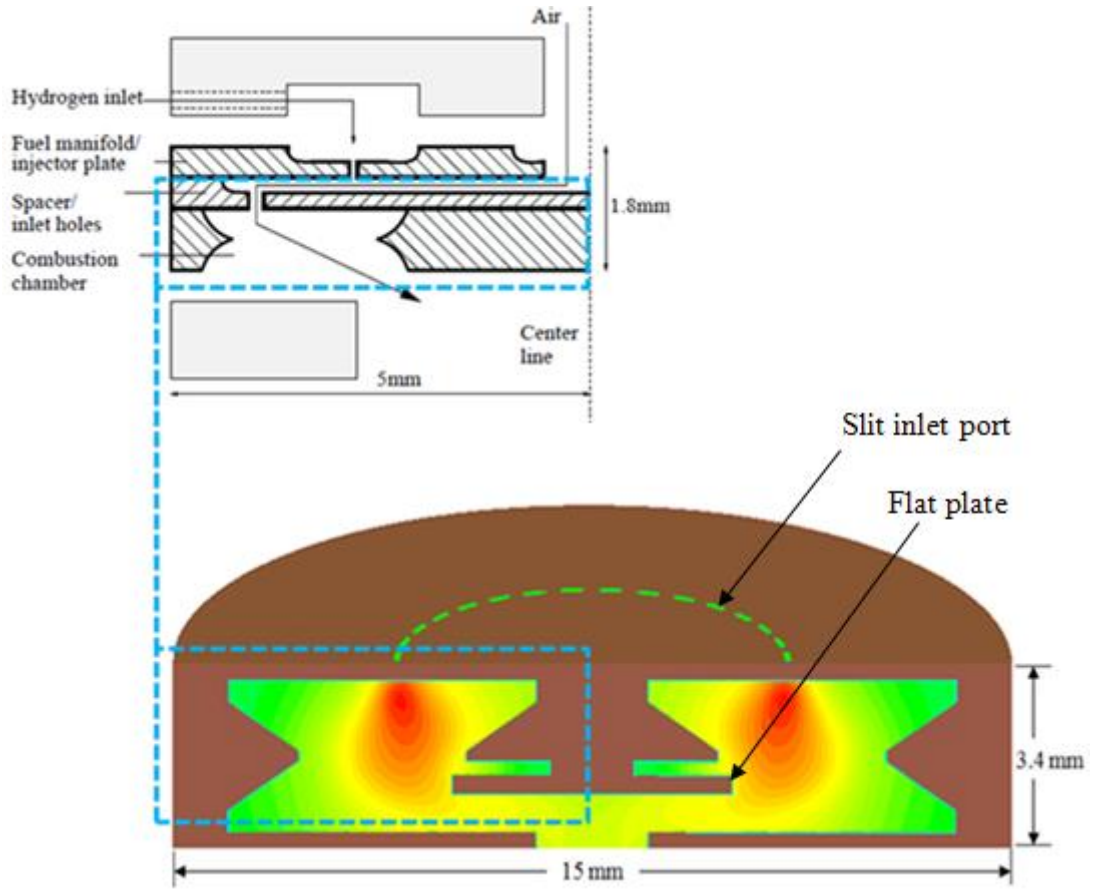

Figure 3-1: 2D schematic cross-section of half of the 3-stack microcombustor by (Mehra, 2000) – Top. 3D cross section of half of the baseline microcombustor design implemented in this work – Bottom

- **Combustor geometry and sizing**

The baseline design shown in the above figure has a total diameter of 15 mm and a total height of 3.4 mm; this resulted in chamber volume of 301 mm^3. The microcombustor was designed to use premixed hydrogen-air with an equivalence ratio varying from (0.4 - 1.0) at 1.0 atm. The reactants mixture was injected directly into the chamber through the inlet ports, and then the combustion products were designed to leave the chamber through a circular shape outlet with a diameter of 2.0 mm.

Type 316L stainless steel was chosen to model the combustor structure with the aim of manufacturing the device in-house by adopting a novel technique of the micro injection moulding - lost core approach.

- **Combustor inlet ports design**

Instead of a conventional circular inlet port, a slit shape was used as shown above in Figure 3-1. This design was chosen to provide the following:

Firstly, in order to make the combustor design physically possible to be built in-house for the first time at this scale, the slit inlet configuration must be deployed. This measure highlights one of the trade-offs between design and manufacturing feasibility for such scale device.

Secondly, the dimension of the inlet port must provide a local minimum velocity higher than the flame speed in order to prevent upstream burning which might cause a severe damage to the structure of the device.

- **Flat plate design**

The idea behind the introduction of the flat plate to the chamber design which is located above the chamber exit as shown in Figure 3-1 was to increase the fluid flow path thus, the residence time when the device operated with a high mass flow rate. It was recognised that this design will add complexity to the manufacturing process and the possibility of sustaining a maximum thermal stress by acting as an extended surface (Fin) which might result in a structure failure. Nevertheless, it was considered within the datum design in order to investigate the benefit mentioned above. In terms of an optimisation investigation, this plate was modelled using two design parameters; the plate diameter and thickness. Two design scenarios are demonstrated in Figure 3-2.

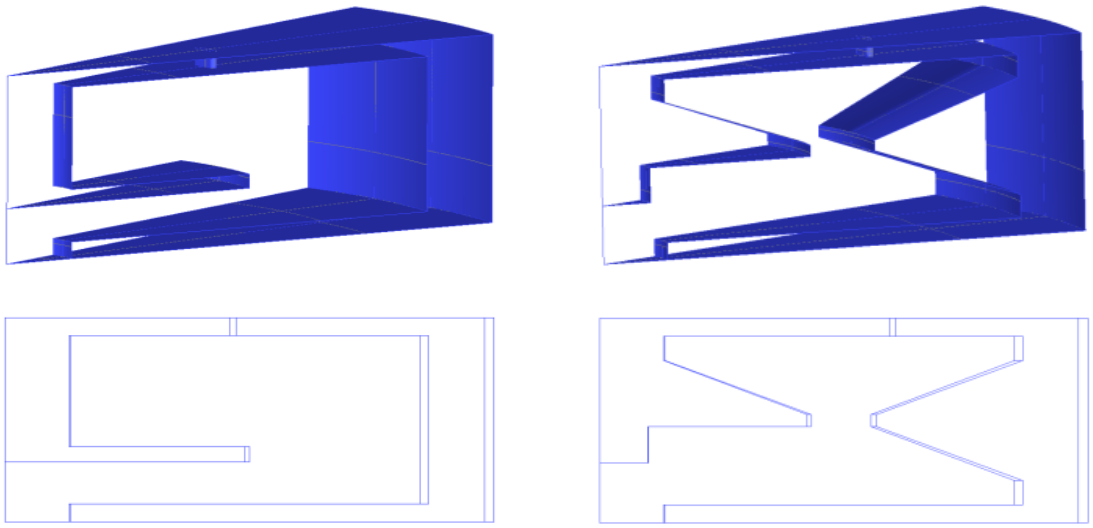

Figure 3-2: Possible design scenarios. With flat plate (left) and without plate (right)

3.2 Parameterisation

3.2.1 Introduction

Parameterisation is an important stage in any optimisation problem. The main objectives of this work are to maximise the microcombustor efficiency and at the same time minimise the fuel consumption. The computational cost of the whole optimisation process is directly proportional to the number of the design parameters hence, this number must be kept as small as possible, but sufficient to allow the optimiser algorithm to explore the design space of the problem and locate any optimal designs.

3.2.1.1 Geometrical parameters

The preliminary microcombustor baseline design was represented by 14 geometrical parameters which model the design problem. These parameters are shown in Figure 3-3 and Figure 3-4. The chamber height was defined using three parameters (P3, P8 and P9). This strategy provides the optimisation algorithm the choice of changing both P3 and P9 or either in a design scenario similar to that shown above in Figure 3-2 – right.

The baseline design parameters values and descriptions are illustrated in Table 3-1.

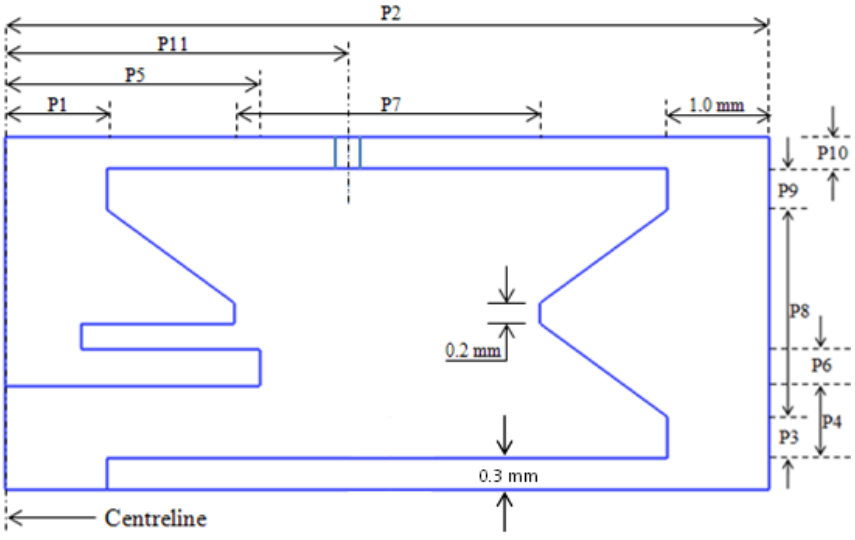

Figure 3-3: Microcombustor main geometry design parameters

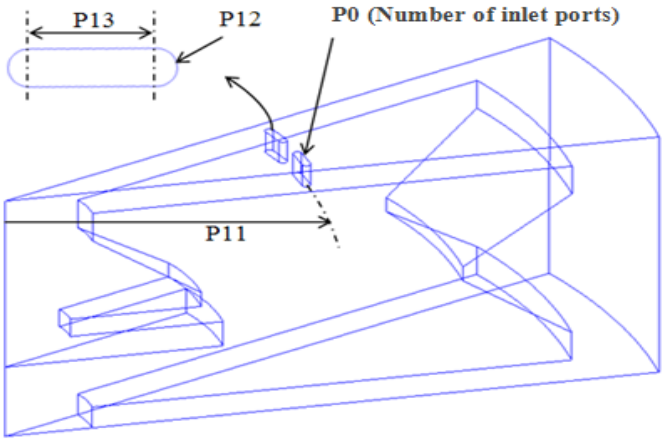

Figure 3-4: Inlet port geometrical parameters (P0, P11, P12 and P13)

Table 3-1: Geometrical parameters descriptions and the datum design parameters values

Parameter	Parameter Description	Lower limit (mm)	Datum (mm)	Upper limit (mm)
P0	Number of inlets *	1 (--)	2 (--)	3 (--)
P1	Outlet radius	0.7	1.0	2
P2	Device total radius	5	7.5	9
P3	Chamber height 1	0.37	0.4	0.8
P4	Flat plate distance to the lower wall of the chamber	0.3	0.7	0.7
P5	Flat plate radius	1	2.5	4
P6	Flat plate thickness	0.3	0.35	0.5
P7	Horizontal distance between the middle section of the chamber	1	3.0	7
P8	Main chamber height	1	2.0	3
P9	Chamber height 2	0.37	0.4	0.8
P10	Top wall thickness (inlet port layer)	0.25	0.3	0.6
P11	Inlet port location in x-direction from the device centreline	1.5	3.5	5.5
P12	Inlet port arc diameter	0.05	0.1	0.2
P13	Inlet port width	0.2	0.3	0.6

Note: (*) number of inlets at a segment of 22.5 degree and (--) refer to dimensionless

3.2.1.2 Operational parameters

The associated operational design parameters are chosen to be the equivalence ratio (ER) and the mass flow rate (MFR) of the reactants mixture.

- **Equivalence Ratio**

Equivalence Ratio is defined as the mass ratio of fuel-to-oxidiser ratio to its value at stoichiometry. One of the design objectives is to reduce fuel (H_2) consumption at normal operating conditions while at the same time targeting high power and efficiency, and a stable combustion, under the design constraints considered.

From the above definition, ER is directly proportional to the amount of fuel intake during the combustion process and thus, was chosen as design optimisation parameter.

- **Mass flow rate of the reactants mixture**

As outlined previously in subsection (1.3.1.2) that, the microcombustor power density is proportional to the mass flow rate per combustor chamber volume hence, it is important to consider this parameter in the preliminary design optimisation investigation. On one hand, increasing the MFR results in the increase in combustor power and energy released during combustion but then this increases the heat loss of the chamber to the surrounding environment due to the increase in flame temperature and thus, the external walls temperature of the device.

3.2.1.3 Microcombustor parameterisation methodology

The microcombustor geometry is represented by simple curves i.e. straight-lines and circular arcs, which is not required the implementation of a parameterisation approach such as the Partial Differential Equation (PDE) (Bloor and Wilson, 1989) or the Free-Form Deformation (FFD) (Sederberg and Parry, 1986). These two approaches can be used to represent irregular shapes such as aerofoil instead, the coordinates of the end-points of a line and points of an arc are used as design parameters in this investigation.

The microcombustor baseline design parameterisation started by choosing the location of the global coordinate system to be at the centre of the combustor exit plane as shown in the magnified view in Figure 3-5 - Bottom, where point 1 (pnt. 01) was located x=0 and y=0 coordinates, then point 2 (pnt. 02) had the same value in the y-direction, but a

P1 value in the x-direction, hence point 2 coordinates were (P1, 0). Point 3 then had a P1 value in x and 0.3 mm (lower combustor wall thickness) in y.

Randomly selected points from Figure 3-3 are highlighted in Figure 3-5 and the associated design parameters representing their coordinates are illustrated in Table 3-2.

In summary, the microcombustor height was controlled by the sum of the P3, P8, P9 and P10 parameters as well as the constant value of 0.3 mm, on the other hand, design parameter P2 was used to control the device total diameter. Therefore, any change in value applied to P4 and/or P6 by the optimiser algorithm was not affecting the device total height. Also, this was true for P5, the parameter associated with the flat plate radius, on the device total diameter.

From the above, the following question may be asked:

Is there any possibility that the combustor geometry features overlap each other when changing the design parameters within their operating ranges? And if the answer is yes, then how this can be avoided?

The answer is yes, overlapping is a possibility. Two scenarios are shown in Figure 3-6, the overlapping of the design on the LHS is caused by reducing the total height from 3.4 to 2.4 mm and P4 was set to 0.75 mm. However, scenario two (RHS) is caused by the reduction in total diameter from 15 to 10 mm and the increase in P5 from 2.5 to 4.0 mm. Geometry overlap was avoided during the optimisation process through the implementation of a set of rules within the optimiser code; any new design vector generated by the optimiser algorithm which violated one of those rules was then rejected.

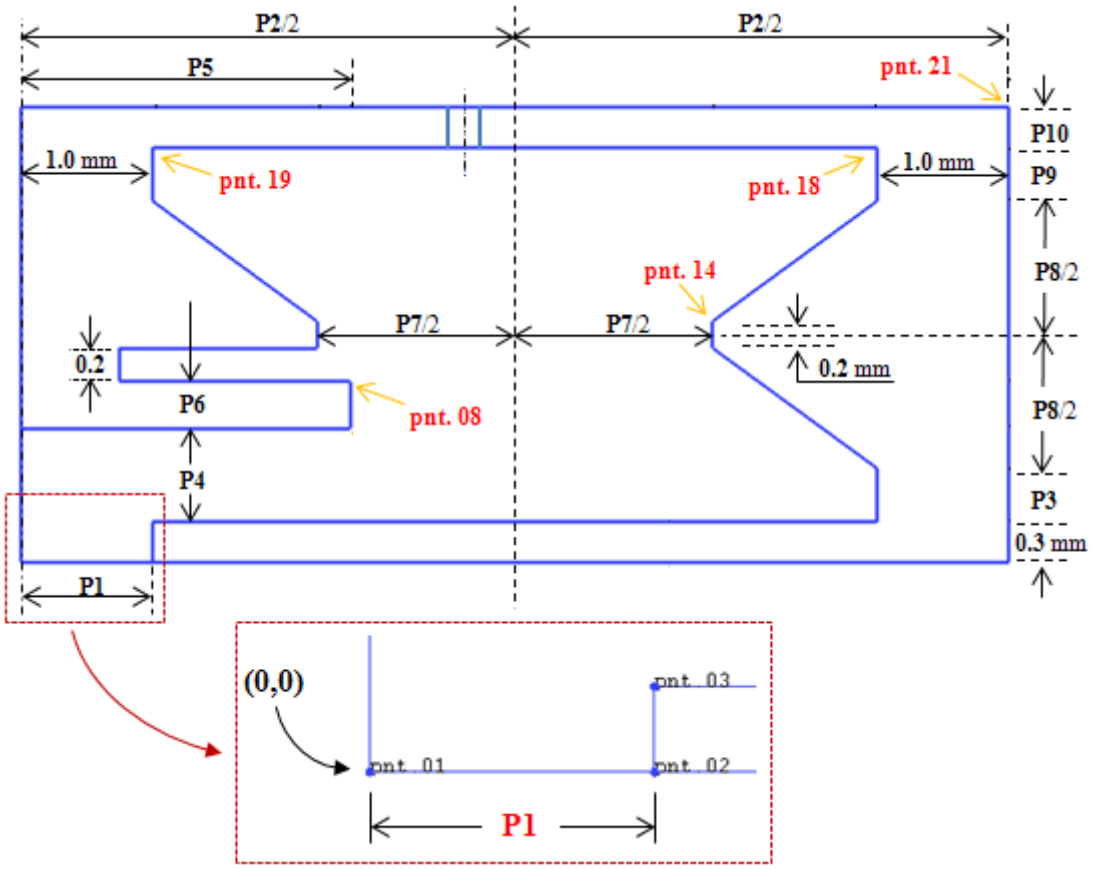

Figure 3-5: Highlights randomly selected points of the baseline combustor design and the main design variables – Top. A magnified view of the global coordinate system location – Bottom

Table 3-2: Parameterisation of randomly selected points highlighted in Figure 3-5

Point	Coordinate		Corresponding values (Table 3-1'datum')
	x	**y**	
pnt. 08	P5	0.3 + P4 + P6	(2.5, 1.35)
pnt. 14	P2/2 + P7/2	0.3 + P3 + P8/2 + 0.1	(5.25, 1.8)
pnt. 18	P2 – 1.0	0.3 + P3 + P8 + P9	(6.5, 3.1)
pnt. 19	1.0	0.3 + P3 + P8 + P9	(1.0, 3.1)
pnt. 21	P2	0.3 + P3 + P8 + P9 + P10	(7.5, 3.4)

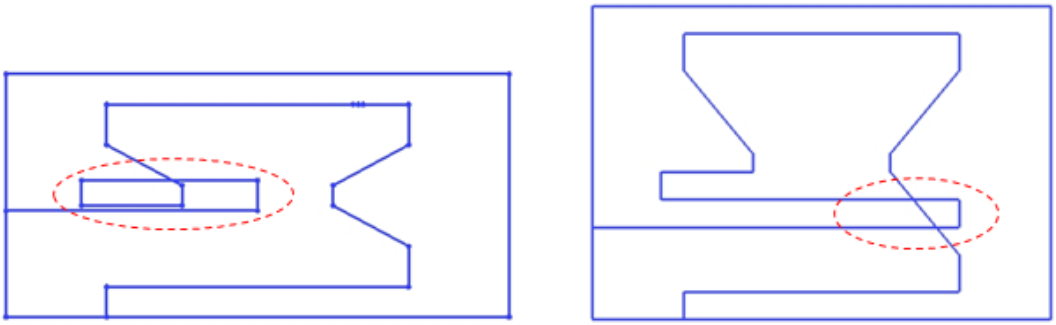

Figure 3-6: Possible scenarios of combustor features overlap. P8=1.0 and P4=0.75mm – left and P2=5.0 and P5=4.0mm – Right

In order to avoid the possible overlap scenarios shown in Figure 3-6, the following rules were respected:

For the LHS : $P4 + P6 + 0.2 < P3 + P8/2 - 0.1$

And for the RHS : $P5\ max < P2 - X$

Where X and other design parameters within the above rules are defined in Figure 3-7

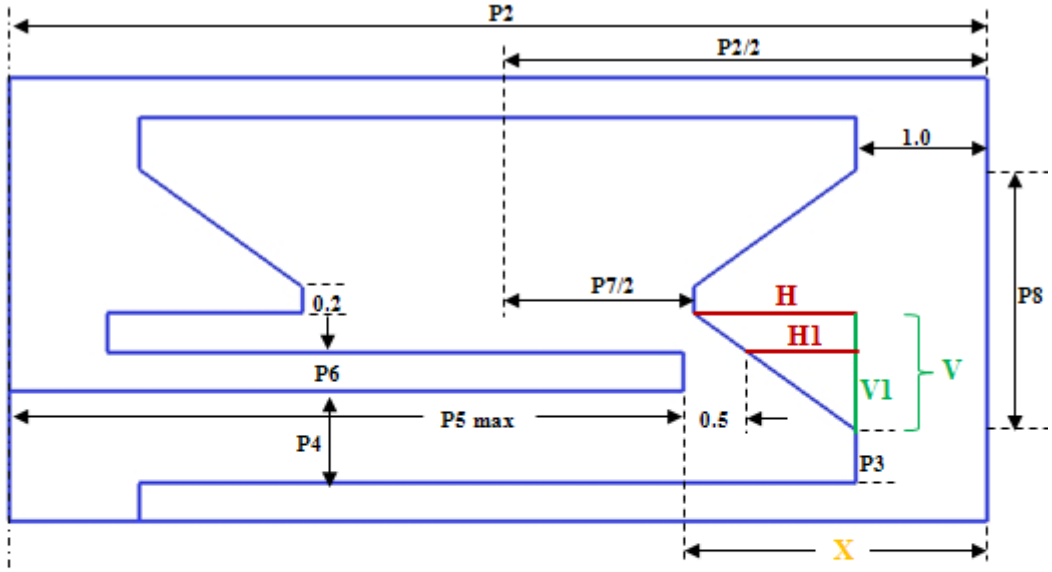

Symbol	Representative value
X	0.5 + H1 + 1.0
H1	H * V1 / V
H	P2/2 – P7/2 – 1.0
V1	P4 + P6 – P3
V	P8/2 – 0.1

Figure 3-7: Description of the design parameters within the sample of the overlap rules avoidances relations

3.3 Description of the numerical grid

3.3.1 Introduction

Such combustion problems are characterised by a complex flow field, as well as chemical reaction modelling, which both demand a high quality mesh to capture the physics of the problem. Hence another important task, after the geometry parameterisation step, is the generation of sufficiently high quality and reliable computational grids throughout the multi-objective design optimisation process. Not only does the accuracy of the CFD results depend on the mesh, but also the required computational time to solve the numerical equations of the flow field of interest. A poorly constructed mesh can lead to convergence difficulties and hence increase computational cost as well as potentially producing invalid simulation results.

In multi-objective design optimisation (MODO) study, the optimiser algorithm relies completely on the results produced by the CFD calculations which are greatly influenced by the grid quality in order to evaluate the objective metrics and upon that, it directs the search to explore a new design space and try to locate new optimum designs (Pareto Optimal Set).

3.3.2 Numerical grid representation

Different types of numerical grids can be used to represent this problem such as the structured, the unstructured and the hybrid grid. In this investigation, the hybrid grid was chosen which comprises structured and unstructured grids. The microcombustor geometry was modelled using three-dimensional section of 22.5 degree thus, the structured and unstructured grids were represented by hexahedral and tetrahedral elements respectively.

The generation of such a grid using commercial software named ANSYS ICEMCFD required a defined volume and a maximum volume element size. However, it is also possible to refine a specific part of a volume, area or a curve before the start or even after the mesh completion by assigning a smaller element size to the individuals and generates or re-generates the computational grid.

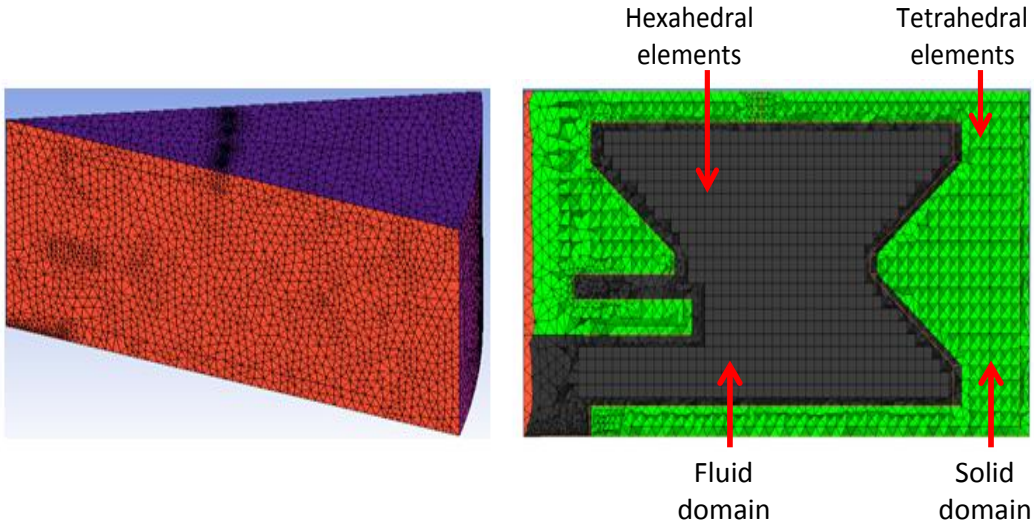

Figure 3-8: Microcombustor datum design hybrid grid. 22.5 degree isometric view - left and a cross-sectional view at midplane - right

3.3.2.1 Hybrid grid

In order to create a microcombustor hybrid grid, the mesher algorithm starts by generating (filling all design volumes with) tetrahedral elements then converting the core of the fluid domain into hexahedral elements wherever possible, but keeping the elements attached to all boundaries as tetrahedral. The conversions of those elements require the activation of "*Create Hexa-Core*" command within the desire domain (volume). Moreover, it is also easy to create boundary layers if required by selecting the boundary of interest, the initial height, the number of layers and the height ratio away from that boundary.

This type of grid (boundary layers) was not implemented within the microcombustor investigation in this work, due to the laminar nature of the flow inside the device. Then again, it was used within the numerical study of a microthruster and precisely at the convergent-divergent nozzle part of this device.

Figure 3-8 represents the hybrid numerical grid of the microcombustor baseline design.

3.3.2.2 Structured grid

Structured grid was also investigated for microcombustor numerical calculations. Figure 3-9 and Figure 3-10 represent the blocking strategies followed and the final numerical grid assembly respectively. However, the following disadvantages were

encountered when generating such a grid in the context of automated optimisation process:

- The strategy and construction of blocking to a robust level were time consuming and difficult to implement to a complex geometry as that of a microcombustor. But most importantly, it was
- Difficult to achieve a consistent mesh density (grid size) expected throughout the optimisation process. Although an "if statement" can be embedded within the replay script to control the number of nodes assigned to the individual edge of a block, it was difficult to predict all geometry design configurations.
- For this particular application, it was required to record the construction of three different grid scenarios in order to account for the possible change in the number of inlet ports i.e. from two (the baseline) to one or three thus, a major change was required to the blocking system which was a lengthy and a time consuming task.

From the above, particularly the second point, from a test case carried out to compare the results of interest achieved from the structured to the hybrid grid it was decided to use the hybrid grid in all the optimisation case studies in this work.

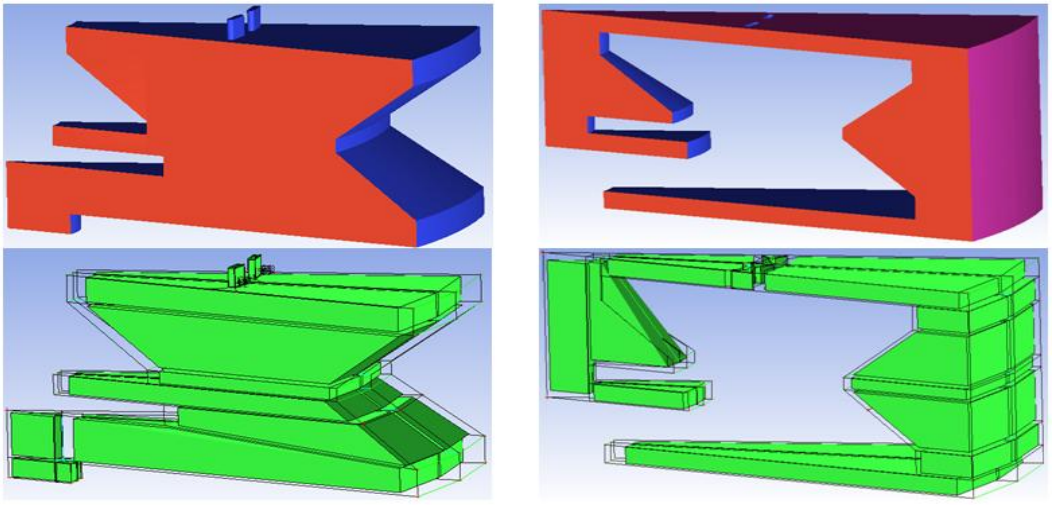

Figure 3-9: Fluid and solid blocking strategies of the microcombustor datum design for structured grid generation

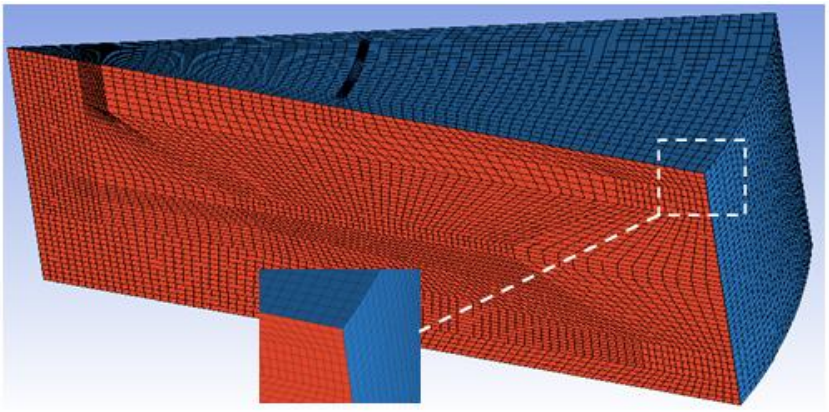

Figure 3-10: Structured grid of the microcombustor datum design at its final assembly

3.3.3 Grid optimisation study

High quality and adequate mesh in any flow field of interest are the main mesh design characteristics to obtain an accurate CFD results. Increases in the number of elements leads to the increase in computational time and no gain within the CFD results accuracy and a reduced grid size results in an inaccurate prediction of the results therefore, finding the necessary balance (grid optimisation) between the two is crucial factor to be considered in a multi-objective optimisation.

Norton and Vlachos (2003) studied optimal node spacing and density of a 2D microcombustor model which reduces computational cost within the required numerical calculations accuracy. They found that by using very coarse mesh the CFD calculations failed to capture the required flow metrics, but when a fine grid was implemented the numerical solutions obtained were more accurate. A similar investigation was carried out by Motsamai et al. (2008) to find the right balance between grid size and computational cost in a multi-disciplinary design optimisation of a combustor problem.

From the above, and in order to optimise the microcombustor grid, different types of hybrid mesh configurations were considered starting from a grid size of approximately 93000 elements up to 224000 as shown in Figure 3-11.

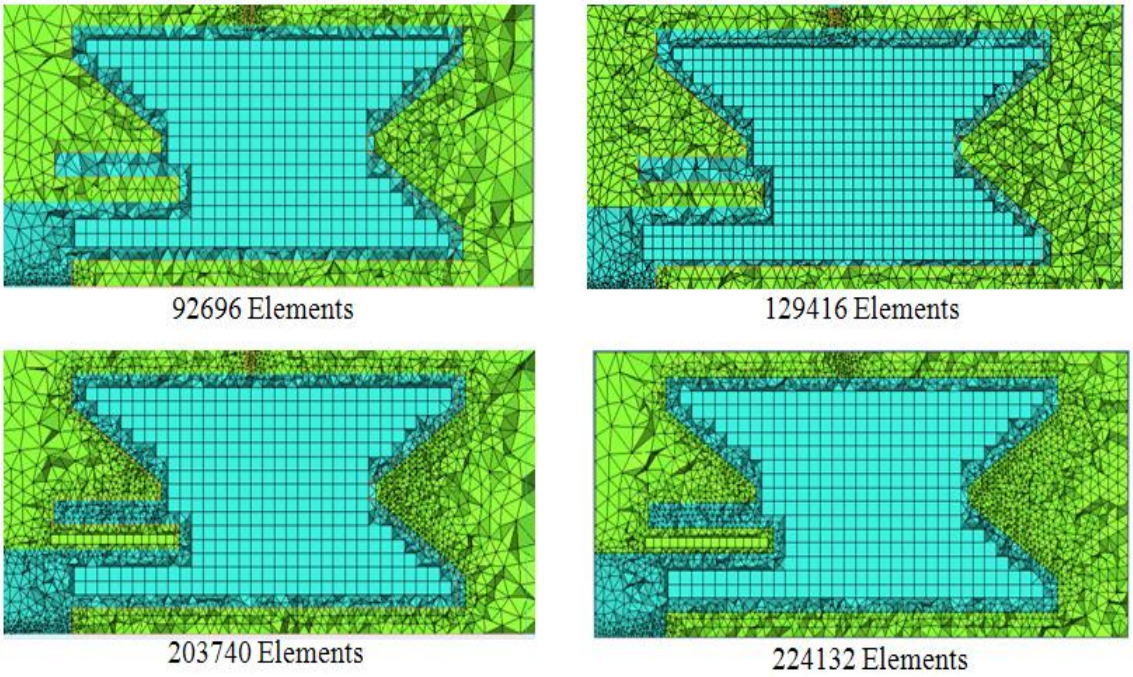

Figure 3-11: Different grid density combinations of the datum design at a midplane section

The CFD simulation results using the CFX - Eddy dissipation combustion model[1] showed that increases in maximum volume element size of the fluid domain i.e. coarsen the total grid from 129416 to 92696, led to non-converged solutions.

On the other hand, when the mesh density increases above 129416 elements, the results obtained from the CFD calculations shown in Table 3-3 demonstrated no significant difference in the flow metrics results of interest at a convergence target criteria of 1.0E-06 set to all numerical equations.

From the above investigation, the optimum microcombustor datum grid size was mainly influenced by the following mesh parameters: The fluid volume element size and the surface element size of the interface wall (contact area between fluid and solid domains).

The optimum grid parameters setting of the datum design which correspond to a grid size of 129416 elements obtained from the above study cannot be used to model the numerical grid of all possible design configurations generated by the optimiser algorithm during the optimisation process.

[1] The Reynolds number calculation at the combustor inlet (based on mean flow velocity and hydraulic diameter) suggested the flow inside the chamber of the datum design is predominantly laminar. The use of the EDM model was intended to capture any turbulence effect of the type reported by Sjostrand and D'Angelo (2011) in a similar non-premixed, centimetre-scale combustor.

Table 3-3: CFD simulation results obtained from different grid sizes of the datum design

Grid size	129416	203740	224132
Fluid maximum velocity (m/s)	8.22	8.43	8.36
Outlet velocity (m/s)	4.69	4.69	4.69
Fluid maximum temperature (K)	1483	1492	1482
Outlet temperature (K)	1166	1167	1166
Interface wall temperature (K)	686	693	692
Upper wall temperature (K)	662	669	668
Vertical wall temperature (K)	658	664	664
Lower wall temperature (K)	659	665	665
Heat convection upper wall (W)	0.103	0.105	0.105
Heat convection vertical wall (W)	0.091	0.093	0.093
Heat convection lower wall (W)	0.045	0.046	0.045
Total Heat Loss (W)	0.240	0.245	0.244

For example, for a new combustor geometry with a total radius of 5.5 mm and a total chamber height of 1.8 mm, which in comparison is smaller in chamber volume to that of the datum design, using the optimum grid settings found above will lead to a coarse grid as shown in Figure 3-12 – left, and this may affect the accuracy of the CFD results.

Therefore, to overcome this issue during the optimisation process, four microcombustor geometry scenarios have been considered depending on the combustor total diameter (P2) and chamber height (P3, P8 and P9), where both extremes in terms of the total volume of the chamber are covered. Advantage was taken of the datum grid parameters analyses outlined above by identifying the influential parameters to find compromise values that produce a relatively small grid size with acceptable numerical results, as well as minimum computational cost. The results are presented in Figure 3-13 which maps the influential grid parameters settings as a function of the microcombustor geometrical features where the x and y axes represent the device radius and the chamber total height respectively. These values are assigned to the correspondent geometry configuration by the optimisation algorithm during the optimisation process.

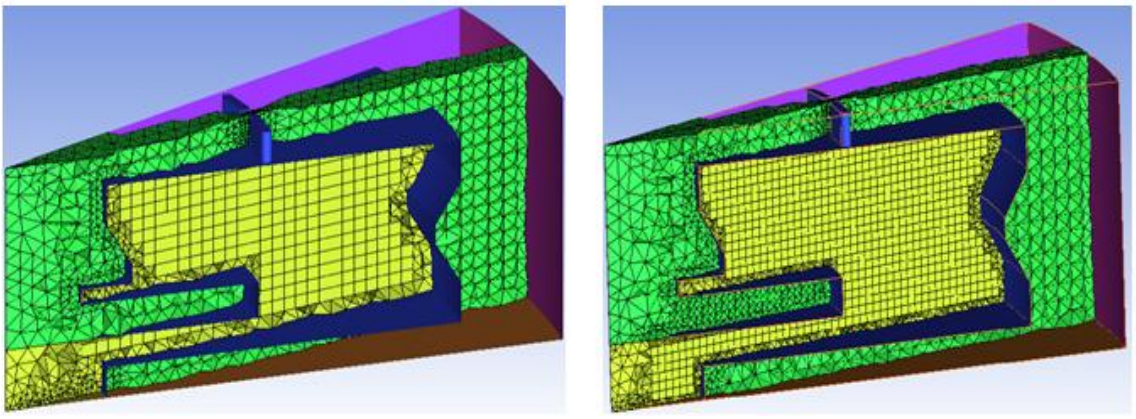

Figure 3-12: A coarse grid resulted from using the datum grid parameters values (left). A fine grid achieved after tuning the grid parameters (right)

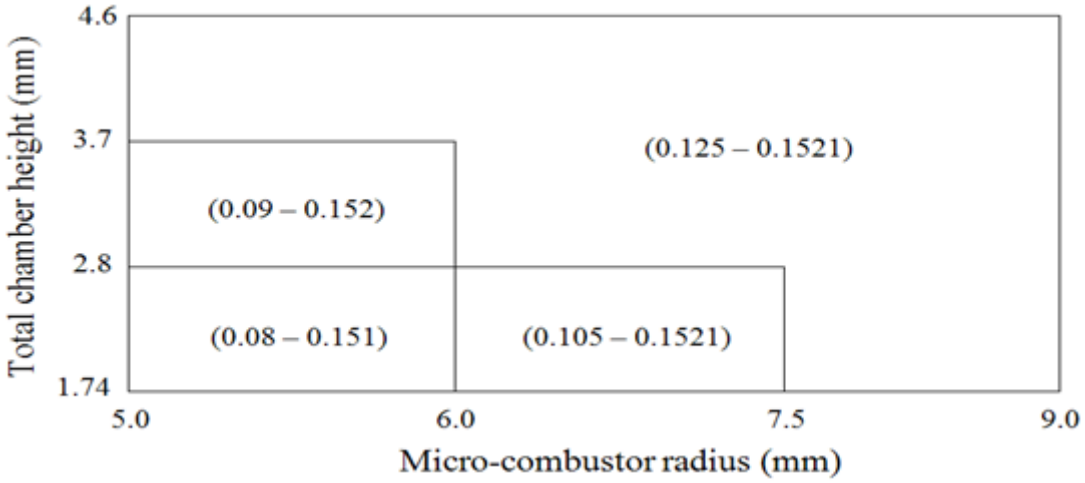

Figure 3-13: Grid density setup within the optimiser algorithm

Note: Values in ( ) are fluid maximum volume element size – interface maximum surface element size. Also, these values are dimensionless[2]

[2] The grid generator used (ANSYS ICEMCFD) is dimensionless. The maximum volume element size does not mean the actual element volume i.e. 0.08 is not 0.08 mm^3. It is the spacing between two nodes of a single element. This is also true for the surface element size.

3.4 Chapter summary

This chapter presented the microcombustor initial design configuration, the main geometry features and sizing, type of fuel intended to be used and structure material considered. Moreover, it outlined all design parameters used within the optimisation investigation and detailed the parameterisation approach adopted to automatically generate new microcombustor design configurations and also, briefly discussed some of the design rules respected in order to avoid design features overlapping which lead to infeasible design.

Furthermore, it presented the numerical grid used and also investigated the possibility of using another type of grid and outlined the drawbacks associated with it. Finally, a grid optimisation study was carried out in order to find the influential grid parameters settings that offer a balance between grid size which leads to an acceptable CFD results accuracy and optimisation cost. As a result, a map of those parameters was presented as a function of the device total radius and chamber total height.

Chapter 4
Multi-objective design optimisation

This chapter introduces the optimisation, the need for optimisation in an engineering environment and discusses previous implementation in combustion devices. It also discusses the choice of a particular algorithm. Furthermore, it presents an overview of the developed multi-objective Tabu Search and is main space exploration features and enhancements.

4.1 Introduction

The increase in popularity of numerical simulation methods in the product engineering environment has resulted in significant reduction in product design cycle and development costs. Results obtained from numerical simulations in different product design disciplines when compared with their counterparts from experiments have demonstrated reliability, high level of accuracy and in some scenarios such as in micro-scale combustion devices, the ability to provide an insight into the flow fields and combustion behaviour in a microchamber where no experimental test currently does. Therefore, more designers particularly in industrial companies are confident using such methods in modern product design and development environments. Due to the advances in engineering in the last half century, a reduction of 60% in the operating cost, an increase in thrust-to-weight ratio by 70%, a reduction in unburned hydrocarbon (UHC), CO, smoke and soot by 90% and a NOx emission reduction of 40% have been achieved in aircraft engine performance (Jones et al., 2001).

However, a product designer still encounters increasing demand toward a further reduction in a product design cycle, product complexity, quality and performance due to the competitive nature of the current market even with the help of modern numerical simulation techniques. Numerical results achieved by applying certain boundary conditions do not necessarily correspond to the optimum design configuration even with the currently available numerical tools and computational power. This required all the designer's expertise and knowledge gained over the years to find the right geometry and or boundary conditions combinations in order to achieve near optimum design

performance. This is achieved by tuning the influential design parameters in a trial and error approach; this is a tiring, lengthy and time consuming process. Even when the optimum performance of a design was found, the influential parameters setting are still unique to the problem under investigation and cannot be used in future product development.

This is true for the design of a micro-scale combustor for power and propulsion applications. These parameters for example, reactants mixture mass flow rate and fuel-air ratio (FAR) which have conflicting outcomes on the design objectives such as maximising the overall efficiency and at the same time minimising the fuel consumption. On the other hand, the complex and nonlinear response of the design space to the objective space[3] (Myers et al., 2009; Forrester et al., 2008; Kipouros et al., 2008) of a combustor makes the manual optimisation job harder if not challenging to achieve the optimum combustor design performance.

Lefebvre (1998) has stated that a design of a staged combustor has been considered by some designers, which implies from the method name "*staged*" that a combustor is divided to sections or zones where a single design objective is optimised by targeting specific combustion performance at the individual zone. For example, improved mixing of reactants at the mixing zone or optimise the pattern factor at the dilution zone. However, the outcome of the design performance of the whole device (optimum zones collectively) showed that improved performance objectives could not be achieved at lower cost and within a reasonable time.

Therefore, fine tuning the design parameters to achieve the optimum performance of the device necessitates the use of an automatic optimisation process in some parts of the design cycle such as performance improvement and design robustness.

Rinz and Mongia (1986) stated that scaling combustors and obtaining improvement in technology levels are some of the limitations of the conventional optimisation methods. Also, the previously developed empirical methods for particular design configurations may not be applicable in future designs for more advanced or novel combustor concepts (Motsamai et al., 2008). Moreover, the use of the conventional optimisation techniques

[3] This relationship between the design parameters and the responses of the objective functions will dictate the type of optimiser to be used and its respective settings.

in the design of a combustor and due to a number of strongly linked design variables, a complex and nonlinear design space usually with more than one conflicting design target, made the application of the traditional methods practically challenging in this design field (Rogero, 2003).

The modern metaheuristic[4] optimisation (non-traditional optimization) methods emerged in recent years as powerful techniques for solving complex optimization problems in engineering by overcoming the issues represented by using the conventional methods. These are genetic algorithms (GA), simulated annealing (SA), Tabu Search algorithm (TS), particle swarm optimization (PSO), ant colony optimization (ACO) and many others (Rao, 2009).

4.2 Selection of an optimisation algorithm

The correct selection of an algorithm for a given problem as stated by Yang (2010) mainly depends on

- Type of the problem
- Algorithm's nature
- Solutions quality
- Available computing resource and time frame
- Algorithm implementation availability, and finally
- Knowledge of the decision maker

In the design optimisation of a combustor, which is a type of problem where the design space is highly complex and nonlinear, the traditional algorithms such as hill-climbing and downhill simplex which are derivative- (gradient-) based are local search algorithms in nature and they tend to be trapped in local minima. Figure 4-1 presents a schematic of an optimisation problem with a single design parameter and a single design objective. If a gradient-based algorithm is to be used starting from point 1 then it would possibly find the global minima of the problem. On the other hand, if the same algorithm started from point 2 then it is likely to get trapped in the local minima. This

[4] There is no common definition for the term metaheuristic. Metaheuristic derives from the composition of two Greek words. *Heuristic* derives from the verb *heuriskein* which means "to find", while the suffix *meta* means "beyond". Metaheuristics is a category of algorithms that deploy high-level strategies (diversification and intensification) which guide an underlying, more problem specific heuristic, to increase their performance. (Blum and Roli, 2003; Bianchi et al., 2009)

then presents a risky strategy based on pure luck of finding the global minima when implementing such algorithms in such a problem. Therefore, a global search for optimum designs represented by one of the modern metaheuristic algorithms mentioned in the previous subsection (GA, SA, TS, etc.) should be deployed.

In a practical environment the available computational time and power dictate the type of algorithm to be used. Also, a compromise between the available optimisation time and the quality of the solution must be decided which means achieving good solutions (not the best) within the available time frame (Koziel and Yang, 2011). In terms of optimisation time and as a rule of thumb for engineering practice, it is appropriate to perform an optimisation involving the implementation of CFD solver to evaluate the targeted objective when the duration of a single CFD run does not exceed a few hours at most (Thevenin and Janiga, 2008).

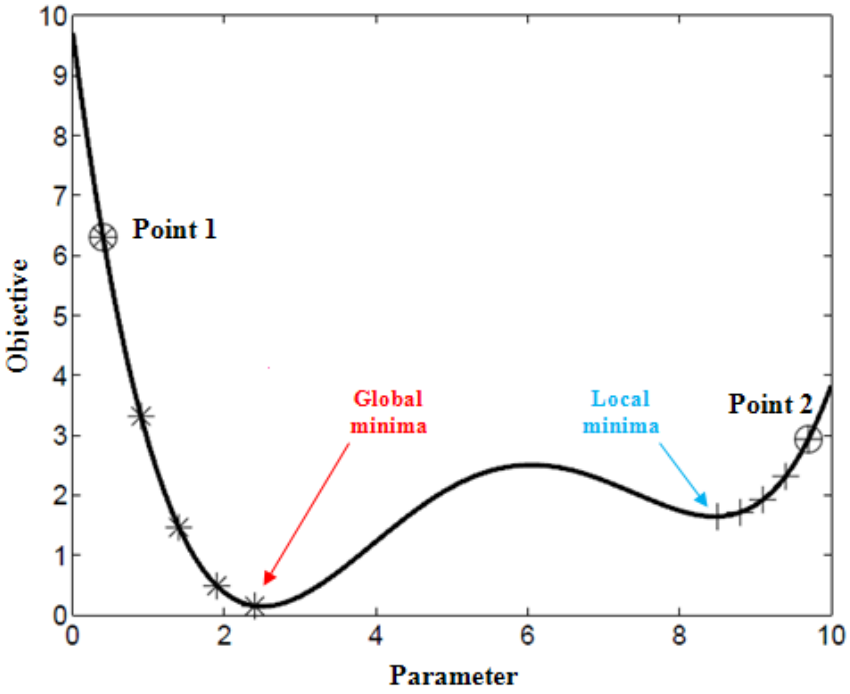

Figure 4-1: Schematic of an optimisation problem with a single variable and a single design objective

(Thevenin and Janiga, 2008)

4.3 Optimisation of combustion problems – Previous investigations

In many engineering design fields, the implementation of optimisation techniques within a product design cycle help the designers not only by carrying out the iterative (trial and error) design process for performance evaluations, which eventually improves profitability, but also obtaining new configurations or improving the existing design performance and in some cases it finds a novel design.

In combustion, a method for achieving optimum mixing performance in a tubular gas turbine combustion chamber was presented by Lefebvre and Norster (1968). A number of graphs were constructed based on series of experimental data on the flow and mixing characteristics with the ultimate aim of facilitating the design procedure of a tubular combustion chamber.

Murthy (1988) simplified a combustor design process by developing a one-dimensional computer code based on experimental tests and empirical data to reduce the workload and helps conventional combustor designers in the preliminary design and evaluation stages. As the code was developed based on experimental test data, in order to use such a computational program in different combustor designs and to achieve reasonable accuracy, the new design must be similar to the tested design.

Stuttaford (1997) developed a one-dimensional code using a network algorithm which divides the combustor under investigation into a number of independent interconnected semi-empirical sub-flows with the ability to be applied to any gas turbine combustor type. The author also suggested that the code could be enhanced significantly if it is to be integrated with a decision based algorithm such as GA.

Despierre et al. (1997) carried out a preliminary design optimisation of a gas turbine combustor for the first time using a genetic algorithm coupled with a previously developed one-dimensional code by Stuttaford (1997). The design problem also considered all heat transfer mechanisms (conduction, convection and radiation). Simple design requirements were used to demonstrate the capability of the developed optimisation method.

Buche et al. (2001) performed an automated design optimisation of the spatial distribution of fuel injection rates in a gas turbine burner using an evolutionary algorithm. The problem consisted of eight design parameters and two objective functions represented by the emissions and the burner pulsation. The evaluation tool of

the design objectives was an experimental test-rig for a gas turbine burner. The authors concluded that the automated optimization using multi-objective evolutionary algorithm can be considered as a supporting tool in the design process of a gas turbine combustor.

An extended optimisation investigation into the latter (Paschereit et al., 2003) kept the same design objectives but implemented 16 design parameters (16 fuel injectors) which controlled the amount of fuel entering the chamber from the individual fuel injector. The chosen compromised design achieved a reduction of 30 % in NO_x and attained the same initial design pressure pulsation.

Rogero (2003) developed a genetic algorithm based optimisation tool for the preliminary gas turbine combustor design. The optimisation algorithm was integrated with a semi-empirical simulation solver based on network algorithm previously proposed by Stuttaford (1997) also the developed tool was able to handle a large number of design parameters up to 30. But in order to achieve a detailed and accurate design where the results are greatly influenced by the dimensionality of the flow inside the combustor, such as exhaust temperature profile and hot spots predictions which cannot be captured using one-dimensional modeller, a CFD solver must be used.

Catalano et al. (2006) presented the design optimization of a duct-burner for combined cycle and cogenerative plants using finite-difference gradient based optimisation with the objective to firstly minimise the outlet temperature gradient and secondly to minimise the near-wall temperature of the combustion zone. Optimum designs were achieved with respect to their targeted objectives. This optimisation study was only considering a single-objective design a time which highlighted again the limitation of using a gradient based algorithm in such a complex and nonlinear design problem.

Janiga and Thevenin (2007) implemented a fully automated optimisation system consisting of an in-house two-dimensional CFD code combined with an optimisation algorithm in order to minimise the CO emission associated to a laminar burner by varying the fuel/air ratio. Two different optimisation algorithms where tested the first was Simplex by Dantzig and Thapa (1997), a proven gradient based algorithm known from literature that often get trapped in a local minima, and the other tested algorithm which demonstrated its superior search by finding a global minima, which was the GA, an evolutionary based algorithm.

Motsamai et al. (2008) carried out an optimisation work with the objective of smoothing the exhaust temperature profile of a can-type atmospheric combustor by integrating a 3D CFD solver with a gradient based algorithm. The authors reported an improvement in the combustor performance regarding the targeted design objective. This case represented a single design objective with a relatively small number of design variables (four in total).

Other optimisation work related to combustion devices is that of Edwards et al. (1998) where the genetic algorithm is used to reduce an 18-reaction with ten species network, where the quality of the optimisation results was compared with global solutions found using complete enumeration.

Foli et al. (2006) studied the performance improvement of a micro heat exchanger channel by implementing firstly an analytical approach coupled with a CFD solver then a multi-objective design approach replacing the analytical one. In the latter, two conflicting objectives, the heat transfer and the sum of pressure drops (Cold & hot channels) and ten design parameters were considered. The NSGA-II algorithm (Non-dominated Sorting Genetic Algorithm) was deployed representing the optimiser. The results of the multi-objective optimisation were a Pareto optimal set and the chosen optimum design was found to outperform the design obtained from the analytical approach.

4.4 Multi-objective Tabu Search algorithm

4.4.1 The choice

As learned from past literature the selection of an optimisation algorithm is dictated by the point mentioned in section (4.2). The design of a micro-scale combustor involves fluid dynamics, combustion reactions modelling and heat transfer which makes the design space of the problem highly constrained, complex and nonlinear. Moreover, the optimum design performance of a device to be used in real-world applications suggests that there are many design objectives can be targeted during the design and development phase. For example, maximum power density and efficiency, lower emissions and pressure drop, combustor instability due to pressure pulsation, smooth exhaust temperature traverse, minimum manufacturing cost and meeting durability design requirement. These objectives are usually conflicting which implies the use of multi-objective optimisation algorithm in order to find an optimum design satisfying the

design requirements and constraints. Therefore, a multi-objective optimisation algorithm is required in this research project. The Multi-objective Tabu Search (MOTS) has been used which is a heuristic optimisation technique that exhibits local search characteristics and it has the capability of locating global optima in a highly constrained and complex design space. The philosophy behind the Tabu Search algorithm was presented in detail by Glover (1986) which he viewed as a "meta-heuristic" superimposed on another heuristic approach. The algorithm locates optimality by a strategy of forbidding certain moves mainly to prevent revisiting previous candidate design. This was achieved by constructing a Tabu list which records information about moves recently made.

Al-Sultan and Al-Fawzan (1997) developed a hybrid algorithm which consisted of the Tabu Search and Hooke & Jeeves algorithms with the aim of finding the global optima for an unconstrained optimisation problem.

An enhanced continuous Tabu Search was developed by Chelouah and Siarry (2000) for global optimisation of multi-minima functions. It was constructed to follow Glover's TS basic approach as close as possible. A diversification move was performed first in order to locate the most promising search area then the search continued by performing the intensification move within one promising area identified previously. One of the main findings was its good performance for a large number of design parameters (greater than ten).

A study was made by Hedar and Fukushima (2006) where a continuous, nonlinear global optimisation method was developed. The TS algorithm was combined with the Nelder-Mead method (a gradient based algorithm), the Pattern search method which is an exploratory move, a subclass of a direct search method to generate a trial moves (Hedar and Fukushima, 2004) in addition to diversification and intensification search moves. In conclusion, high quality results were obtained from the developed method.

Youssef et al. (2001) compared the performance of the GA, SA and TS on the floor-planning problem of VLSI (very-large-scale integration) circuits. All tested algorithms were judged upon certain criteria among those, quality of best result achieved, exploration of the design space and the optimisation time required. The TS came first followed by the GA and finally the SA.

Tabu Search algorithm has been implemented in a range of problems such as flow shop scheduling, time tabling, and architectural design (Al-Sultan and Al-Fawzan, 1997). However, this does not mean that the TS algorithm has a superior performance to all other optimisation algorithms. According to Wolpert and Macready (1997) for any algorithm, higher performance over one group of problems is compensated by lower performance over another set of problems.

Tabu Search algorithm has been selected as the optimiser for continuous, nonlinear and constrained optimisation problems in this current research investigation. This is based on the success achieved in the aerodynamic field, specifically shape optimisation, by Kipouros et al. (2008) who studied axial compressor blades optimisation, and Trapani (2009) who addressed the design of multi-element aerofoil. Also in structure optimisation, Singh (2008) investigated the optimisation of an aircraft turbo cooler system and D'souza (2008) who studied the structural design of gears in helicopter transmission systems and in fluid dynamics field as in the work of D'ammaro (2010) who optimised the performance of micro-reactor mixing problem. Therefore due to the similarity of problems, it is anticipated that there will also be a benefit from the same merits for the design optimisation of micro-scale combustors.

4.4.2 MOTS overview

MOTS code was first developed by Jaeggi et al. (2005) building on the single-objective TS algorithm for continuous optimisation problems developed by Harvey (2002), and described by Dawes et al. (2003). The underlying strategies of the MOTS algorithm are listed as follows: - see also Kipouros (2006)

1. Exploration mechanism
2. TS memories
    - Short Term Memory (STM)
    - Medium Term Memory (MTM)
    - Intensification Memory (IM)
    - Long Term Memory (LTM)
3. TS specific moves
    - Search intensification (SI)
    - Search diversification (SD)
    - Step Size Reduction (SSR)
4. Parallelisation of TS

4.4.2.1 Exploration mechanism

In order to make clear precisely how the design space investigation precedes, the exploration mechanism is shown in Figure 4-2 where three random design variables are considered just for demonstration purposes. It is based on the single-objective TS implemented by Conner and Tilley (1998). This mechanism uses Hooke and Jeeves (H&J), the best-known direct search method as described by Lewis et al. (2000). The TS search process can be summarised as follows:

- Step 1 - Figure 4-2

  The search starts from an initial point (datum) in the design space with its design vector and objective functions' values being known.

- Step 2

  New candidate points are generated by H&J's method. The number of the candidates to be generated is called "n_{sample}" which is pre-set to a value equal or less than twice the number of design variables (n_{var}) i.e. $n_{sample} \leq 2\ n_{var}$. The cost of an optimisation of a real-world engineering design problem, usually with many design parameters, becomes extremely expensive if not impossible to be carried out and thus this element (n_{sample}) is created to overcome this issue by reducing the sampling points to a manageable number in this step. In addition, each individual parameter (variable) increases and decreases by the same step size (SS) value (will be discussed in the next chapter) in which the overall number of parameters are equal to $n_{sample.}$ For example, if the problem in hand consisted of three design parameters then at the H&J step (Step 2) and after assigning the corresponding step sizes (-SS & +SS) to the individual parameter, the accumulated number of candidates to be evaluated in the next step is equal to six which in terms represents the n_{sample}. Moreover, all the sampled points are now stored in the *short term memory* (STM). This memory is designed to prevent revisiting the recently visited (Tabu) point by the optimiser algorithm. It is also designed in a way that the first stored visited point will be removed from this memory at the addition of a new point (first-in-first-out approach). Also, the STM is constantly updated at the end of each search iteration.

- Step 3

  The sampling points are evaluated individually and their corresponding objective functions are obtained. In this research work, this is achieved by obtaining the

numerical results from the CFD calculations. Moreover, to reduce the optimisation cost, the developed parallelisation capability of the algorithm is deployed herein where the evaluation of the sampling points are carried out in parallel using message passing interface (MPI).

- Step 4

  In this step, the evaluation of the numerical results by means of the objective functions' values are examined. If a value of one of these sampling points dominates the current base point then it superseded the base point. In the current scenario shown in step 4 – scenario-a, there are four points with better values than the base point, thus a randomly selected one within those is used as the new base point and as for the others (1, 3 & 4), they are stored in the search *intensification memory* (IM). Step 4 scenario-b shows that there is no recently evaluated point with better objective performance than the current base point. Therefore, a randomly selected point among those is used as the new base point and the search starts again from Step 1.

- Step 5

  If a point found to dominate the base point in scenario-a, then the vector of this point is increased or decreased by the same step size value given initially in Step 2 (in this scenario, the value was + SS as previously assigned in Step 2 for point 2) in order to perform a search pattern move. The idea behind this is that the search speed can be increased along a previously investigated downhill direction.

- Step 6

  The new point is evaluated in similar fashion as in Step 3 and the results of the objective functions are obtained.

- Step 7

  If the new point performance in terms of the targeted objectives are found to be worse than the base point then the randomly selected point in Step 4 is used as a new base point – scenario-a and the search continues from Step 1. On the other hand, if it is found to be better (scenario-b) then this point is used as the new base point. Again, the search is resumed from step 1.

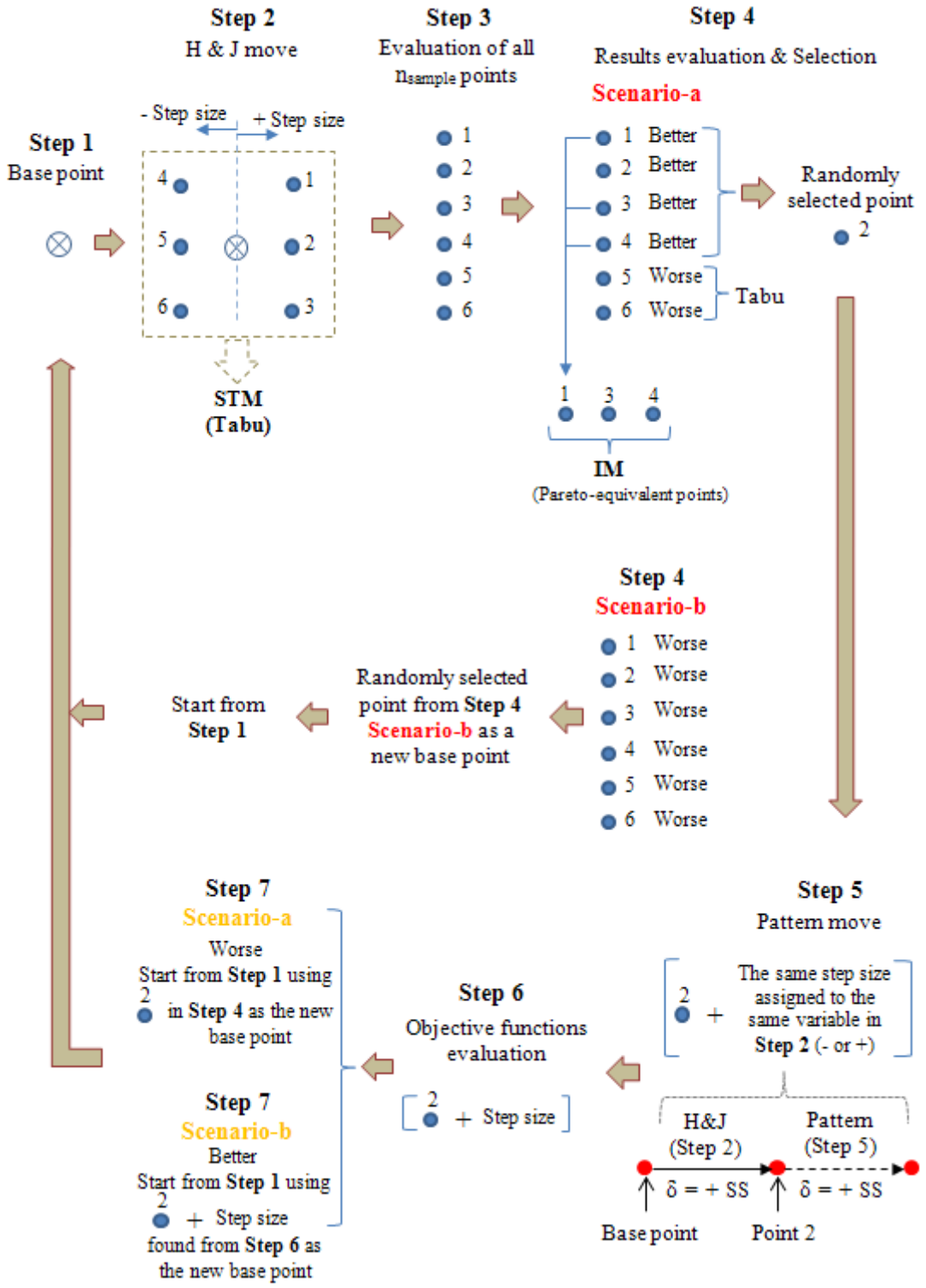

Figure 4-2: Modified version of Hooke & Jeeves's move implemented in the MOTS algorithm

4.4.2.2 TS memories

There are four different types of memories used by the TS algorithm to direct the search of a complex design space and they are:

- Short term memory (STM)

  This was explained in the previous subsection Step 2.

- Medium term memory (MTM)

  This memory is created to store all the Pareto optimal points found as yet during the search of a design space. The points in this memory are characterised by being non-dominant to each other and potentially represent the final optimum designs to be found.

- Long term memory (LTM)

  This memory keeps a statistical record of the entire design space and it is used when the TS required performing *search diversification* (SD) when certain conditions exist in order to explore less visited regions in the design space. This is done by monitoring the individual design variable usage within its operating limit. Before any search is performed, all design parameter's limits are divided into small ranges allocated by the designer. In the example shown in Figure 4-3, the parameter design space is divided into four regions and if it is assumed that region 3 is least visited i.e. C < A, B, D then when SD is performed, a random value from region 3 is used and this is true for the other design parameters (different regions might be used).

- Intensification memory (IM)

  This was explained in the previous subsection Step 4 that this memory stores the point which dominates the base point after H&J's move and it is not selected to supersede the base point. This memory is updated after the completion of a search iteration cycle and if a new point is added to this memory that dominates any existing point, then the latter is eliminated. Points are stored in this memory called the *Pareto equivalent* as they should be on or near the Pareto front thus the IM can be reviewed as a part of the MTM.

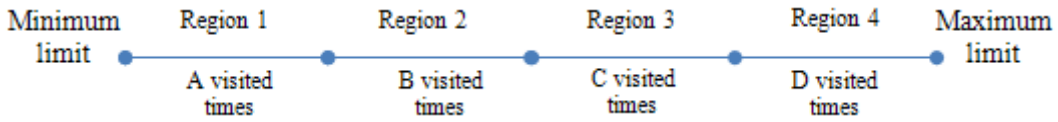

Figure 4-3: Operating limit segmentations of a design variable

4.4.2.3 TS specific moves

In order to track the number of iterations performed by the algorithm, a local counter called *i_local* is implemented. The maximum allowed number of unsuccessful iterations in finding a point in the design space that dominates a point stored in the MTM is predefined to a value chosen by the designer based on experience. The iteration counter allows the TS algorithm to control important features, the SI, the SD and the SSR moves during the optimisation process. For example, the algorithm performs SI when the i_local reaches a user-defined threshold's value of search intensification by selecting a random point stored in the intensification memory (IM) in order to intensify the search in the optimum zone of the design space. If the search continued without any success of finding a new base point until the i_local reaches a predefined threshold value of search diversification (SD) then the algorithm checks whether there is enough points in the IM, i.e. the IM has a number of points above the pre-set threshold value, then the algorithm performs SI rather than SD with the logic that there are enough candidate designs to be tested from the Pareto-equivalent set (Intensification Memory) when the intensification move is executed. On the other hand, if the IM size is below its pre-set value, then the TS performs SD by randomly selecting a design vector using the information provided by the LTM. These features are shown within the TS flow chart in Figure 4-4.

Finally, if the search is exhausted in finding new design after the SD execution and at the time where the i_local reaches the threshold value of *reduce*, then the TS algorithm performs step size reduction (SSR) move by selecting a random point from the MTM (optimal point) in order to vigorously investigate the neighbouring area of the selected optimum point.

The i_local is reset to zero by the algorithm after a successful addition of a point to the MTM, also after each SSR move.

In the case of continuing unsuccessful moves the order of performing SI followed by SD can be flipped by increasing the SI threshold value to one greater than that of the SD. In this

current investigation this order was kept as presented in Figure 4-4 following the success achieved by Kipouros (2006) in the design optimisation study of a gas turbine compressor blades in which he found that search intensification was beneficial to the overall optimiser performance.

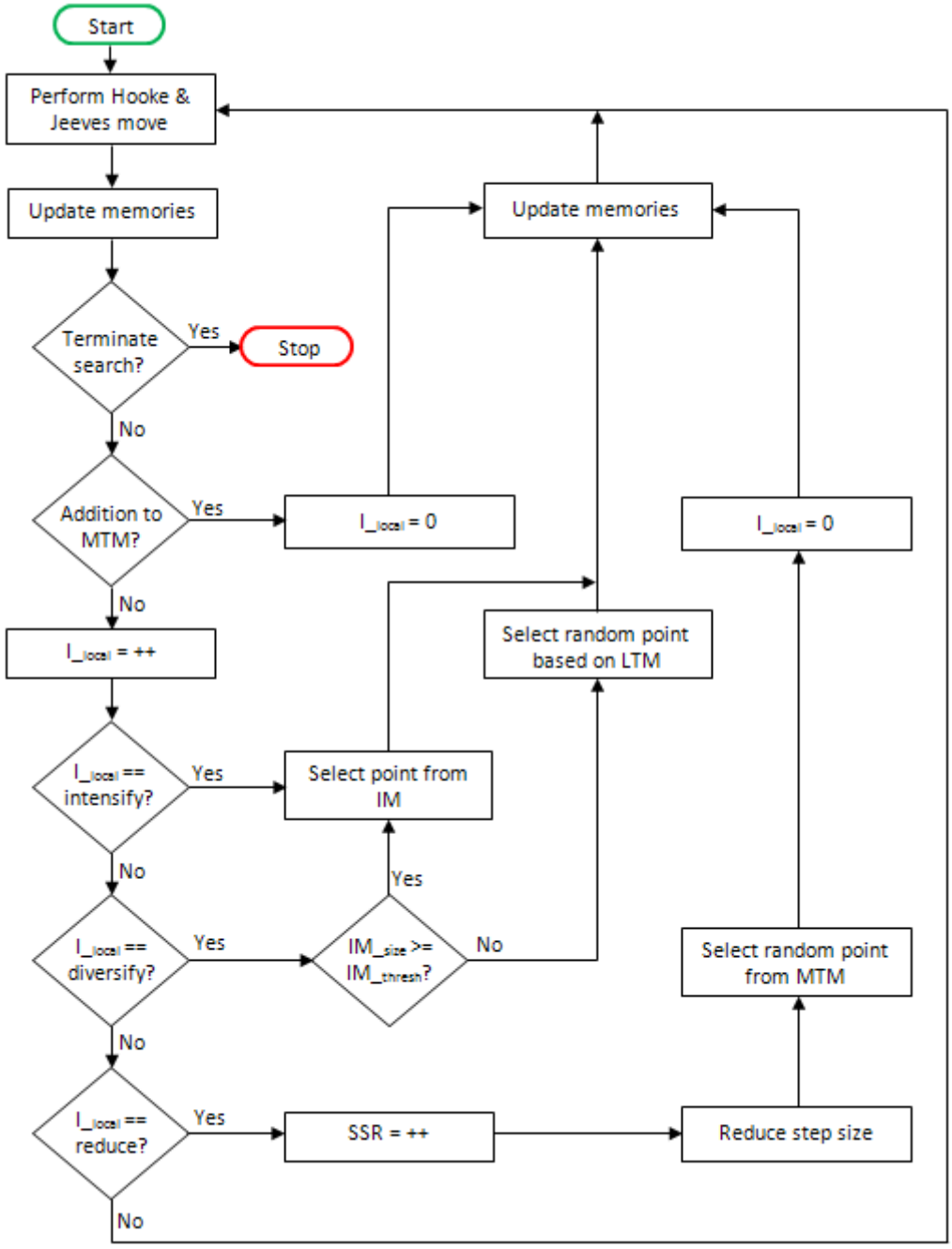

Figure 4-4: TS algorithm flow chart

4.4.2.4 TS parallelisation

Optimisation of a complex and nonlinear design space of a real-world engineering application requires achieving its objectives and at the same time, meeting a strict timeframe. Therefore, the modern optimisation algorithm must be designed with this in mind. The MOTS developed by Jaeggi et al. (2005) used in this research has the capability of evaluating a number of design vectors generated by Hooke & Jeeves's move at once, i.e. in parallel execution by using Function Decomposition strategy, also known as low level parallelism (Kipouros, 2006).

Figure 4-5 presents an overall description of the MOTS parallelisation strategy within the optimisation system framework. Parallelisation is carried out using MOTS - Master and a user-defined numbers of MOTS – Salves (two slaves are shown for demonstration reasons). The master can be viewed as the brain of the TS algorithm; it provides the individual slave in the process with a design vector (point in the search space) and upon receiving back the normalised values of the objective functions for evaluations it directs the search to a promising area in the search space hoping to find the global minima/optima of the problem. Also, the master carries out all the search memories updates and the decisions such as search intensification, diversification and step size reduction. As for the slaves, they mainly interface with geometry and grid generators, and the CFD tool. It sends the design vector received previously from the master to the geometry and grid tool and in return receives a numerical grid to be used in the evaluation of the problem numerically by a CFD tool. The latter sends the flow metrics results of interest back to the salve and so on. The optimisation process continues until stopping criteria is met.

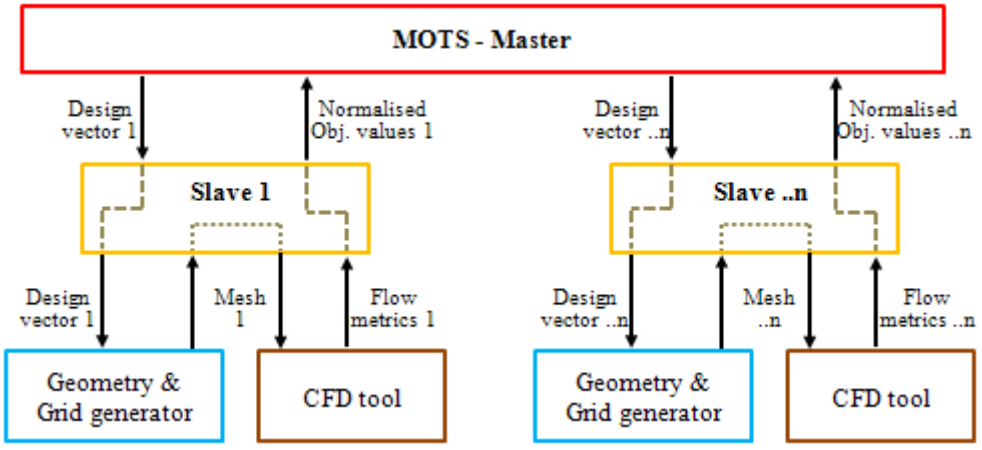

Figure 4-5: Parallelisation of MOTS framework

4.5 Chapter summary

This chapter presents optimisation in an engineering environment and particularly in combustion. A literature review was carried out to identify the type and the choice of a suitable optimisation algorithm to be used within a multi-objective optimisation framework. The multi-objective Tabu Search (MOTS) algorithm was chosen based on the success achieved by tackling a complex and nonlinear design space of a gas turbine compressor bladed shape optimisation which is similar in nature to that found in a micro-scale combustor. The search exploration strategy moves and the main MOTS algorithm features were also discussed.

Chapter 5

Definition of the design problem

5.1 Introduction

This chapter presents the definition of the optimisation design problem with emphasis on the following points:

1. Objective functions, evaluations and design constraints
2. Parametric design study
3. Additional expressions integrated within the CFD model and finally
4. Multi-objective Tabu Search parameter settings

5.2 Objective functions

As stated in the previous chapter the design space of a microcombustor is complex, highly constrained, nonlinearly related and there are more than one conflicting design objectives. Therefore, optimisation of a multi-objective problem implies either minimising or maximising a number of design objectives, satisfying a number of design constraints simultaneously. The multi-objective problem can be described as follows:

Obtain $f_i(\boldsymbol{x})$ minimum or maximum, where $i = 1, 2, .., N_{objective}$

at $\boldsymbol{x} = (vi)$ where $vi = 1, 2, .., N_{design\ variable}$

subject to $c_i \geq$ or ≤ 0 where $i = 1, 2, .., N_{design\ constraint}$

Where $f_i(\boldsymbol{x})$ and $N_{objective}$ is an objective function and the number of the objective functions respectively. $\boldsymbol{x}$ and vi is a design vector and the number of design variables respectively. Finally, c_i and $N_{design\ constraint}$ is a design constraint and the number of deign constraints respectively.

Therefore, solving such a problem requires a set of design variables (geometrical and operational) which results in minimising or maximising the design objectives considered and at the same time respects all the design constraints applied.

There are two approaches to obtain a solution for this kind of optimisation problem. First, is to combine all the design objectives linearly into one objective applying fixed weights and solve the problem as a single objective. Srinivas and Deb (1994) stated that

the obtained solution from this approach was highly influenced by the user applied weights to the individual design objective during linearization process. Also, the designer is only represented with a single solution rather than multiple points, a set of optimum designs known as the *Pareto optimal* set when solving the problem as multi-objective problem. The second approach incorporates directly the multi-objective functions of the problem in optimisation. This latter approach is implemented in this work.

As mentioned, a multi-objective optimisation results in a Pareto optimal set which consists of a number of optimum designs found so far during the optimisation process by the optimisation algorithm. For example, if two randomly selected designs from the Pareto optimal set are to be compared with each other, then each design is set to dominate the other in one of the design objectives – as in the work. Moreover, for the same example, the optimum designs cannot share the same value of either objective unless one design is within the Pareto set and the other outside i.e. Tabu.

5.3 Objective functions formulation

Multi-objective optimisation studies carried out in this work were targeting the improvement in microcombustor efficiency and the amount of fuel consumption. The former was chosen based on the principle that in order to achieve higher power density which mandates operating with higher mass flow rate there is a shorter residence time for a complete combustion inside the microchamber, therefore lowering the overall combustor efficiency. As for the fuel consumption, this objective was chosen based on the design requirement of reducing the overall weight of the device and at the same time operating at maximum efficiency for space application as a micro-thruster. Therefore, both objectives can be expressed mathematically in normalised form as follows:

$$\text{Objective1} = \frac{\eta}{\eta_{\text{datum}}} \tag{5-1}$$

$$\text{Objective2} = \frac{\text{H}_2\text{mass}}{\text{H}_2\text{mass}_{\text{datum}}} \tag{5-2}$$

Where Objective1 and Objective2 represent the normalised efficiency and fuel consumption functions respectively, η and H_2mass are the efficiency and the amount of fuel consumption respectively which correspond to the recently tested design vector, and η_{datum} and H_2mass_{datum} are the efficiency and the fuel consumption of the baseline design respectively.

The microcombustor datum design previously shown in Figure 3-1 has efficiency and fuel consumption values of 56.1% and 0.01558 (g/hr) respectively calculated at 22.5 degree, three-dimensional section. The efficiency value was numerically obtained. On the other hand, the fuel consumption was mathematically calculated. Both values were achieved based upon an equivalence ratio of 0.6, a mass flow rate of 2.5E-7 kg/s, an initial reactants temperature of 300 K, combustor reference pressure of 1 atm and high heating value for hydrogen of 140 MJ/kg (Cengal and Boles, 2002). The efficiency and fuel consumption formulations are represented in detail in subsection 5.6.1.

5.4 Design constraints

In this work, the multi-objective optimisation algorithm handles all the design constraints in one fashion as follows: any new point (design vector) in the design space that violates any of the problem defined constraints, even in some scenarios where the evaluation of this point resulted in better performance in one or both design objectives, is disallowed and considered as a Tabu point in a future design space exploration. A new search point must pass two different types of constraints before considering being a valid design at the end of the optimisation iteration loop. The first test that must be passed before carrying out the CFD evaluation is the geometrical constraints where a set of pre-defined rules must be respected in order to avoid any geometry overlapping or any technical issues. Geometry overlapping may result in an unrealistic physical model. It also shows that a grid tool cannot generate an accurate numerical grid when this scenario exists. As for the latter, this may result in blocking the fluid flow path inside the chamber. For a demonstration on these geometry problems caused by geometry constraints violation - see Figure 3-6. The second test before declaring a new point fit for performance comparison after the numerical evaluation is to pass the operational design constraints. In the preliminary optimisation study, only two operational constraints are applied; the maximum structure operating temperature and the microcombustor maximum exit temperature. Increasing the number of the design

constraints results in narrowing the feasible design space of the problem under investigation.

In some engineering problems such as aerodynamic shape optimisation a penalty function is used to allow for small constraint violation. Three types of penalty functions are defined by Bäck et al. (1997) and they are: barrier method, partial penalty function and global penalty function. Some examples of applying a penalty function to the design objectives of an engineering problem can be found in the work of Kipouros (2006) and Trapani et al. (2012).

5.5 Parametric design study

Parametric design study is a manual, iterative and time consuming process undertaken by the designer, which starts from building the geometry from a defined design vector and then its associated mesh followed by the evaluation of the objective target of interest using CFD flow calculations. In a scene, it is similar to a manual engineering optimisation task (trial and error) but for specific values of the individual design parameter within its bounded operating limits. The aim is to study the influence of each design variable individually on a selected design objective when changes to the value of the studied parameter are applied. After that, a suitable step size is defined to allow the optimisation algorithm to change the design parameter upon at each Hooke & Jeeves's move during the search for optimum designs.

5.5.1 The methodology

It was recognised from literature that the operational design parameters (total mass flow rate and fuel/air mixture) implemented throughout this research have significant impact on the microcombustor design objectives under study for performance improvements. Thus, these two parameters are excluded from the current study (parametric study).

The process starts by evaluating the objective function of interest (here is the combustor efficiency) of the baseline design and use the obtained value as a benchmark for comparison during this study. All design parameters are tested separately at least three times, mainly using the two extreme operating limits (the lowest and the highest values) of the design parameter and another from the middle of this limit, also applying the baseline design values for the other parameters. Initially, the total number of CFD

evaluations required to test all the design parameters is at least 52 (14 parameters x 3 design points).

5.5.2 The results

The parametric design study results are shown in Figure 5-1. The influence of some of the design parameters on the selected objective function (efficiency) can be seen clearly. For clarification purposes, the lower part of this figure is used to emphasize the objective space response to the design space. The effect of changing the design parameter P5 (randomly selected) from its lower to the upper operational limit resulted in the increase in the device efficiency by 1.76 %. On the other hand, the same changes were applied to design parameter P12 (randomly selected) resulting in a significant increase in the design objective by almost 10 %. Upon these evaluations, if the parameter has a big influence on the design objective value, then a small step size is assigned to this parameter. All the microcombustor baseline design parameters, their limits and step sizes are listed in Table 5-1. Also, all design parameters (P0 – P13) were detailed in Table 3-1.

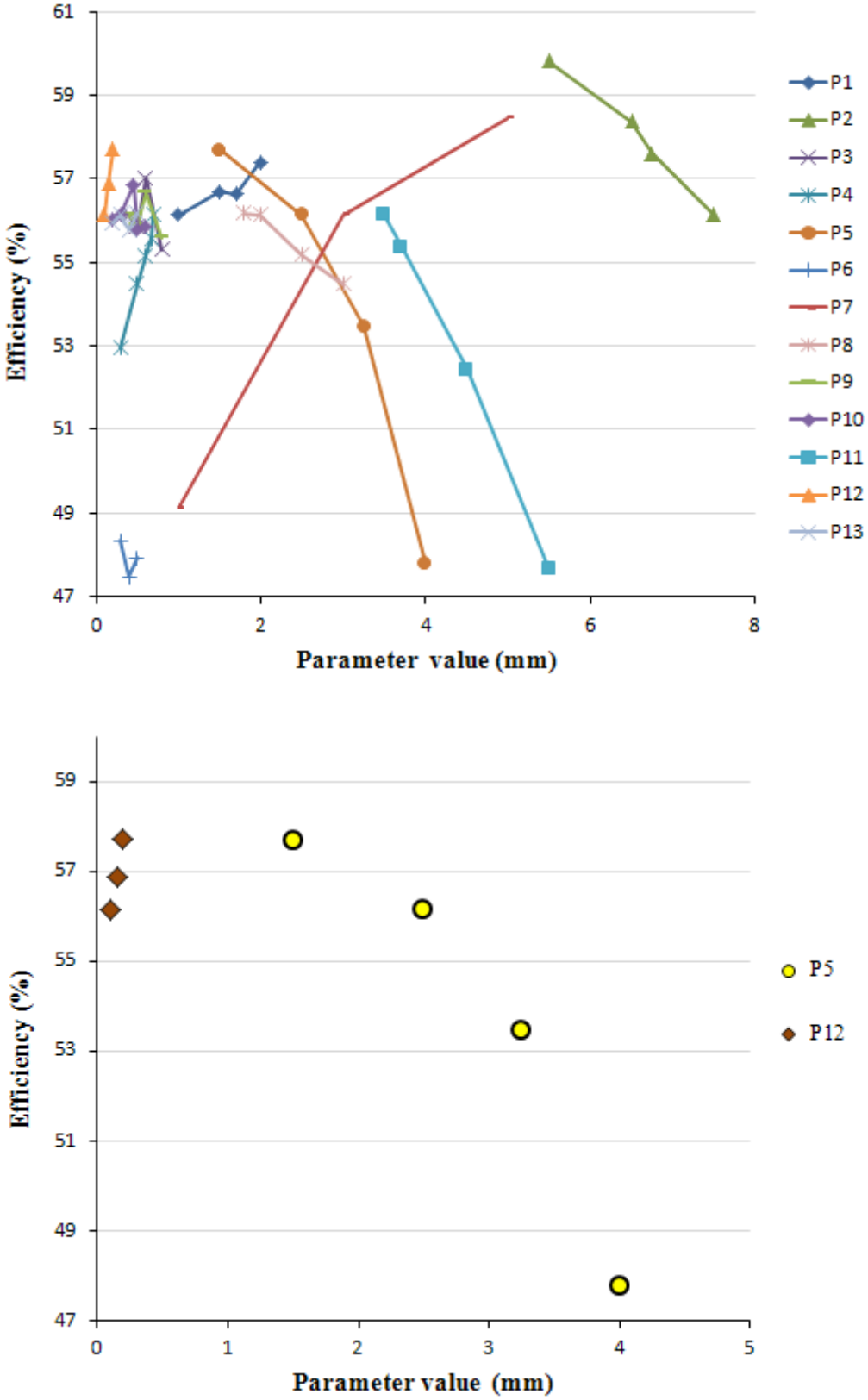

Figure 5-1: Parametric design study results. All studied parameters (Top) and randomly selected parameters for clarity (Bottom)

Table 5-1: Geometrical and operational datum design parameters, limits and their step sizes

Parameter	Unit	Lower limit	Datum	Upper limit	Step size
Geometrical					
P0	(--)	1	2	3	1
P1	mm	0.7	1.0	2.0	0.1
P2	mm	5.0	7.5	9.0	0.1
P3	mm	0.37	0.4	0.8	0.025
P4	mm	0.3	0.7	0.75	0.025
P5	mm	1.0	2.5	4.0	0.025
P6	mm	0.3	0.35	0.5	0.025
P7	mm	1.0	3.0	7.0	0.05
P8	mm	1.0	2.0	3.0	0.02
P9	mm	0.37	0.4	0.8	0.025
P10	mm	0.25	0.3	0.6	0.025
P11	mm	1.5	3.5	5.5	0.02
P12	mm	0.05	0.1	0.2	0.01
P13	mm	0.2	0.3	0.6	0.05
Operational					
ER	(--)	0.4	0.6	1.0	0.01
MFR (H_2+air)	kg/s	0.07E-6	0.25E-6	0.36E-6	0.014E-6

(Note: (--) referred to dimensionless)

5.6 Expressions integrated within the CFD code

The following expressions are integrated within the CFD code in order to calculate specific physics of the problem. Some of these are used during the CFD iterations; others are used in the phase of post processing of the flow metrics results of interest. These expressions are listed as follows:

5.6.1 Device efficiency and fuel consumption calculations

- Microcombustor efficiency (η) is calculated from the following equation:

$$\eta\,(\%) = \frac{\mathrm{MFER}\,(\mathrm{H_2}) - \mathrm{Total\ Q_{loss}}}{\mathrm{MFER}\,(\mathrm{H_2})} \times 100 \qquad (5\text{-}3)$$

where the maximum fuel energy released (MFER) is calculated as

$$\mathrm{MFER} = \mathrm{HHV} \times \mathrm{MFR} \times \mathrm{Y_{H_2,u}} \tag{5-4}$$

HHV is the high heating value of hydrogen of 140 MJ/kg.

- The fuel consumption is calculated as follows:

$$\mathrm{H_2 mass} = \mathrm{Y_{H_2,u}} \times \mathrm{MFR} \tag{5-5}$$

5.6.2 Fuel and oxidiser calculations

Hydrogen, oxygen and nitrogen mass fractions are calculated respectively as follows:

$$\mathrm{Y_{H_2,u}} = \frac{1}{1 + \left(\frac{\mathrm{AFR_{st}}}{\mathrm{ER}}\right)} \tag{5-6}$$

$$\mathrm{Y_{O_2}} = 0.233 \times \left(1 - \mathrm{Y_{H_2}}\right) \tag{5-7}$$

$$\mathrm{Y_{N_2}} = 1 - \left(\mathrm{Y_{H_2}} + \mathrm{Y_{O_2}}\right) \tag{5-8}$$

5.6.3 Heat loss calculations – convective and radiative

The energy loss (Q_{loss}) term appeared in the efficiency equation above is the sum of the convective and radiative energy losses from the individual outer walls of the microcombustor device.

Holman (2002) defined the laminar natural convective heat transfer coefficient as:

For vertical plate

$$h_{conv} = 1.42 \times \left(\frac{T_w - T_a}{L}\right)^{0.25} \quad (5\text{-}9)$$

Horizontal plate, hot surface facing upward

$$h_{conv} = 1.32 \times \left(\frac{T_w - T_a}{d_h}\right)^{0.25} \quad (5\text{-}10)$$

Horizontal plate, hot surface facing downward

$$h_{conv} = 0.59 \times \left(\frac{T_w - T_a}{d_h}\right)^{0.25} \quad (5\text{-}11)$$

(Al-Shemmeri, 1990) defined radiative heat transfer coefficient as follows:

$$h_{rad} = \varepsilon \sigma F_{12} (T_w + T_a)\left(T_w^2 + T_a^2\right) \quad (5\text{-}12)$$

5.6.4 Structure material properties

For stainless steel type 316L, the following material parameters are defined according to the European Standard - Eurocode 3 for the design of steel structures (prEN1993-1-2, 2003) as follows:

- The density is 7850 kg/m^3 at STP
- The thermal conductivity (λ) in (W/m.K) and is

$$\lambda = 14.6 + 0.0127\, T_s \quad (5\text{-}13)$$

- The stainless steel specific heat (C_a) in J/Kg.K is defined as

$$C_a = 450 + 0.28\, T_s - 2.91 \times 10^{-4}\, T_s^2 + 1.34 \times 10^{-7}\, T_s^3 \quad (5\text{-}14)$$

where T_s is the steel temperature in (C^o) for the above equations

5.7 MOTS parameters settings

The parameters correspond to the preliminary design optimisation of a micro-scale combustor (Case study 1 – Chapter 6) used to control the multi-objective Tabu Search algorithm navigating the design space of the problem are listed in Table 5-2. However, these parameter values are defined based upon the user experience. Also, the TS algorithm's performance is found to be comparatively unaffected by those parameter settings (Kipouros, 2006).

Table 5-2: Tabu Search parameter settings

TS parameter	Value	Description
n_stm	25	STM size - last *n_stm* visited points are Tabu
n_regions	4	Each design parameter is divided into *n_regoin* in LTM to define which regions of the search have been less visited
Intensify	25	Intensify search starting from a randomly selected point from IM when *i_local == intensify*
Diversify	55	Moves the search to unvisited regions from LTM when *i_local == diversify*
Reduce	75	Step size reduction is an intensive search in the region of the current optimal solutions (Pareto) which starts when *i_local==Reduce*
SSRF	0.5	Step size reduction factor (hard coded)
im_thresh	10	Intensification memory size threshold. Intensification replaces diversification move above this value (hard coded)
n_sample	32	Number of points sampled randomly at each Hooke & Jeeves move

5.8 Chapter summary

This chapter described the objective function in general form, the microcombustor design objectives used and their formulations. Also, it presented the type of constraints implemented throughout the optimisation investigations carried out in this research. The necessity to conduct a manual, iterative and time consuming process of parametric design study and the methodology undertaken in order to identify a suitable step size to be used by the TS algorithm during the optimisation process for the individual design parameter is considered.

This chapter also detailed additional expressions integrated within the CFD code with the aim to calculate the device efficiency and fuel consumption at each CFD evaluation, the heat transfer calculations which are detailed descriptions of the convective and radiative heat transfer coefficients applied as well as the material properties. Finally, it presented the Tabu Search parameter settings implemented during the preliminary design study of a microcombustor.

Chapter 6

Testing of the developed optimisation system (Case studies)

This chapter represents the results of two case studies obtained from the integration of the multi-objective Tabu Search algorithm with a well-known computational fluid dynamic package in an automated manner. The first case represented a simple microcombustor configuration, where a single and then multi-objective optimisation investigations were carried out, implementing 14 geometrical and two operational parameters with the objectives to improve the overall efficiency of the device and to reduce the fuel consumption.

A microcombustor with a complex geometry was optimised in the second case where the benefit of adding a micro-cooling channel into the design was firstly recognised in a separate investigation. By gaining knowledge from the above case study (case 1) in identification of the geometry topology of the combustion chamber that produced improved behaviour of the device in terms of the design objectives, it was also possible to represent the design with only five geometrical parameters including the micro-cooling channel height and three other operational parameters thus, minimising the optimisation cost by reducing the dimensionality of the design space.

In the last part of test case 2, two out of the three operational parameters, the compromised design configuration (i.e. constant geometrical parameters) as well as the same objective functions and design constraints, were considered in the optimisation investigation in order to find the operating limits and effects of the MFR and ER fluctuations on the combustion behaviour and the overall device performance.

The final case study was specifically intended to replace the hydrogen with a hydrocarbon fuel and study the effects numerically using single-step reaction modelling on the combustion and combustor performance starting with the compromised design configuration found from case study 2. Moreover, to identify the key issues and find solutions involving the migration from using the hydrogen as a fuel, which has wide flammability limit and also fast reaction rates compared to the hydrocarbons to achieve a sustained combustion inside the microchamber.

In all case studies, the objective function/s used was/were previously defined in section 5.3. Also, the applied boundary conditions such as the heat loss and fuel-oxidiser calculations as well as the efficiency were detailed in section 5.6.

6.1 Case study 1 (Optimisation of a simple combustor configuration)

6.1.1 Single-objective function investigation – Case study 1-A

A single-objective optimisation is carried out to improve microcombustor efficiency using ANSYS CFX EDM (Eddy Dissipation Model) combustion model. The optimisation was initiated from the datum geometry shown previously in Figure 3-1.

The advance made by MOTS algorithm, exploring the design space of the problem within 117 optimisation iterations, is presented in Figure 6-1 where the objective function was evaluated 23 times on average per optimisation iteration. The combustor efficiency was obtained each time from a fully converged CFD solution with convergence targets of 1.0E-6, satisfying both hard design constraints; the maximum structure < 1000 K and the average exit flow temperatures < 1800 K.

At the initial stages of the optimisation system development and testing, this case was executed on a single slave using four parallel PC cluster. The average wall clock time required to obtain a fully converged CFD solution starting from geometry representation was 45 minutes.

From Figure 6-1, it is clear that significant improvement in the normalised efficiency is achieved. The optimal design has an efficiency value of 71.1 % in comparison to the datum design of 56.1 %. This is due to the following factor: the optimal design has a higher mass flow rate and higher equivalence ratio; therefore more energy is released by the combustible fuel than that dissipated from the external walls of the device.

The reduction in total volume of the optimum design by approximately 25 % compared to the initial design (Figure 6-1, right) was expected resulting in a smaller surface area of the chamber and therefore less energy loss to the surrounding environment but it is clear from Table 6-2 that the total heat dissipation increased by 22 %, which is caused by the increase in flame temperature and hence the temperature of the structure's external walls. It is also apparent that increasing the device efficiency at the same applied thermal boundary conditions mandates the increase in fuel consumption by either increasing the mass flow rate and/or the reactants equivalence ratio.

Table 6-1 lists the geometrical and operational design parameters of the datum design and optimum designs found at different optimisation iterations. Interestingly, all those designs are configured to use the maximum allowed value of the mass flow rate of 3.48E-7 kg/s [5] and it is also apparent that the optimum design at the 117 optimisation iteration has the highest equivalence ratio of 0.84 compared to the previous optimum deigns found, which validates the above statement.

As a result of the increase in total mass flow and equivalence ratio, the combustion temperature of the optimum design has risen by 400 K approximately and a significant increase in the average exit flow temperature of 500 K is calculated from the numerical simulation results when compared to the datum design.

The values of the flow metrics of interest obtained from the datum design and from different optimisation iterations are illustrated in Table 6-2.

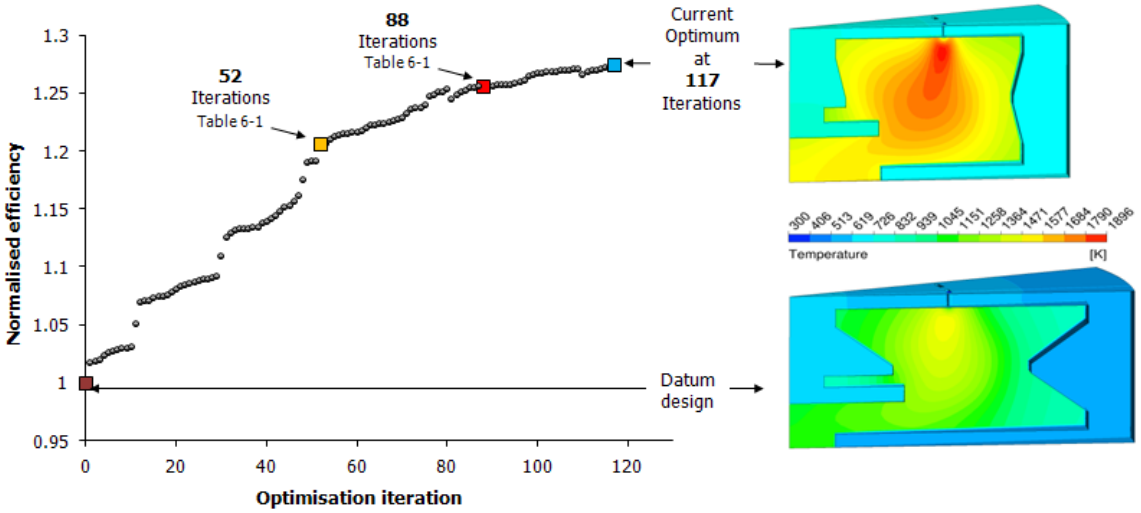

Figure 6-1: Single-objective design space search and the optimal design found (Left). Design configurations & temperature contours at a vertical plane and the external walls (Right)

Note: For visual comparison, both geometries are on the same dimensional and temperature scales

[5] The maximum total mass flow rate is defined previously in Table 5-1 equals to 3.6 E-7 with a design parameter step size of 0.14 E-7.
3.48 E-7 + 0.14 E-7 > 3.6 E-7 therefore, 3.48 E-7 is the maximum allowed design value at the defined step size but the optimisation algorithm is capable of searching the whole design space for this design parameter by performing step size reduction move.

Table 6-1: Combustor design parameters at different optimisation iterations for a single-objective investigation

Parameter (Table 3-1)	Initial (datum)	Optimisation iterations		
		52	88	117
Geometrical				
P0	2 (--)	2 (--)	2 (--)	2 (--)
P1	1.0	1.9	2.0	2.0
P2	7.5	6.9	6.0	6.1
P3	0.4	0.45	0.475	0.45
P4	0.7	0.7	0.7	0.7
P5	2.5	2.35	2.15	1.95
P6	0.35	0.325	0.35	0.325
P7	3.0	3.3	3.6	3.65
P8	2.0	2.0	2.02	2.02
P9	0.4	0.425	0.425	0.425
P10	0.3	0.275	0.275	0.25
P11	3.5	3.46	3.46	3.4
P12	0.1	0.09	0.08	0.09
P13	0.3	0.2	0.2	0.2
Operational				
Equivalence Ratio	0.6	0.68	0.72	0.84
Mass flow rate (kg/s)	2.5 E-7	3.48 E-7	3.48 E-7	3.48 E-7

Note: all units are in (mm) unless stated otherwise. (--) referred to dimensionless

Table 6-2: Design flow metrics of interest at different optimisation iterations (Single-objective test case)

Flow metrics	Datum	Optimisation iteration		
		52	88	117
Efficiency (%)	56.1	67.1	70.5	71.1
Maximum flame temperature (K)	1432	1642	1729	1896
Gases average exit temperature (K)	1101	1396	1501	1665
Maximum structure temperature (K)	623	704	719	745
Maximum velocity (m/s)	7.2	14.8	17.0	17.2
Total heat loss (W) *	4.3	5.07	5.0	5.49
Fuel consumption (g/hr) *	0.249	0.392	0.415	0.482
Maximum fuel energy released (W) *	9.8	15.4	16.3	19.0
Micro-chamber volume (mm^3)*	301	271	215	222

* Values are calculated from a complete geometry of 360^o

6.1.2 Multi-objective functions investigation - Case study 1-B

In this test case, two-objective functions are used with the aim of maximising the combustor efficiency and at the same time minimising the fuel consumption, applying the same hard design constraints mentioned in the single-objective investigation; the maximum structure temperature and average exit flow temperature. Both functions were previously defined in section 5-3.

A hydrogen-air combustion reaction was implemented using the ANSYS CFX-EDM model. The optimisation process was initiated from the datum geometry shown previously in Figure 3-1, and on average 23 objective function evaluations were required per optimisation iteration.

In order to explore the complex design space of the problem in a shorter time and to test the MOTS algorithm performance and its capability to find new design vectors meeting the design criteria set; only 101 CFD iterations are implemented to evaluate the objective functions. The progress made by the MOTS algorithm at different optimisation iterations is presented in Figure 6-2. The MOTS pattern shows that significant improvements in normalised efficiency and fuel consumption have been achieved relative to the datum design. It is also apparent that the majority of the Tabu designs (not optimum) found and a large number of the optimal designs represented by the Pareto front performed better than the initial design with respect to both design objectives.

The optimum geometrical and operational designs parameters at 794 optimisation iterations and the initial (datum) design parameters are illustrated in Table 6-3, the flow metrics values corresponding to the above designs are shown in Table 6-4.

From Table 6-4, the design obtained from the Pareto front representing the maximum normalised efficiency has achieved an increase of ~22 % compared to the initial design and 1.6 % decrease in the fuel consumption. In contrast, the maximum flame temperature was reduced by 75 K which resulted from lower fuel energy being released during the combustion process. Moreover, the increase in total mass flow rate by ~ 22 % has contributed to the flame being stabilised further downstream closer to the combustor exit and a shorter residence time which led to a reduction in the thermal diffusion time hence, the flow average exit temperature was increased by ~ 12 % despite the minor decrease in flame temperature.

Furthermore, the second objective function (to minimise the fuel consumption) has produced a reduction by 77.5 % compared to the initial design value at the cost of 2.9 % decrease in the device efficiency. This is represented by the minimum fuel consumption design found at the right-hand end of the Pareto-optimal set. Then again, the reduction in fuel consumption has led to a significant drop in flame temperature hence, a reduction in average exit flow temperature and structure temperature.

However, the chosen compromised design has an efficiency value of 66 % in comparison to the datum design of 56.1 % and 12.5 % lower than the maximum efficiency design configuration, but then, it is optimised to consume less fuel than those designs by 53.4 % and 52.6 % respectively.

It is also important to emphasise that all the optimum designs found have a chamber volume 41 % less than the datum design; the change in total diameter of the combustor represented by the design parameter P2 from 15.0 mm (initial) to 11.2 mm (optimum) and the total chamber height represented by the sum of the design parameters P3, P8 & P9 (from Table 6-3) contributed to the reduction in chamber volume. From the latter and further study of the geometrical design parameters of the optimum designs found at 794 optimisation iterations it was suggested that there are two design groups. The first is those found between the compromised (highlighted in Figure 6-3) and the minimum fuel consumption designs which have identical geometry configurations. The second group, with minor changes compared to the previous are found between the compromised and the maximum normalised efficiency designs. Therefore this finding might lead to the following initial conclusion; if any new optimum designs found after the 794 optimisation iterations then they are expected to have similar geometrical design configurations to those already found.

The temperature distribution at mid-plane and combustor external walls are shown in Figure 6-3 for the optimum designs found at 794 optimisation iterations; in addition, this figure reflects the geometrical changes achieved by the optimisation algorithm compared to the initial design.

A randomly chosen optimum designs from a previous and the final Pareto set which demonstrated the geometrical changes in comparison to the initial design are shown in Figure 6-4. It is clear from this figure that increasing the efficiency of the combustor requires the reduction in thermal losses to the surrounding environment and this was

achieved by reducing the overall volume as well as the chamber surface area (fluid-solid area), the latter was represented by straight interior chamber walls and larger device exit diameter. Moreover, the fuel-oxidiser injection location appeared to move inward towards the axial centreline away from the vertical wall of the combustor, this can be seen from the values of the design parameter P11 listed in Table 6-3 and design (C) shown in Figure 6-4. Furthermore, only 16 compared to the initial 32 fuel-oxidiser injections[6] are used in 360 degree combustor geometry but larger dimensions were required, represented by parameters P12 and P13 (Table 6-3), this also demonstrates the effectiveness of the MOTS optimisation algorithm utilised in this investigation.

Finally, and regarding the geometrical design parameters, the following conclusion can be drawn from the optimum designs found which might aid future microcombustor optimisation development by reducing the optimisation cost under the current boundary conditions and design constraints:

Note: All geometrical parameters below were previously defined in Table 3-1.

- P0, P1, P2, P5, P6, P7, P10, P12 and P13 are kept constant and therefore, all can be removed from the optimisation process.
- The combustor chamber total height represented by the sum of P3, P8 and P9 can be replaced by a single design parameter.
- P4 value was shared by the compromised and the minimum fuel consumption designs of 0.7 mm and was configured to 0.675 mm in the maximum efficiency design found; it is a minor difference between the two configurations considering the parameter range of 0.3 - 0.75 mm hence, this parameter can be discarded from future optimisation study.
- P11 has a similar scenario to P4, when comparing the values related to P11 of the optimum designs, a small difference of 0.04 mm within an operating range of 1.5-5.5 mm was found therefore this parameter can also be fixed during future optimisation work.

[6] Three different sets of injectors were available for the optimiser to choose from and they are: 16, 32 & 48 subject to the total device diameter P2 and the injector's radial locations P11 in order to achieve feasible real-world component design.

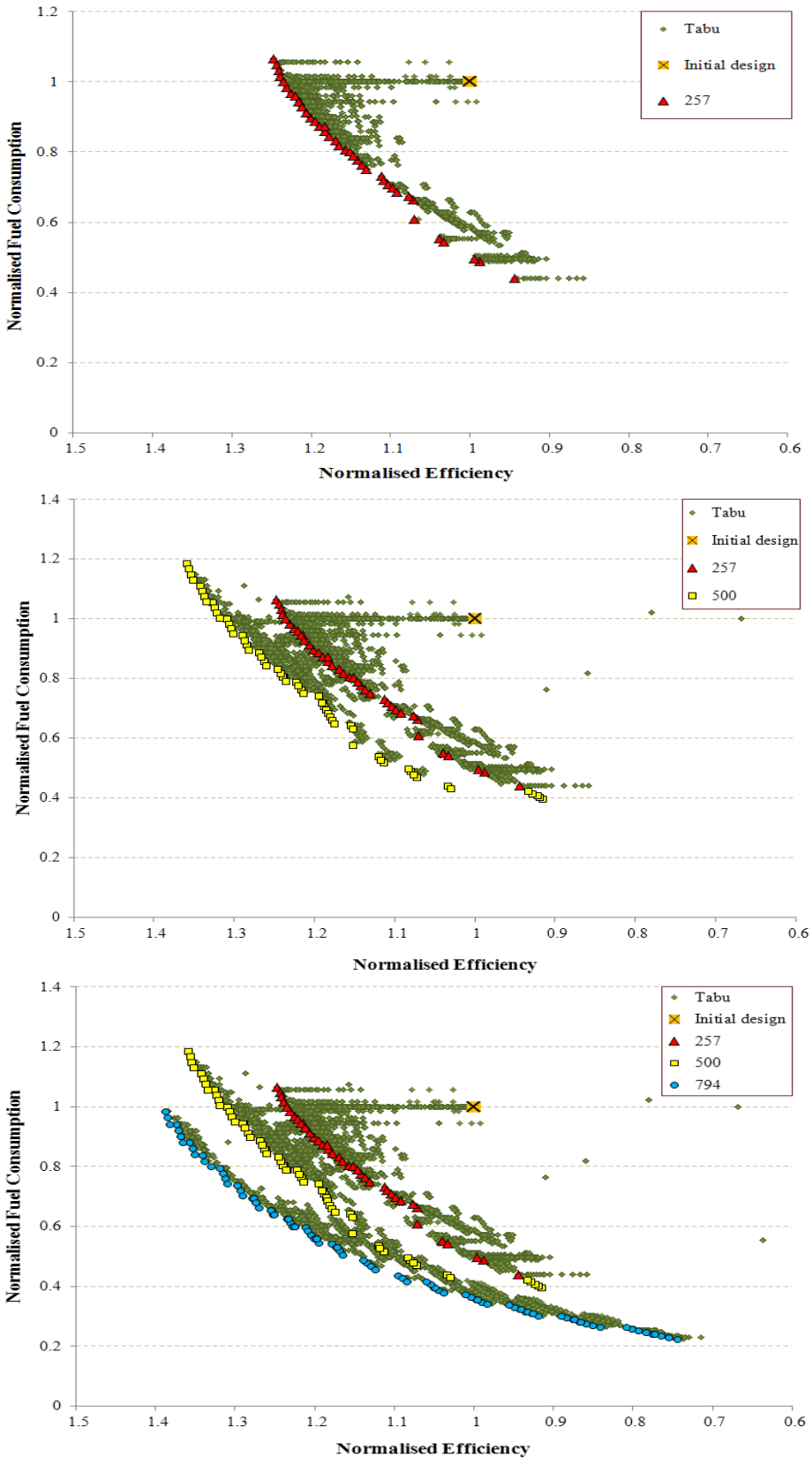

Figure 6-2: The optimisation search pattern at different optimisation iterations (257, 500 & 794) and the corresponding Pareto optimal set found

Table 6-3: Optimum design parameters at 794 optimisation iterations

Parameter	Datum	Max. efficiency	Min. H_2 consumption	Compromised
Geometrical				
P0	2 (--)	1 (--)	1 (--)	1 (--)
P1	1.0	2.0	2.0	2.0
P2	7.5	5.6	5.6	5.6
P3	0.4	0.375	0.375	0.375
P4	0.7	0.65	0.7	0.7
P5	2.5	1.0	1.0	1.0
P6	0.35	0.325	0.325	0.325
P7	3.0	3.6	3.6	3.6
P8	2.0	1.8	1.9	1.9
P9	0.4	0.375	0.4	0.4
P10	0.3	0.25	0.25	0.25
P11	3.5	2.14	2.18	2.18
P12	0.1	0.2	0.2	0.2
P13	0.3	0.5	0.5	0.5
Operational				
ER (--)	0.6	0.46	0.41	0.42
MFR (kg/s)	2.5E-7	3.2E-7	0.82E-7	1.66E-7

Table 6-4: Flow metrics at 794 optimisation iterations obtained from fully converged CFD solutions

Flow metrics	Datum	Max. efficiency	Min. H_2 consumption	Compromised design
Efficiency (%)	56.1	77.7	53.2	66.0
Maximum flame temperature (K)	1432	1357	940	1153
Gases average exit temperature (K)	1101	1256	845	1032
Maximum structure temperature (K)	623	563	449	505
Maximum velocity (m/s)	7.2	4.8	1.5	2.9
Total heat loss (W) **	4.3	2.15	1.04	1.56
Fuel consumption (g/hr) **	0.249	0.245	0.056	0.116
Maximum fuel energy released (W) ***	9.8	9.67	2.21	4.58
Micro-chamber volume (mm^3)**	301	168.1	175.9	175.9

** At a complete geometry of 360^o

*** At a complete geometry of 360^o and reference to the high heating value of 141.8 MJ/kg

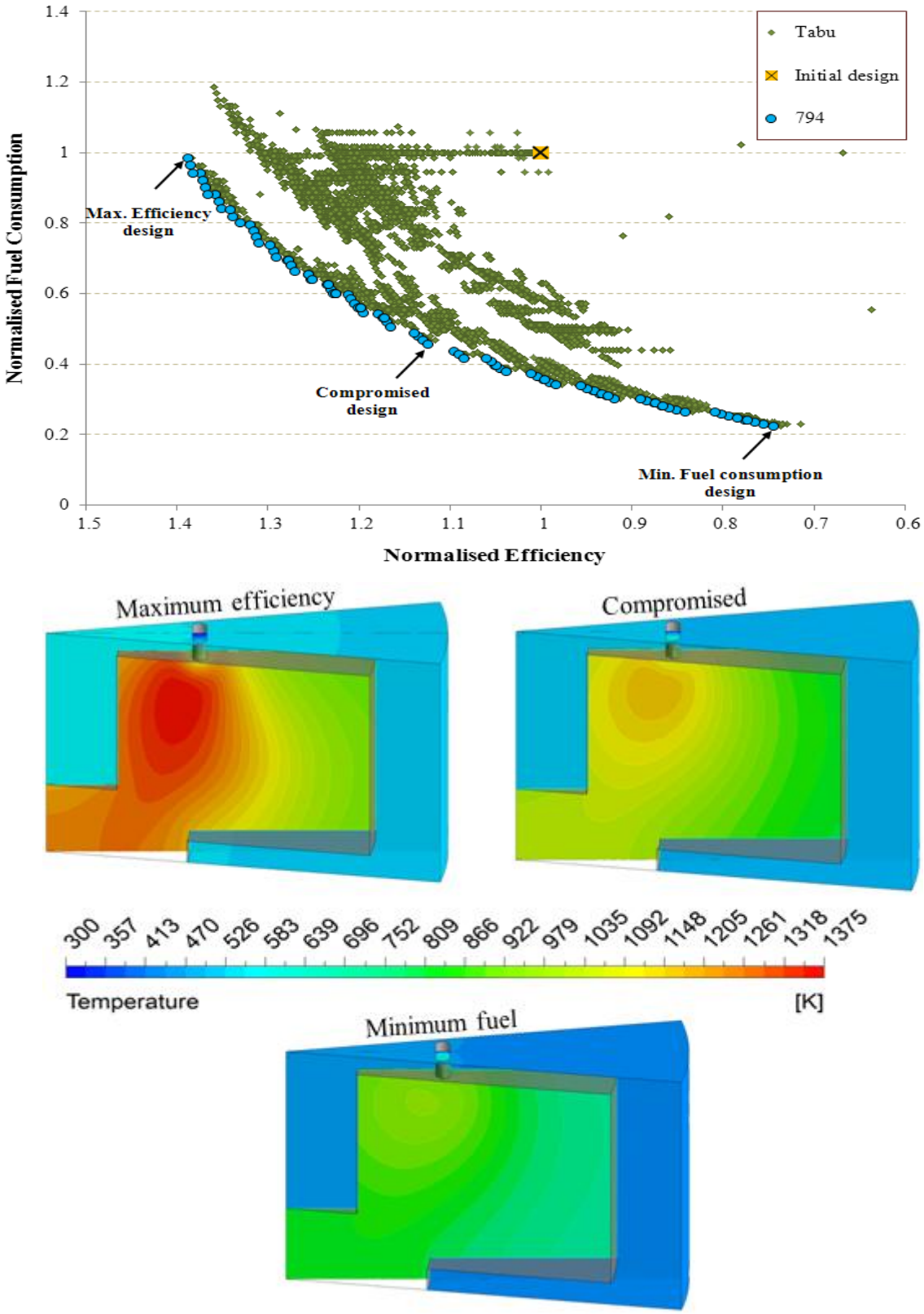

Figure 6-3: Design comparisons of the temperature contours at mid-plane and combustor external walls

Note: all geometries are on the same dimensional scale

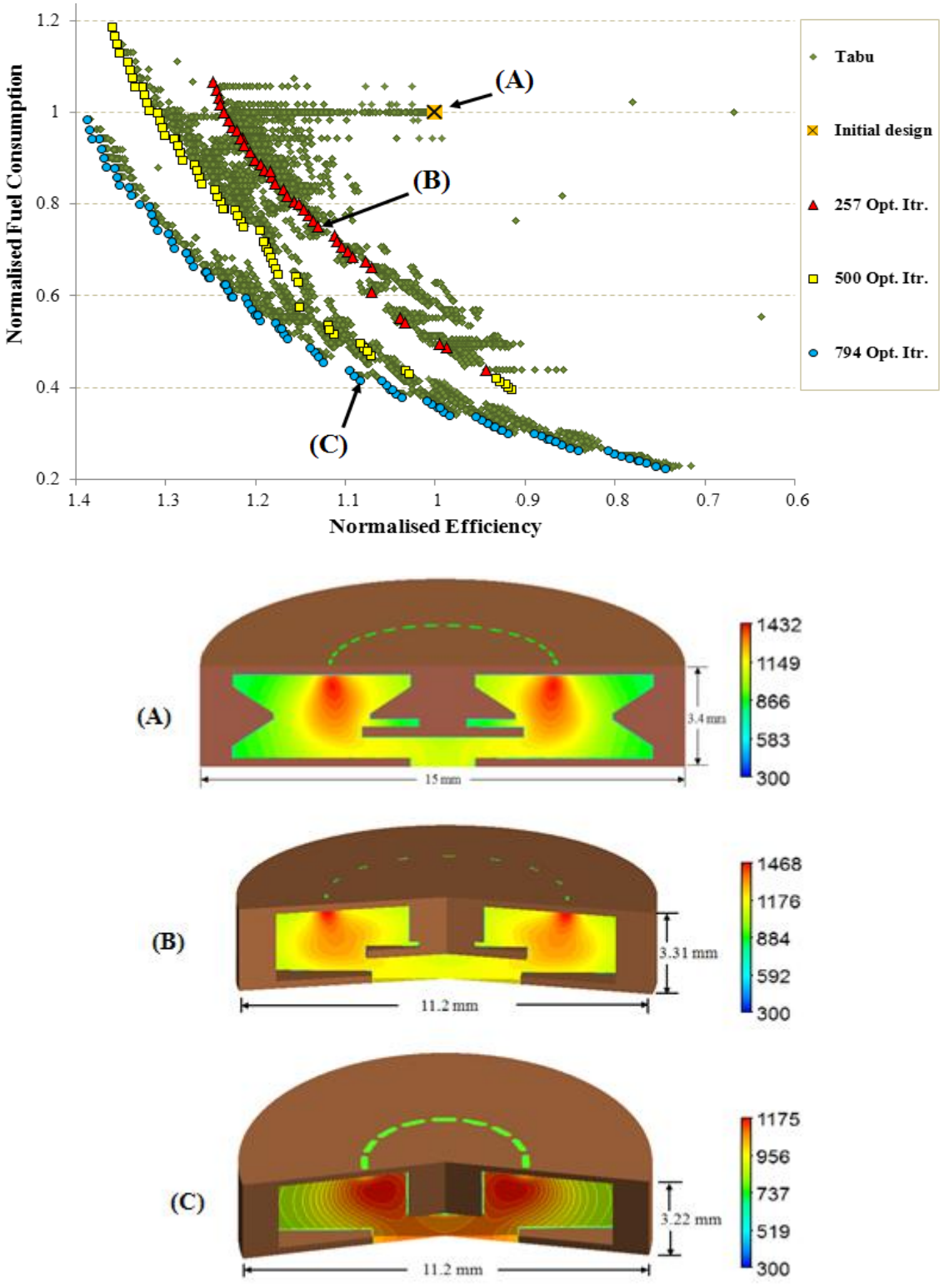

Figure 6-4: Geometrical design comparison, randomly selected optimum designs (B & C) at different optimisation iterations. Fluid temperature contours [K] at vertical midplane for design (A, B & C)

6.1.2.1 Converged and non-converged CFD results' comparisons

As mentioned in the previous subsection the aim of the multi-objective test case was to test the MOTS performance and explore the complex design space of the problem at lower optimisation cost by evaluating the objective functions using a low number of CFD iterations (only 101) which resulted a non-converged numerical solution. Therefore, further investigation of the optimisation results represented by the Pareto optimal sets at 794 shown previously in Figure 6-2 and Figure 6-4, has been carried out. The normalised objective function values of randomly selected design vectors from the Pareto optimal sets as well as the highest efficiency, minimum fuel consumption and the compromised designs have been manually obtained from a high number of fully converged CFD iterations, about 400 on average with numerical equations convergence targets of less than 1.0E-6.

These values are compared with their counterpart values from the non-converged CFD solutions as shown in Figure 6-5. It is apparent that close prediction in normalised efficiency values between both simulations are achieved when the optimum design is configured to operate with the higher value of the total mass flow rate. For example in Table 6-5 design number four, which is optimised to use 11.3 g/hr of the total mass flow rate, has a value difference of 1.59 % whereas design number one has a difference of only 0.26 % which was optimised to use 18.4 g/hr of the total mass flow of the reactants. Furthermore, the results comparison also reveals that the device efficiency is underestimated when the combustor is arranged to use a lower value of the total mass flow rate, those simulation results are obtained from the non-converged CFD optimisation solutions.

But most importantly, the trend of the converged and non-converged CFD solutions is the same, which suggests such micro-combustor designs can be optimised by MOTS using non-converged CFD solutions and the ANSYS EDM combustion modelling with confidence at the initial design and development stages. Moreover, the complex non-linear design space can then be explored faster; allowing significant reductions in computational cost to be achieved.

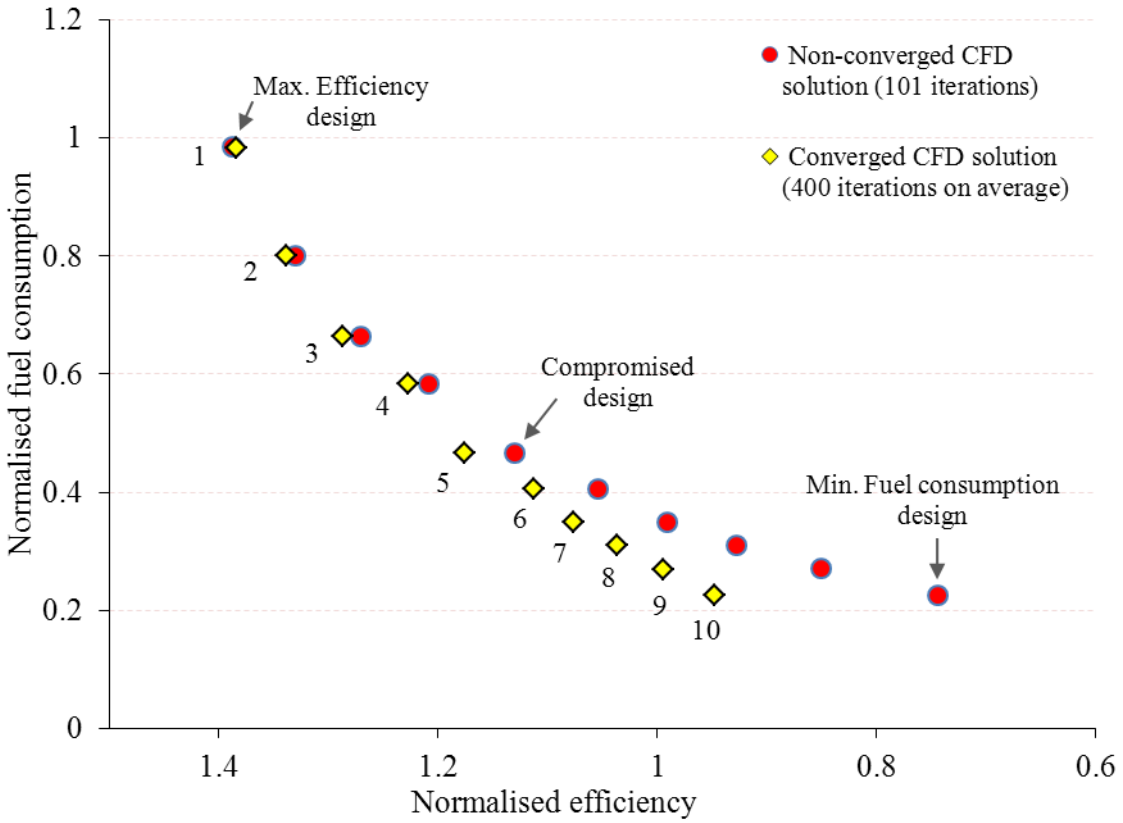

Figure 6-5: Design comparison of the normalised objective functions obtained from converged and non-converged CFD Iterations from the Pareto optimal set at 794 optimisation iterations

Table 6-5: Normalised efficiency and corresponding total mass flow obtained from low & high CFD evaluations for the designs numbered in Figure 6-5

Design No. (Figure 6-5)	Mass flow rate (g/hr)	Normalised efficiency		Difference (%)
		low	high	
1	18.4	1.388	1.384	0.26
2	16.0	1.330	1.338	0.62
3	13.6	1.270	1.287	1.32
4	11.3	1.208	1.228	1.59
5	9.56	1.130	1.176	4.05
6	7.95	1.054	1.112	5.49
7	7.14	0.991	1.076	8.56
8	6.34	0.928	1.037	11.75
9	5.53	0.851	0.994	16.83
10	4.72	0.745	0.948	27.30

6.2 Case study 2 (Optimisation of a complex combustor configuration)

A multi-objective design optimisation study has been carried out with the objectives to improve the overall efficiency of the device and to reduce the fuel consumption for the new micro-scale combustor design configuration. In the previous section (Case study 1), the topology of the combustion chamber that produced improved performance of the device in terms of the above design criteria is identified. The microcombustor design approach is extended in this case study by the addition of a micro-cooling channel that will effectively improve the thermal behaviour of the design as previously suggested in literature.

The computational modelling of the combustion process is implemented in the commercial computational fluid dynamics package ANSYS-CFX using Finite Rate Chemistry combustion model and a single step hydrogen-air reaction. With this modelling approach, a good accuracy of the combustion solution and at the same time practicality within the context of an optimisation process can be achieved.

Finally, the design problem was modelled with five geometrical and three operational design parameters subject to five design constraints that secure practicality and feasibility of the new optimum design configurations.

6.2.1 Micro-cooling channel effects – an illustrative case study

In order to investigate numerically the effects and the benefits of incorporating a micro-cooling channel in a microcombustor design, results comparisons between Design-A which represents a combustor design without a micro-cooling channel and Design-B which incorporates a micro-channel are carried out. The main geometry characteristics of Design-A and Design-B are shown in Figure 6-6 where, Design-A is configured based on the optimum designs found from previous multi-objective design optimisation investigation.

6.2.1.1 Geometry configuration

- **Design-A**

Design-A has a total diameter of 11.6 mm and a total height of 3.8 mm. The fuel-air mixture is injected radially from the lower end of the vertical wall rather than axially from the bottom and directly into the chamber. This was prepared to keep the

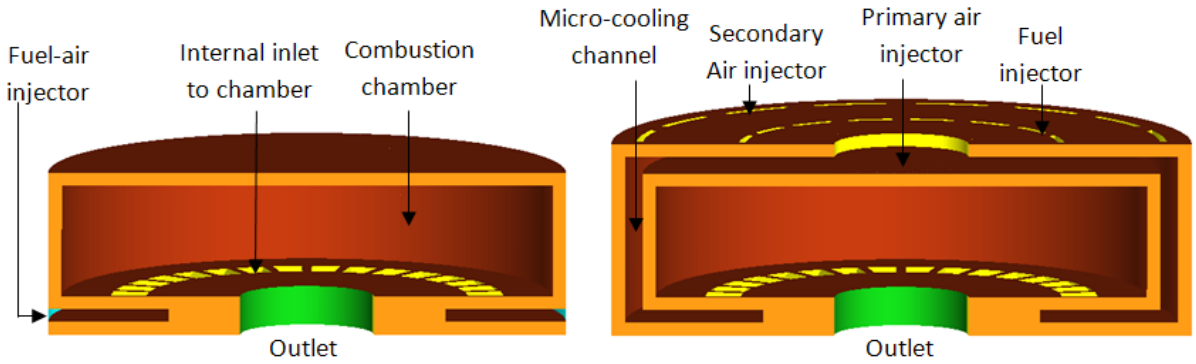

Figure 6-6: Cutaway microcombustor design, Design-A (initial) – left and Design-B (improved) – right

same flow profile before entering the combustion chamber in comparison to the Design-B configuration. A total number of 32 inlets-to-chamber were used and represented by trapezium shapes with dimensions of 0.8 mm in length and an angle of 8.25 degrees measured from the device centreline which describes the width. This shape is chosen to ease the in-house device fabrication process based on a lost-core approach described in Appendix A, also to reduce the overall weight of the component.

- **Design-B**

Design-B has a total diameter of 13 mm and a total height of 4.5 mm, an increase of 1.4 and 0.7 mm in total diameter and total height with respect to Design-A due to the additional layers of the micro-cooling channel. It has one fuel injector and two oxidiser injectors sets. The micro-cooling channel height is modelled to 0.4 mm.

6.2.1.2 Modelling and simulation

3D CFD analysis is carried out using only a 22.5 degree section which represents the main design features such as fuel-air injectors, a combustion chamber and outside walls, micro-cooling channel and a solid (structure) domain. For accurate results comparison both grids are modelled by commercial software named ANSYS ICEMCFD, applying the same grid settings. The unstructured mesh type is chosen with a maximum volume element size of 0.08 and 0.126 for the fluid and the solid domains respectively in which, the total number of elements were 253000 and 603000 approximately for design-A (initial) and design-B (improved) respectively. The element size values applied to all designs in this case study were obtained from a grid sensitivity analysis which was carried out previously in subsection 3.3.3.

The numerical simulation is executed using the finite rate chemistry (FRC) laminar combustion modelling code within the ANSYS CFX 12.1 solver which also accounts for the coupling of heat transfer and fluid dynamics, using a single step hydrogen-air combustion reaction described as follows:

$$H_2 + 0.5\,(O_2 + N_2) \rightarrow H_2O + 0.5\,N_2 \qquad (6\text{-}1)$$

The associated Arrhenius expression parameters used to describe the chemical reaction rate in Eq.((6-1)) are taken from (ANSYS Inc., 2009b) and listed in Table 6-6.

Table 6-6: Arrhenius expression parameters for a single reaction of H_2-air

Arrhenius parameter	Value
Pre-exponential factor (m^3/mol.s)	9.87E+05
Temperature exponent (-)	0
Activation energy (kJ/mol)	31

In addition, the expressions integrated within the CFD code that calculate the combustor efficiency, the maximum fuel energy release, the fuel and oxidiser mass fractions, the heat transfer by means of convection from the combustor outside walls, the radiative heat transfer coefficient and the thermal conductivity of 316L type stainless steel are described and detailed in section 5.6. Finally, the equivalence ratio, the mass flow rate and the radiative emissivity are chosen to be equal to 0.6, 0.0352 g/s and 0.8 respectively, with reference to atmospheric temperature of 300 K and a pressure of 1 atm.

6.2.1.3 Results and discussion

The numerical results of the temperature and velocity distributions at mid-plane are shown in Figure 6-7 and the values of the flow metrics of interest obtained from both numerical simulations are listed in Table 6-7.

The efficiency and flame temperature of Design-B in comparison to Design-A were increased by 2.6 % and 3.8 % respectively. Those increases resulted from the reduction in total heat loss of the combustor walls to the surrounding environment, gained by the

reactants flow inside the micro-cooling channel, despite the fact that Design-B has a total outside surface area larger than that of Design-A therefore; the external wall temperatures which are directly related to the heat dissipation, were decreased as shown in Figure 6-7 and detailed in Table 6-7.

Following from the above outcome, if the structure of the device is constructed from high thermal conductivity material, a micro-scale combustion chamber can be made to operate effectively with higher efficiency and less heat dissipation to the surrounding environment by the addition of a micro-cooling channel. It has been confirmed that the manufacture of such a device represented by Design-B in-house is feasible.

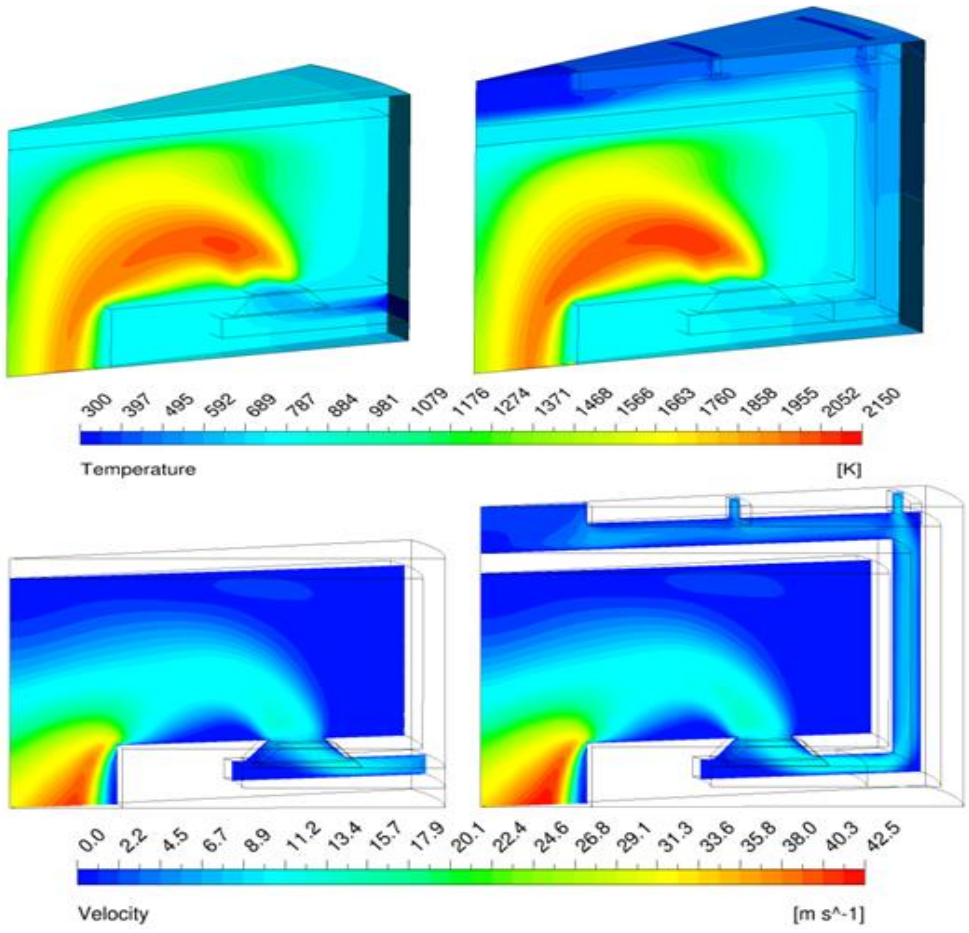

Figure 6-7: Temperature and velocity contours comparison at mid-plane and outside walls

Table 6-7: Design-A and Design-B flow metrics of interest

Flow metrics	Design-A (initial)	Design-B (improved)
Combustor Efficiency (%)	93.0	95.6
Maximum flame temperature (K)	2067	2149
Upper wall temperature (K)	708	459
Vertical wall temperature (K)	666	539
Lower wall temperature (K)	692	664
Total heat loss (W) at 22.5^{o} section	0.38	0.236

6.2.2 Multi-objective optimisation - Case study 2-A

In this test case, a multi-objective design optimisation has been carried out with the objectives to improve the overall efficiency of the device and to reduce the fuel consumption. The overall microcombustor geometry used in this investigation has a similar topology to that of Design-B studied in the previous subsection. The computational modelling of the combustion process is implemented in the commercial computational fluid dynamics package ANSYS-CFX using the Finite Rate Chemistry (FRC) laminar combustion model and a single step hydrogen-air reaction described previously in Eq.(6-1). The optimisation design system comprises also the ANSYS ICEMCFD package for the automatic geometry and mesh generation and the Multi-Objective Tabu Search algorithm for the design space exploration. The next subsections are presented and detail the following:

1. Parameterisation of the design problem
2. Numerical grid modelling
3. Description of the integrated optimisation system
4. Definition of the design problem – Objective functions, hard design constraints and MOTS parameters settings
5. Results and discussions

6.2.2.1 Geometry design configuration

The microcombustor operating strategy in this study differs from the optimum combustor designs found in case study 1-B by deploying non-premixed reactants at the inlets where the fuel and the oxidiser are injected into the device from separate ports. Single fuels set with a total number of 16 injectors and fixed dimensions of 0.15 mm in width and an arc presents the length with an angle of 19 degrees from the device centreline. Two types of air injectors are used; primary and secondary injectors. The primary injector is located at the centre of the external upper wall where the diameter is identified as a design parameter and the secondary set with a total number of 16 injectors and dimensions similar to those of the fuel injectors which are kept constant throughout the whole optimisation process. This configuration will assess the fuel-air mixing when the device is configured to operate with a higher total mass flow rate and secondly, reduces the structure temperature of the vertical wall as well as the reactants mixture which prevents premature combustion (autoignition) inside the micro-cooling channel. The initial design configuration at the start of the optimisation process is similar to that of Design-B (Figure 6-6).

6.2.2.2 Parameterisation of the design problem

Based on the conclusion regarding the design parameters from the previous multi-objective design optimisation investigation carried out in case study 1-B, the microcombustor geometry is represented by five design parameters shown in Figure 6-8 and they are:

- P1: Combustor outlet radius
- P2: Micro-cooling channel height
- P3: Chamber height
- P4: Inlet-to-chamber length (where the width is constant at an arc angle 8.25^{o} from the device centreline)
- P5: Primary air injector radius

It can be seen that the combustor exit design parameter is considered in this study. It had been previously concluded that it can be discarded from the optimisation process. But this parameter is now kept because the hard design constraints (discussed later) have changed at this part of the problem and therefore this parameter may have a positive impact on the design objectives considered.

Similarly, parameter (P5) is considered here because of the following scenario: when the device is configured to operate at a higher total mass flow rate, the flame will be located closer to the chamber upper structure therefore, the fresh air flow impingement from the primary injector on the chamber wall can lower the structure temperature.
The associated operational design parameters are:

- Mixture equivalence ratio (ER)
- Mass flow rate (MFR)
- Percentage of the total air mass flow rate injected through the primary air injector.

The upper and lower limits of those design parameters are listed in Table 6-8 with the initial design parameters values and their step sizes.

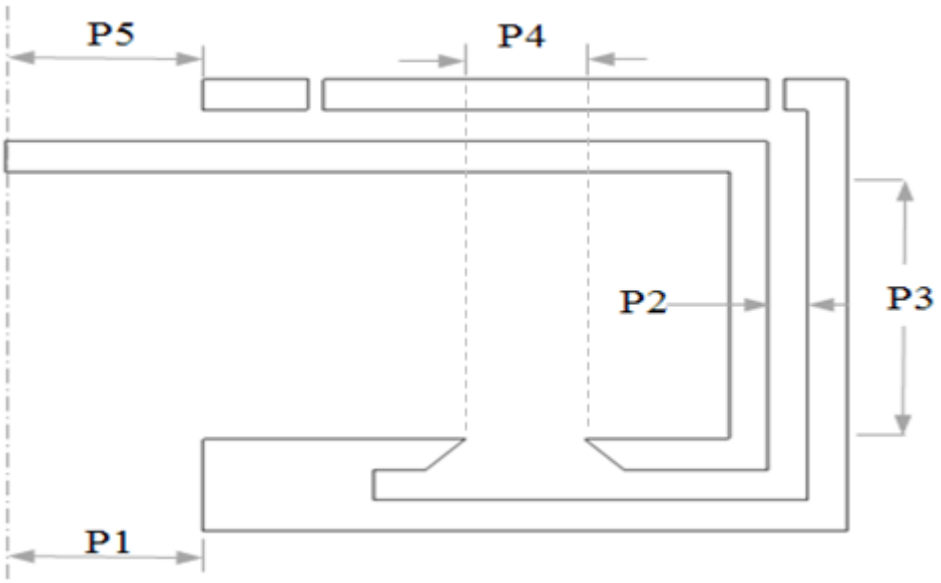

Figure 6-8: Sketch details the geometrical parameters – case study 2-A

Table 6-8: Design parameters–operating limits & their step sizes (Case study 2-A)

Parameter	Unit	Lower limit	Datum	Upper limit	Step size
Geometrical					
P1	mm	0.5	1.0	1.5	0.25
P2	mm	0.2	0.3	0.4	0.05
P3	mm	1.0	1.8	2.0	0.02
P4	mm	0.6	0.9	1.2	0.1
P5	mm	1.0	1.5	2.0	0.25
Operational					
ER	--	0.45	0.6	0.9	0.025
MFR	g/s	0.03	0.035	0.12	0.005
Primary air	%	0.5	0.7	0.9	0.1

6.2.2.3 Numerical grid modelling

Such combustion problems are characterised by a complex flow field, as well as chemical reaction modelling, which both demand a high quality mesh to capture the physics of the problem. Hence another important task after the geometry parameterisation step is the generation of a sufficiently high quality and reliable computational grid throughout the multi-objective design optimisation process. Therefore, a 3D section with an angle of 22.5 degrees is used which represents the main design features of the problem. In general, an unstructured mesh type is implemented with a maximum element volume size equal to 0.09 for the fluid and 0.115 for the solid domain which leads to a total of 500,000 approximately. Also, the core of the fluid domain was converted from an unstructured to a structured mesh type as shown in Figure 6-9.

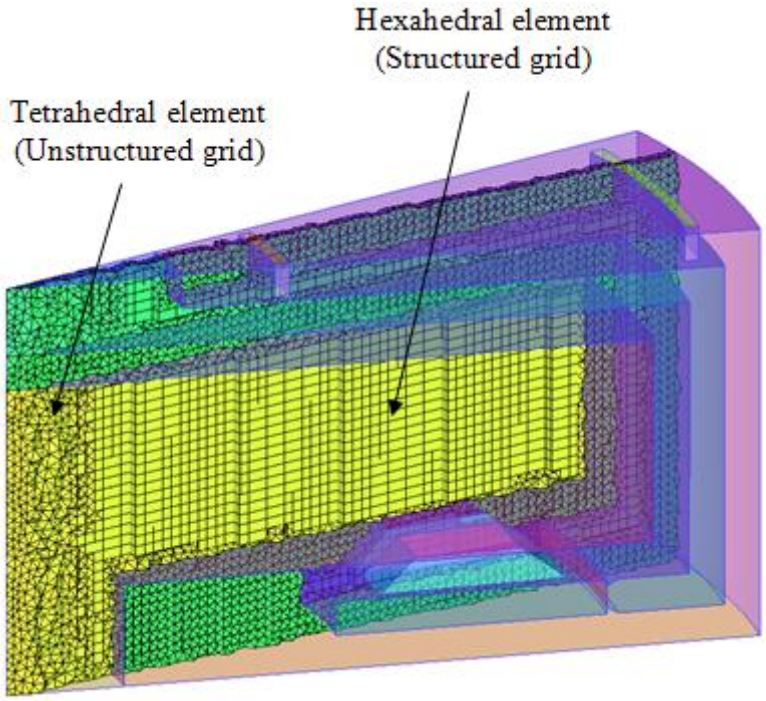

Figure 6-9: Grid configuration at a vertical plane - case study 2-A

6.2.2.4 Description of the integrated optimisation system

The integrated optimisation system was previously described in Figure 2-3. However, as a measure to reduce wall-clock run time and to explore the optimisation system capability, the optimisation was run on a three-node parallel PC cluster with four CPUs per node. Another measure to reduce the optimisation cost is to initialise the CFD calculations for the new design with the simulation result obtained from the datum or even the previously investigated design, in which the flow, the heat and the reactant species and their products are well developed within the numerical grid. Therefore, it is faster to obtain converged solutions that meet the criteria set. All numerical equations in this work have convergence criteria of 1.0E-06.

6.2.2.5 Definition of the design problem

1. Objective functions

The main combustor design requirements are to achieve high power density and efficiency, low fuel consumption and emission with wide flammability limits and stable flame inside the combustion chamber. Therefore, in this multi-objective design study two-objective functions are used with the aim of maximising the combustor efficiency and at the same time minimising the fuel consumption where both functions expressions were presented in section 5.3. The benchmark values of the initial design efficiency and its total fuel consumption are calculated as 95.8 % and 34.9 g/hr respectively based upon an equivalence ratio of 0.6, initial reactants temperatures of 300 K, combustor reference pressure of 1 atm and low heating value for hydrogen of 121 MJ/kg.

2. Hard design constraints

In this optimisation study, there are five hard design constraints considered and they are:

- 1000 K < average outlet temperature < 1800 K
- Maximum structure temperature < 1000 K
- Micro-cooling channel maximum temperature < 850 K
- Maximum unburned fuel at the outlet =< 0.1%

The first constraint above is set upon the minimum thermal cycle requirement and the maximum operating temperature of the turbine blades. Shan et al. (2005) have reported the requirement of 1600 K of temperature from the combustor outlet for their micro gas turbine engine in order to produce 39 W of power. The second constraint is set as the maximum allowable structure operating temperature. For 316L type stainless steel, the maximum operating temperature is 1000 K (Attia, 2011). The third constraint is applied to prevent immature combustion taking place inside the micro-cooling channel. Hydrogen-air stoichiometric mixture has an autoignition temperature of 858 K at 1 atm (Glassman, 2008). The final constraint is considered in order to ensure almost complete combustion. Any design violating these constraints during the optimisation process is not accepted.

3. MOTS parameters settings

The multi-objective Tabu Search algorithm is a heuristic optimisation technique that exhibits local search characteristics. The algorithm is controlled by the parameters listed in Table 6-9 (Case study 2-A).

Table 6-9: Tabu Search parameters settings for Case study 2-A & 2-B

TS parameter	Case 2-A	Case 2-B	Description
n_stm	25	25	STM size - last *n_stm* visited points are Tabu
n_regions	4	4	Each design parameter is divided into *n_regoin* in LTM to define which regions of the search have been less visited
Intensify	25	15	Intensify search starting from a randomly selected point from IM when *i_local == intensify*
Diversify	55	45	Moves the search to unvisited regions from LTM when *i_local == diversify*
Reduce	75	75	Step size reduction is an intensive search in the region of the current optimal solutions (Pareto) which starts when *i_local==Reduce*
SSRF	0.5	0.5	Step size reduction factor
im_thresh	10	10	Intensification memory size threshold. Intensification replaces diversification move above this value
n_sample	6	4	Number of points sampled randomly at each Hooke & Jeeves's move

6.2.2.6 Results and discussions

The progress made by the MOTS algorithm within 870 optimisation iterations is presented in Figure 6-10, where 11 objective function evaluations were executed on average per optimisation iteration and a total number of 8 weeks was required to obtain the final optimisation results represented in this subsection.

The history of the search pattern revealed that 11 optimum designs were found after 156 optimisation iterations, the maximum design improvement in normalised efficiency was 3.2 % at the cost of 82 % increase in the fuel consumption. Thereafter a further 185 iterations, seven more optimum designs were obtained, all those designs were located at the top end of the Pareto front which indicated a further improvement in the device efficiency and further increase in the fuel consumption. An improvement of 3.7 % in normalised efficiency has been achieved in comparison to the datum design at the cost of 161 % increase in the normalised fuel consumption. Analysing the latest finding, a minor improvement of 0.5 % is calculated in the optimum design which corresponds to the highest value in the normalised efficiency in comparison to its counterpart found at 156 optimisation iterations at a significant increase in the normalised fuel consumption of 80 %. Following this analysis, the optimisation search criterion was limited up to a value of 1.2 in the normalised fuel consumption. This meant that any new optimum design found with a normalised fuel consumption value higher than the 1.2 was discarded. This demonstrated the flexibility of the MOTS algorithm, directing the optimiser search by the designer if required, to a specific design target within either or both objectives considered at any time of the optimisation process and without the need of restarting from the initial design stage. A total number of 64 optimum designs were found after 870 optimisation iterations represented by the Pareto front shown in Figure 6-11, in which 32 designs were found after the modification applied to the search criteria mentioned above as well as the execution of the diversify, the intensify and the step size reduction moves by the TS algorithm. An example of such a design is the compromised (design 3) which is highlighted in Figure 6-11.

Further investigation into the Pareto front revealed that 19 design vectors were found to be sharing a total number of 11 optimum designs which suggested the existence of multimodality design performances. As an example, four optimum design vectors were found to have the exact objective function values as illustrated in Table 6-10.

Furthermore from the optimisation search results, all the designs found including the dominated designs by the optimal design set performed better in one of the objectives and a total number of 17 optimum designs had superior performances in both design objectives compared to the initial design.

Moreover, a large reduction in normalised fuel consumption of 35.5% was achieved as represented by design 4 (Figure 6-11) compared to the datum design at the cost of 1.1 % and 35.7 % decrease in the device efficiency and the net power respectively.

In comparison to the datum design, the chosen compromised design (design 3) preforms better in terms of both objectives; an efficiency improvement of 1.46 % and a reduction in fuel consumption of 10.1 % despite the increase in total mass flow rate, micro-cooling channel height (P2) and chamber height (P3) but, at the price of 8.7 % reduction in the net power generation.

It should be noted that all optimal designs found (design 2, 3 and 4) have lower average outlet temperatures and lower maximum solid (structure) temperatures relative to the initial design. Figure 6-12 shows the temperature and the velocity magnitude contours inside the microchamber at x-y plane of the initial and the optimal designs found.

Table 6-11 illustrates the geometrical and the operational parameters of the datum and the optimal designs found from the Pareto set and Table 6-12 presents the design flow metrics of the above designs at 870 optimisation iterations.

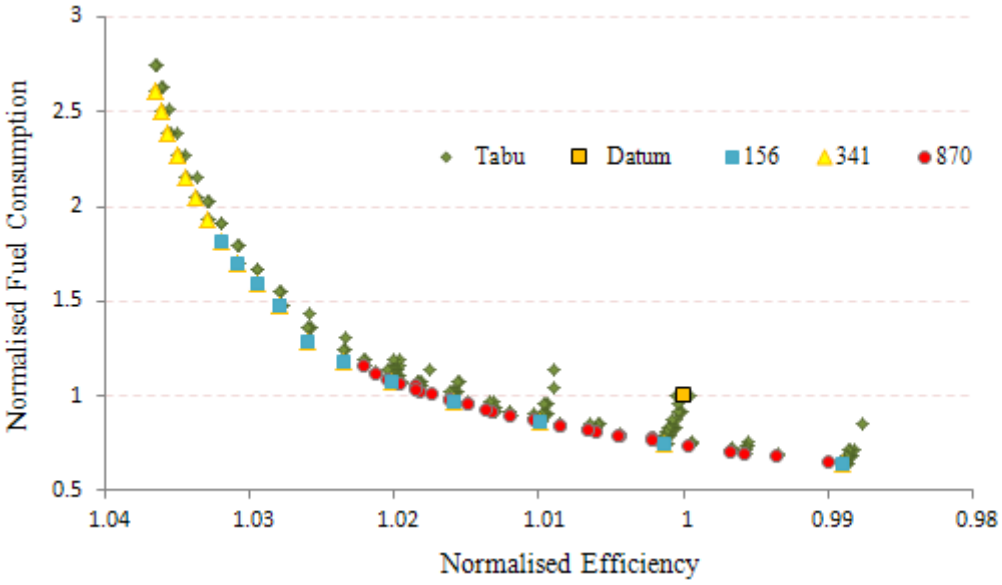

Figure 6-10: Pareto-optimal set at different optimisation iterations

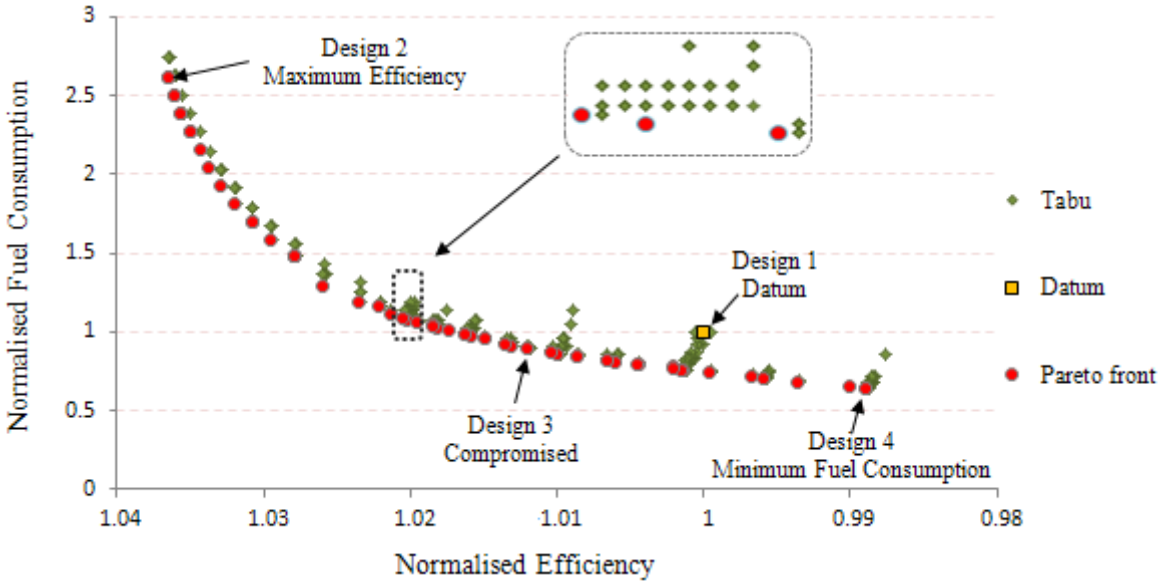

Figure 6-11: Multi-objective design search at 870 optimisation iterations

Table 6-10: Optimum design vectors sharing the same objective values

Parameter	Design vector			
	1	2	3	4
P1	1.5	1.5	1.5	1.25
P2	0.25	0.25	0.2	0.2
P3	2	2	2	2
P4	0.5	0.4	0.6	0.6
P5	1.5	1.5	1.5	1.5
ER (--)	0.475	0.475	0.475	0.475
MFR (g/s)	0.065	0.065	0.065	0.065
Primary air (%)	50	50	50	50
Obj-1 *	1.027	1.027	1.027	1.027
Obj-2 **	1.475	1.475	1.475	1.475

** Obj-1 - Normalised efficiency*

*** Obj-2 - Normalised fuel consumption*

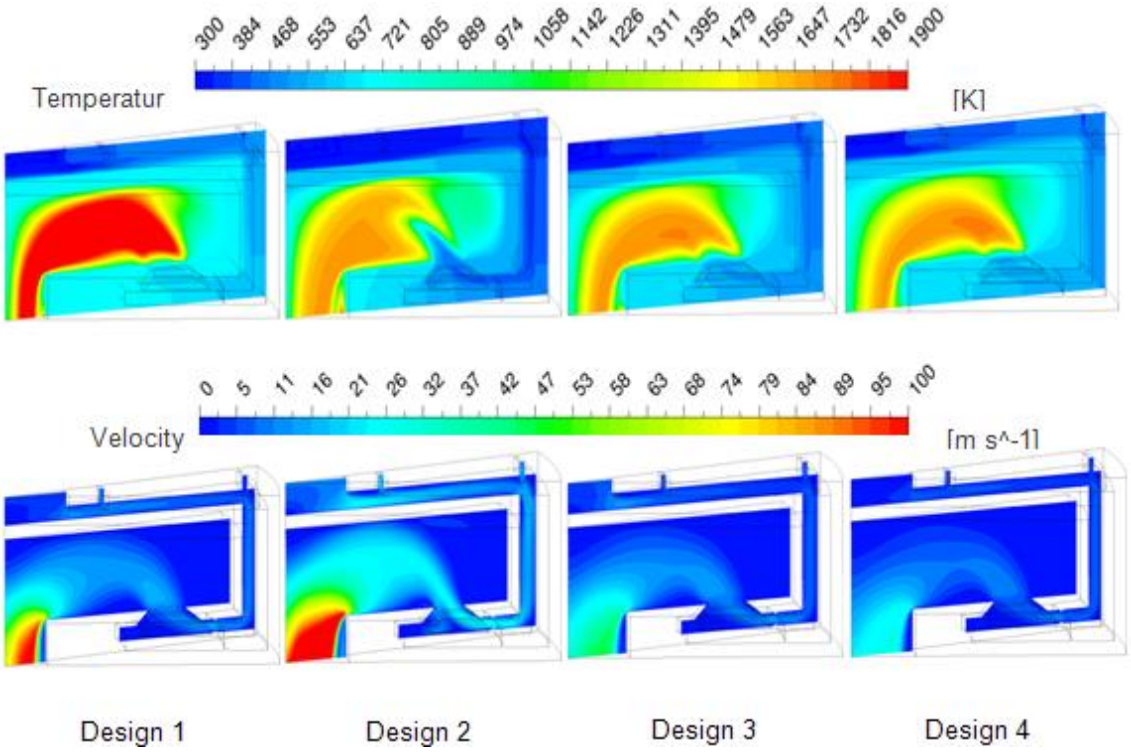

Figure 6-12: Temperature (top) and velocity magnitude (bottom) distributions at x-y plane for the highlighted designs found in Figure 6-11

Note: For visual comparison, all designs at the same temperature and velocity scales

Table 6-11: Geometrical and operational design parameters of the initial and the optimum designs highlighted in Figure 6-11

Design Parameters	Design			
	1	2	3	4
P1	1.0	1.5	1.445	1.5
P2	0.3	0.4	0.375	0.3
P3	1.8	2.0	1.955	2.0
P4	0.9	0.7	0.335	0.9
P5	1.5	1.5	1.089	1.5
ER (--)	0.6	0.475	0.4521	0.45
MFR (g/s)	0.035	0.115	0.0416	0.03
Primary air (%)	70	60	56.45	50

Table 6-12: Datum, maximum efficiency, minimum fuel and compromised designs flow metrics at 870 optimisation iterations (Case study 2-A)

Design configuration	Design 1 (Datum)	Design 2 (Max. Eff.)	Design 3 (Compromised)	Design 4 (Min. Fuel)
MFR (g/hr)	126	414	150	108
ER (--)	0.6	0.475	0.452	0.45
T_{out} (K)	1788	1586	1516	1490
T_{solid} (K)	739	663	633	635
Efficiency (%)	95.84	99.3	97.3	95.8
Net power (W)	70.3	190.1	64.2	45.2
Fuel consumption (g/hr)	34.9	91	31.4	22.4

Figure 6-13 presents the optimisation search history for the thermally improved combustor design concept and details the benefit of the TS algorithm characteristics to advance the search through the complex and nonlinear design space of the problem. It can be seen from this figure that the optimisation search located four regions defined by the optimisation steps as illustrated in Table 6-13.

During the whole optimisation search, the intensification, the diversification and the step size refinement (reduction) were performed nine, six and two times respectively as illustrated in Figure 6-13 (Top). For example, Region-1 was located by performing search diversification precisely after 137 optimisation steps following 55 unsuccessful iterations. As a result, eight Pareto designs were discovered and then the search intensification was deployed at 270 steps following 25 stillborn iterations, a further two optimum designs were added to the MTM. In contrast, the combination effect of the search diversification, the local step size refinement and the search intensification moves were evident in finding Region-4. The search progressed in the design space without any success in finding an optimum design after the execution of search diversification at 682 optimisation steps, the SSR was implemented following a further 20 unsuccessful iterations at 702 steps. Thereafter, new optimum designs were found but then, it was necessary to implement search diversify and intensify moves in order to obtain all the 18 optimum designs found in Region-4.

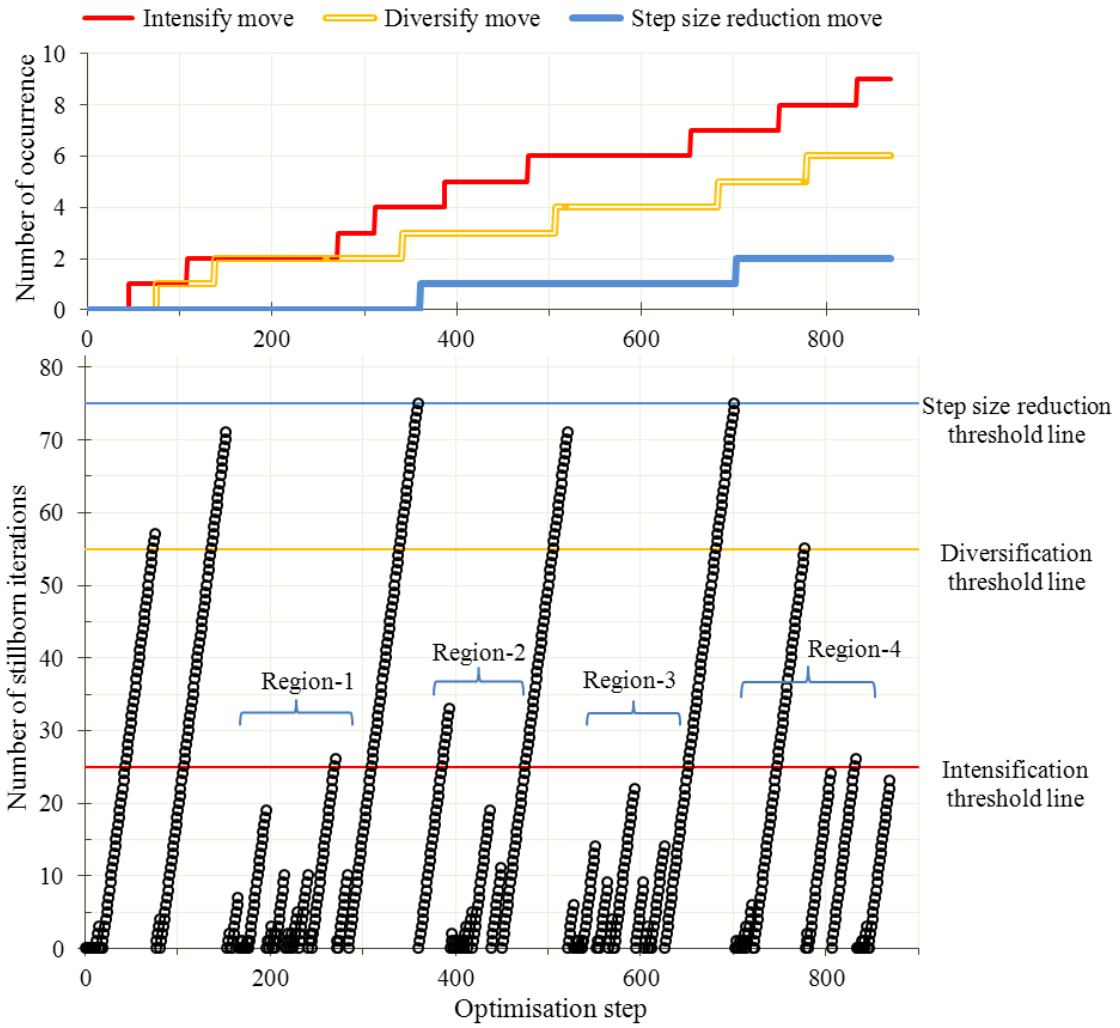

Figure 6-13: The history of the optimisation search for case study 2-A. Number of stillborn iterations vs. Optimisation step (bottom) & Number of intensify, diversify and step size reduction moves (top)

Table 6-13: The optimisation progress and the main TS characteristics used

Region (Figure 6-13)	New optimum	Optimisation step	Comments Region was found as a result of
Region - 1	10	155-275	SD & SI
Region - 2	5	360-440	SD, SSR & SI
Region - 3	22	520-625	SD
Region - 4	18	700-840	SD, SSR, SI, SD & SI

Where *SD* *Search Diversification*
SI *Search Intensification*
SSR *local Step Size Refinement*

6.2.3 Multi-objective optimisation - Case study 2-B

In the previous case study, a complex combustor concept was optimised using the MOTS optimisation algorithm, in which two conflicted objectives (the combustor efficiency and the fuel consumption) were improved. The individual optimum designs represented by the Pareto front were characterised by a single operating design point i.e. having only single values of the mass flow rate and the reactants equivalence ratio will lead to the following questions if the device is utilised in a real-world application;

1. What happens if the mass flow rate is fluctuated?
2. What happens if the reactants equivalence ratio is slightly changed?
3. Will the flame be stabilised inside the microchamber if any/both of the above is/are taken place? And what is the impact on the device performance?

The effect of these design parameters on the design objectives were previously discussed in chapter 1. The increase of the mass flow rate may result in a flame blowout (flame swept outside the combustion chamber), while the decrease in this value may result in a flame blow-off (flame extinction). Regarding the equivalence ratio, an increase of this value may result in autoignition of the fuel in undesired locations, such as the mixing zone; while on the contrary, a decrease of its value may result in flame extinction.

Therefore, the aim of this investigation is to find all the answers to the above questions in order to ensure the functionality and the compatibility of the device. This can be achieved by focusing the optimisation search only on the operational design parameters' aspects since the new optimisation search starts from the compromised design (design 3) highlighted previously in Figure 6-11 and its optimum geometrical parameters are listed in Table 6-11. The objective functions remain the same as defined in section 5.3 subject to the same set of design constraints listed in subsection 6.2.2.5.

6.2.3.1 Parameterisation of the design problem

In this case study and since the initial design (the compromised) was previously optimised, the five geometrical design parameters that were previously considered were kept constant throughout the optimisation process.

Regarding the operational parameters, even though initially three different operational design parameters; the MFR, the ER and the Primary air were considered, the latter

which controlled the amounts of air passed through the individual air injectors is now kept constant.

After the examination of the design parameters' history in the previous case study (2-A) and as briefly indicated by the two design extremes (design 2 & 4) in Table 6-11, it was clear that parameter *Primary air* was only configured to use values between 0.5 - 0.6, despite the fact that the corresponding parameter range has been defined between 0.5 - 0.9. This meant that only the lower 25 % of the total range of the variability of this operational design parameter was effective in the optimum level achieved. Hence, in order to further reduce the dimensionality of the optimisation in this investigation this design parameter is given a constant value of 0.56 % which corresponds to the compromised design value found previously in case study 2-A.

In comparison to the previous study, the step sizes of the most significant design parameters were reduced in order to investigate the performance behaviour of the device subject to minor variations of the design parameters and study their effect on the shape of the Pareto front. More specifically, the equivalence ratio (ER) and the mass flow rate (MFR) step sizes were changed from 0.025 to 0.02 and from 0.005 to 0.0025 respectively. Since the search step is shortened, it is expected to discover more Pareto optimal points. This time, the datum design of the optimisation search is the compromised which was found from the previous study (2-A). The datum design parameters, the upper and the lower limits of those parameters and their step sizes are listed in Table 6-14.

Table 6-14: Design parameters, operating limits & their step sizes - Case study 2-B

Parameter	Unit	Lower limit	Datum	Upper limit	Step size
ER	--	0.45	0.5	0.9	0.02
MFR	g/s	0.03	0.04	0.12	0.0025

6.2.3.2 Description of the optimisation system

The multi-objective integrated design optimisation system shown previously in Figure 2-3 is modified. The new system is presented in Figure 6-14.

The optimisation process starts from the input of the compromised design mesh file to the main loop of the design system every time the CFD calculations are executed. Therefore, there are no geometry parameterisation, geometry build and meshing

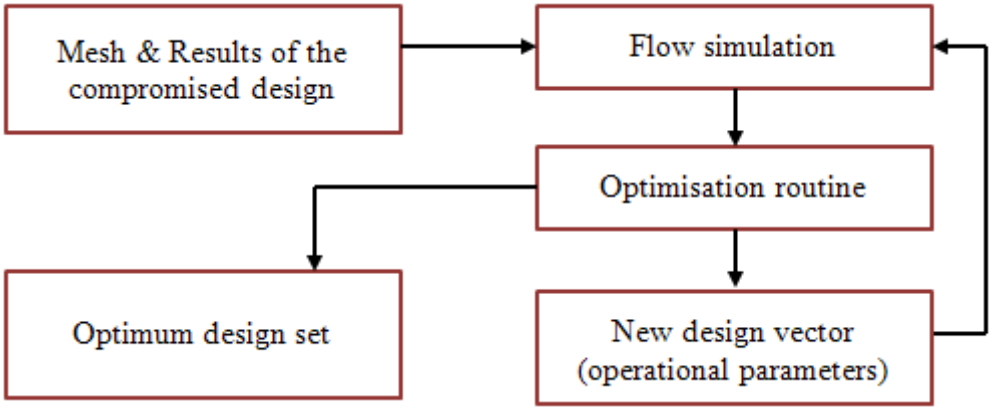

Figure 6-14: Schematic of the multi-objective optimisation system – Case study 2-B

processes involved. This contributes to a reduction in optimisation cost. The results of the flow metrics of interest were obtained from this stage. Based on this evaluation, the optimisation routine generates a new design vector (MFR & ER values). This vector is passed directly to the CFD code. This process continues until a stopping criterion is met. Again, the optimisation result is a set of optimum designs (Pareto set). The Tabu Search parameters configurations for this case were listed previously in Table 6-9.

6.2.3.3 Results and discussions

The progress made by the MOTS algorithm within 876 optimisation iterations is presented in Figure 6-15. The optimisation process was initiated from the "*compromised"* design obtained from case study 2-A. 1345 objective function evaluations were achieved over a period of ten days where the optimisation process was run on a three-node parallel PC cluster with 4 CPUs per node in order to further reduce the computational cost, in addition to the implemented measures mentioned above.

Three operating configuration sets were found, those sets are represented by the Pareto front after 876 optimisation iterations and are categorised by the reactants' equivalence ratio as shown in Figure 6-15 and Table 6-16. The Pareto front history investigation under the design objectives (amending the fuel consumption and the combustor efficiency) and constraints revealed after the start of the optimisation search, an optimum region of the design space with lower ER and MFR was located by the TS algorithm. This represented half of the designs found in set 1 with a total number of 21 designs in which three of those performed better in both design objectives. Thereafter, the optimisation algorithm located set 2 which is represented by 27 designs. All were

configured to use 0.455 of the reactants ER also characterised by higher normalised efficiency values relative to the initial design at the cost of the increase in the fuel consumption due to the increase in MFR. The final set found 78 optimum designs where 18 of these recorded an increase in the normalised efficiency and further increase in the fuel consumption with respect to the designs found in set 2, even though all the designs were adjusted to use a lower ER value of 0.4525 in comparison to the value of 0.455 in set 2. Then again, set 3 outclassed set 1 in terms of the combustor efficiency performance but at the price of an increase in the fuel consumption by up to 200 %.

From the above, the optimum operating sets of ERs found as illustrated in Table 6-16 don't represent the whole MFR design range of 0.03-0.12 g/s. For example, all optimum designs corresponding to ER of 0.46 represented by set 1 were found to operate within a MFR range of 0.03-0.058 g/s. Therefore, in order to answer all the questions mentioned at the beginning of this case study, both design MFR extreme values (i.e. 0.03 and 0.12 g/s) were tested numerically with the lowest and the highest ER values of 0.4525 and 0.46 found as a result of the optimisation investigation respectively.

The flow metrics results values of interest are shown in Table 6-15. Those results revealed that the combustion can be sustained inside the chamber within the whole MFR design range using the lowest and the highest ER values above and respecting all the hard design constraints considered. Also, it can be seen from this Table that changing the ER value from 0.4525 to 0.46 at the same applied MFR had negligible effect on the device efficiency and minor influence on the fuel consumption and the net power generation. However, this is not the case when the MFR varies; the datum design has an ER value of 0.5 and MFR of 0.04 g/s thus the effect of operating the device with a reduced MFR of 0.03 g/s has resulted in the efficiency being decreased by 2 % and net power generation by ~27 % but an improvement of 25 % in the fuel consumption. In contrast, operating the device with a higher MFR of 0.12 g/s increased the combustor efficiency by 2.7 % and net power by 67.5 % at the cost of increasing the fuel intake by 66.7 %.

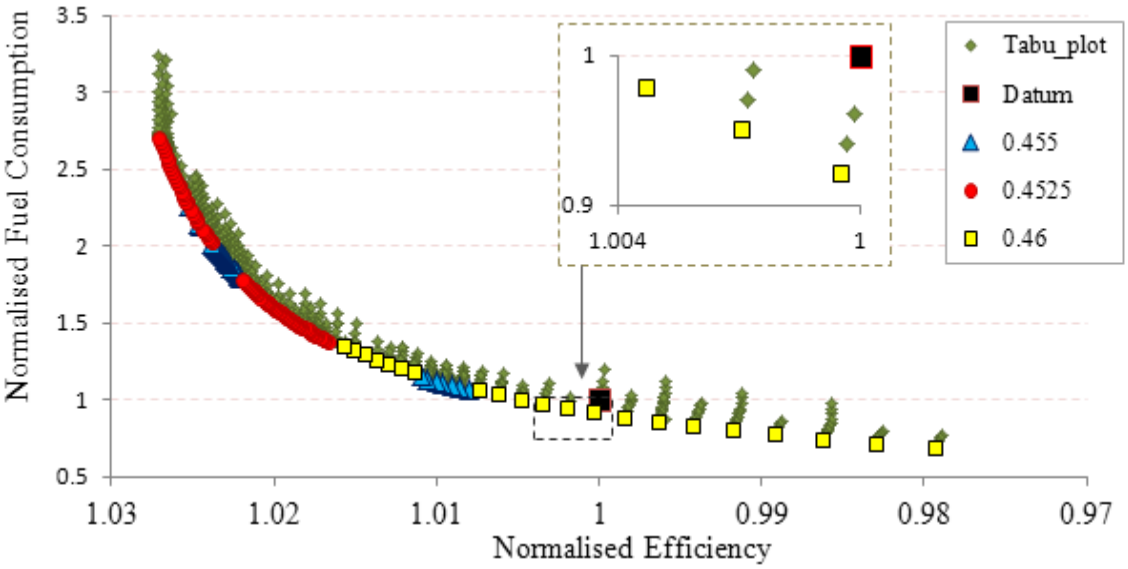

Figure 6-15: Optimisation search pattern and the Pareto set found after 876 iterations (Case study 2-B)

Table 6-15: Flow metrics values of interest of the datum, the lowest and the highest ERs at both MFR design points extremes – case study 2-B

ER	MFR (g/s)	Efficiency (%)	Fuel intake (g/hr)	Net power (W)	T_{max} (K)	T_{ex} (K)	T_s (K)
0.5	0.03	94.7	25	49.7	1893	1578	702
	0.04	96.7	33.3	67.7	1865	1604	690
	0.12	99.4	100	208.6	1841	1637	684
0.4525	0.03	94.77	22.6	45.1	1777	1482	675
	0.12	99.2	90.6	157.3	1724	1536	657
0.46	0.03	94.76	23.0	45.8	1795	1497	680
	0.12	99.2	92.1	159.9	1741	1552	661

Table 6-16: Optimum operating parameters sets found from the Pareto front shown in Figure 6-15

Operating configuration	ER	Number of optimum designs	Normalised fuel consumption range	MFR range (g/s)
Set 1	0.46	21	0.69 – 1.35	0.030 – 0.058
Set 2	0.455	27	1.06 – 2.26	0.046 – 0.100
Set 3	0.4525	78	1.38 – 2.70	0.060 – 0.120

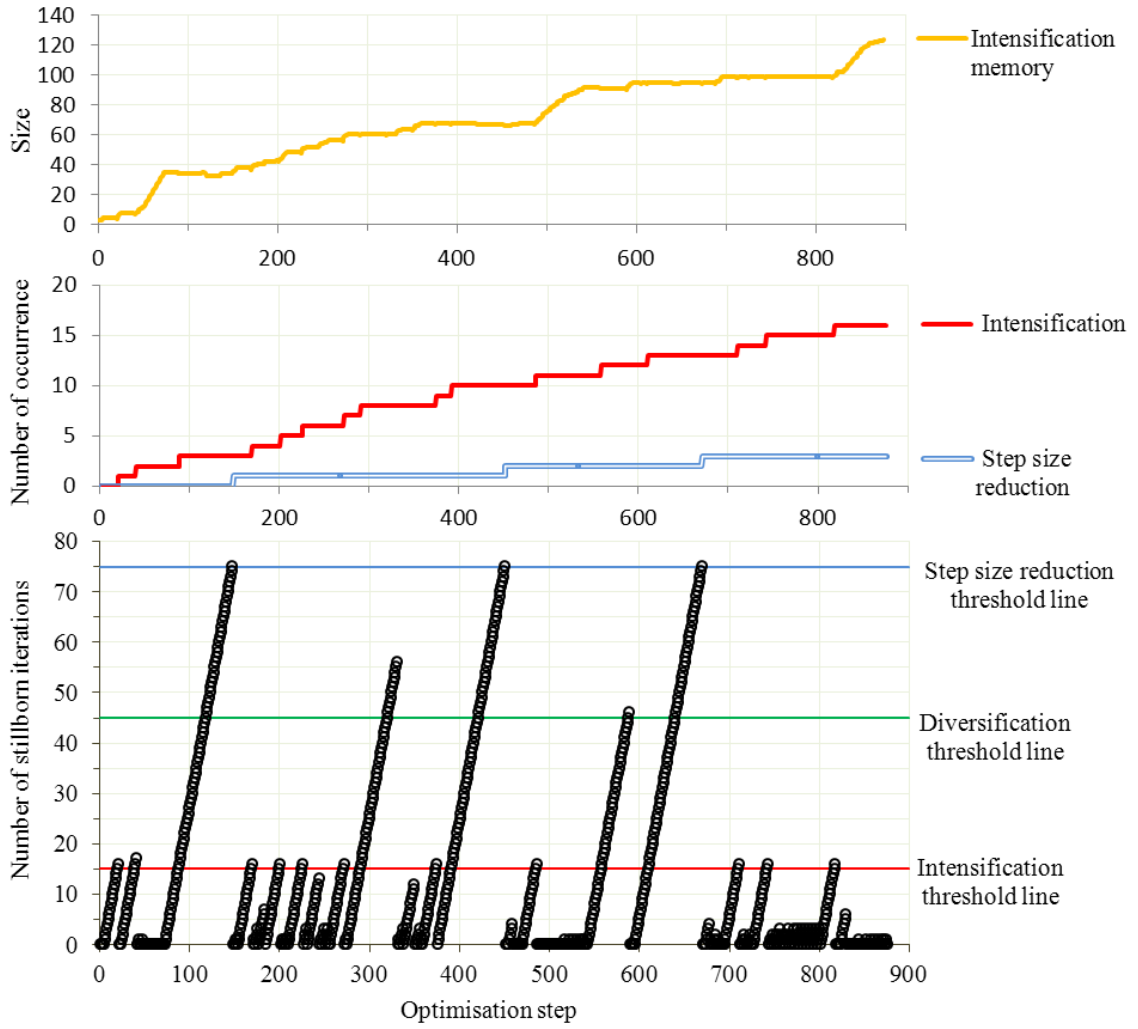

Figure 6-16: Optimisation search history for case study 2-A. Intensification memory (top), Number of intensification and SSR moves (middle) & Number of stillborn iterations vs. Optimisation step (bottom)

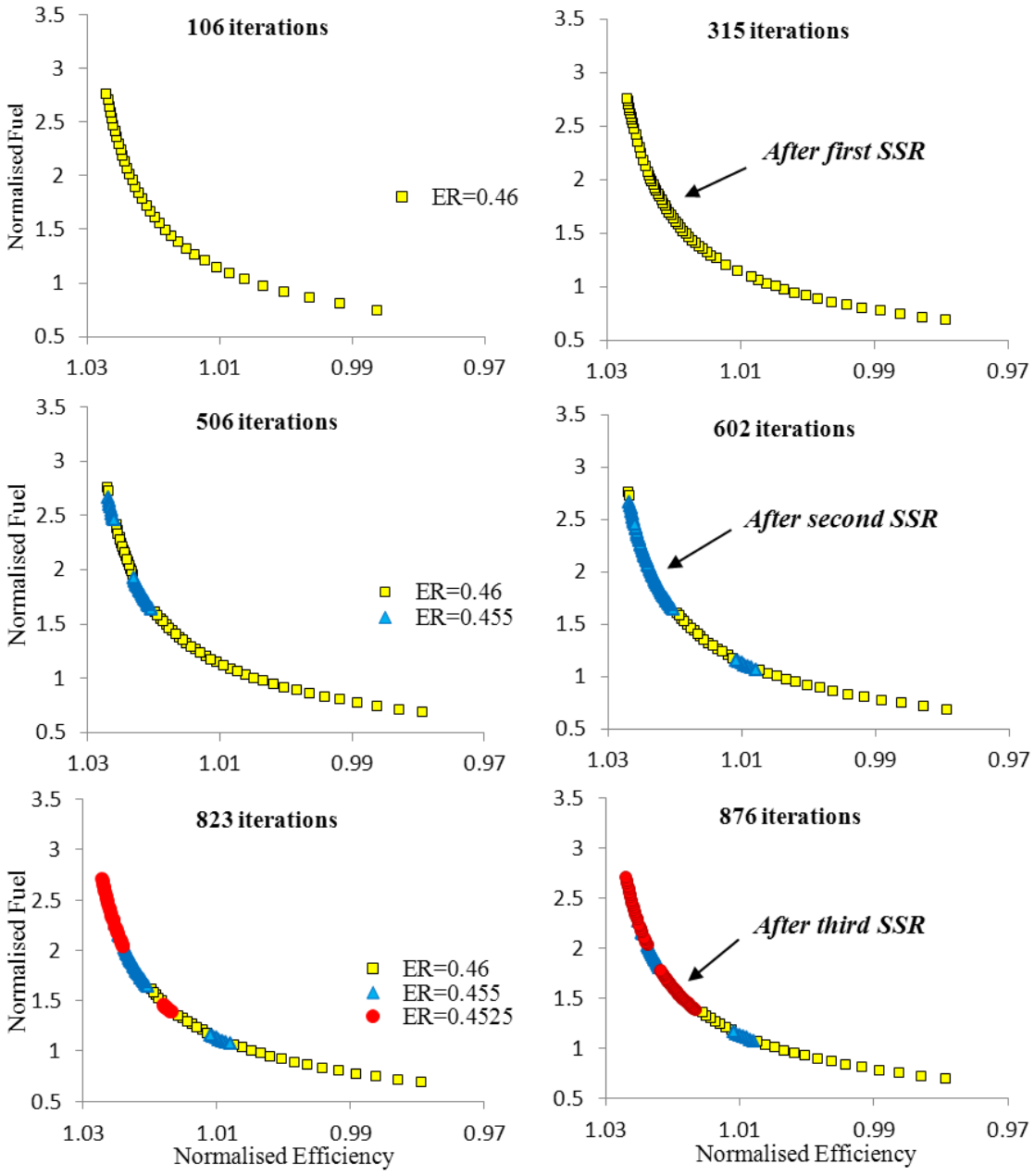

Figure 6-17: The Pareto front advancement at different optimisation iterations for case study 2-B

Figure 6-16 presents the optimisation search behaviour and demonstrates the TS algorithm characteristics' benefits, navigating and advancing the search through the highly complex and nonlinear design space of the problem. In this figure, the unsuccessful optimisation iteration (i.e. no new optimum designs found) were plotted verses the optimisation step (bottom), it also highlights the design threshold lines for the intensification, the diversification and the step size reduction used in this investigation. The number of the occurrence throughout the search progress of the intensification and the step size reduction moves were plotted (middle) and finally, the intensification memory size history vs. optimisation steps is shown (top).

The effect of the step size reduction move which was performed by the TS algorithm three times in total during the whole design process can be seen firstly after 149 optimisation steps as shown in Figure 6-17 (top left), where a rich Pareto front was unveiled at 315 optimisation steps. Subsequently, the second and the final step size reduction moves were carried out after 450 and 670 optimisation steps respectively. Yet again the impact of the SSR is shown in Figure 6-17, middle left compared to middle right for the second SSR and bottom left compared to bottom right for the third and final SSR.

In this case study, the diversification move wasn't performed by the optimisation algorithm despite the number of the unsuccessful iterations reaching the diversification threshold value of 45 in five separate occasions, but instead the intensification move was implemented with the logic that if the intensification memory size exceeded the threshold value of ten[7], then it is assumed that there are enough candidate designs to be tested from the Pareto-equivalent set (Intensification Memory) when the intensification move is executed. This is demonstrated in Figure 6-16 (top) which shows the intensification memory size was of a number higher than the threshold value, precisely by 25 before the first diversification threshold value of 45 was reached and the size of this memory was kept above its threshold during the whole optimisation process.

[7] This value is hard-coded - see Kipouros (2006)

6.3 Case study 3 (Hydrocarbon-fired combustor performance investigation)

This case study was carried out in order to investigate the possibility of replacing the hydrogen with a hydrocarbon fuel and to study the effects on the device performance in terms of the efficiency and the operating parameters (MFR & ER) under the new fuel strategy. However, a stable combustion inside the microchamber is expected under the condition that the maximum allowable material and the maximum micro-channel temperatures are also respected. Three different hydrocarbon fuels were considered and they are: Propane (C_3H_8), Ethane (C_2H_6) and Butane (C_4H_{10}), the individual reaction equation and the reaction order are defined below:

$$C_3H_8 + 5.0\ (O_2 + N_2) \rightarrow 4\ H_2O + 3\ CO_2 + 5.0\ N_2 \tag{6-2}$$

Order of reaction: $C_3H_8 = 0.10$ & $O_2 = 1.65$

$$C_2H_6 + 3.5\ (O_2 + N_2) \rightarrow 3\ H_2O + 2\ CO_2 + 3.5\ N_2 \tag{6-3}$$

Order of reaction: $C_3H_8 = 0.10$ & $O_2 = 1.65$

$$C_4H_{10} + 6.5\ (O_2 + N_2) \rightarrow 5\ H_2O + 4\ CO_2 + 6.5\ N_2 \tag{6-4}$$

Order of reaction: $C_3H_8 = 0.15$ & $O_2 = 1.6$

The associated Arrhenius expression parameters (ANSYS Inc., 2009b) used to describe the chemical reactions above are listed in Table 6-17.

Since the reaction rates for typical hydrocarbon fuel are an order of magnitude lower than that for hydrogen (Waitz et al., 1998), it is likely at high operating mass flow rate and equivalence ratio (near/or unity) that a small quantity of the hydrocarbon fuel escapes unburned from the combustor chamber. Therefore, equation (5-4) that calculates the MFER was modified, as defined below in Eq.(6-5), in order to account for the unburned fuel thus, accurately predicts the combustor efficiency which is a function of the MFER.

$$\mathrm{MFER} = \mathrm{LHV} * \mathrm{MFR} * \left(\left(\frac{1}{1 + \frac{\mathrm{AFR_{st}}}{\mathrm{ER}}} \right) - (\mathrm{UCHmf}_{ex})_{\mathrm{CFD}} \right) \tag{6-5}$$

Table 6-17: Arrhenius expression parameters for 1-step hydrocarbon fuel reactions

Reaction	Pre Exp. Factor ($cm^{2.25}/s \cdot mol^{0.75}$)	Temperature exponent (-)	Activation Energy (kcal/mol)
Propane-air (6-2)	8.6 E +11	0	30
Ethane-air (6-3)	1.1 E +12	0	30
Butane-air (6-4)	7.4 E +11	0	30

6.3.1 CFD modelling

In this investigation, the initial (datum) design and numerical grid configuration used previously in case study 2-A are implemented. The numerical simulation is accomplished using the finite rate chemistry (FRC) laminar combustion modelling code within a well-known commercial CFD solver named ANSYS CFX 12.1 which also accounts for the coupling of heat transfer, fluid dynamics and chemical reaction modelling. 95 % of the total mass flow rate of the oxidiser (air) was injected through the *primary air injector*; this setting was kept throughout this case study. Moreover, the heat transfer from the combustor chamber walls to the surrounding environment by means of the convection and the radiation were also numerically considered, the radiative emissivity of 0.8 was set. Furthermore, the total mass flow rate of the reactants mixture and the equivalence ratio were tested over a range of 0.01-0.04 g/s and 0.6-1.2 respectively, at initial reactants temperatures of 300 K and numerical calculations reference to a pressure of 1 atm.

6.3.2 Results and discussions

6.3.2.1 Design configuration effect on combustor performance

The results obtained from the numerical simulations using propane-air as reactants mixture for different MFR and ER revealed that the combustion couldn’t be sustained inside the chamber of the initial design under the applied boundary conditions. The attempt of increasing the chamber residence time by increasing its height from 1.8 to 3.0 mm has led to the same outcome above. Therefore, and using the latter geometry, different boundary conditions scenarios were considered as illustrated in Table 6-18.

Table 6-18: Different applied boundary conditions scenarios for the datum design considered with a total height of 4.8 mm

Scenario	MFR (g/s)	ER (-)	External walls (K)	Initial reactants temperature (K)	Combustion sustained? (Yes/No)
1	0.01	0.8	Adiabatic	450	Yes (Micro-Channel)
2	0.01	0.8	Non-adiabatic	450	No
3	0.02	0.8	Adiabatic	300	No
4	0.02	0.8	Adiabatic	450	No
5	0.01	1	Adiabatic	450	Yes (Micro-Channel)
6	0.02	1	Adiabatic	300	No
7	0.02	1	Non-adiabatic	800	No
8	0.02	1	Non-adiabatic	1000	No

The results relative to their boundary conditions described in Table 6-18 demonstrated that the combustion couldn't be sustained inside the microchamber even when the external walls were adiabatically treated. The applied boundary conditions in scenario 1 resulted in upstream burning inside the micro-cooling channel but then, the non-adiabatic external walls represented by scenario 2 demonstrated that the flame was blown out. Therefore tuning the operational parameters in scenario 2, such as increasing the ER and or the initial reactants temperatures, might lead the flame to be stabilised inside the microchamber however if possible, this suggests the limitation in the operating design parameters' ranges.

From the above and in order to achieve the design target, different geometry configurations shall be considered based on the fact that the hydrocarbon fuels have lower reaction rates to that of the hydrogen which aggravate chamber residence time. The requirement of an effective recirculation zone inside the chamber becomes more important to maintain stable combustion and better heat management to reduce the combustion energy loss to the surrounding area and to increase the reactants mixture temperature prior to chamber which reduces the chemical reaction time.

The first design considered is shown in Figure 6-18-(A) with a single set of inlets-to-chamber in a single row configuration which, located at the vertical wall of the chamber with the purpose of increasing the fluid path inside the chamber increases residence time. In addition, a new air inlet set was introduced at the lower wall of the chamber where fresh air was injected axially followed by a right angle turn prior to entering the chamber at 2 m/s and a temperature of 300 K. This air serves as an insulator between the hot combustion gases and the lower structure of the device.

Yet again, the numerical result predicted that the flame would be blown out of the chamber. This might be caused by the small cross-sectional areas of those inlets in comparison to the initial design which resulted in higher reactants velocity inside the chamber which exacerbates the residence time. Therefore a new geometry configuration represented by Figure 6-18-(B) was conceived. The cross-sectional areas of the inlets-to-chamber were increased by the introduction of the second row. This time, those areas were modelled to be identical in size to that of the initial design; this allows the effects on the fluid flow behaviour to be studied and the results of the same applied boundary conditions for different geometry configurations to be compared. Furthermore, the boundary conditions were similar to those of scenario 3 - Table 6-18 but non-adiabatic external walls were applied.

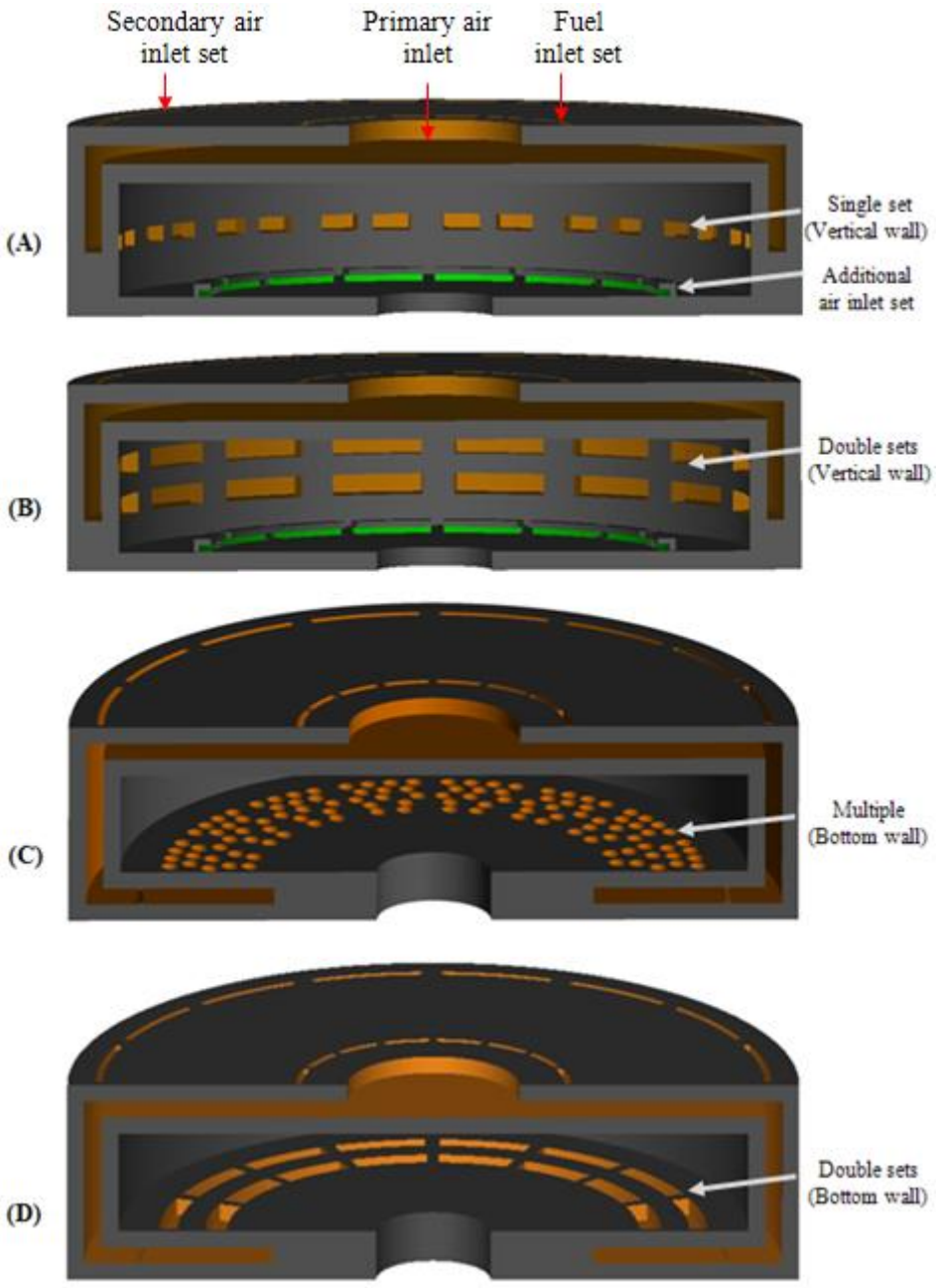

Figure 6-18: Cutaway of different geometry design configurations tested using hydrocarbon fuels

The numerical simulation results predicted a stable combustion inside the microchamber as presented in Figure 6-19 (top-left). Also, the following conclusions can be drawn from those results:

The flame was stabilised downstream near to the chamber exit which suggested the device was operated with a high MFR and or relatively long chemical reaction time.

- The flow recirculation zones at the current locations highlighted in Figure 6-19 (bottom) inside the combustion chamber appeared to be inadequate to ignite the fresh gases entering the chamber. Those zones should recirculate the combustion products of higher temperatures than the ignition temperature of the reactants mixture in order to effectively aid the combustion process.
- Operating with lower wall temperatures, particularly the upper and the vertical, has resulted in a small increase in the reactants flow temperatures inside the micro-cooling channel which implies lower initial enthalpy of the reactants prior to chamber. Consequently, this increases the chemical reaction time and lowers the

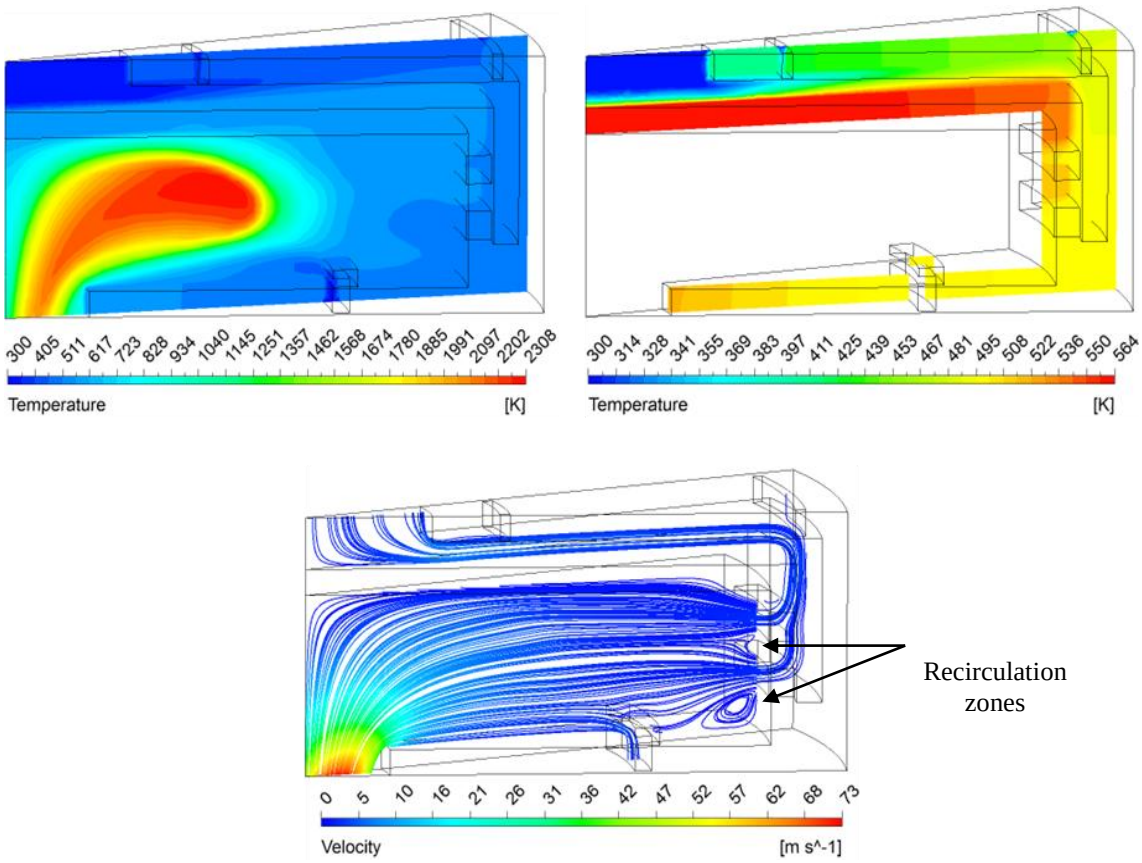

Figure 6-19: Temperature contours (top-left), Structure and micro-cooling channel temperature distributions (top-right) and streamlines velocity (bottom) of design (B)-Figure 6-18. All at the same vertical plane

flame temperature but operating the device with lower structure temperatures reduces the convective and the radiative heat loss of the combustor to the surrounding thus increasing the device efficiency.

- The results also demonstrated the effectiveness of the third air inlet set added to the design at the bottom wall of the chamber. The maximum structure temperature predicted numerically was 564 K compared to 923 K obtained from the same problem but without using the lower wall cooling as shown in Figure 6-20. The injection of the fresh air to the chamber at 300 K resulted in lowering the reaction temperature thus lowering the structure temperatures and increasing device efficiency.
- Unburned propane of 1 % in mass fraction was calculated at the chamber outlet plane; this value was decreased to 0.07 % when the initial reactants' temperatures were increased from 300 to 450 K. But when the device was configured to operate using a higher mass flow rate of 0.03 instead of 0.02 g/s, this value was 4.4%. In contrast, the fuel was completely consumed i.e. zero fuel mass fraction at the exit, when the third set of air inlets was not deployed.

This demonstrated another combustor design trade-off between cooling the chamber walls internally through the injection of fresh air directly into the chamber such as the introduction of the third air inlets set, which increases the overall device efficiency and the possibility of incomplete combustion at higher mass flow rate of the reactants thus, reduces the combustor output power generation when hydrocarbon fuels are to be utilised.

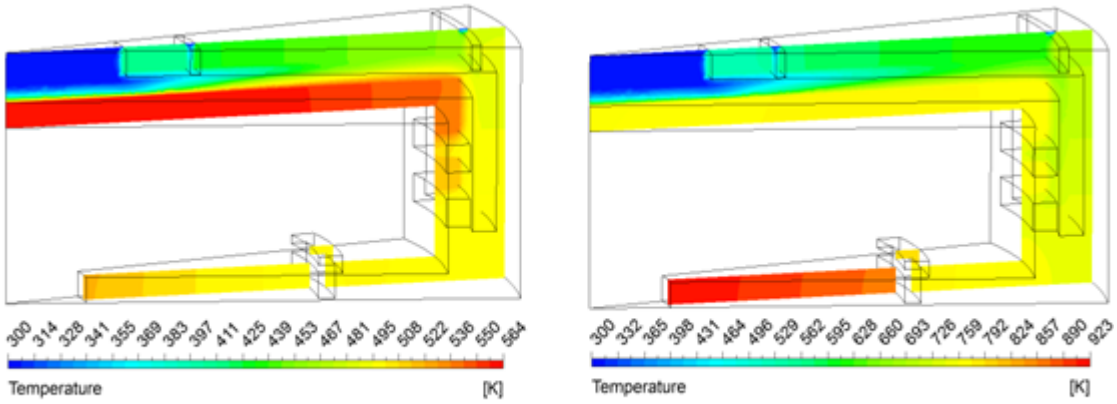

Figure 6-20: Temperature contours design comparison-The effect of the third air inlets set

Design configuration (C) - Figure 6-18 was considered with the aim to create small recirculation zones after the injection of the reactants mixture from the lower wall into the chamber and to demonstrate the possibility of achieving the design target (stable combustion) even though the current in-house manufacturing technique doesn't facilitate the production of such inlets-to-chamber design configuration. Fourteen circular inlets with a diameter of 0.3 mm each were modelled with the cross-sectional areas of those inlets and the chamber height equal to that of the initial design. A total MFR of 0.02 g/s, an ER of 0.8, initial reactants temperatures of 300 K and non-adiabatic external walls conditions were used to describe and model the problem.

The numerical results shown in Figure 6-21 predicted a stable combustion inside the microchamber. The maximum flame and structure temperatures were increased by 287 K and 277 K respectively in comparison to the previous design configuration (case (B)); this resulted from the increase in the initial enthalpy of the reactants mixture flowing inside the micro-cooling channel. Also, the numerical results demonstrated that the flame was blown out of the chamber when the total MFR was increased from 0.02 to 0.03 g/s. This suggested that the current design configuration is constrained by insufficient residence time despite the fact that effective recirculation zones were achieved compared to the previous case (B).

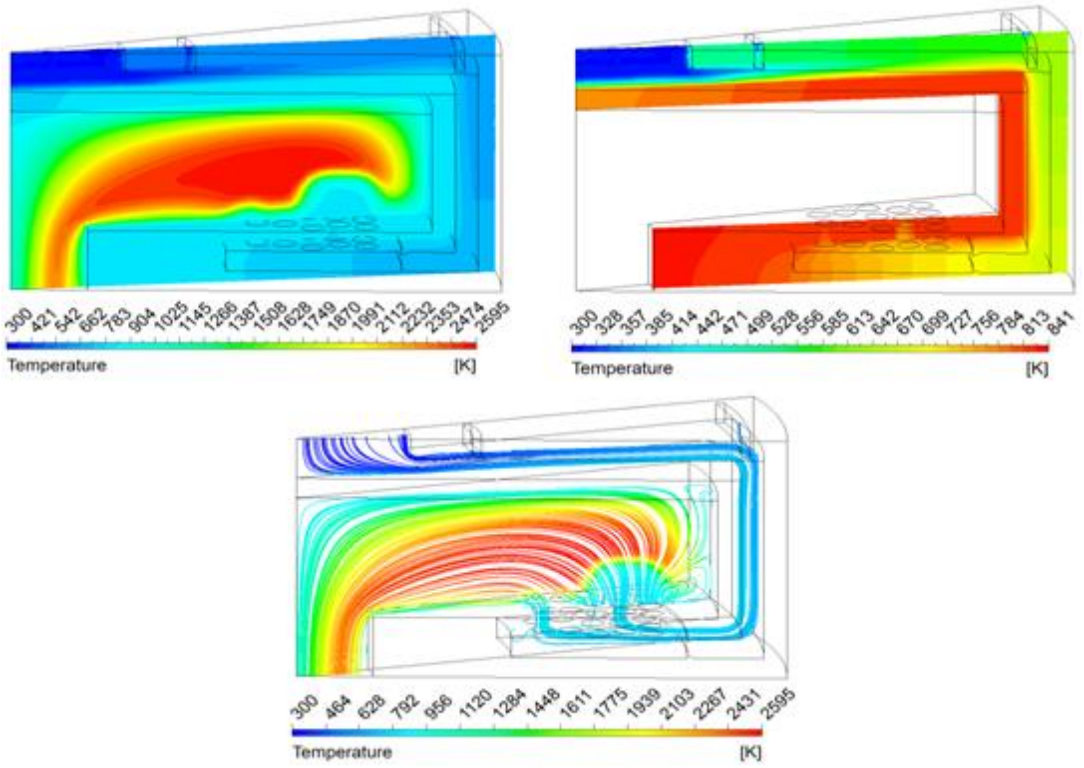

Figure 6-21: Temperature contours (top-left), Structure and micro-cooling channel temperature distributions (top-right) and temperature streamlines (bottom) shown at the same vertical plane - design (C)-Figure 6-18

The final design configuration considered as shown in (D) - Figure 6-18 was based on the results obtained from the previous designs (A, B, & C), which combines firstly, the inlets-to-chamber configuration from design B, where the combustion was stabilised at a relatively wider range of MFR and secondly, the location of those inlets as in design C where the reactants mixture entering the combustion chamber from the lower wall proved to create an effective recirculation zones which help to sustain rapid and stable combustion inside the microchamber.

The results obtained from the numerical simulation applying the same boundary conditions from the above cases and varying the MFR in other studies are presented in Figure 6-22. Those results demonstrated that a stable combustion can be achieved at different MFRs and most importantly, no unburned fuel was traced at the exit of the chamber when the device was configured to operate using 0.03 g/s compared to 4.4 % of the fuel mass fraction calculated at the chamber exit of design (B). However, the flame was blown out of the chamber when the design was tested to operate with an MFR of 0.04 g/s.

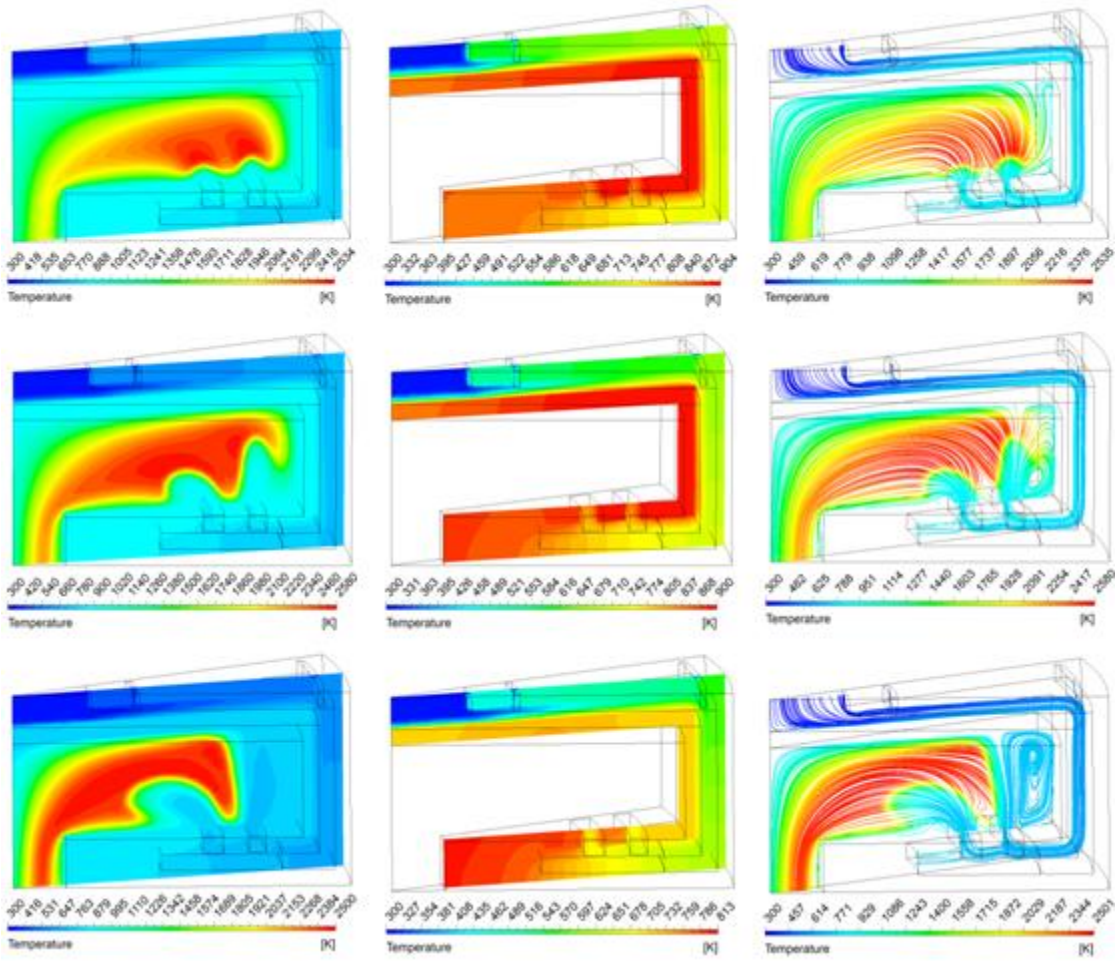

Figure 6-22: Temperature contours (left column), Structure and micro-cooling channel temperature distributions (middle) and temperature streamlines (right), MFR=0.01, 0.02 and 0.03 g/s at the first, second and third row respectively and are shown at the same vertical plane - design (D)-Figure 6-18

Those results also showed that increasing the MFR from 0.02 to 0.03 g/s not only reduces the flame and the structure temperatures but also increases the size of the recirculation zone near to the chamber vertical wall thus, pushes the flame downstream towards the chamber exit. From the latter, the size of this recirculation zone at a high MFR setting, i.e. $\geq$ 0.03 g/s can be minimised by moving the location of the inlets-to-chamber set closer to the vertical wall. By doing so, it is expected to increase the flow path which then increases residence time inside the chamber.

The results of this study are illustrated in Figure 6-23, where a smaller recirculation zone near the vertical wall and a stable combustion were both achieved even at an MFR of 0.045 g/s but at the cost of 1.8 % unburned fuel calculated at the chamber outlet.

Table 6-19 illustrated the flow metrics results of interest of those cases studied in this section where different geometry configurations were used, in particular the inlets-to-chamber ports. All those results were obtained from using propane and air as fuel and oxidiser respectively.

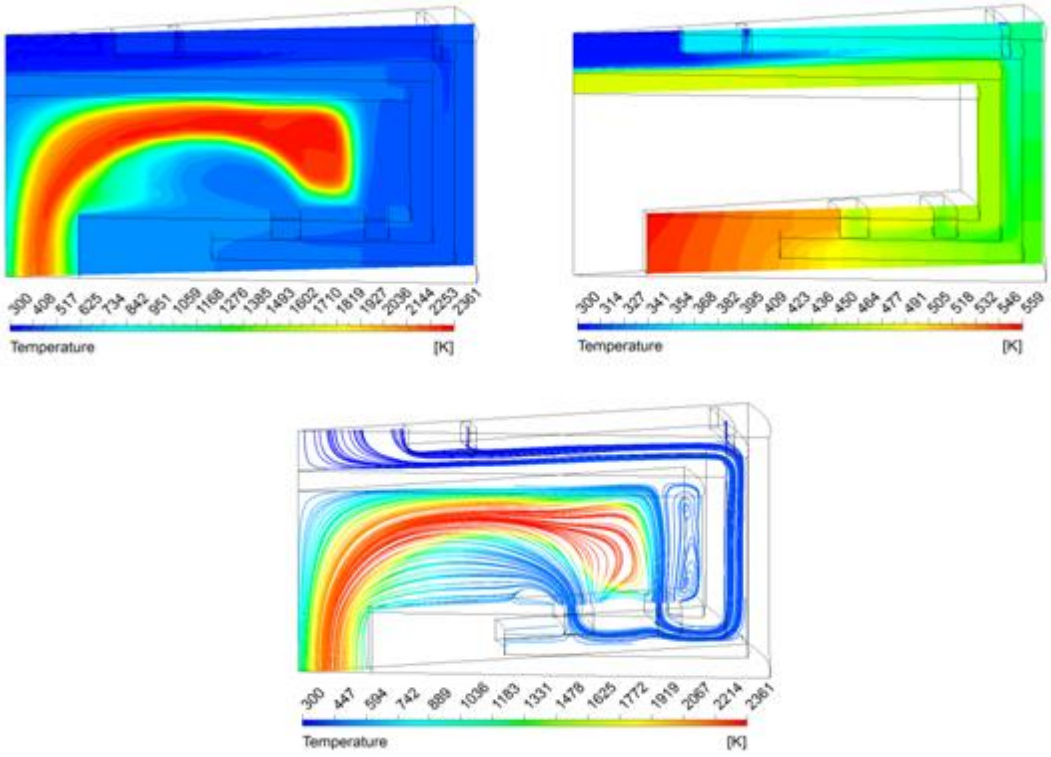

Figure 6-23: Temperature contours (top-left), structure and micro-cooling channel temperature distributions (top-right) and temperature streamlines (bottom). All shown at the same vertical plane – Modified inlets-to-chamber set location at MFR of 0.045 g/s

The main significant findings which can be observed from this table are:

1. The design configuration with two sets of inlets-to-chamber at the vertical wall (design B - Figure 6-18) has an efficiency value 10 % higher than its counterpart of design D, where the inlets are positioned at the bottom wall of the chamber also, the previous has lower exit and structure temperatures compared to the latter at the same applied boundary conditions.
2. Two sets of inlets-to-chamber design at the vertical wall but without cooling the bottom (i.e. no air passing through the third air inlets set) performs similarly to that of design D. From those points, the benefits of cooling the lower wall of the combustion chamber as well as the location of the inlets sets are observed and most importantly these design measures can have a big impact on the combustor performance if the hydrocarbon fuel is replaced by hydrogen which has faster reaction rates. Therefore, not only higher combustor efficiency is expected but also higher output power and stable flame inside the combustion chamber.
3. The results obtained from the modified inlets-to-chamber set design at the lower wall demonstrated the effect of increasing the residence time, which in this case

Table 6-19: Flow metrics of interest using propane-air for different designs and operating configurations at ER=0.8

Design configuration	MFR (g/s)	Efficiency (%)	UHC (%)	T_{max} (K)	T_{ex} (K)	T_s (K)
Initial (baseline)	0.02	-	-	-	-	-
1-set vertical wall	0.02	-	-	-	-	-
Two sets vertical wall (with lower wall cooling)	0.01	77.6	0	2545	1162	678
	0.02	94.7	0.1	2308	1556	565
	0.03	93.1	4.4	2128	758	371
Two sets vertical wall (No cooling)	0.02	83.4	0	2547	1947	924
Multi inlets bottom wall	0.02	86.7	0	2595	1980	842
	0.03	-	-	-	-	-
Two sets bottom wall	0.01	65.3	0	2535	1646	904
	0.02	84.2	0	2580	1935	900
	0.03	93.3	0	2500	2081	814
Two sets modified location bottom wall	0.045	98	1.8	2361	1864	562

allowed the device to be configured at elevated MFRs.

4. The flame was sustained inside the chamber at an elevated MFR of 0.045 g/s for the first time when the distance between the inlets-to-chamber and the combustor exit was increased. This design was represented by the modified two sets of inlets at the lower wall therefore, this suggests the highly constrained design space of the microcombustor by inadequate residence time particularly when hydrocarbon fuel is used.

- **6.3.2.2 Hydrocarbon fuel effects on combustor performance**

In order to compare the effect of using different fuels on the device performance; design (D) - Figure 6-18 was chosen based on the propane-air results shown in Table 6-19. Another suitable design configuration that could be used for this investigation is the modified inlets sets at the lower wall of the microchamber.

Propane, ethane and butane were tested over MFR and ER ranges of 0.01 – 0.04 g/s and 0.6-1.2 respectively. The calculated design efficiencies from the numerical results are illustrated in Table 6-20, where the efficiency values obtained from the individual fuel at the same applied boundary conditions were almost identical. For example, at a MFR of 0.02 g/s and ER of 0.9, the difference is less than 0.1 % between the ethane and the butane, and this value is 0.3 % between those individual fuels and the propane. Those differences might be greater if comprehensive combustion reaction mechanisms of those fuels were used instead of the current single-step reaction modelling. The exothermic, the endothermic and the dissociation reactions have an impact on the flame temperature and therefore on the efficiency of the device when multi reaction mechanisms library is deployed.

Moreover, the ethane-air combustion has a higher reaction rate than those of propane and butane therefore, it is expected the combustion to be sustained inside the microchamber at higher MFR and or ER compared to the other hydrocarbons tested. This was demonstrated by the numerical results shown in Table 6-20 where the ethane-air combustion was stabilised at MFR of 0.04 g/s compared to 0.03 g/s for the other fuels and a wider ER range at MFR of 0.03 g/s.

Table 6-20: Hydrocarbon fuel efficiency and feasible operating space using design (D) - Figure 6-18 at sea-level

Propane	Equivalence rate (ER)					
Total MFR (g/s)	0.6	0.7	0.8	0.9	1	1.2
0.01	60.1%	62.7%	65.3%	67.2%	68.7%	69.8%
0.02		83.4%	84.2%	85.0%	85.4%	85.8%
0.03			93.3%	93.8%	93.9%	
0.04						

Ethane	Equivalence rate (ER)					
Total MFR (g/s)	0.6	0.7	0.8	0.9	1	1.2
0.01	61.0%	63.7%	66.2%	68.0%	69.3%	70.4%
0.02		83.8%	84.5%	85.3%	85.6%	86.1%
0.03		91.4%	91.6%	92.1%	92.1%	92.9%
0.04			95.8%	95.7%	95.7%	

Butane	Equivalence rate (ER)					
Total MFR (g/s)	0.6	0.7	0.8	0.9	1	1.2
0.01		65.4%	66.6%	67.9%	69.2%	69.9%
0.02			84.9%	85.3%	85.7%	85.9%
0.03			94.0%	94.1%	94.1%	
0.04						

Furthermore, the calculated efficiencies of the device using an ethane-air combustion reaction were higher than their vis-à-vis of the propane-air over the tested boundary conditions except when the MFR was equal to 0.03 g/s. The numerical results presented in Figure 6-24 at the latter setting revealed that the recirculation zone near the vertical wall of the chamber held a higher temperature field compared to the propane-air case, which was shown previously in Figure 6-22 (bottom). This elevated temperature is likely to be caused by the secondary combustion zone rather than from the recirculated combustion products of the primary zone. Consequently, more heat was lost to the surrounding environment by increasing the structure temperature therefore, lower device efficiencies were obtained compared to the propane-air at this operating setting and different ERs. The higher chemical reaction rate of the ethane-air and the amount of the energy released during the combustion process compared to the propane-air reaction made it possible for the flame to be sustained in this location of the flow field inside the microchamber.

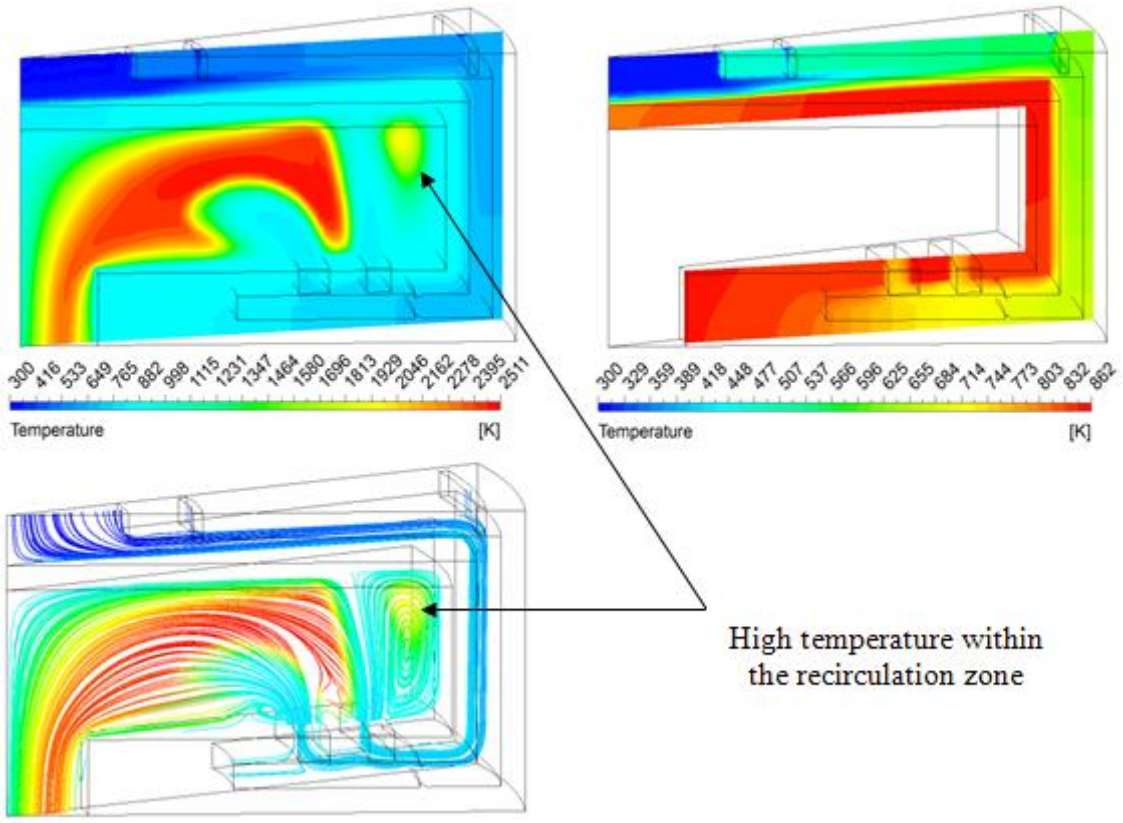

Figure 6-24: Temperature contours (top-left), structure and micro-cooling channel temperature distributions (top-right) and temperature streamlines (bottom). All are shown at the same vertical plane for ethane-air at MFR=0.03 g/s and ER of 0.8

6.3.2.3 Two sets of inlets at the lower wall vs. Initial design - Flow comparison

It was concluded earlier that the combustion of the propane-air reaction could not be sustained inside the microchamber of the initial design over the tested boundary conditions but was possible when the two sets of inlet-to-chamber design was considered; firstly when those sets are located at the vertical wall, the combustion was sustained for a limited operating range of MFR and secondly, at the lower wall of the chamber. Figure 6-25 presented the flow behaviour inside the microchamber of the two inlets sets at the lower wall (left) and the initial design (right). If a flow particle was tracked through the main streamline after leaving the inlet closer to the vertical wall as in the location indicated by the arrow, then the flow path to the chamber exit in this case is longer than that of the initial design thus resulting in a longer residence time. This is due to the main flow stream trajectory entering the combustion chamber as a result of the inlets-to-chamber layout.

Also, another benefit of using the two sets of inlets at the current configuration can be seen from the velocity contours shown in Figure 6-26 (left). The fluid flow velocity in the main stream is less in magnitude after leaving the inlets near the vertical wall compared to the inlets close to the chamber exit, even though the cross-sectional areas are identical. This suggests that the flow of the previous was blocked by the latter therefore; this configuration increases the residence time compared to the inlets of the initial design.

From the above and for hydrocarbon fuels, the cross-sectional areas of the two sets, in particular the width in the radial direction, should be considered as a design parameter in future optimisation investigations as this can improve the device performance under the design constraints and over a wider range of MFR.

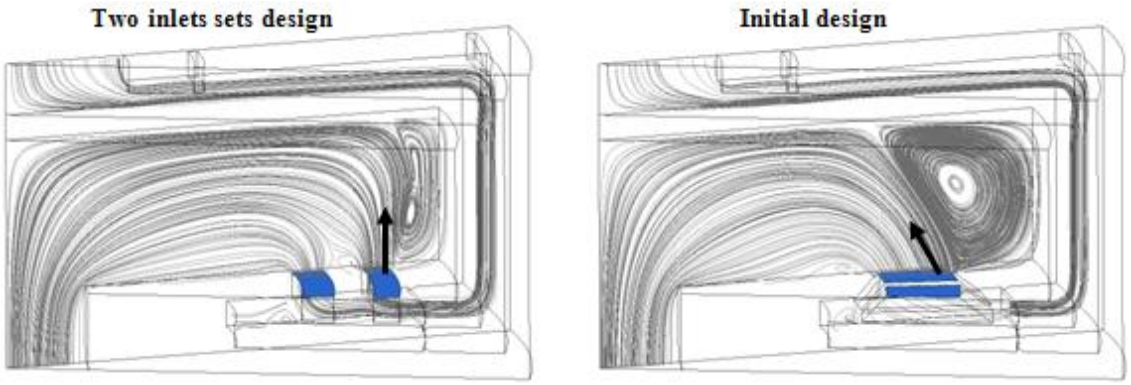

Figure 6-25: Fluid flow field streamlines of the 2-set of inlets at the lower wall (top left), initial design (top right)

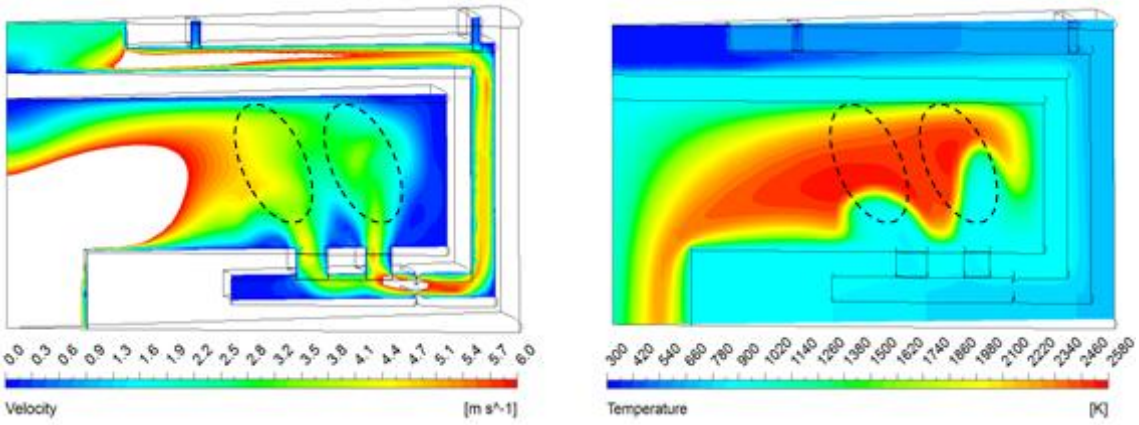

Figure 6-26: Velocity (left) and temperature (right) contours of the two inlets sets at lower wall burning propane-air at MFR=0.02 g/s and ER=0.8

Note: For visual comparison, the velocity contour presented above was trimmed up to 6 m/s

6.3.2.4 The effect of increasing a chamber diameter on flame stabilisation

In order to validate the initial design being constrained by a short residence time the flame was blown out of the chamber over the tested operating range of MFR and ER; the combustion chamber diameter was increased arbitrarily from 11 to 17 mm. This increases the fluid flow path from the inlets to the chamber outlet. In addition it allows for the increase in the inlet-to-chamber cross-sectional areas therefore reducing the reactants mixture velocity entering the chamber thus, further increasing the residence time. The design was tested using propane-air reaction over MFR and ER ranges of 0.02 – 0.05 g/s and 0.55 – 1.0 respectively.

The flow metrics results of interest obtained from the numerical simulations are illustrated in Table 6-21. The numerical results demonstrated that combustion was stabilised inside the chamber with the initial design configuration with larger chamber diameter over a wide range of MFR and ER and it was possible to operate with an MFR of 0.04 g/s which exceeded the maximum operating range of MFR achieved in design D – see Table 6-20.

Furthermore, combustion could not be sustained at an MFR of 0.02 g/s and ER of 0.55, and at an MFR of 0.05 g/s and ER of 1.0. At the first, this might be caused by the energy loss from the combustion to its surroundings being equal to that generated by the fuel and at the second setting; this was possibly due to inadequate recirculation zones and large heat loss caused by lower chamber wall temperatures.

The temperature contours and the velocity which is represented by the streamlines plot for two different operating settings are shown in Figure 6-27.

Table 6-21: Flow metrics values of interest of the initial design configuration with extended chamber diameter and larger inlets areas

MFR (g/s)	ER (-)	Efficiency (%)	Net power (W)	T_{max} (K)	T_{ex} (K)	T_s (K)
0.02	0.55	Combustion couldn't be sustained				
0.02	0.7	65.3	25.9	2471	1628	874
0.03	0.9	79.7	60.2	2605	1932	909
0.04	0.9	85.6	86.2	2600	2022	937
0.05	1.0	Combustion couldn't be sustained				

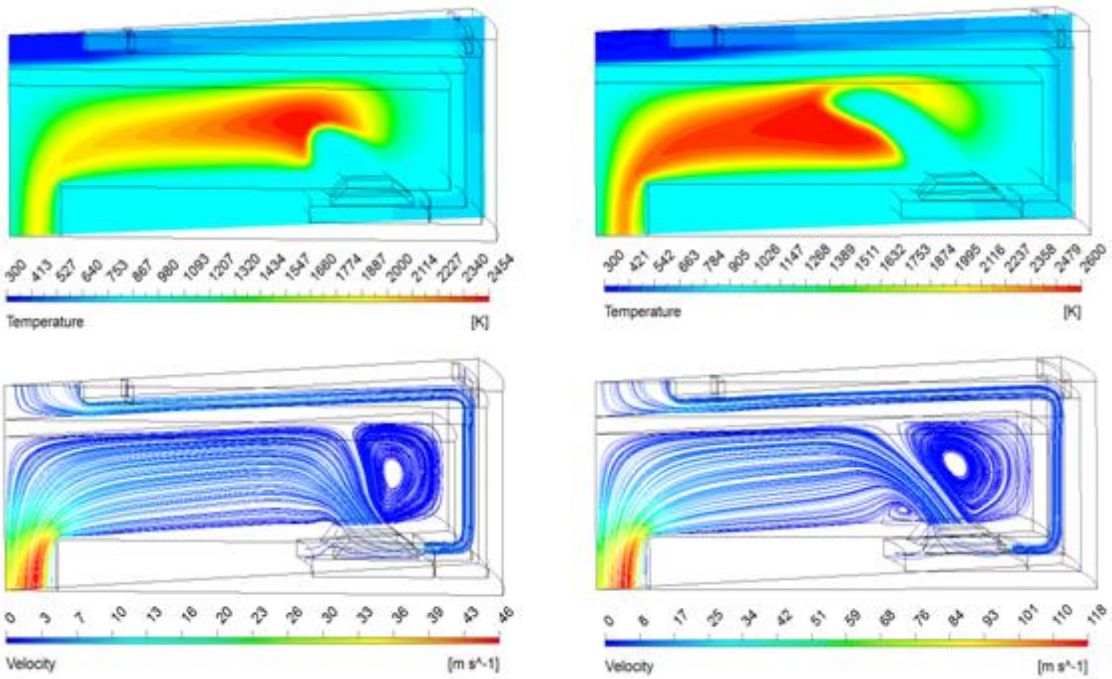

Figure 6-27: Initial design with large chamber diameter. Temperature contours (top), velocity streamlines (bottom) – MFR=0.02 g/s & ER=0.7 (left) and MFR=0.04 g/s & ER=0.9 (right)

6.4 Chapter summary

This chapter presented the results achieved from the implementation of the integrated, automated multi-objective design optimisation system which comprises a well-known commercial CFD package and the Multi-Objective Tabu Search algorithm for the design space exploration. The optimisation system was tested in two case studies, a brief description of the individual and the main conclusions can be summarised as follows.

6.4.1 Case study 1

This case related to a simple microcombustor design configuration, represented by a combustion chamber (fluid domain) and a stainless steel structure (solid domain) where premixed hydrogen-air reactants were injected directly into the chamber through 16 slotted inlet ports. The combustor model was represented by 14 geometrical and two operational design parameters with the aim to improve the device efficiency and fuel consumption. Two hard design constraints were also considered: the maximum exit and structure temperatures of 1800 K and 1000 K respectively.

In addition, the computational fluid dynamics calculations within the optimisation system were achieved using ANSYS CFX - EDM combustion modelling and convergence targets less than 1.0E-6, but the CFD calculations were limited to only 101 iterations in the second part of this study. As predicted this resulted in a non-converged energy equation but importantly, optimum designs and wider design space exploration were achieved.

In the first part, a single-objective function was used, the optimisation results revealed the following:

- The combustor efficiency was increased from 56.1 to 71.1 %, a total reduction in chamber volume of 25 % and chamber exit temperature of 1665 K.

  However, in the second part, the optimisation results achieved from the multi-objective functions case which correspond to the compromised design found from the Pareto set revealed,
- The combustor efficiency was up by 9.9 %, a huge reduction of 53.4 % in fuel consumption and 41.5 % in overall device volume at chamber exit temperature of 1032 K.

After further investigation into the results obtained from the non-converged CFD solution, it was found that the trend of the Pareto front of the converged and non-converged CFD solutions is the same, which suggests that this micro-combustor design can be optimised by MOTS using non-converged CFD solutions and the ANSYS CFX-EDM combustion model with confidence at the initial design and development stages. Furthermore, the poor combustor performance in terms of the efficiency is due to a large portion of the combustion energy was lost of the chamber to the surrounding environment at low mass flow rate. In contrast, when the MFR was increased ten-fold, the overall combustor efficiency, chamber exit and structure temperatures were also increased, but the latter was calculated to have exceeded the design limit of 1000 K.

6.4.2 Case study 2

In order to improve the combustor performance by reducing the heat loss of the chamber walls to the surrounding environment, a micro-cooling channel was configured. In addition, for accurate prediction of the flame positioning and the overall numerical results, ANSYS CFX Finite Rate Chemistry (FRC) laminar reaction modelling was deployed within the optimisation system, utilising a single-step hydrogen-air reaction which was described by the Arrhenius type expression.

The topology of the combustion chamber that produced improved behaviour of the device in terms of the design objectives was identified from the above case study so it was only required to represent the problem with five geometrical and three operational design parameters, this measure led to a total reduction in the optimisation time.

The main conclusions from the first part are:

- The benefit of the introduction of the micro-cooling channel into the combustor design was found to increase the efficiency by 2.6 %.
- The optimisation results represented by the compromised design found from the Pareto-optimal set recorded an increase in efficiency of 1.5 % and a reduction of 10 % in fuel consumption, those results were also in respect to five hard design constraints applied throughout the optimisation process.

In the second part of this case, the compromised design above was optimised in order to find the operating limits and effects of the MFR and ER fluctuations on the combustion behaviour and overall device performance using only two out of the three operational parameters and no change was made to its geometry configuration. Therefore,

- It was found that the ER fluctuation within a range of 0.4525 – 0.5 has little effect on the device performance unlike the MFR which recorded an increase in the combustor efficiency of 2.7 % and net power by 67.5 % at the cost of increasing the fuel intake by 66.7 % when the combustor was configured to operate at 0.12 instead of 0.04 g/s.
- In contrast, the efficiency was decreased by 2 % and net power generation by ~27 % but there was an improvement of 25 % in the fuel consumption when it was operated at 0.03 g/s.
- Most importantly, the flame was stabilised inside the chamber over the design ranges of the MFR and ER 0.03 – 0.12 g/s and 0.4525 – 0.5 respectively.

6.4.3 Case study 3

This case study was specifically intended to replace the hydrogen with a hydrocarbon fuel and study the effects numerically using single-step reaction modelling on the combustion and combustor performance initially using the compromised design found from case study 2. Moreover, to identify the key issues and the solutions involving the migration from using hydrogen as a fuel, which has wide flammability limit and also fast reaction rates compared to hydrocarbons such as propane, ethane and butane to achieve a sustained combustion inside the microchamber.

The primary findings were as follows:

- It was found that the propane-air combustion could not be sustained inside the datum design (the compromised design obtained from case study 2) but,
- It was possible when the design of the two inlet-to-chamber sets were located firstly at the vertical with a limited operating range of MFR and secondly, at the lower walls of the chamber.
- The ethane-air reaction demonstrated that its combustion can be stabilised over a wider range of MFR compared to the propane and butane fuels due to its fast reaction rates and the amount of energy released during the combustion process.
- The propane-air combustion reaction was sustained inside the datum design when the chamber diameter was increased arbitrarily from 11 to 17 mm; this suggested that the initial design was highly constrained by inadequate residence time inside the microchamber due to slow reaction rates of the hydrocarbon fuels.

Finally, the two sets of inlets at the vertical wall (design B - Figure 6-18) could be a promising design for future device development, considering the use of the hydrogen-air combustion reaction instead of the hydrocarbon fuels and keeping the third air injection set at the lower wall of the chamber. This suggestion is based on the device performance found numerically and is illustrated in Table 6-19. Using propane-air, an increase in efficiency was made of over 10 % compared to its counterpart of design D at the same applied boundary conditions but the design suffered insufficient residence time when operated at high MFR thus, the latter can be avoided if the hydrogen-air is used due to its superior fast reaction rates to hydrocarbons.

Chapter 7

Development of a microthruster concept for propulsion applications

This chapter presents the design of a microthruster to be utilised on-board a spacecraft as a propulsion system for attitude control and station-keeping applications.

The bi-propellant microthruster type using gaseous hydrogen as fuel and air as an oxidiser will be examined here in depth, based on previously developed micro-combustor design through the multi-objective optimisation work achieved in subsection 6.2.2 (Case study 2-A).

This chapter opens with a general introduction into the need for a propulsion based MEMS technology and the motivation behind the use of this technology, types of systems and the currently available concepts, the advantages and disadvantages, also the performance and the capability of the individual concept.

This chapter also describes the proposed microthruster concept and the numerical modelling approach and the design of a Convergent-Divergent nozzle or the "de Laval nozzle" in which the implementation of "Bell-like" contour of the divergent section design are detailed. CFD modelling is set up and numerical grid representation is also presented. The results from three different case studies considering the microthruster operating at sea-level and at high altitude (vacuum) are illustrated and discussed. Two microcombustor design improvements for low thrust and high specific impulse applications are investigated and detailed. Finally, this chapter ends with summary and important findings.

7.1 Introduction

The advances made in the field of microfabrication technology and micro-electro-mechanical systems (MEMS) at the National Aeronautics and Space Administration (NASA) have led to the possibility of building a new generation of micro-spacecraft which weigh less than 20 kg. The motivation behind this investigation and development is to reduce launch cost by reducing the launch mass and mission risk. The total

scientific payload carried by a single spacecraft can be distributed among a group of micro-spacecrafts. This scenario can increase mission flexibility and also, the loss of one micro-spacecraft is less costly and will not jeopardise the entire mission (Mueller et al., 1997).

An example of a cluster of microsatellites and mission flexibility is the Space Technology 5 (ST5) mission by NASA. The aim was to explore the Earth's magnetic fields by deploying formation flying. Three microsatellites weighing approximately 25 kg each when fully loaded were launched into space in 2006 for 90 days. The mission demonstrated the benefits of using a constellation of micro-spacecraft to perform scientific studies and also to test and validate new technologies (miniaturised spacecraft) for future science missions (NASA Science, 2012).

Recent NASA requirement for such small spacecraft is demonstrated by the announcement in 2010 for a nano-satellite launch challenge competition. The mission objective was to deliver a payload with a mass of at least 1 kg and dimensions of at least 10 x 10 x 11 cm into Earth's orbit (NASA, 2010).

In order to build a micro-spacecraft, all the subsystems on-board a spacecraft must be miniaturised including the propulsion subsystem which has a substantial effect on the mass and the volume of the spacecraft. This subsystem has an estimated mass percentage of 20 to 90 of the total spacecraft mass (deGroot, 1998).

At present, low thrust devices capable of producing a thrust of approximately 0.1 N are deployed on a large satellite for attitude control (ACS) and course corrections when slew is not vital (Bayt et al., 1997). It is anticipated that the propulsion system of a micro-satellite is characterised by its small size and its light weight, and to be able to deliver low thrust force ranging from a micro to a milli-Newton with high specific impulse and a very small total impulse of 10^{-5} Ns or less in order to provide a high degree of manoeuvrability, attitude control and station keeping (Kundu et al., 2012; Mueller, 1997).

Several types of micro-propulsion systems are under investigation using micro-fabrication and MEMS technologies which benefit from lower process cost of the batch products over time with their small size and weight, a compact module can be designed which allows for the distribution mounting of thrusters on the micro-spacecraft.

The micro-propulsion system can be divided into two categories depending on the system configuration; thermal and electrical based systems. Mueller (1997) stated that among those investigated by aerospace companies and academia under the electrical category are: Vaporising liquid Micro-thruster (VLM), Micro Ion Thruster (μIT), Hall Effect Thruster (HET), Field Emission Electric Propulsion (FEEP), and Pulsed Plasma Thruster (PPT). Under the thermal category are: cold gas thruster, solid thruster, subliming solid thruster and bi-propellant thruster.

7.2 Electrical–based propulsion system

An electrical-based micro-propulsion system is typically consists of four main components:

1. Power source, usually solar.
2. Power Processing Unit (PPU) or Power Conditioning Units
    a) Voltage conversion and delivering to the subsystems on-board the spacecraft
    b) Regulating the current and the required voltage
3. Propellant storage system
4. Thruster, Propellant acceleration

Figure 7-1 shows the electric-based propulsion system main components currently in use on-board the Dawn spacecraft.

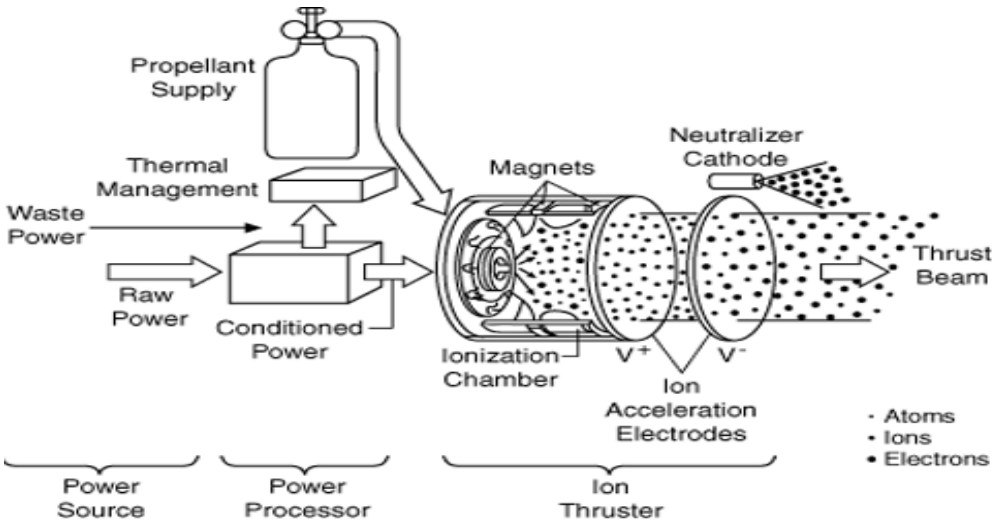

Figure 7-1: Ion propulsion system concept currently on-board the Dawn spacecraft (NASA JPL, 2012)

7.2.1 Types of electrical-based propulsion system

7.2.1.1 Vaporising liquid micro-thruster

The main components of the Vaporising liquid micro-thruster (VLM) or resistojet thruster system are: the propellant storage tank, the vaporising chamber, electric heater and the expansion nozzle. In order to generate thrust using VLM propulsion system, the liquid propellant is vaporised inside the chamber using thin-film deposited heaters. Hence, the propellant vapor is isentropically expanded in the divergent section of the nozzle thereafter the nozzle throat area, which generates thrust. The common liquid propellant used in VLM is water, ammonia or hydrazine.

The VLM system is characterised by its simplicity, no moving parts are required such as micro-turbo pumps and it has a lower rate of propellant leakage than that of the cold gas thrusters due to a high liquid viscosity in comparison to gaseous propellant. In contrast, the propellant vaporisation process required power consumption by the electric heaters. Furthermore, the heat loss from the vaporising chamber to the environment exacerbates the thrust/power ratio. The laminar nature of the flow inside the vaporising chamber reduces the convected heat to the propellant therefore longer residence time, a larger surface area of contact or additional power is required. Extended surfaces "Fins" can be used to increase the heat transfer rate from the solid to the fluid at the expense of increasing the propellant pressure-fed from the storage tank to the thruster assembly.

The design and fabrication of a vaporizing liquid micro-thruster concept was presented by Mueller et al. (1997) and proof-of-concept testing was carried out by Mueller et al. (1998). It was found that the chip temperature of 150 ^{o}C was reached at heater power of 5.5 W and a voltage less than 5 V. Moreover, the thruster then insulated from the packaging in order to reduce the heat conduction losses. The test revealed the chip temperature of 150 ^{o}C was achieved at half the required power of 2.5 W. 7 Watts of input power was used to vaporise water inside the vaporising chamber.

VLM design, fabrication and testing were reported by Maurya et al. (2005) using water as the propellant. The experimental test revealed a thrust force ranging from 5 – 120 μN using heater power of 1 W to 2.4 W can be achieved at a volume flow rate of 1.6 μl/s.

The experimental test by Kundu et al. (2012) achieved a thrust force ranging 0.15 – 1.01 mN and a specific impulse of 50 – 105 s utilising water as propellant at a mass flow rate of 0.2 – 2.0 mg/s with a heater power of 1.6 – 3.6 W.

7.2.1.2 Micro ion thrusters

Micro ion thruster (μIT) is an electrostatic micro-propulsion system. This concept is based on applying an electric discharge to xenon which is usually used as a propellant to generate plasma. About 1 kV potential difference is used to accelerate the plasma through the discharge chamber towards the exit. The speed of plasma exiting the chamber is about 25 mile/sec hence, thrust is generated. Beattie et al. (1993) described and tested a 13 cm in diameter thruster using xenon as a propellant. The test results revealed a 17.8 mN of thrust force and a specific impulse of 2585 s at a power input of 439W.

7.2.1.3 Hall effect thruster

Hall effect thruster (HET) is another electrostatic-base system which is similar to the micro ion thruster where xenon is the propellant, except for the plasma creation and plasma beam acceleration. A scaled-down version of the conventional annular Hall thruster "Cylindrical Hall Thruster (CHT)" was tested by Polzin et al. (2010). The measured thrust ranged from 1.3 – 7.3 mN corresponding to a specific impulse ranging from 400 – 1940 s at an input discharge power spanning from 50 – 350 W.

7.2.1.4 Field emission electric propulsion

Field emission electric propulsion (FEEP) is an electrostatic propulsion system similar to the ion and Hall thruster concepts, based on the acceleration of plasma by a strong electric field after the ionisation process of a liquid metal propellant in order to generate thrust. A propellant such as Caesium (Cs) or Indium (In) is used which is characterised by low ionisation potential and high atomic weight. For example, the design and the development of FEEP thruster reported by Marcuccio et al. (1998) is capable of delivering very low thrust ranging from 1 μN – 2 mN with very high accuracy and very low propellant consumption corresponding to high specific impulse ranging from 4000 – 10000 s.

7.2.1.5 Pulsed plasma thruster

The electric discharge from an energy storage unit or capacitor causes a spark to be generated by the thruster igniter located near a solid propellant commonly Teflon, this ablates and ionises the propellant surface hence, generating plasma. Thrust is achieved by the acceleration of the propellant plasma out of the thruster caused by a magnetic

field and an electric current interaction. The Earth Observing 1 (EO-1) spacecraft propelled by pulsed plasma thruster (PPT), developed at NASA (NASA Glenn Research Center, 2004) and manufactured by Primex Aerospace Company, was launched in year 2000. The PPT on-board this spacecraft consumes 70 Watts of power and is capable of delivering an exit velocity of 13.7 km/s at a thrust force of 0.86 mN. State-of-the-art thrusters are able to produce thrusts of 220 – 1100 μN at specific impulses in the range of 800 – 1500 s.

7.2.2 Electrical-based propulsion system disadvantages

All electrical-based propulsion systems discussed above have a superior delivery of high specific impulse and low thrust force at the required specific impulse bits compared to that of chemical-based thrusters for accurate attitude control, micro-spacecraft positioning and for drug compensation applications. This is achieved by simply regulating the voltage potential through the PPU on-board the spacecraft which controls the plasma acceleration out of the thruster. In contrast, and for example, the VLM suffers heat loss from the vaporising chamber to the environment. The plume neutralization, micro-spacecraft contamination caused by the metallic nature of the plume and a heavy high-voltage PPUs are the issues faced in the development of the FEEP propulsion system. The miniaturisation of ion thruster poses many design challenges such as generating plasma in a small discharge chamber, mass and high voltage reduction of the power processing unit and the design of the cathodes and the neutralisers. Moreover, this type of propulsion system and the pulsed plasma thruster can only be used in a vacuum. PPT also generates low thrust which can’t be used to perform the required slew rate for micro-spacecraft.

7.3 Chemical-based propulsion system

Chemical-based micro-propulsion system typically consists of four main components:

1. Propellant storage system, low or high pressurised tank/s
2. Ignition device
3. Combustion chamber, where the chemical energy of the fuel is converted to thermal energy except for the cold gas thruster

4. Convergent-divergent nozzle, where the fluid is accelerated throughout the nozzle sections from subsonic to supersonic velocities, producing thrust at the outlet of the nozzle.

Some chemical propulsion systems require micro-valves and micro-turbo pumps in addition to the above components.

7.3.1 Types of chemical-based propulsion system

7.3.1.1 Cold gas thrusters

A cold gas propulsion system is characterised by a lower degree of architectural complexity and lower manufacturing costs. On the other hand, the system is only capable of delivering low thrust and low specific impulse which makes it suitable for attitude control and station keeping. This system also suffers from a high rate of propellant leakage and is restricted to a large and heavy storage tank due to high pressure requirement. From the above, this system allows for short duration missions (Mueller et al., 1997; Rossi et al., 2001; deGroot et al., 1998; Larangot et al., 2002). The MOOG Inc. design (Morash and Stand, 1994) is an example of such a system, which has a length and chamber dimension of 4.3 cm and 1.4 cm respectively. The system was delivering a thrust force of 4.5 mN and a specific impulse of 65 s. Köhler et al. (2002) have developed a hybrid cold gas microthruster system using nitrogen as a propellant. The system consisted of micro-electro-mechanical system and conventional fine machining parts integrated together. Moreover, the system utilised four independent thrusters, four piezoelectric proportional valves and two particle filters. The total generated thrust ranged from 0.1-10 mN and a maximum specific impulse of 45 s. In 2000, a 6.5 kg micro-spacecraft (SNAP-1) was launched by Surrey Space Centre – England. The SNAP-1 uses butane as the cold gas propellant and it is capable of delivering 2.4 m/s in order to perform its inspection of the mothercraft for maintenance purposes or in case of failure after separating from the latter craft. The low velocity increments (delta-v) giving low thrust and specific impulse allows this micro-spacecraft to perform fine inspection manoeuvres (Mueller et al., 2001).

7.3.1.2 Solid propellant thrusters

The solid propellant thruster concept is based on a single solid propellant stored in a combustion chamber which generates gases when ignited. The gases of combustion are

accelerated by the use of convergent-divergent nozzle hence, thrust force is generated. This type of propulsion is used for orbit insertion of spacecraft as it generates a high specific impulse which is higher than the mono-propellant but lower than the bi-propellant propulsion system. Other advantages are its relative small size, its high reliability and there are no moving parts but the system lacks restart capability which is the main disadvantage as it is a single-shot. Larangot et al. (2002) have compensated for the lack of restart capability by the fabrication of a micro-thrusters array which contains 100 individual thrusters on 24 x 24 mm silicon chip. The result obtained from the experiment for the total impulse was 6 mN.s.

7.3.1.3 Subliming solid propellant thrusters

The subliming solid propulsion system was described by Mueller et al. (1997) and Mueller (1997) being based on the high sublimation pressure of the solid propellant such as ammonium hydrosulfide (NH_4HS) or ammonium carbamate ($NH_4CO_2NH_2$), the gas pressure increases inside the storage tank due to heat exposure. The thrust is generated following the flow of the vapor through a valve and a convergent-divergent nozzle. The main advantages of this system are its simplicity, its compact size and its light weight propellant storage tank due to its low pressure requirement. In contrast, its low specific impulse and ground special handling requirements are the main system disadvantages.

7.3.1.4 Mono-propellant thrusters

A Mono-propellant propulsion system is characterised by its reliability and restart capability, Greater propellant densities and its ability to generate a thrust force ranging from 0.9 – 18 N with an average specific impulse of 220 s make it suitable for attitude control and primary micro-propulsion applications. Primary delta-v is defined by deGroot (1998) as large changes in orbit parameters such as orbit transfer, orbit repositioning, deorbit and planetary escape). Moreover, the system has a lower degree of complexity in terms of parts counts and the feed system than that of a bi-propellant engine. The design concept of this system is that the mono-propellant is decomposed after passing through a catalyst bed, generating products and heat. Three different propellants are found in literature, the hydrazine (N_2H_4), the hydrogen peroxide (H_2O_2) and HAN/TEAN which is a mixture of HAN (Hydroxylammonium Nitrate -

NH_3OH+NO_3), TEAN (Triethanolammonium Nitrate - $(HOCH_2)_3HNOH+NO_3$) and water. Toxicity and flammability are the main disadvantages of the hydrazine mono-propellant which increase handling cost. It was noticed in the past that the hydrogen peroxide is slowly decomposed (auto-decomposition) inside the storage tank or feed lines even without the presence of a catalyst, which resulted in pressure rise and a loss of propellant. The latter is due to the product's generation. In year 2000, NASA's objective was to design a MEMS-based propulsion system using high test hydrogen peroxide mono-propellant with a performance target of: 10 – 500 μN of thrust, a specific impulse of 145 s, an impulse bit ranging from 1 – 1000 μNs and an adiabatic flame temperature less than 1700 K (Rhee et al., 2000).

The implementation of HAN/TEAN mixture as mono-propellant propulsion system in micro-spacecraft requires significant development due to reaction chamber thermal design issues. A reaction temperature of 2500 K and specific impulse of 270 s for a HAN-based propellant was observed experimentally (Mueller, 1997; Larangot et al., 2002).

7.3.1.5 Bi-propellant propulsion system

Bi-propellant propulsion system is characterised by high thrust, high specific impulse, high thrust to weight ratio and restart capability with relatively low power requirement which makes it suitable and is commonly known for primary propulsion applications. The micro-scale of this system can be deployed on a large spacecraft currently in use for positioning and attitude control purposes. The amount of thrust force generated by the system can be controlled by regulating the mixture property and/or chamber pressure. Moreover, the reactants are stored in separate tanks on-board the spacecraft therefore, this propulsion system is considered to be safe. In contrast, they are relatively complex, because of the chamber thermal issue due to the large surface area to volume ratio, short residence time which leads to incomplete combustion and structural material issue resulting from high flame temperature.

A high pressure bi-propellant system was micro-fabricated by London et al. (2001a, 2001b) from six individual silicon wafers etched together using Deep Reactive Ion Etching (DRIE) and aligned fusion wafer bonding. The propulsion system of 18 x 13.5 x 2.9 mm in size with a combustion chamber size of ~100 mm^3 was designed to operate at a chamber pressure of 125 atm using liquid oxygen/ethanol as propellants which

would generate 15 N of thrust at a specific impulse of 300 s. The test results from a proof-of-concept design utilising gaseous oxygen and methane at chamber pressure of 12.5 atm was produced a thrust force of 1 N yields to a thrust power of 750 W.

Another bi-propellant propulsion system was designed and fabricated using low temperature co-fired ceramic (LTCC) with a combustor chamber size of 9.9 mm^3 by Wu and Lin (2010). A non-premixed gas of ethylene and oxygen were used. The measured thrust was ranging from 0.2 – 1.97 mN where the maximum thrust value was obtained at the propellants chemical energy release of 37 Watts.

deGroot (1998) suggested a hybrid propulsion system, the concept in which bi-propellant and cold gas thrusters are used on-board the spacecraft. The products of electrolysis water are hydrogen and oxygen which can be stored or consumed at once. The combination of both products as a bi-propellant could be used for high thrust and high specific impulse primary propulsion and a single cold gas propellant could be used for attitude control and course correction benefiting from low thrust and lower impulse bit generated by the cold gas thruster configuration.

7.4 A summary of micro-propulsion systems operating ranges

The potential operating ranges of the chemical and the electrical micro-propulsion systems discussed above can be summarised in Figure 7-2. The propulsion system choice depends on mission objectives and mission requirements. The selection of bi-propellant propulsion system is apparent when high thrust, high thrust to weight ratio and high velocity increment (large delta-v for manoeuvres) are required for primary propulsion applications but as mentioned previously, the micro version of this system can be deployed for attitude control in large satellites when the slew rate is not vital. The subliming solid thruster system highlighted in Figure 7-2 and the cold gas thruster system presented by Rossi (2002) are characterised by their capability of producing lower thrust level and lower delta-v (<0.2 m/s for a 50 kg and <1 m/s for a 10 kg spacecraft) which potentially could be used in applications such as secondary propulsion (secondary delta-v) for station keeping and drag compensation or attitude control. This figure also presents the electrical-based micro-propulsion systems as candidates for long to very long primary delta-v duration where small thrust levels and high specific impulse are desired. It is obvious that more research and development in both types of micro-propulsion systems are still needed in order to design a system

capable of delivering high level of thrust as in the bi-propellant system combined with high specific impulse as represented by the micro ion thruster system. This will allow deep space exploration missions which are not possible within the current propulsion system technologies.

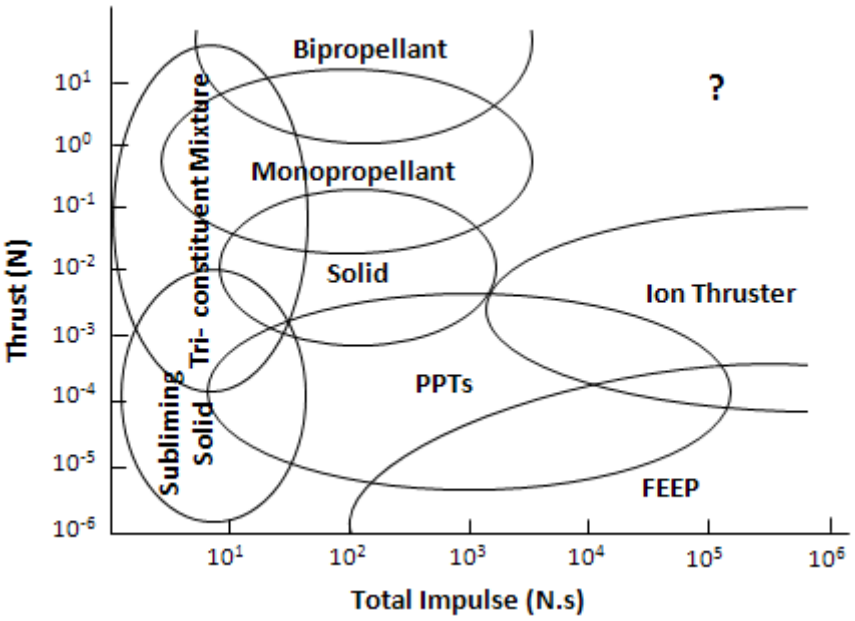

Figure 7-2: Micro-propulsion systems operating ranges (deGroot, 1998)

7.5 Previous microthruster numerical investigations

A convergent-divergent nozzle is one of the main components in the design of a chemical-based propulsion system. Micronozzle design and performance has been investigated in a number of published literature, especially when the research and development focus is diverted toward the possibility of building a new generation of micro propulsion systems for micro-spacecraft, capable of delivering low thrust and high specific impulse bit for attitude control and station keeping.

Micronozzle design and performance evaluation have gained the most attention with the measurements obtained experimentally by Rothe (1971) using an electron-beam technique to study the flow in a supersonic conical nozzle utilising nitrogen with a throat diameter of 5.1 mm, a 30^{o} and a 20^{o} half convergent and half divergent angles respectively at a low throat Reynolds number of 590 exhausting to vacuum.

Kim (1994) has used an axisymmetric Navier-Stokes calculation to study and compare the results of different conical and contoured nozzle shapes and lengths in terms of the

effect of viscous and divergent losses on nozzles' performances. The author also validated the code using Rothe's nozzle (Rothe, 1971) with a chamber pressure and temperature of 474 Pa and 300 K respectively, a throat Reynolds number of 270 and an area ratio of 66. He concluded that the results agreed with the experimental data.

Grisnik et al. (1987) have studied experimentally four different nozzles (conical, bell, trumpet and modified trumpet) with throat diameters of 0.653, 0.711, 0.671 and 0.640 mm respectively over a Reynolds number range of 500 – 9000 using two different propellants (hydrogen and nitrogen). From the experimental results of Reynolds numbers less than 1000, the authors concluded that all divergent nozzles' sections were filled with a large boundary layer which was demonstrated by the loss in specific impulse efficiencies when the Reynolds number was decreased.

Lin and Gadepalli (2009) studied numerically the flow in a conical micronozzle over the range of Reynolds numbers 5 to 2000 under slip and no-slip divergent boundary conditions using a two-dimensional grid and a continuum model. The numerical results were compared with the experimental data from literature and they concluded that the thrust values agreed with the data from the experimental except at very low Reynolds number.

Bayt et al. (1997) have carried out two-dimensional numerical calculations on a micronozzle similar to those investigated by Kim (1994) and Grisnik et al. (1987). The tested Reynolds numbers span over the range of 200 – 10000. It was observed from a conical micronozzle calculation with a Reynolds number of 1000 and a 4.2:1 area ratio that the subsonic boundary layer occupied 2 % of the exit area of the nozzle. Furthermore, they concluded that the velocity slip near the nozzle exit has insignificant effect on the outcome of nozzle performance.

Bayt and Breuer (2001) performed numerical calculations on a conical 2-D extruded micronozzle with an area ratio of 16.9:1 and a nozzle throat of 37.5 μm, the chamber pressure and temperature of 50 psia and 299 K respectively, which correspond to 1940 Reynolds number. The calculated exit Mach number based on the simulation result is slightly lower than the quasi 1-D theory by 8.8 %.

Ivanov et al. (1999) have compared the micronozzle results of the flow field and performance characteristics over throat Reynolds number range 130 – 1300. Those results were obtained from the finite volume approximation of the Navier-Stokes (N-S)

equations (the continuum method) and the Direct Simulation Monte Carlo (DSMC), a kinetic approach based on molecular gas dynamics. Two types of conical micronozzle designs were investigated. Extrapolation at the exit plane of the nozzle for the subsonic boundary layer was used. However, the divergent section was modelled applying no-slip and adiabatic conditions as suggested by the experimental results and no-slip with constant wall temperature of 297 K in order to evaluate the effect of the wall boundary conditions on the flow structure. The authors concluded that the vacuum specific impulse was over-predicted within the tested throat Reynolds number range when the outflow extrapolation at the nozzle exit was used for the Navier-Stokes equations. In the DSMC model an extended numerical domain downstream of the nozzle exit was implemented in order to accurately simulate the exit boundary.

Alexeenko et al. (2002) have compared the numerical results obtained from the N-S with DSMC for two micronozzle design configurations, an axisymmetric and three-dimensional (2-D extruded) at a low throat Reynolds number of 200. Both designs have a throat diameter of 300 μm and a divergent expansion angle of 15 degrees. A no-slip wall with a constant temperature equal to the chamber stagnation temperature was considered, as well as an extended numerical domain downstream from the nozzle exit. The authors concluded that the Navier-Stokes solution agrees well with the DSMC numerical results inside the micronozzle and downstream from the nozzle exit at the core flow. Moreover, the two solutions only disagree near the region of the nozzle exit lip, which highlighted the incapability of the N-S to capture the gas rapid expansion and flow rarefied in that region.

Rossi et al. (2001) have demonstrated the use of the continuum approach to investigate the effect of different divergent section configurations by varying the expansion angle and the length on their solid propellant thruster design performance at high Reynolds number. They also extended the computational grid away from the nozzle exit.

Wu and Lin (2010) have carried out a steady state 3-D cold flow CFD modelling during the initial phase of a bi-propellant microthruster development in order to predict and eventually improve the flow fields and propellants mixing characteristics of design concepts. The Navier-Stokes equations with no-slip and turbulent modelling at a Reynolds number between 1000 and 4000 were used.

7.6 Bi-propellant microthruster model description

A three-dimensional schematic cross-sectional view of a micro-scale thruster is shown in Figure 7-3. The model integrates two parts; mainly the micro combustion chamber and the convergent-divergent nozzle. The microchamber design configuration is obtained from previous multi-objective design optimisation investigations discussed in subsection 6.2.2. This part consists of a combustion chamber where the chemical energy of the fuel is converted to a thermal energy under specific fuel-oxidiser mixture, pressure and temperature conditions, to form products and release heat. Two sets of air inlets are used in order to firstly, reduce the energy loss to the environment by means of natural convection and radiation from the outside walls of the chamber by lowering the gases mixture temperature downstream inside the micro-cooling channel hence, lowering the outside walls temperature and secondly, to achieve a higher degree of fuel-oxidiser mixing before entering the combustor chamber in order to improve the chemical combustion efficiency at different operating conditions.

The microchamber part also features the implementation of a micro-cooling channel. It was shown previously in subsection 6.2.1 that the implementation of this channel into the design increases the overall efficiency of a micro-scale combustor by 2.6 % at specific operating conditions.

The adaptation of a micro-cooling channel into the microcombustor design has the following benefits: Firstly, it is acting as a heat transfer barrier or a “thermal insulator” due to a lower thermal conductivity of the flowing mixture of gaseous propellants inside the channel compared to that of the solid part of the device hence, reducing energy loss to the environment by reducing the conductive surface area of the solid domain. Secondly, it partially recovers the heat loss of the chamber and preheats the incoming fresh propellants before entering the microchamber which reduces the required reaction time.

The second part of the microthruster model is the convergent-divergent nozzle. It is the only nozzle that is capable of accelerating the flow throughout its sections (described below) beyond a sonic flow, thus achieving the desired supersonic flow velocity at the exit part of the divergent section. The exit velocity is one of the design parameters that calculate the amount of thrust delivered by the nozzle. A convergent-divergent nozzle was a main part of a micro rocket engine which was experimentally tested by London (2000).

The nozzle consists of three different sections. Those sections are highlighted in Figure 7-3

1. The "*convergent section"* where the flow increases from subsonic to near sonic velocity by decreasing the cross-sectional area. This section is characterised by a flow Mach number less than 1 (M<1).
2. The second is the "*throat section"* or the *critical area* which is characterised by the minimum cross-sectional area of the entire nozzle, where the flow is chocked and sonic condition is achieved. (M=1)
3. Finally, the flow goes supersonic at the "*divergent section"* of the nozzle caused by the isentropic expansion of the flow thereafter the throat area of the nozzle. (M>1)

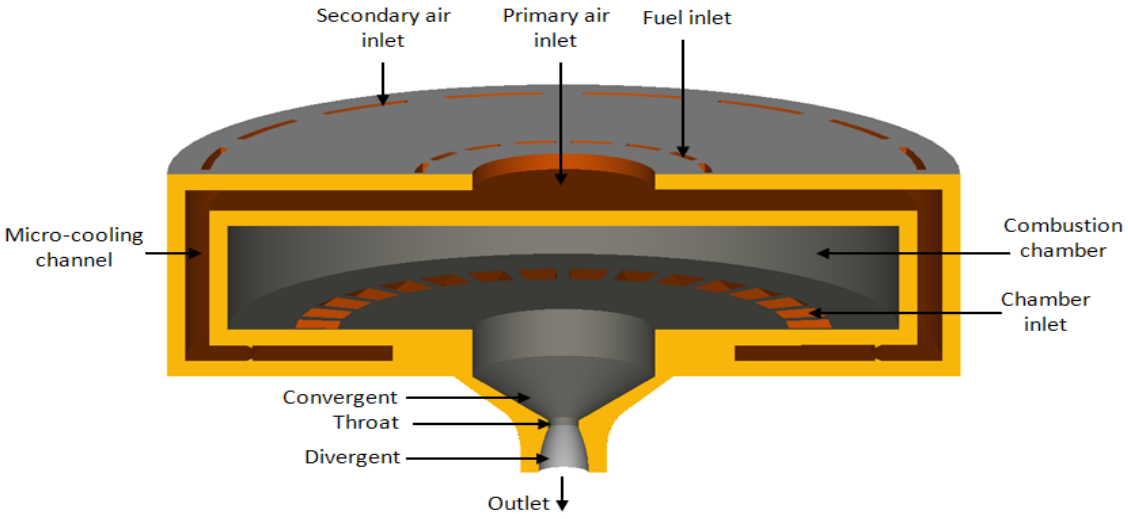

Figure 7-3: Cutaway of a bi-propellant microthruster design

7.7 Numerical modelling approach

From the above section and in order to numerically model the microthruster, the design is split into two numerical problems. The first deals with laminar incompressible subsonic flow which represents the microcombustor and half of the total length of the convergent portion of the nozzle as illustrated in Figure 7-4 (top).

The microcombustor configuration used in this investigation was previously analysed through computational modelling in 6.2.2. The numerical results predicted that the exit boundary of the microcombustor experienced flow recirculation as shown in Figure 7-5, when the device was analysed considering a direct discharge to the surrounding environment. The streamlines plot (right) represented the fluid pattern inside the microcombustor highlights two main recirculation zones; the first is located inside the combustor chamber and the second is located at the exit boundary of the combustor.

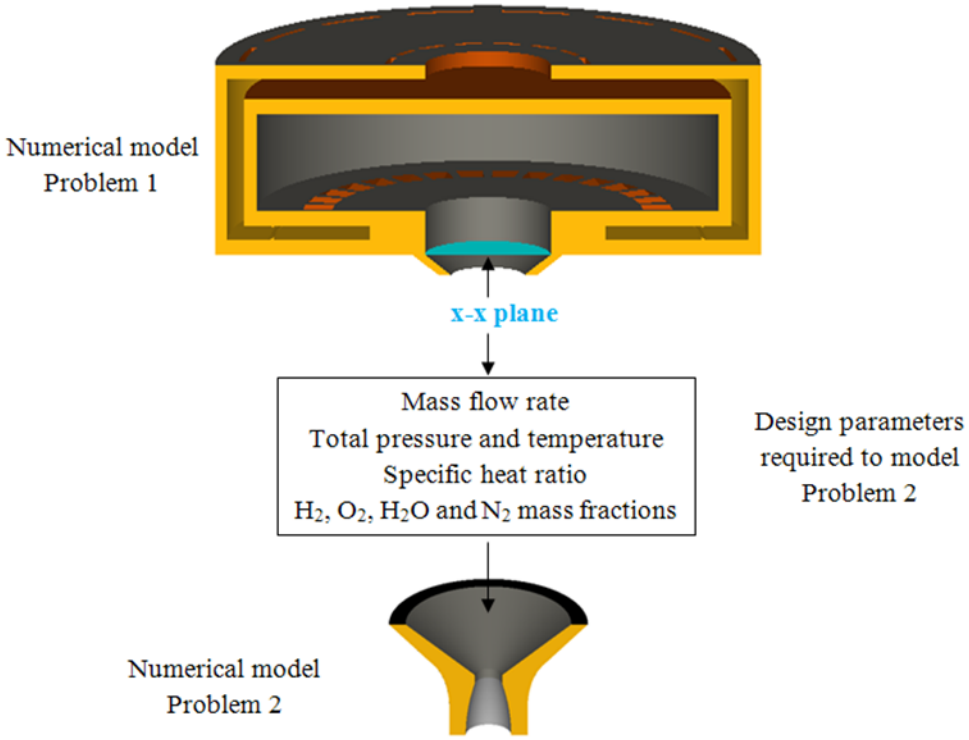

Figure 7-4: Microthruster numerical approach flowchart. Microcombustor and half of the convergent section length (Numerical model 1-Top), Design parameters required by numerical model 2 (middle) and the CD-nozzle (numerical model 2-Bottom)

An enlarged view of the exit boundary shown in Figure 7-5 (left) demonstrate the fluid flow directions across the exit boundary presented by a vector plot.

From the above, the second recirculation zone might lead to an inaccurate prediction of the design parameters of interest at the combustor exit plane. This is confirmed when the proposed configuration (combustor and part of the convergent section) was numerically analysed and the results indicated that the fluid flow across the x-x plane which represents the combustor exit only travelled in one direction as shown in Figure 7-6. Therefore, the proposed design configuration allows an accurate prediction of the design parameters required by the second numerical problem which models the CD-nozzle.

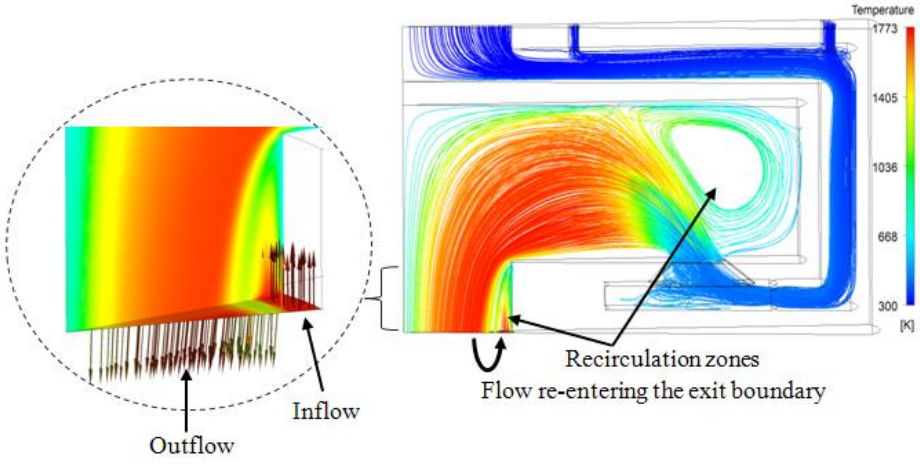

Figure 7-5: Temperature streamlines and recirculation zones inside the chamber previously analysed in 6.6.2 (right). An enlarged view show the flow directions across of the exit boundary (left)

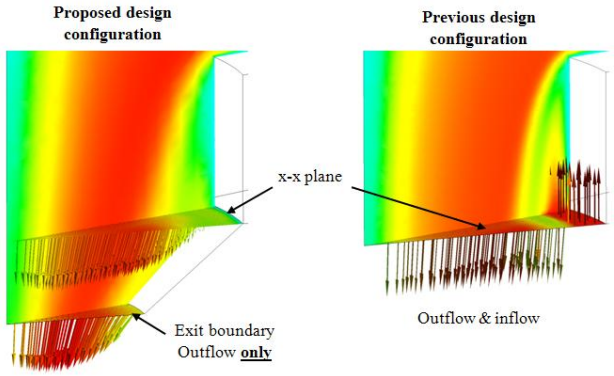

Figure 7-6: Flow direction results comparison between the proposed and the previous design configurations at x-x plane and the exit boundary

The second numerical problem represents the convergent-divergent nozzle sections. This design problem is characterised by compressible flow, high Reynolds number at the throat section and subsonic-supersonic flow velocities. The design parameters' values of interest obtained from the previous numerical simulation (problem 1) at x-x plane (Figure 7-4) will be used to design the divergent section contour and then to be utilised for the inlet boundary condition at the convergent section. This allows the evaluation of the nozzle performance in terms of the thrust force and the specific impulse produced from different nozzle design configurations and most importantly, compares the design exit Mach number (hereafter referred as DeMn) which corresponds to the 1-D compressible flow theory with that obtained from the 3-D numerical simulation results at the nozzle exit.

From the first law of thermodynamics and applying the steady flow energy equation, neglecting the work and the heat flow terms, then the following expression is derived (Anderson, 2004)

$$\frac{T_o}{T} = 1 + \frac{\gamma - 1}{2} M^2 \tag{7-1}$$

Where T_o is the total or stagnation temperature, T is the static temperature, γ is the specific heat ratio and M is the local Mach number. From the above equation, the total temperature obtained from the numerical results at the combustor outlet plane (x-x) is assumed to be equal to the static temperature. This is based on the fact that the flow velocity, hence the Mach number, is very low which is the feature of laminar fluid flow. Although the change in density of the fluid is associated with the temperature rather than the pressure inside the microcombustor, the pressure has significant effect on the fluid density inside the CD-nozzle, which is the characteristic of the compressible flow system. Therefore, the total temperature, the total mass flow rate and the species mass fractions' values used for inlet conditions in problem 2 are not influenced by the change from incompressible to compressible flow systems. This is due to the fact that the exit boundary of the microcombustor represented by x-x plane in problem 1 represents the same inlet boundary of the convergent section of the CD-nozzle in problem 2.

7.8 CFD numerical modelling

7.8.1 Part I: Microchamber and half of the convergent length section model

Three-dimensional CFD analysis accounts for fluid flow, heat transfers, chemical reaction and conjugated heat transfer between the fluid and the solid domains carried out using commercial CFD software named ANSYS CFX 12.1. Only a 22.5 degree section of the microchamber and the convergent section of the nozzle are modelled. The initial throat section diameter which dictates the convergent wall modelling angle is arbitrarily chosen to be ~0.4 mm. A micro rocket engine with a throat diameter of 0.5 mm was experimentally tested by (London, 2000) at a chamber pressure of 12.5 atm.

The main design features are represented within the 3-D model section, such as fuel and air injectors, combustion chamber and outside walls, micro-cooling channel, the solid domain where a stainless steel structure is considered and the outlet of the combustor.

Unstructured mesh is chosen to model the design problem using ANSYS ICEMCFD 12.1 software with a maximum volume element size of 0.09 and 0.11 for the fluid and the solid domains respectively in which, the total number of elements within the 3-D section were 550,000 approximately. The element size values applied in this case were obtained from a grid sensitivity analysis which was carried out previously in 3.3.3.

The numerical simulation is executed using the finite rate chemistry (FRC) laminar combustion modelling code within the ANSYS CFX 12.1 solver and implemented a single-step hydrogen-air combustion reaction described as follows:

$$H_2 + 0.5\,(O_2 + N_2) \rightarrow H_2O + 0.5\,N_2 \qquad (7\text{-}2)$$

The associated Arrhenius expression parameters (ANSYS Inc., 2009b) used to describe the chemical reaction in Eq.(7-2) are listed in Table 6-6. Also, see section 5.6 for details of the expressions integrated within the CFD code that calculate the overall combustor efficiency, the maximum fuel energy release possible, the fuel and oxidiser mass fractions, the heat transfer by means of natural convection using vertical and horizontal plates theory which describe the combustor outside walls, the radiative heat transfer coefficient and the variation of the thermal conductivity with respect to the temperature of 316L type stainless steel.

It has to be noted that all simulation results reported in this chapter are evaluated according to the residuals targets of the individual governing equations with a value less than 1.0E-06.

Two cases are used to evaluate the microthruster performances. In both cases, the microcombustor optimum design parameters are found from a multi-objective design optimisation which was previously investigated in subsection 6.2.2. The first case (Design-A) obtained from the Pareto optimal set corresponds to the maximum value of the total mass flow rate that satisfies the design constraints applied and at the same time achieves a stable combustion inside the microchamber. The second case (Design-B) was selected which represents the compromised design found from the same optimum designs set. In both cases, two conflicting objectives were deployed, the first is to minimise the fuel consumption and the second is to maximise the device efficiency. Both objectives formulas were described previously in section 5.3.

The design parameters and operating conditions for both designs are defined in Table 7-1.

Table 7-1: Combustor optimum design parameters

Geometrical parameters	**Design-A**	**Design-B**
Combustor total height (mm)	3.9	3.83
Combustor total diameter (mm)	13	12.95
Chamber diameter (mm)	11	11
Chamber height (mm)	2	1.95
Micro channel height (mm)	0.4	0.33
Primary air inlet area (mm^2)	7.06	3.73
Fuel inlets area (mm^2)	1.5	1.5
Secondary air inlets area (mm^2)	3.73	3.73
Chamber inlets area (mm^2)	13	17.34
Chamber outlet diameter (mm)	3	2.89
Half of the convergent length (mm)	0.425	0.425
Operational parameters		
Total mass flow rate (g/s)	0.115	0.041
Equivalence ratio	0.475	0.452
Air mass flow at Primary inlet (%)	60	0.56
Fuel, oxidiser inlet temperatures (K)	300	300
Combustor reference pressure (atm)	1	1

The main CFD modelling assumptions using ANSYS CFX can be summarised as:

1. Steady state
2. Finite rate chemistry using laminar modelling
3. Single H_2-air reaction combustion model
4. Thermal energy equation (for low-speed flow modelling)
5. Heat loss from the microchamber walls (convective and radiative)
6. Conjugated heat transfer calculations between fluid and solid domains
7. Smooth walls are assumed
8. Plume is exhausted at sea-level

7.8.1.1 CFD modelling results: Part I

The results obtained from the CFD evaluation at the microchamber outlet represented by x-x plane are illustrated in Table 7-2 are used to calculate and numerically model the convergent-divergent nozzle which will be discussed in the next section. Temperature distribution inside the chamber and the chamber outside walls as well as the Mach number distribution at a vertical plane are shown in Figure 7-7.

Table 7-2: Numerical results obtained from 22.5^o section at x-x plane

Design parameter of interest	**Design-A**	**Design-B**
Combustor exit total temperature (K)	1590	1515
Combustor exit total pressure (kPa) *	14.31	1.126
Specific heat ratio	1.285	1.288
Species mass fractions		
H_2	7.8E-07	5.8E-08
O_2	0.1205	0.1259
H_2O	0.1229	0.1171
N_2	0.7560	0.7569

* Reference to atmospheric pressure of 1

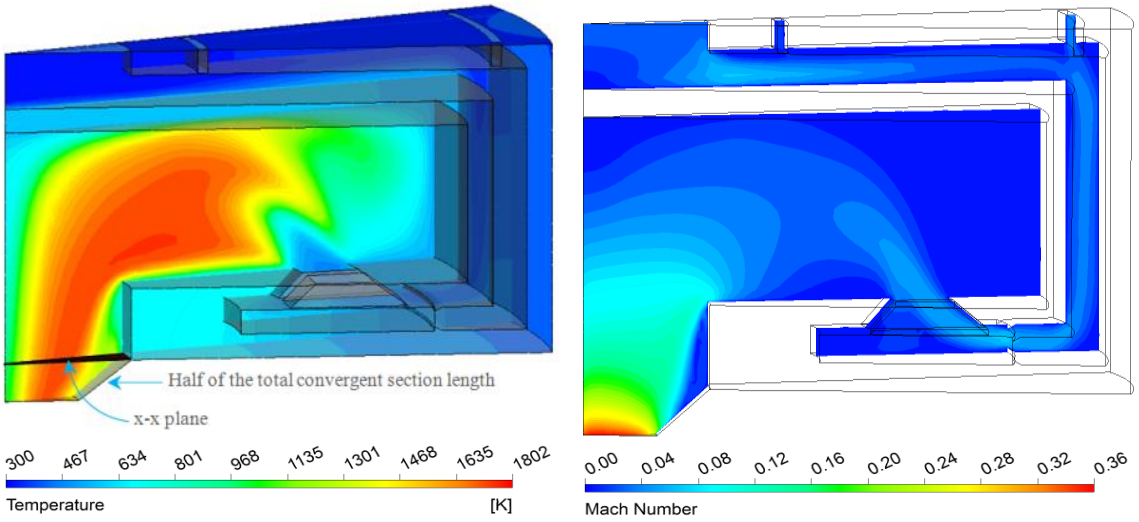

Figure 7-7: Numerical results Part I for Design-A. Temperature distribution at a vertical plane and combustor outside walls (left). Mach number distribution at a vertical plane (right)

7.9 Definition and modelling of the de Laval nozzle

7.9.1 Nozzle design

A schematic of a CD-nozzle is shown in Figure 7-8, which illustrates the main nozzle design sections and also outlines the main bell-like contour design parameters of a divergent section. A conical shape is used to model the convergent section with a total length equal to 0.85 mm, an inlet and outlet diameters equal to 3 mm and 0.468 mm respectively. The convergent inlet diameter takes the value of the combustor outlet diameter listed previously in Table 7-1. The outlet diameter of the convergent section is calculated from Eq.(7-6) presented in the next subsection. A cylindrical shape is chosen to describe the throat section with a total height of 0.15 mm. A bell-like shape is chosen to model the divergent section of the nozzle. The convex contour design of the divergent section is governed by the parabola equation ($y = ax^2 + bx + c$). The convex contour starts at the throat section with one-half of the Prandtl-Meyer angle. This angle represents the sharp increase in the flow area of the divergent section thus generating an expansion fan in which the sonic flow at the throat section is isentropically expanded to achieve the desired exit Mach number at the nozzle outlet. An angle of zero is enforced to model the end wall of the divergent section downstream at the nozzle outlet.

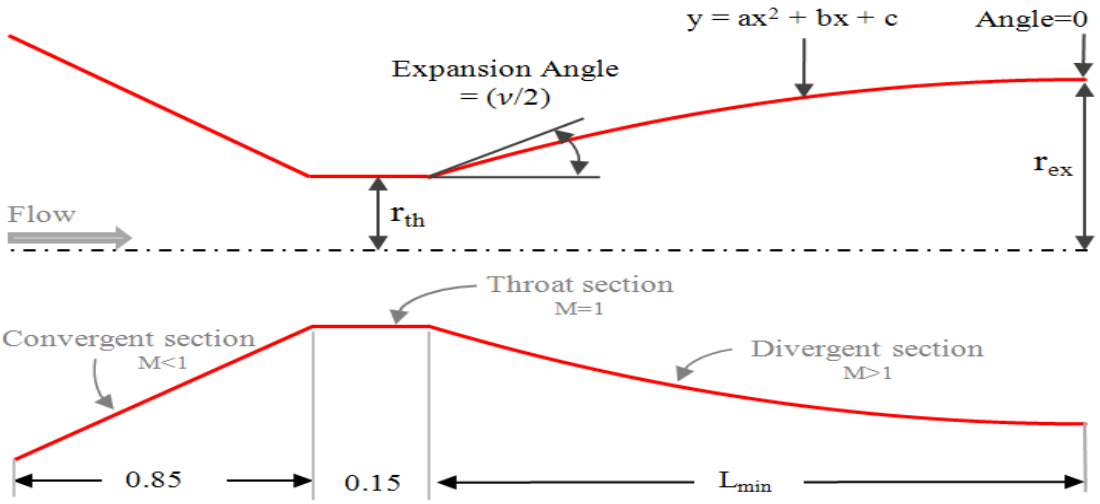

Figure 7-8: Schematic of a CD-nozzle and divergent section design parameters. Scale in millimetre

Where: r_{th} Throat radius, calculated from Eq.(7-6)

r_{ex} Exit radius, calculated from Eq.(7-7)

ν Prandtl-Meyer angle from Eq.(7-8)

L_{min} Divergent minimum length calculated from Eq.(7-9)

7.9.2 Mathematical formulation

7.9.2.1 Calculation of the throat area

The throat or the critical area (A_{th}) of a CD-nozzle is calculated from Eq.(7-6). This equation is applied for isentropic compressible flow of a Perfect gas through a nozzle with the assumption of sonic flow condition (M=1).

$$A_{th} = \frac{\dot{m} * \sqrt{T_t}}{P_t * \sqrt{\frac{\gamma}{R}} \left(\frac{\gamma+1}{2}\right)^{-\left(\frac{\gamma+1}{2(\gamma-1)}\right)}} \tag{7-6}$$

7.9.2.2 Calculation of an area within the CD-nozzle

The area at any location of a convergent-divergent nozzle can be calculated from the Mach number of that area and the throat area using the Area-Mach number relation. For example, the nozzle exit area (A_{ex}) is calculated from the design exit Mach number (M_{ex}) and the throat area of the nozzle as follows:

$$\left(\frac{A_{ex}}{A_{th}}\right)^2 = \frac{1}{{M_{ex}}^2}\left[\frac{2}{\gamma+1}\left(1+\frac{\gamma-1}{2}\,{M_{ex}}^2\right)\right]^{\frac{(\gamma+1)}{(\gamma-1)}} \quad (7\text{-}7)$$

7.9.2.3 Calculation of the Prandtl-Meyer angle

The sonic flow at the throat area of a CD-nozzle can be accelerated thereafter through an expansion fan generated as a result of a sharp increase in the cross-sectional area of the divergent section. The abrupt increase in the flow area which is controlled by the Prandtl-Meyer angle (ν) (the expansion angle) is determined from the DeMn. This angle can be calculated from the following expression

$$\nu = \sqrt{\frac{\gamma+1}{\gamma-1}}\,tan^{-1}\sqrt{\frac{\gamma+1}{\gamma-1}\left({M_{ex}}^2-1\right)} - tan^{-1}\sqrt{\left({M_{ex}}^2-1\right)} \quad (7\text{-}8)$$

7.9.2.4 Calculation of divergent section length

For minimum divergent section length (L_{min}) of a bell shape nozzle, according to Anderson (2004), the expansion angle that models the contour downstream from the throat is equal to one-half the Prandtl-Meyer angle for the given exit Mach number. Therefore, the minimum length of a divergent section is derived from the parabola equation

$$y = ax^2 + bx + c$$

By satisfying the following constrains

1. x = 0, y = 0 → obtain c
2. $\frac{dy}{dx} = \tan\left(\frac{\nu}{2}\right)$ at x = 0, y = 0 → obtain b
3. $\frac{dy}{dx} = 0$ at x = L_{min} and y = ($r_{ex} - r_{th}$) → obtain a

By solving the equations, rearranging and substituting, the following equation is found

$$L_{min} = \frac{2(r_{ex} - r_{th})}{tan\left(\frac{\nu}{2}\right)} \quad (7\text{-}9)$$

7.9.2.5 Calculation of a thrust force and specific impulse

In order to evaluate the thrust force (F) and the specific impulse (I_{sp}) generated by the individual nozzle, the following expressions are used respectively
When discharging at sea-level:

$$F = \dot{m}\, V_{ex} + (P_{ex} - P_{amb})\, A_{ex} \quad (7\text{-}10)$$

$$I_{sp} = \frac{F}{\dot{m}\, g} \quad (7\text{-}11)$$

Equations (7-6) - (7-8), (7-10) and (7-11) can be found in (Anderson, 2004; Benson, 2012)

When discharging to vacuum (Whalen, 1987):

$$F_v = \dot{m}\, V_{ex} + P_{ex}\, A_{ex} \quad (7\text{-}12)$$

$$I_{sp} = \frac{F_v}{\dot{m}\, g} \quad (7\text{-}13)$$

Different divergent nozzle contours designed at given outlet Mach numbers are illustrated in Figure 7-9. These contours are modelled applying the above equations and using the values of the design parameters listed previously in Table 7-2 Design-A.

7.9.3 CFD modelling: Part II (Micronozzle design)

The results of interest found from Part I are used to calculate the nozzle throat cross-sectional area and also design the bell contour of the divergent section. Finally they are applied as boundary conditions at the nozzle inlet in the current numerical model (Part II).

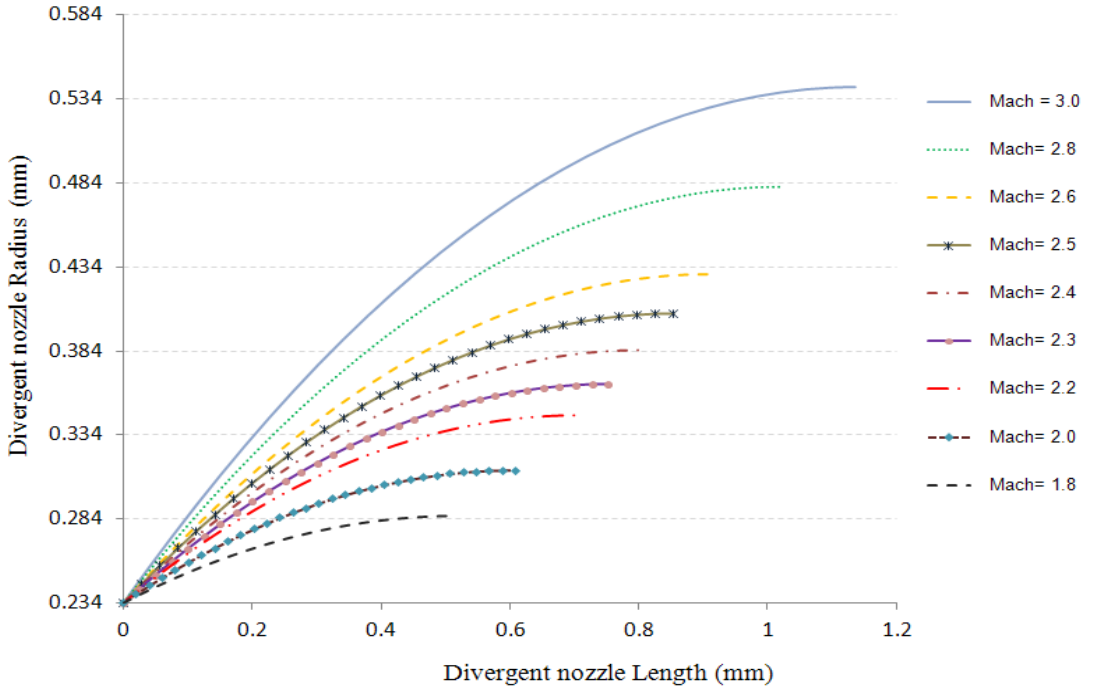

Figure 7-9: Different divergent nozzle shapes designed at giving outlet Mach numbers

7.9.3.1 The computational grid

A numerical grid is built using ANSYS ICEMCFD 12.1 software. Unstructured mesh is used with a maximum global volume element size equal to 0.185. A refined region using a maximum element size of 0.03 and a growth rate of 1.1 is modelled at the core flow inside the nozzle and extended outside downstream from the nozzle exit. Six wall boundary layers are modelled to capture the viscous effects with total height of 50 µm and initial layer height of 5 µm. The total number of elements was 2.67 million approximately. The numerical grid cross section at midplane is shown in Figure 7-10. The computational domain is extended downstream from the nozzle exit in order to assess the flow behaviour outside the nozzle which reveals the nozzle performance (i.e. optimum, overexpanded or underexpanded nozzle) as well as accurately predicting the thrust force magnitude at the nozzle exit plane by avoiding outflow extrapolation of the subsonic layer at the nozzle exit.

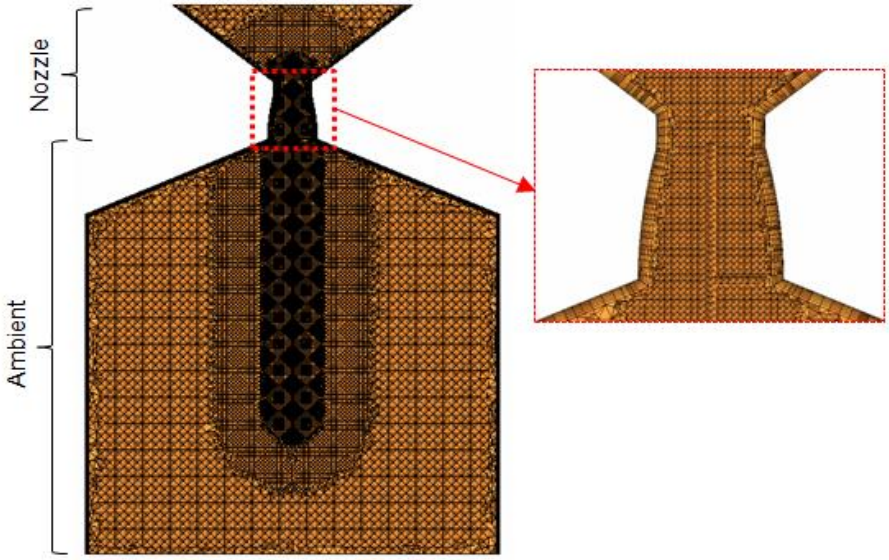

Figure 7-10: Microthruster numerical grid at mid plane. Nozzle and ambient space (left). Enlarged section view (right)

The values correspond to the grid settings reported above are selected when there was no significant difference recorded in the flow metrics results of interest with further grid refinement applied. The percentage difference of 0.69 was calculated when the grid size was increased from 1.4 to 2.67 million elements, whereas a lower value of 0.38 % was calculated by increasing the grid size from 2.67 to 5.85 million elements. Therefore, the grid setting corresponding to 2.67 million elements was chosen for the micronozzle investigation. The flow metrics results obtained at a DeMn of 2.4 for different grid sizes are shown in Table 7-3.

Table 7-3: Mesh sensitivity analysis for design exit Mach number of 2.4

Design parameter	Grid size (million)		
	1.4	2.67	5.85
V_{ex} (m/s)	1308.9	1316.5	1319.6
P_{ex} (Pa)	- 46819.6	- 46564	- 46462.3
$\dot{m}$ (g/s)	0.115	0.115	0.115
A_{ex} (m^2)	4.64E-7	4.64E-7	4.64E-7
F (mN)	128.9	129.8	130.2

7.9.3.2 Numerical model configuration and boundary conditions

In general, the flow inside a convergent-divergent nozzle is characterised by subsonic-sonic-supersonic velocities at the convergent, the throat and the divergent section respectively. In this study, the throat Reynolds number is exceeding 15000 in all investigated nozzle design configurations. Therefore, the Eddy Dissipation (EDM) with k-ε turbulent model is applied. The *Total Energy* equation is used, replacing the *Thermal Energy* equation. The latter is an alternative form of the energy equation and it is suitable for low-speed flow modelling (ANSYS Inc., 2009a). Hence it was applied previously in modelling Part I, where the maximum flow Mach number of ~0.4 was recorded inside the computational domain.

A test case is carried out in order to evaluate the effect of the heat transfer from the nozzle wall to the surrounding environment. It was concluded that there is no effect on the design parameters of interests at the nozzle exit. This is due to the high flow velocities across the nozzle sections (throat and divergent) and the short characteristic length of the nozzle. Therefore, an adiabatic boundary condition is chosen to model the nozzle wall in all investigated cases.

It is appropriate to model all the extended computational grid boundaries downstream from the nozzle exit using an opening type boundary. This boundary allows the fluid flow to cross in both directions (i.e. inflow and outflow) therefore, avoiding zero velocity near these boundaries if they modelled using wall boundary rather than opening type, which might influence the numerical calculations especially the region near the nozzle exit lip.

Figure 7-11 illustrates the type of boundaries utilised and their locations in order to numerically model the micronozzle problem.

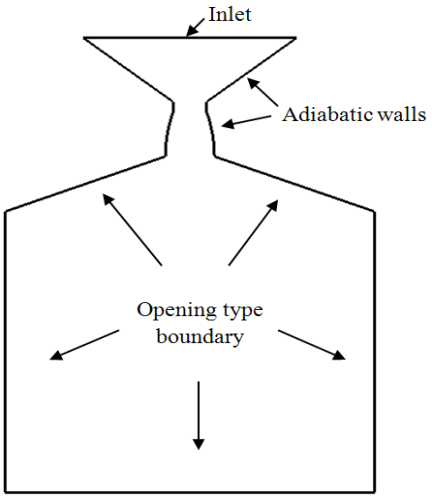

Figure 7-11: Microthruster Part II - Boundary conditions of the numerical model

The main numerical model assumptions using ANSYS CFX are:

1. Steady state
2. Ideal gas
3. Eddy Dissipation with k-ε turbulent model
4. Total energy equation (for high-speed flow modelling)
5. Adiabatic nozzle wall
6. No-slip boundary condition inside the micronozzle
7. Smooth nozzle wall
8. Plume is exhausted at sea-level

7.9.4 CFD Results and discussion: part II

7.9.4.1 Case 1 (Design-A configuration, nozzle discharging at sea-level)

Three-dimensional numerical simulations are executed in order to evaluate the CD-nozzle performance, the prediction of the thrust and the specific impulse, and to investigate the flow characteristics in and outside the individual nozzle.

Based on the design parameters previously listed in Table 7-1 & Table 7-2 which correspond to Design-A, the fluid Mach number and the pressure profiles for different DeMns at the midplane of the computational domain are shown in Figure 7-12.

As anticipated, the flow inside the micronozzle represented by the Mach number shown in Figure 7-12 is increased linearly at the convergent section from subsonic to

near sonic velocity. Sonic flow is observed at the throat section where the Mach number is equal to unity. The flow Mach number at the divergent portion of the nozzle is further increased downstream thereafter the throat section of the nozzle. This increase is caused by the isentropic expansion of the fluid inside the divergent section.

Moreover, an oblique shock wave is formed caused by the difference between the nozzle exit pressure and the atmospheric pressure as shown in Figure 7-13. This wave is attached to the end wall of the divergent section (Nozzle lip) and located downstream from the nozzle exit, which forces the flow to turn inwards towards the jet centreline ($P_{atm} > P_{ex}$).

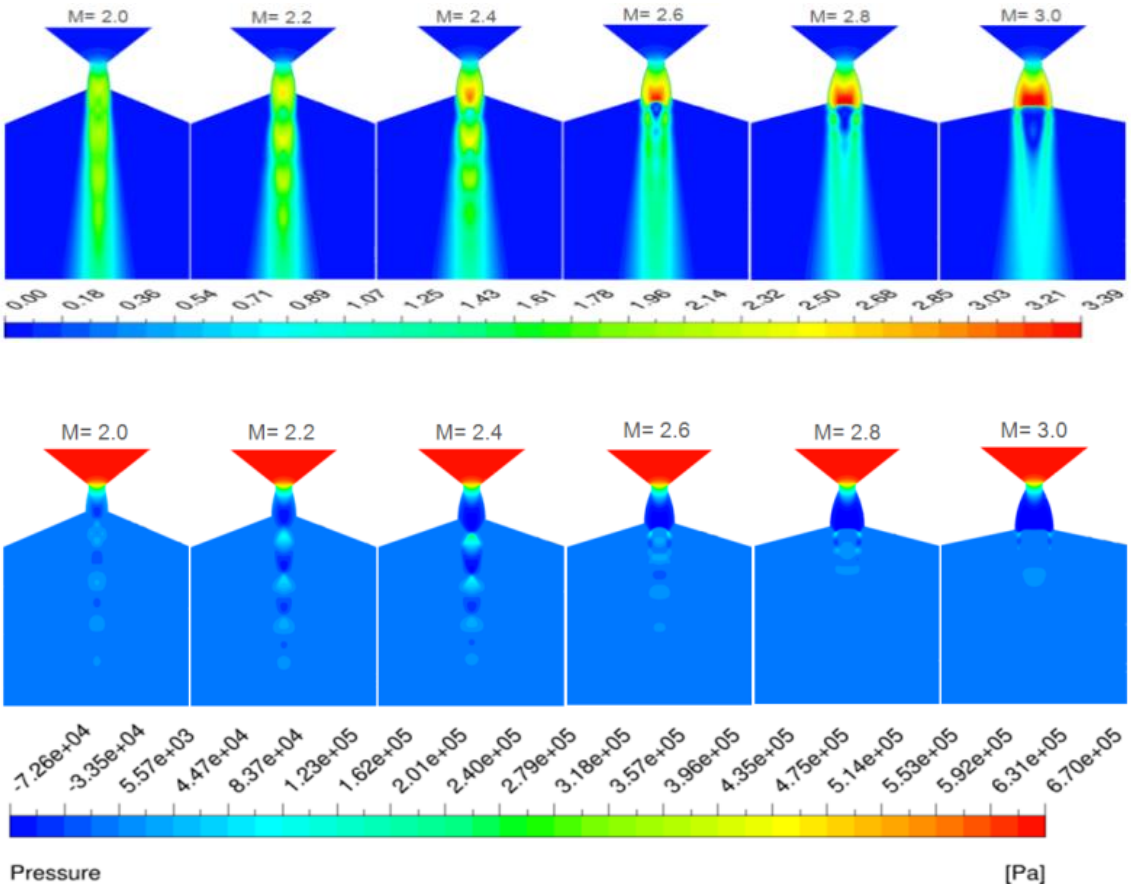

Figure 7-12: Fluid Mach number (top) and pressure (bottom) distributions inside the nozzle and the extended grid for different exit design Mach numbers – Design-A

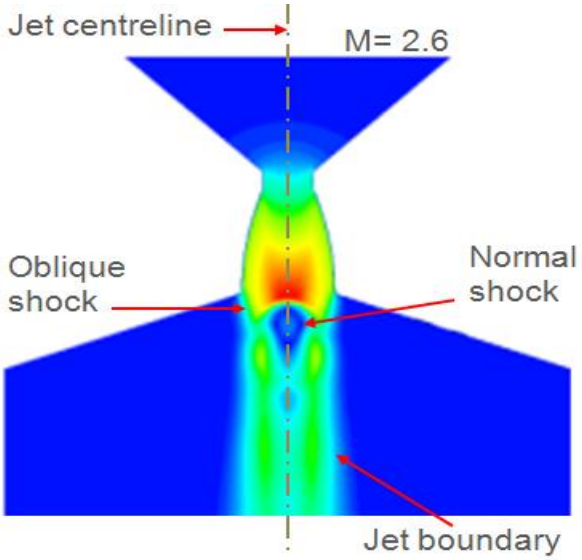

Figure 7-13: Oblique and normal shock waves at design exit Mach number of 2.6

The numerical results represented by the static pressure contours shown in Figure 7-12 and Table 7-4 revealed that the exit pressure in all studied designs over a Mach number range of 2.0 – 3.0 was less than the atmospheric pressure. Hence from this finding it can be concluded that the flow inside the divergent sections are *overexpanded*.

The diamond-like wave pattern downstream away from the nozzle exit can be observed

Table 7-4: Nozzle performance parameters of interest discharging at sea-level obtained from the numerical results correspond to Design-A configuration

Design Parameters	Underexpanded	Overexpanded					
M_{ex} (assumed)	1.8	2.0	2.2	2.4	2.6	2.8	3.0
M_{ex} (CFD)	1.74	1.9	2.05	2.19	2.32	2.46	2
Difference (%) Eq.(7-14)	3.3	5	6.8	8.8	10.8	12.1	33.3
P_{ex} (kPa)	+ 28.6	- 3.53	- 28.3	- 46.5	- 59.7	- 69.7	- 53.5
F (mN)	140	139	136	129	120	107	88
I_{sp} (s)	125	124	121	115	106	95	78

at DeMns over a range of 2.0 – 2.4. These waves are formed from various reflected waves (compression and expansion) between the jet boundary and the jet centreline. The decay of the wave pattern is caused by the turbulent mixing with the surrounding fluid and the effect of the viscous losses after few numbers of compression and expansion wave cycles.

Furthermore, at 2.6 of a DeMn, a normal shock wave is developed downstream thereafter the nozzle exit, which is caused by a further reduction in the exit pressure as shown in Figure 7-12 and Figure 7-13. The normal shock magnitude and the effect are increased by increasing the DeMn above 2.6. For example, at 3.0, the normal shock wave is located at the nozzle exit. This wave occupies a larger exit flow area which increases the back pressure and reduces the exit flow velocity hence, reduces the thrust performance of the nozzle by 31% approximately in comparison to the thrust force generated by the DeMn of 2.4 – see Table 7-4.

The fluid temperature profiles from different design configurations along the flow centreline were plotted in Figure 7-14. The influence of the normal shock wave is demonstrated by the sharp increase in temperature after the nozzle exit and the disappearance of the diamond-like flow pattern (bottom). The diamond pattern is represented in this figure by a repeated cycle of decreasing and increasing in temperature along the flow centreline downstream from the nozzle exit (top). The DeMn of 2.4 represents a transient case as it exhibits a sharp increase in the fluid temperature after the nozzle exit**,** which indicates a normal shock existence and then is followed by the formation of a diamond-like flow pattern which represents reflected waves only.

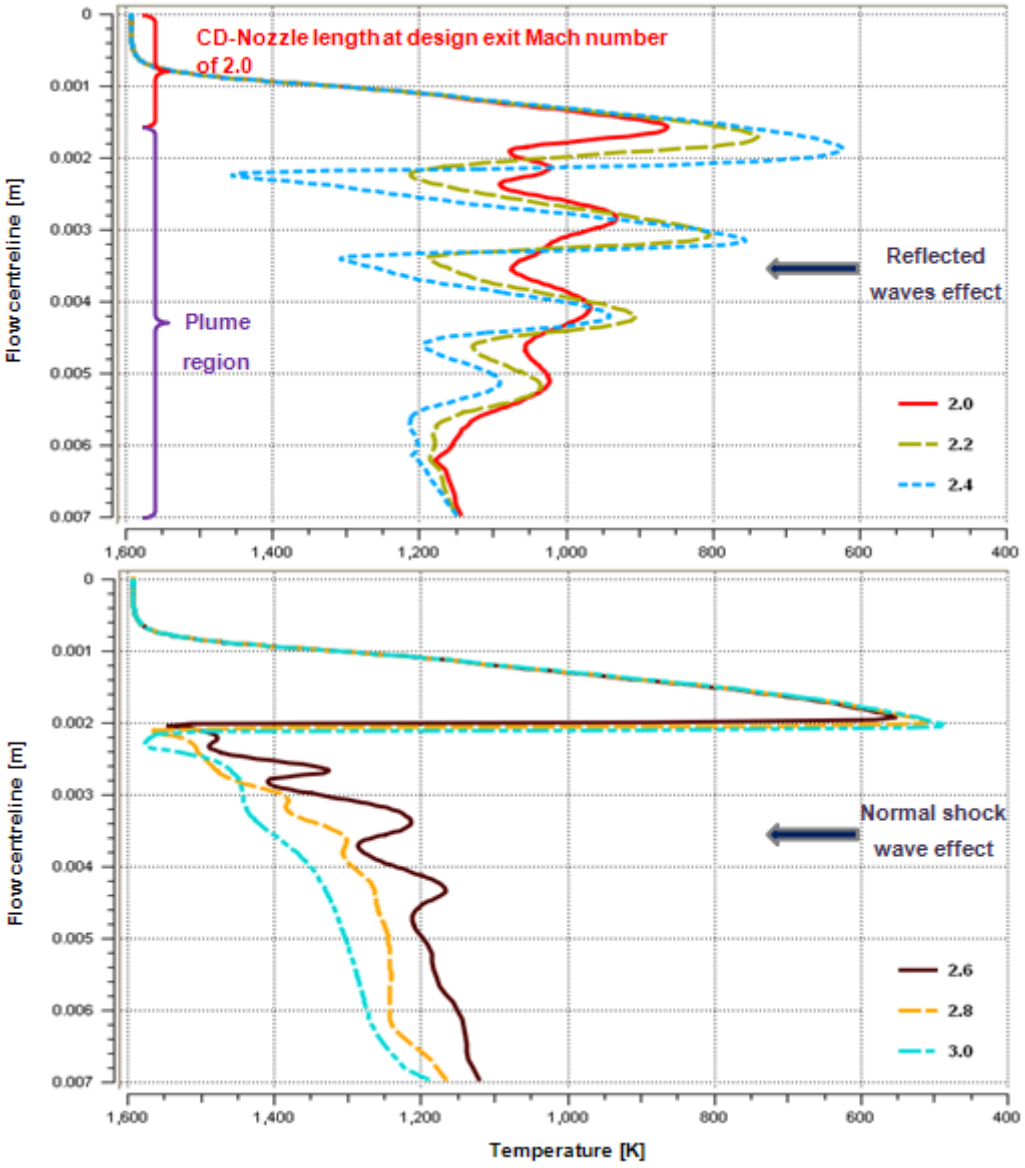

Figure 7-14: Temperature variation along the flow centreline for different design exit Mach numbers from Design-A configuration

7.9.4.2 Case 2 (Design-B configuration, nozzle discharging at sea-level)

In this test case the design parameters were illustrated previously in Table 7-1 & Table 7-2 which correspond to the Design-B configuration. Three-dimensional numerical simulation results of the flow Mach number distributions inside the computational domain for various exit design Mach numbers are shown in Figure 7-15.

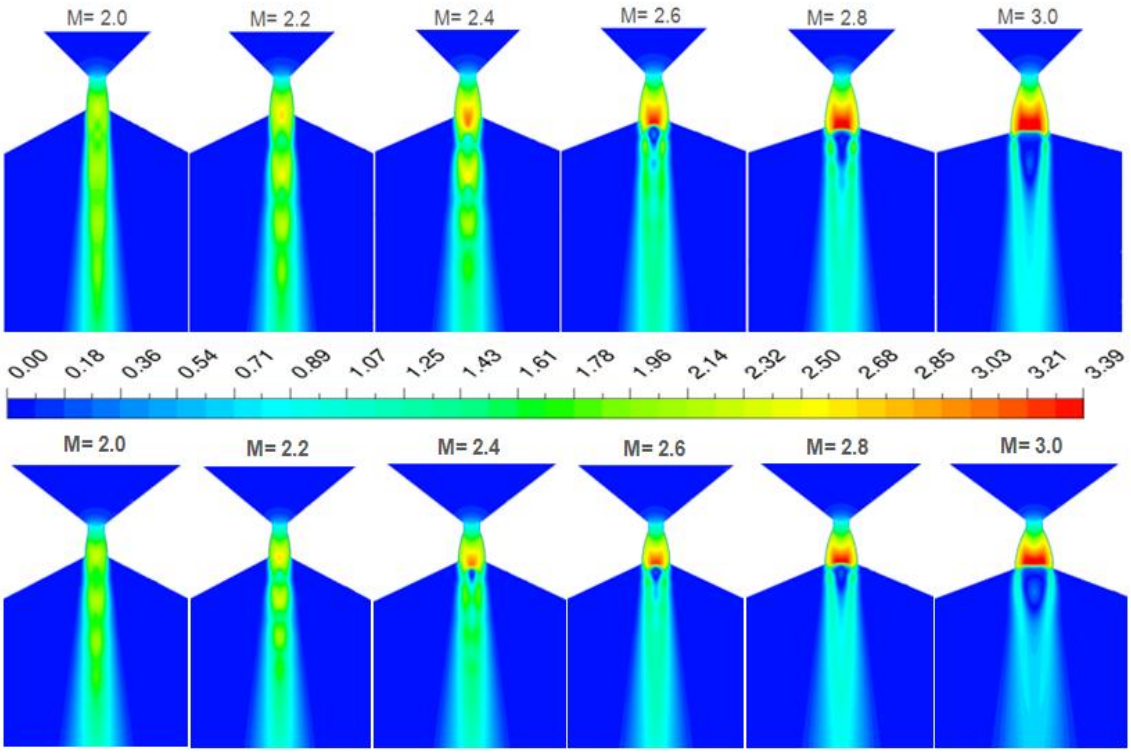

Figure 7-15: Mach number distributions for various design exit Mach numbers at midplane. Design-A (Top) and Design-B (Bottom)

Note: For visual comparison, all designs share the same Mach number scale

Table 7-5: Nozzle performance parameters of interest discharging at sea-level - Design-B configuration

Design parameters	Underexpanded	Overexpanded					
M_{ex} (assumed)	1.8	2.0	2.2	2.4	2.6	2.8	3.0
M_{ex} (CFD)	1.71	1.85	2.05	2.14	2.26	2.25	1.46
Difference (%) Eq.(7-14)	5.0	7.5	9	10.8	13.1	19.6	51.3
P_{ex} (kPa)	+ 15.6	-11.5	-33.1	-49.5	-61.5	-68.3	-29.6
F (mN)	47.7	47	46	43	40	34	28
I_{sp} (s)	117	115	112	106	97	83	70

The performance of the individual nozzle obtained from the numerical simulation is illustrated in Table 7-5. The same flow characteristics are observed from the Design-B configuration in comparison to the results obtained from Design-A as shown in Figure 7-15. However, the normal shock wave is developed downstream from the nozzle exit at lower DeMn of 2.4 in comparison to 2.6 at Design-A. This is due to a lower exit pressure value which resulted from lower operating pressure at the combustor chamber in Design-B to that of Design-A. The flow Mach distribution along the nozzle exit diameter for different DeMns which was predicted from the Design-B configuration is shown in Figure 7-16. The normal shock wave effect at the nozzle exit is demonstrated by a sharp decrease in the inviscid flow Mach number of 2.8 at the nozzle centreline. Moreover, it is clearly observed that the normal shock wave is attached to the nozzle exit at the DeMn 3.0. A large nozzle exit surface area is occupied by the normal shock wave, which is illustrated by the subsonic flow velocities corresponding to an average Mach value of 0.3.

The sharp increase in the Mach value near the nozzle exit wall is reduced by increasing the DeMn. This is due to the increase in delta pressure ($P_{atm} - P_{ex}$) hence, a stronger oblique wave is developed which forces the flow to turn inward toward the flow centreline after the nozzle exit.

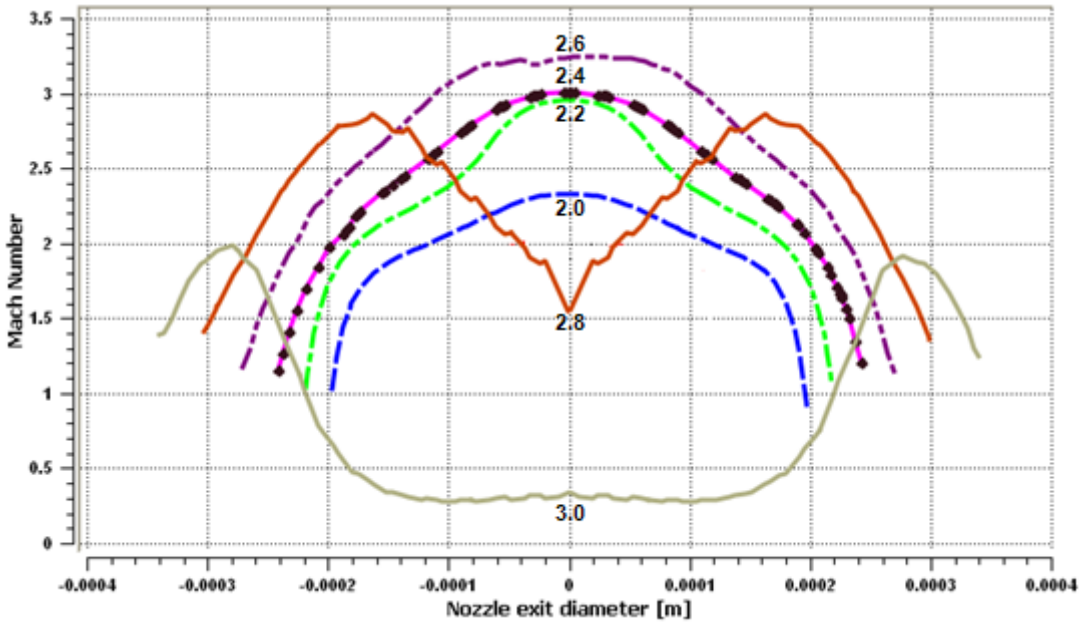

Figure 7-16: Mach number profile along the nozzle exit diameter for different design exit Mach numbers. Design-B configuration

Nozzle performance comparison between Design-A and Design-B in terms of the thrust force predicted by the numerical simulations and the specific impulse for different DeMns are shown in Figure 7-17. It is evident that the reduction in the total mass flow rate represented in Design-B of 150 g/hr compared to that of 414 g/hr in Design-A has led to a lower thrust force generated at the nozzle exit. Moreover, slight differences in the specific impulse values are observed when comparing the data between both designs (A and B). This is due to the fact that the specific impulse is indirectly related to the combustor chamber exit temperature through the value of the nozzle exit velocity (1-D compressible flow theory). The predicted temperatures by the numerical solutions were 1515 K from Design-B and 1590 K in the Design-A configuration at the exit of the combustor chamber.

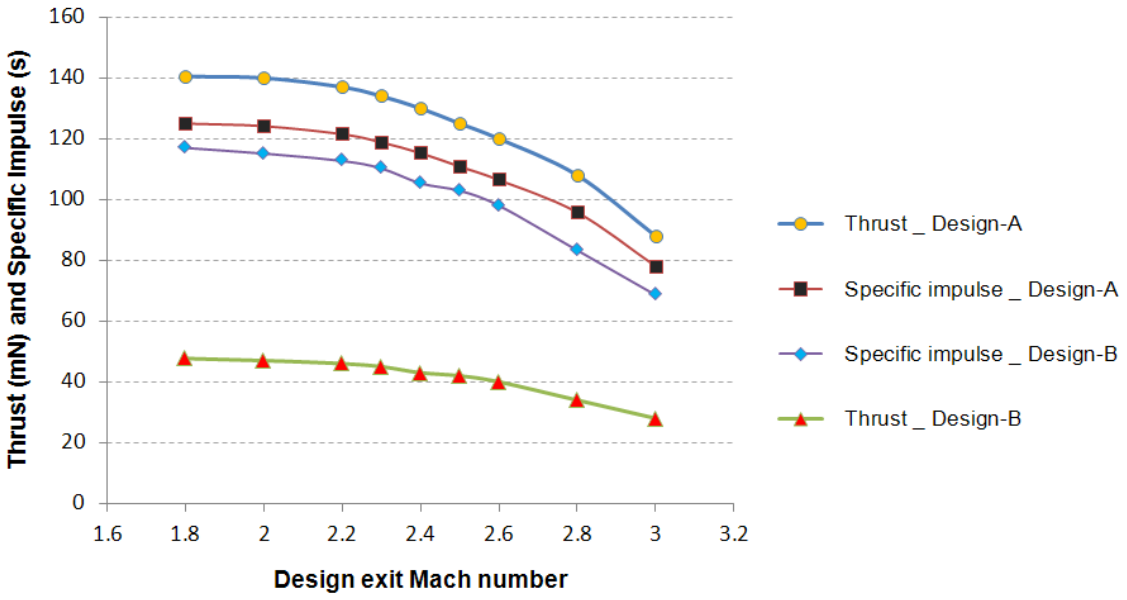

Figure 7-17: Thrusts and specific impulses results comparison

It was found that using the proposed CD-nozzle design approach will result in a Mach design difference of 5 – 10 % over a range of DeMn 2.0 – 2.4 which is subjected to Design-A and B configurations.

The design difference is calculated from the following expression:

$$\text{Mach no. Design difference (\%)} = \frac{(\mathrm{M_{ex}}\,(\text{assumed}) - \mathrm{M_{ex}}\,(\text{CFD}) * 100}{\mathrm{M_{ex}}\,(\text{assumed})} \qquad (7\text{-}14)$$

Where $\mathrm{M_{ex}}$ (assumed) Calculated from the 1D compressible flow theory

$\mathrm{M_{ex}}$ (CFD) Predicted by the numerical solution

It is well known that the optimum nozzle performance can be achieved when the nozzle exit pressure is equal to the atmospheric pressure. As concluded earlier all investigated designs are characterised by an overexpanded flow inside the divergent section. Therefore, a smaller Prandtl-Meyer angle is required to achieve the optimum nozzle performance which corresponds to a DeMn less than 2. Hence, 1.8 is randomly chosen.

Three-dimensional numerical simulation results of the velocity and pressure distributions inside the computational grid are shown in Figure 7-18 based on Design-A configuration. Those results indicated that the maximum velocity and the minimum pressure values are located downstream from the nozzle exit. The average static pressure at the nozzle exit obtained from the numerical result is above the atmospheric pressure by 28.6 kPa. From this finding, it can be concluded that the flow inside the nozzle is underexpanded. The flow expansion process is continued outside the divergent section. Therefore, the optimum design is located somewhere between DeMn of 1.8 and 2.0.

The numerical solution also revealed that the predicted value of the average Mach number at the nozzle exit is 1.74, which is underestimated by 3.3 % compared to the design value based on the 1-D compressible flow theory of 1.8 – see Table 7-4 and from Design-B at DeMn of 1.8 – see Table 7-5.

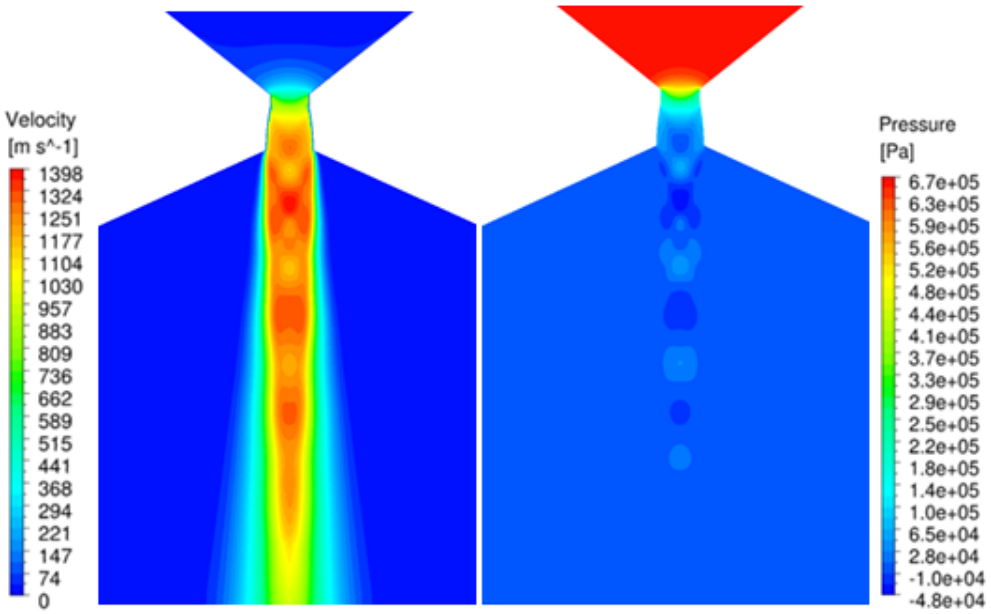

Figure 7-18: Velocity and pressure distributions at midplane for design exit Mach number of 1.8: Design-A configuration

7.9.4.3 Case 3 (Design-A configuration, nozzle discharging to vacuum)

Three-dimensional numerical simulations based on the design parameters correspond to Design-A were executed in order to evaluate the CD-nozzle performance in terms of the thrust and the specific impulse, and also to investigate the flow characteristics inside the individual nozzle and downstream from the nozzle exit.

Three design exits Mach numbers were chosen to model the CD-nozzle and they are 2.0, 2.2 and 2.4. The Mach and the pressure distribution inside the computational domain obtained from the numerical simulation are shown in Figure 7-19. The fluid temperature and the velocity variations along the flow centreline are illustrated in Figure 7-20.

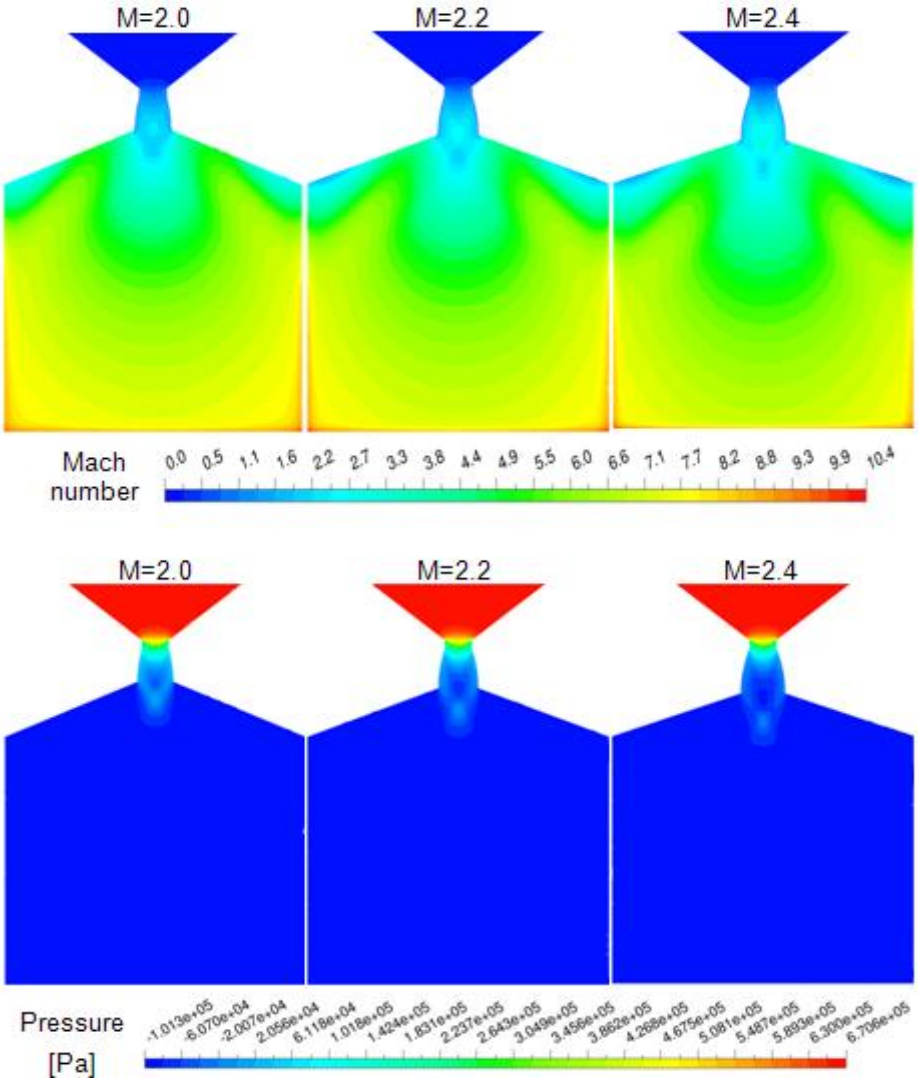

Figure 7-19: Mach (top) and pressure (bottom) distributions at the computational grid midplane for different design exit Mach numbers, correspond to Design-A configuration and plume discharging to vacuum

Note: The computational domain reference pressure is 1 atm

It can be observed from Figure 7-19 that the flow inside the CD-nozzle in all studied designs is underexpanded. This is demonstrated by the increase in Mach number and the decrease in the pressure values downstream from the nozzle exit. The expansion process which continued outside the nozzle is illustrated by the increase in the flow velocity and the reduction in temperature as shown in Figure 7-20. The sudden change in the flow properties at the extended computational grid boundaries downstream from the nozzle exit, as captured in Figure 7-19 and also highlighted in Figure 7-20 as an "extrapolation error", suggested that a bigger computational grid is required if the study of the exhausted plume effect is of interest.

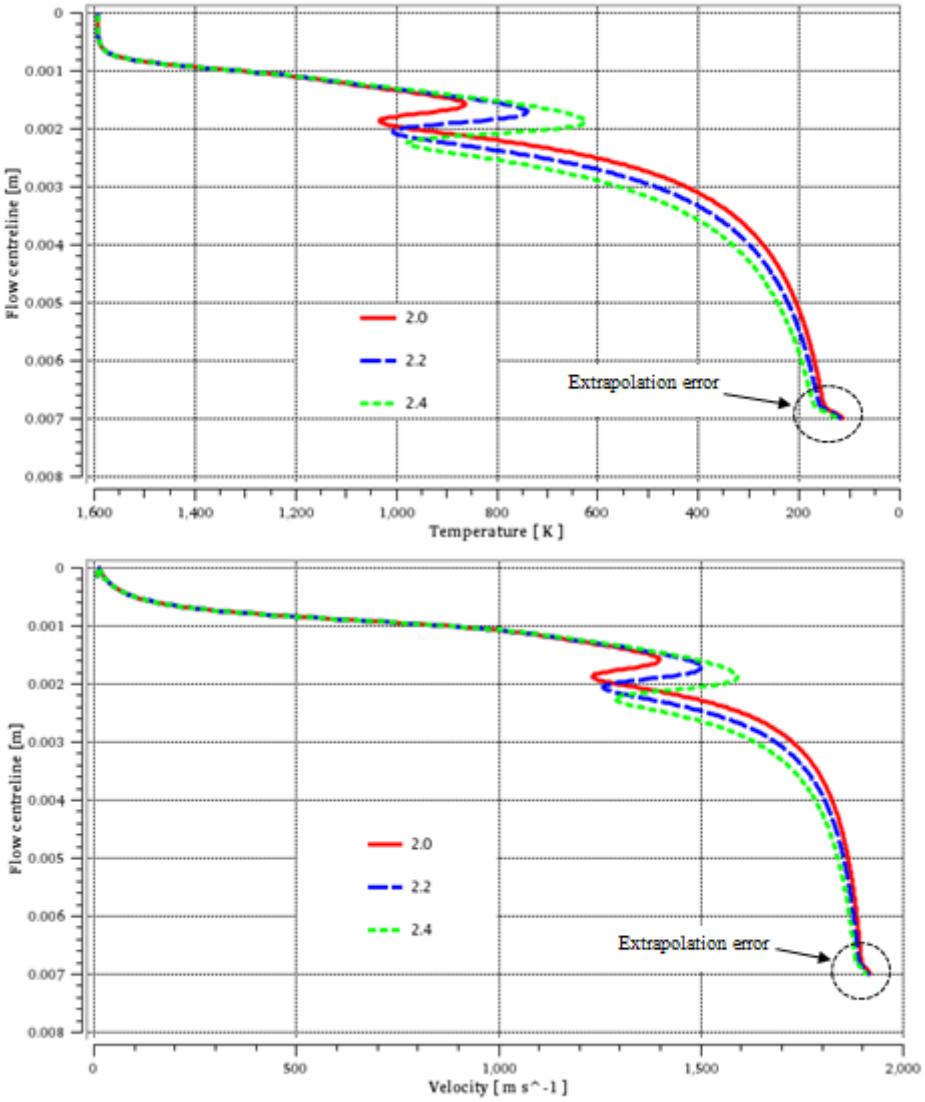

Figure 7-20: Temperature (top) and velocity (bottom) variations along the flow centreline for different design exit Mach numbers from Design-A configuration and plume discharge to vacuum

The numerical results also highlighted the difference between a nozzle that operates in a vacuum and the same nozzle that operates at sea-level as shown in Figure 7-21. The existence of the diamond-like waves when the nozzle was considered exhausting at atmospheric pressure no longer appear within the plume of the same nozzle configuration when operating in a vacuum. This is due to the rapid expansion of the plume and the absence of the pressure effect outside the nozzle exit.

The thrusts and the specific impulses calculated from the numerical simulations' results at different DeMns are listed in Table 7-6. Two important facts can be observed from this Table in comparison to the same nozzle designs listed previously in Table 7-4.

Firstly, the thrust and the specific impulse values are higher in a vacuum to that obtained at sea-level. This is due to a zero value of the vacuum pressure and therefore the free stream pressure-area term (P_{amb} . A_{ex}) in Eq.(7-10) is neglected. Furthermore, increasing the DeMns resulted in higher values of thrust and specific impulse which is opposite to the case where the nozzle is considered discharging at atmospheric pressure. This is caused by the underexpanded flow inside the divergent section hence increasing the expansion angle results in higher exit velocity thus a higher value of thrust is generated at the nozzle exit.

Secondly, the Mach number design difference calculated from Eq.(7-14) is 1.5 – 4.2 in a vacuum to 5 – 8.8 at sea-level for the same DeMns. In a vacuum, the exhausted flow is rapidly expanded after the nozzle exit without generating an oblique wave attached to the nozzle exit, in which it may force the flow to turn inward toward the flow centreline in the case of the overexpanded nozzle or it forces the flow to turn outward in the underexpanded nozzle.

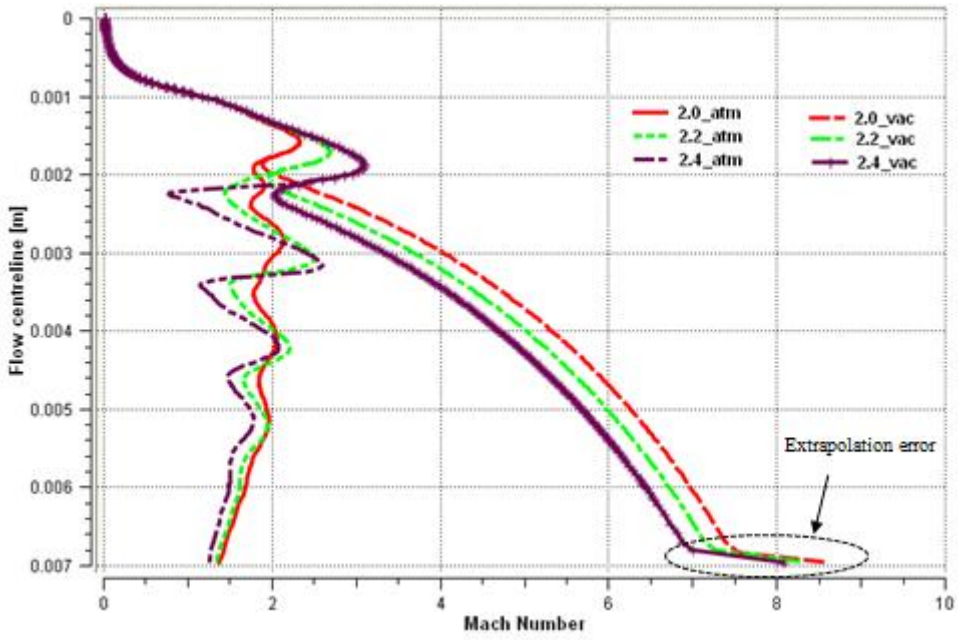

Figure 7-21: A design comparison of the Mach number variation along the fluid flow centreline within the computational domain. Nozzle discharging at sea-level vs. discharging to vacuum

Table 7-6: Nozzle performance parameters of interest discharging to vacuum obtained from the numerical results correspond to Design-A configuration

Design parameter	Value		
M_{ex} (assumed)	2.0	2.2	2.4
M_{ex} (CFD)	1.97	2.13	2.3
Difference (%) Eq.(7-14)	1.5	3.2	4.2
P_{ex} (kPa) [##]	- 12.4	- 36.4	- 54.9
F (mN)	172	176	180
I_{sp} (s)	153	156	160

[##] *Note: Zero pressure (Vacuum) is equivalent to a reference domain pressure of (-101.325) kPa, hence the nozzle in all cases was underexpanded.*

7.10 The integration effect of microthruster components on stable combustion inside the microchamber

As discussed previously, the proposed numerical design approach starts by modelling the microcombustor chamber in order to obtain the required design parameters of interest at the chamber exit plane. These can then be used to describe the CD-nozzle contour and for boundary conditions. Secondly, it models the convergent-divergent nozzle in order to assess the performance of the nozzle in terms of the thrust and the specific impulse.

The first step was modelling the microcombustor and half the length of the convergent section. The numerical results from Design-A configuration of the pressure at the exit plane of the combustor was slightly higher than the atmospheric pressure by approximately 13 kPa. Then again, the simulation results of the CD-nozzle from the second numerical model suggested a maximum pressure value of 6.6 atm at the convergent section of the nozzle as shown previously in Figure 7-12. This pressure value must correspond to the microcombustor operating pressure when considering the integration of the CD-nozzle with the combustor chamber. The constant mass flow rate of the fuel and the oxidiser applied at the combustor inlets and the reduction in the exit area of the combustor chamber at the final assembly, which represented by the throat section of the nozzle were resulting in the operating pressure elevation of the convergent section as well as the combustor. The increase in combustor operating pressure impacts the fluid flow velocity. The fluid velocity profile inside the microchamber before and after the nozzle integration is demonstrated in Figure 7-22. The average velocity of 3.8 m/s was observed at the inlet-to-chamber when the full convergent nozzle section was integrated with the microchamber, but an average value of 16.7 m/s was obtained when half of the convergent section length was considered.

Moreover, a further reduction in the average flow velocity at the inlet-to-chamber planes was indicated by the numerical results when the Design-B configuration was used. This is due to lower total mass flow rate applied at the inlets of the combustor in comparison to that of Design-A. The velocity profile corresponds to Design-B before and after the nozzle assembly is shown in Figure 7-23.

The reduction in fluid velocity inside the combustion chamber after the CD-nozzle integration might lead the flame front to propagate upstream (Flashback) from the

chamber into the micro-cooling channel which might damage the structure of the device. The laminar flow velocity of the incoming fresh gases inside the micro-cooling channel should be of a value greater than the flame speed of the reactants mixture in order to prevent flashback occurrence.

The laminar flame speed of H_2-air calculated numerically at the equivalence ratio 0.5 and at a pressure of 1 atm is equal to ~40 cm/s and at a pressure of 4 atm this value is ~20 cm/s according to Ströhle and Myhrvold (2007) and as shown in Figure 7-24. Also, the experimental data by the latter authors under the same conditions suggested a flame speed less than 50 m/s. Therefore, based on the post analyses of the numerical results shown in Figure 7-22 and Figure 7-23, it is expected that a stable combustion inside the microchamber can be achieved in both combustors studied as represented by Design-A and Design-B configurations.

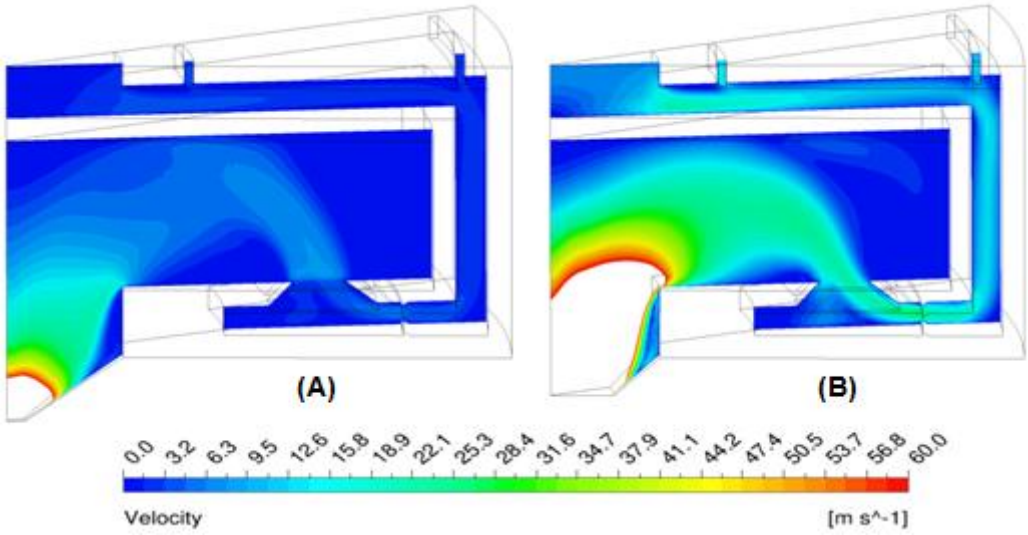

Figure 7-22: Velocity profile results comparison represents Design-A configuration

A) Chamber + Full convergent section of the nozzle.

B) Chamber + Half the length of the convergent section.

Note: For visual comparison reason, the results were presented up to a maximum of 60 m/s

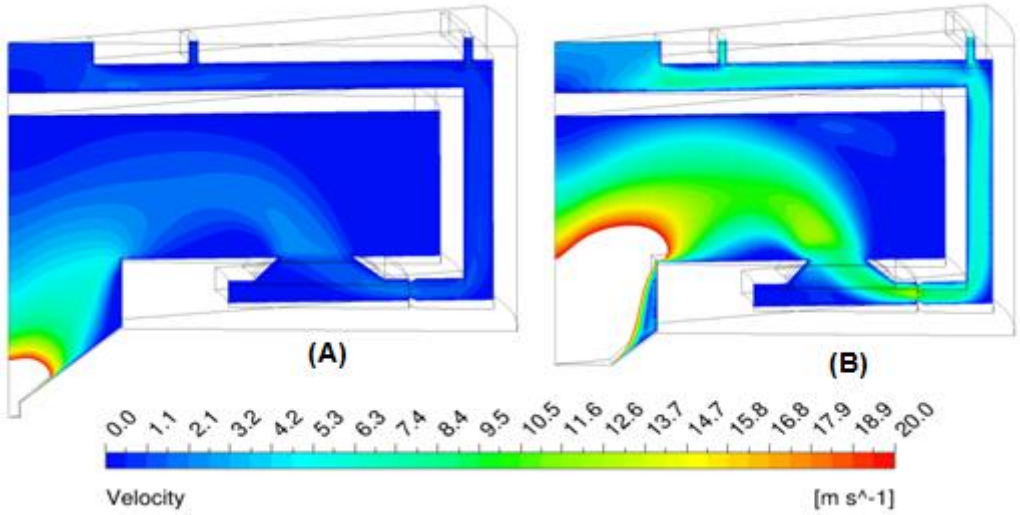

Figure 7-23: Velocity profile results comparison represents Design-B configuration

A) Chamber + Full convergent section of the nozzle.

B) Chamber + Half the length of the convergent section.

Note: For visual comparison reason, the results were presented up to a maximum of 20 m/s

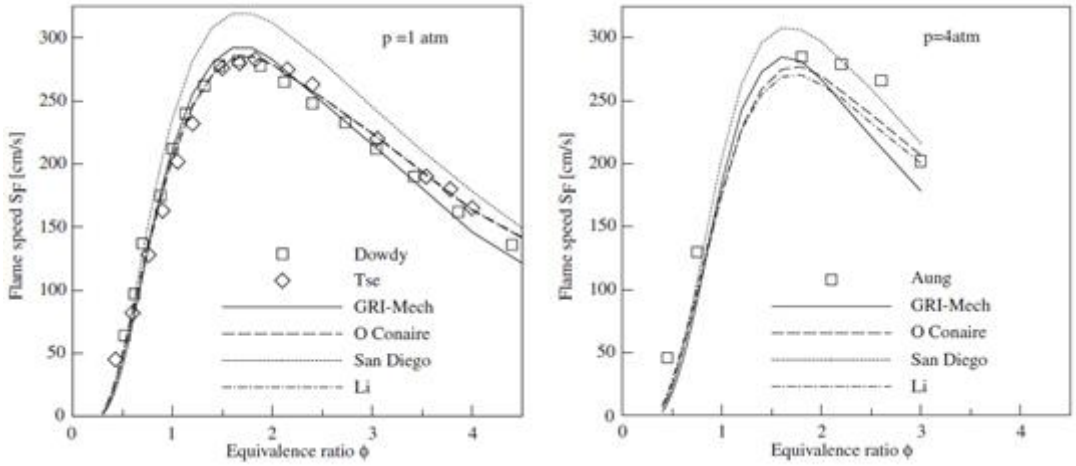

Figure 7-24: Experiment and numerical data of the laminar flame speed of H_2/air at 1 atm (left) and at 4 atm (right)

Note: Experimental data (symbols) and numerical results (lines) for different reaction mechanisms. (Ströhle and Myhrvold, 2007)

7.11 Combustor design improvement for low thrust and high specific impulse applications

In order to achieve lower thrust value from an optimum thruster design compared to that obtained from Design-B configuration then the following must be applied:

- The propellant's total mass flow rate must be reduced and, or
- The throat section area of the CD-nozzle must be decreased

The reduction in the propellant's mass flow without reducing the cross-sectional area of the micro-cooling channel results in lower fluid flow velocity inside the cooling channel hence, the design will be susceptible to flashback and/or autoignition phenomena. As described above, the reduction in the throat cross-sectional area of the nozzle results in an increase in the combustor operating pressure which lowers the fluid velocity, and yet again might lead to flame propagation upstream inside the micro-cooling channel.

On the other hand, in order to increase the specific impulse it is mandatory that the microcombustor operates at higher temperature. This can be achieved by increasing the equivalence ratio of the propellants mixture. From Figure 7-24, increasing the equivalence ratio from 0.5 to 1.0 resulted in the flame speed rising four-fold at a pressure of 1 atm and by three-fold at a pressure of 4 atm which might lead to higher flame velocity compared to the local flow velocity.

From the above, the following design improvements can be considered which will be investigated in detail in the following subsections:

- Inlet geometry configuration to combustor chamber
- Fuel injection location along the micro-cooling channel

7.11.1 Inlet geometry configuration to combustor chamber

The combustor design can be improved to prevent flame propagation upstream at a lower value of the total mass flow rate than 150 g/hr by modifying the inlets-to-chamber configuration as shown in Figure 7-25.

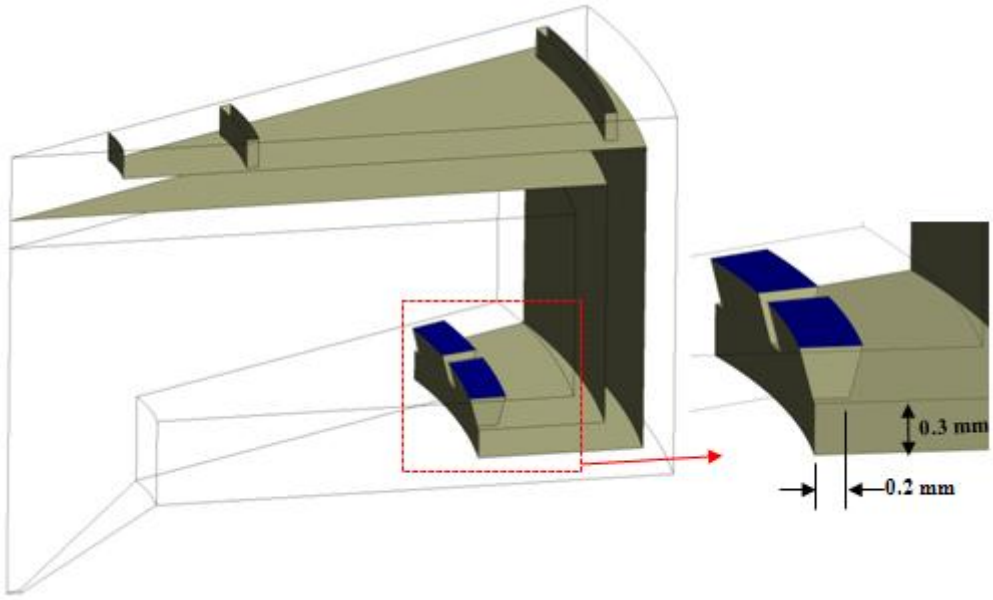

Figure 7-25: Inlet-to-chamber new design configuration

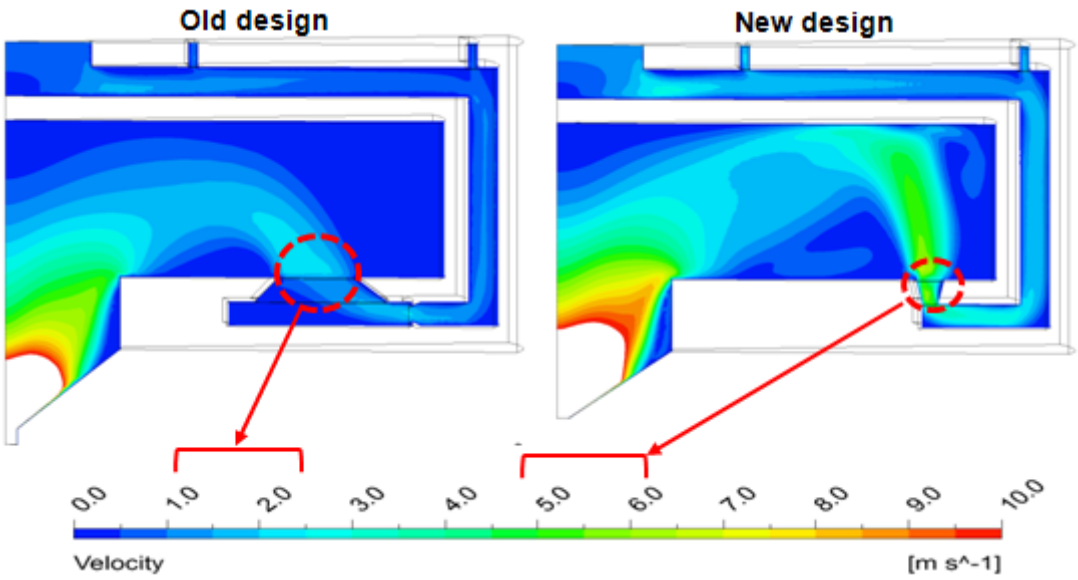

Figure 7-26: Velocity profile results comparison (Design-B parameters). Old design (left), new design (right)

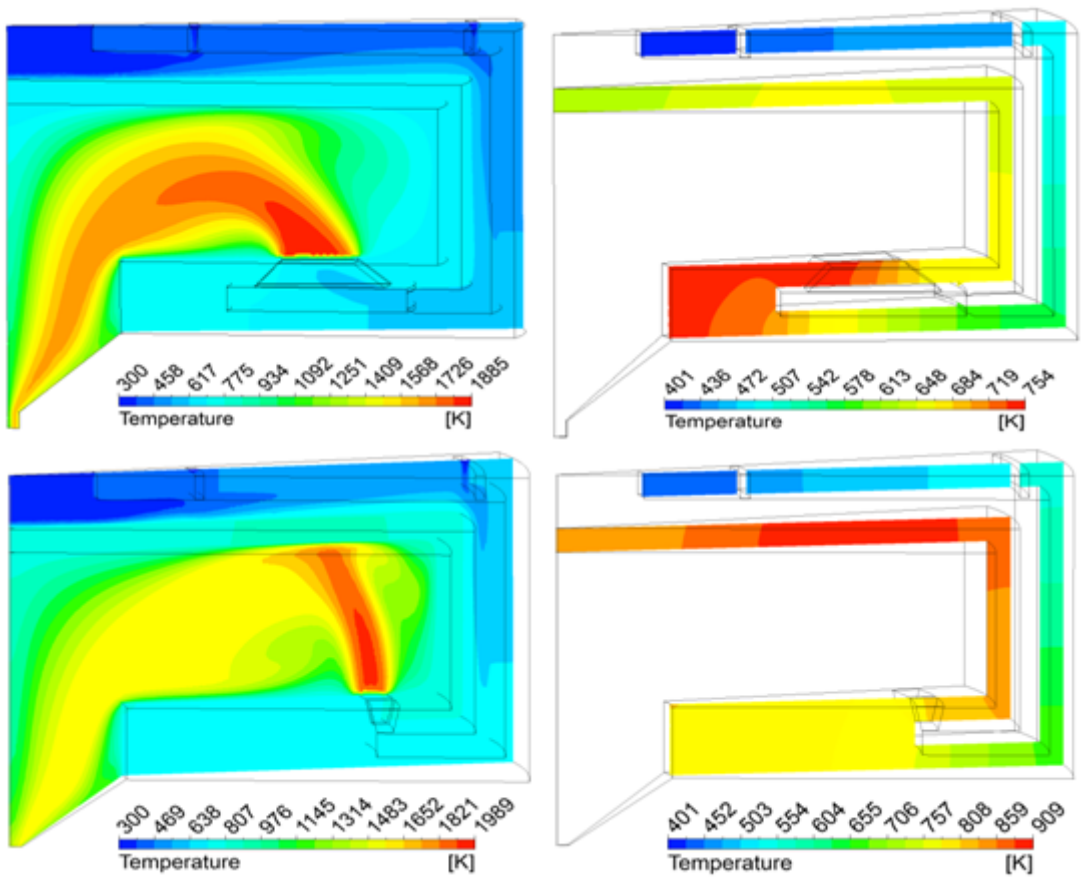

Figure 7-27: Temperature distribution in fluid (left) and structure (right) domains. Old design (top), new design (bottom)

The velocity profile obtained from the numerical results which corresponds to Design-B operating parameters in comparison to the previous geometrical design is shown in Figure 7-26.

The numerical simulation results shown in Figure 7-27 predicted a three-fold increase in the average flow velocity at the inlet-to-chamber plane compared to the previous design configuration. Furthermore, there is an increase in the flame temperature from 1885 K in the previous design to 1989 K in the new design configuration. This is due to the increase in the initial enthalpy of the reactants mixture caused by the increase in chamber structure upper wall temperature as shown in Figure 7-27 (left). Therefore, more heat energy was transferred to the flowing reactants mixture inside the micro-cooling channel before entering the combustor chamber.

7.11.2 Fuel injection location along the micro-cooling channel

Spadaccini et al. (2002b) have experimentally evaluated a six-wafer microcombustor which is compatible with the MIT micro-engine by using three different fuel injections along the micro-cooling/mixing channel. The calculated combustor efficiency over a range of equivalence ratio 0.4 – 0.6 was compared to that of the premixed design values. They have concluded that the injection of fuel should occur as far upstream as possible in order to insure an adequate fuel mixing length with the oxidiser for a non-premixed arrangement. Then again, a numerical case study of the aforementioned combustor was carried out by Hua et al. (2005a) This was to evaluate the effect of different equivalence ratios on the design using a detailed hydrogen-air reaction mechanism with nine-species and 19 reversible reactions, applying the following main boundary conditions; total mass flow rate of 720 g/hr, an external wall heat transfer coefficient of 200 W/m^2 K and a thermal conductivity of 149 W/m K. The temperature distribution within the 12 degree 3-D section of the combustor chamber computational grid at equivalence ratio of 0.6 & 0.7 is shown in Figure 7-28.

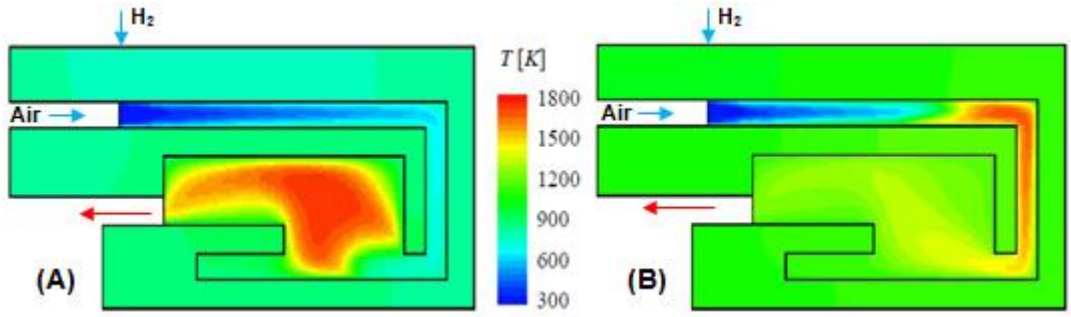

Figure 7-28: Temperature distribution within the MIT six-wafer microcombustor. (A) ER = 0.6 & (B) ER = 0.7 (Hua et al., 2005a)

The simulation results demonstrated that the increase in the equivalence ratio from 0.6 to 0.7 resulted in flame propagation upstream or possibly reactants autoignition inside the micro-cooling channel, but most importantly, it was the final flame location which suggested that a shorter mixing length for hydrogen-air reaction is adequate under the studied design parameters for sustain combustion.

Design-A configuration in comparison to the above case study has the same micro-cooling channel height of 0.4 mm. It is also configured to operate using approximately half the total mass flow rate and a lower order of magnitude for the external wall heat transfer coefficient. This implies that the flame anchors even closer to the fuel inlets if

the boundary conditions of Design-A are used in the above case study with an equivalence ratio of 0.7.

In order to validate the implication of the operational parameters (i.e. mass flow and heat transfer coefficient) on the final flame location and the mixing length required, 3-D numerical simulations are carried out using different CFD solvers namely ANSYS CFX 12.1 and ANSYS FLUENT 12.1.4. The numerical model shown in Figure 7-29 accounts for fluid flow, heat transfer and chemical reaction. The simulations were executed using the finite rate chemistry (FRC) laminar combustion modelling. A single step of hydrogen-air combustion reaction mechanism described previously in Eq.(7-2) is used within the ANSYS CFX whereas ten-species, 23 reversible reactions listed in Appendix C by University of Leeds (2009) were solved using CHEMKIN-CFD a plug-in chemistry solver that is linked to FLUENT software in the second numerical model. The applied boundary conditions are illustrated in Table 7-7. The computational grid was modelled using 410,000 tetrahedral elements approximately. The solution convergence was judged according to the residuals targets of the governing equations less than 1.0E-06. The computational wall-clock time was approximately 40 minutes for the CFX case which was performed using four-CPU machines and ten days was required to achieve convergence for the FLUENT case.

The temperature distribution inside the computational domain for both numerical models is shown in Figure 7-30.

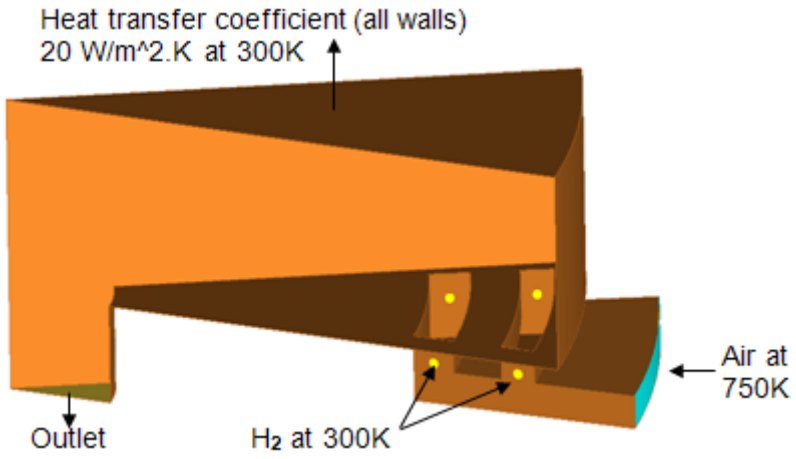

Figure 7-29: Flame location test case geometry design and boundary conditions

Table 7-7: Boundary conditions of the flame location test case

Boundary condition	Value
Total reactants mass flow rate (g/hr)	72
Equivalence ratio	0.6
Hydrogen inlet temperature (K)	300
Air inlet temperature (K)	750
External walls heat transfer coefficient (W/m^2 K) at ambient temperature of 300 K	20

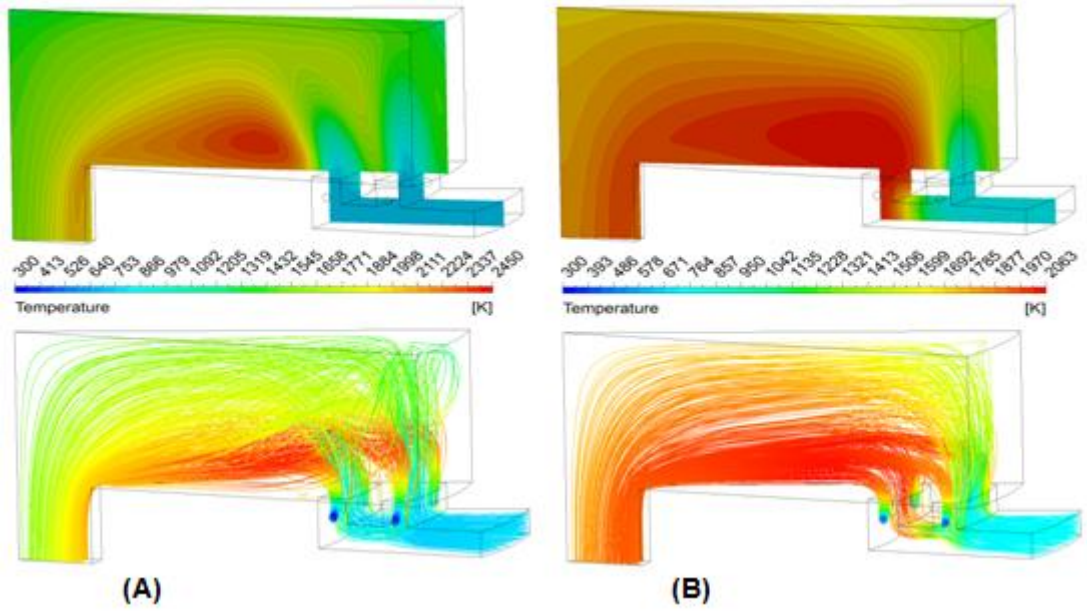

Figure 7-30: Temperature distribution at midplane (Top) and 3D Streamlines (Bottom)

(A) CFX Single-step reaction

(B) FLUENT and ChemKin-CFD ten-species, 23 reversible reactions

The numerical results represented by the temperature profile inside the computational domains for both simulation models using different CFD codes predicted a shorter mixing length of the reactants species to sustain combustion under the applied boundary conditions. Moreover, there are two facts which can be also observed, firstly, the results obtained from the detailed chemical kinetics (FLUENT and ChemKin-CFD) demonstrated an even shorter mixing length, represented by the flame location, compared to the results obtained from the single-step reaction (CFX). Secondly, higher

flame temperature of 2450 K was calculated from the single-step reaction compared to 2063 K from the multi-step reactions. The over-prediction in temperature is a limitation of the single-step reaction modelling which is exothermic in nature. On the other hand, there are in addition to the exothermic reactions, endothermic reactions and species dissociation which both lower the overall reaction temperature when using a detailed reactions modelling.

Furthermore, Design-A operational parameters were implemented to model a single-step combustion reaction in ANSYS CFX using the above computational domain. The simulation results of the temperature distribution at midplane, H_2 and H_2O mass fractions illustrated by the streamlines plots are shown in Figure 7-31. The simulation results of the temperature, the consumption of the fuel and the water generation revealed again, that the combustion can be sustained inside the chamber when the fuel is injected closer to the chamber, downstream at the end of the micro-cooling channel. Three different combustion locations can be seen in Figure 7-31 where the recirculation zones were established. The flame profile can be improved by increasing the surface area of the inlet-to-chamber, which lowers the reactants mixture velocity before entering the chamber as demonstrated previously in Design-A geometry configuration.

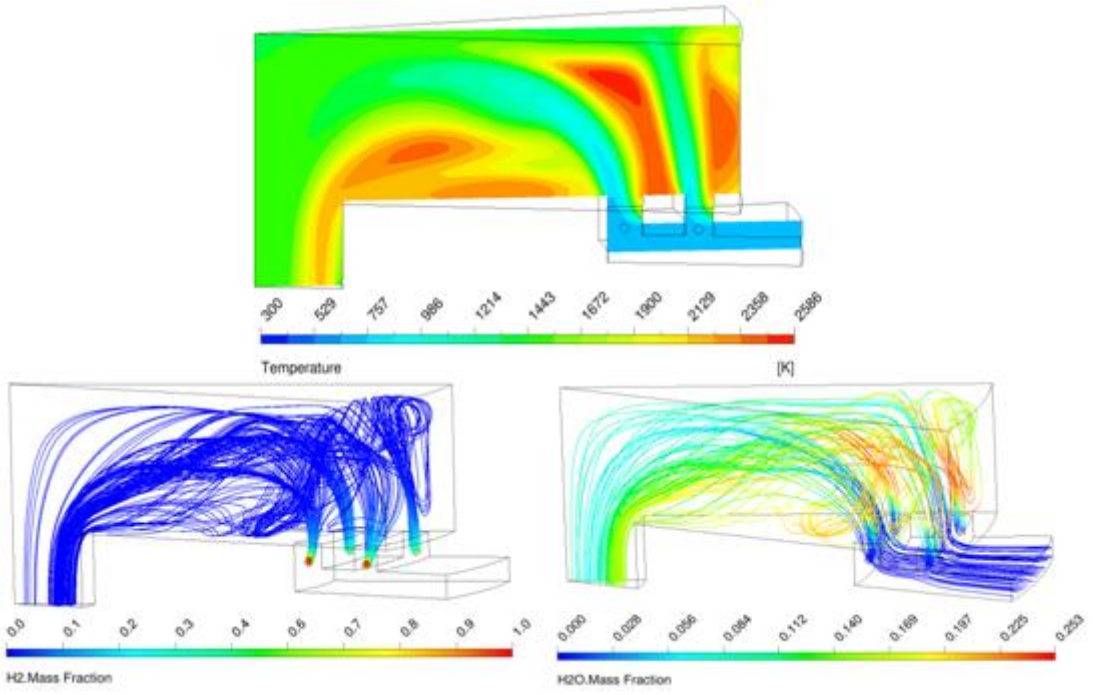

Figure 7-31: Temperature profile at midplane (Top) and 3-D Streamlines (Bottom). H_2 mass fraction (Bottom left) and H_2O mass fraction (Bottom right)

7.12 Chapter summary

This chapter presented the design of a microthruster to be utilised on-board a spacecraft as a propulsion system for attitude control and station keeping applications. A bi-propellant type of hydrogen-air microthruster is considered in this study and a bell-like shape used to describe the divergent section of the nozzle. Two case studies were investigated in which, the microcombustor geometrical design and the operational parameters were obtained from a multi-objective design optimisation carried out previously in subsection 6.2.2. The first case design parameters corresponded to the maximum mass flow rate design from the Pareto optimal set whereas the second case corresponded to the chosen compromised design parameters.

A summary of the main conclusions from the chapter are as follows:

- The thrust force achieved at sea-level and design exit Mach number of 2.0 were 139 mN and 47 mN from Design-A and Design-B respectively. A 172 mN of thrust was achieved from Design-A when the device was configured to operate in a vacuum. Those values of thrust suggested the possibility of deploying such a device as a propulsion system on-board current large spacecraft for attitude control and station keeping.

- The predicted value of the Mach number at the nozzle exit from the proposed two steps CD-nozzle numerical simulation appeared to approach the idea design value based on the 1-D compressible flow theory within 5 – 10 % over a range of DeMn 2.0 – 2.4 which is subjected to Design-A and B configurations. A better prediction was obtained in vacuum 1.5 – 4.2 % over the same Mach design range corresponding to Design-A parameter configurations.

- The integration of the CD-nozzle with the microcombustor chamber has led to an increase in chamber operating pressure when the total mass flow rate is kept constant at the inlets of the chamber. Hence, a reduction in flow velocity inside the chamber and the micro-cooling channel. This might cause the flame to propagate upstream (flashback) and/or propellants autoignition inside the cooling channel.

- The proposed geometry modification of the inlets-to-chamber at lower operating mass flow rate than 150 g/hr demonstrated the increase in local flow velocity at the end section of the micro-cooling channel prior to chamber in comparison to the initial design configuration which was intended to be used at high propellants mass flow rate. Therefore, the inlet-to-chamber design parameters should be considered to be of importance when optimising the chamber geometry with the intention to be integrated as a part of a microthruster device. The local velocity should also be considered as a hard design constraint at the interface plane between the micro-cooling channel and the combustor chamber.

The injection of the hydrogen downstream near the end of the micro-cooling channel at a device low operating mass flow rate is proven to be an effective approach to reduce the risk of flashback, autoignition and at the same time achieves a stable combustion inside the microchamber. This approach can be also considered at a higher total mass flow rate as demonstrated by the case study in section 7.11.2.

Chapter 8

Conclusions and future work recommendations

8.1 Conclusions

The development of a multi-objective automated optimisation system to be used for the design optimisation of micro-scale combustion devices is successfully achieved in this work. The system developed integrates a commercial computational fluid dynamics package and a multi-objective variant of the Tabu Search optimisation algorithm, a heuristic optimisation technique that exhibits local search characteristics. The objectives were set to optimise the main micro-scale combustor design characteristics and to satisfy manufacturability considerations from the very beginning of the whole design process.

At the beginning the combustor main design requirements, the design challenges and the design parameters that influence the device performance at a micro-scale were defined and were based on previous literature. Understanding the design requirements and parameter relations with respect to the design objectives and problem design constraints are important factors in establishing the right choice of an optimiser algorithm to be used in navigating the design space, searching for a promising area that improves the objective targets of the problem.

Therefore, the multi-objective variant of the Tabu Search algorithm was chosen based on its past performances in the area of aerodynamic shape optimisation for gas turbine compressor blades, aerofoils and a helical gear pair in helicopter transmission systems, among others. All of these problems have complex, nonlinear and highly constrained design spaces with many local minima which are similar in nature to that of a microcombustor.

Following the previous task, a robust parameterisation scheme, geometry and numerical grid representations were implemented within the optimisation design cycle. These were

achieved by incorporating the knowledge gained from the parametric design study by understanding the design space in a greater detail, identifying the solutions for issues encountered during this design study from geometry overlapping, mesh refinement and mainly studying the influence of the individual parameter on the design objective.

In order to represent a microcombustor device in a real-world application, additional expressions which accurately describe the applied boundary conditions within the numerical model such as the convective and radiative heat losses of the external walls and the variation of the structure material's thermal conductivity with temperature were considered.

The optimisation results of the preliminary case study (chapter 6 – case study 1) of a simple microcombustor design utilising 14 geometrical, two operational design variables and two design constraints demonstrated the improvement achieved in both design objectives using the developed multi-objective optimisation system. The combustor efficiency using premixed hydrogen-air reactants was up by 9.9 %, a huge reduction of 53.4 % in fuel consumption and 41.5 % in overall device volume at chamber exit temperature of 1032 K.

A thermally improved microcombustor design configuration by implementing a micro-cooling channel into the chosen optimum design found from case 1 was investigated in this case (case study 2). The optimisation results represented by the compromised design found from the Pareto-optimal set recorded an increase in efficiency of 1.5 % and a reduction of 10 % in fuel consumption. Those results were also in respect to eight design parameters (five geometrical and three operational) and five design constraints applied throughout the optimisation process.

It was found that the optimisation cost can be reduced if no geometry parameterisation, geometry build and meshing processes involved, as in case study 2–B. Another important measure to reduce the optimisation cost for this type of a problem is to initialise the CFD calculations for the new design with the simulation result obtained from the datum or even the previously investigated design, in which the flow, the heat and the reactant species and their products are well developed within the numerical grid.

The investigation of using alternative fuels to hydrogen was carried out in case study 3 where the hydrocarbons of propane, ethane and butane were numerically tested, applying a single-step reaction and the finite rate chemistry model. Different microcombustor design configurations were considered and finally, a map was constructed describing the hydrocarbon fuels' efficiencies and feasible operating spaces (Table 6-20) using a specific design configuration (Figure 6-18, design D).

Two microcombustor optimum designs chosen from the Pareto front of case study 2 – A, were used in the design of a micro-thruster for space applications. A method was suggested to design a bell-like shape to describe the divergent section of the convergent-divergent nozzle based on the numerical calculations of these microcombustor designs at sea-level. The thrust force achieved at sea-level and design exit Mach number of 2.0 were 47 - 139 mN. A 172 mN of thrust was also achieved from one of the tested designs when the device was configured to operate in a vacuum. Those values of thrust suggested the possibility of deploying such a device as a propulsion system on-board current large spacecraft for attitude control and station keeping. The predicted value of the Mach number at the nozzle exit from the proposed design method appeared to approach the ideal design value based on the one-dimensional compressible flow theory within 5 - 10 % over a range of design exit Mach number 2.0 – 2.4.

Finally, the effect of integrating the CD-nozzle with the microcombustor chamber using the suggested design approach is highlighted and a possible solution was also provided.

8.2 Recommendations for future work

Based on the conclusions of this work, the recommendations for future work related to micro-scale combustions are as follows:

1. The main micro-scale combustors' design characteristics achieved in this work using the developed multi-objective optimisation system can be further enhanced by the integration of a structural analysis package. The additional FEA tool to the MOTS framework as shown in Figure 8-1 results firstly in analysing the structure of a device during the optimisation process for an excepted level of thermal stress which may lead to a structure failure. Secondly, decreasing the combustor's weight, thus decreasing the operating cost by optimising the thickness of the structure walls. The latter is an important measure when the device is to be implemented in propulsion applications. Also, this is encouraged by the fact that the required time to perform the additional analysis is much shorter than that of the reaction and fluid flow calculations and it only requires a structure numerical grid therefore fewer elements in the domain of interest are needed.

2. For better CFD predictions of the fluid flow and reaction behaviour inside a microchamber, the optimum blades of a compressor and a turbine need be included within the microcombustor design either by presenting the boundary conditions implicitly, e.g. by assigning an angle of attack for the air at the inlet and using a specific outlet's cross-sectional area with a height corresponding to turbine blade's

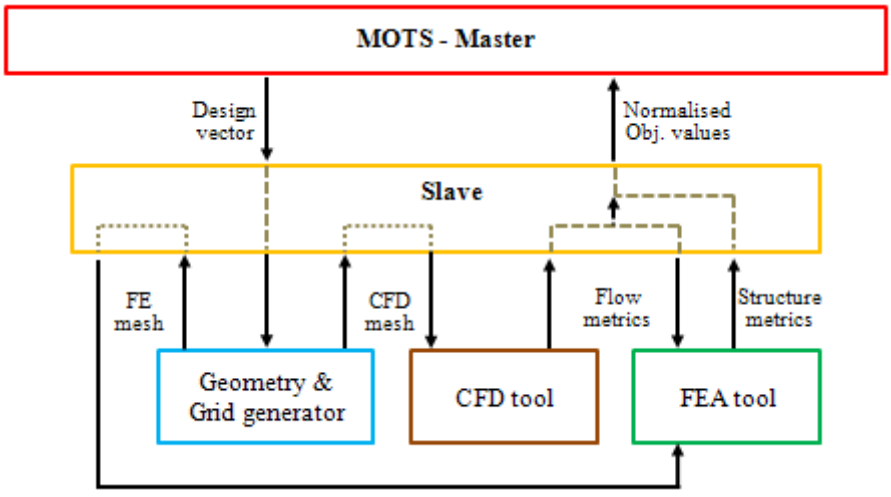

Figure 8-1: MOTS framework including CFD and FEA analyses

height or integrating both geometries within the combustor design. The latter will increase the computational time. Air enters the combustor through the compressor with a specific angle resulting in air swirling. The effect of the swirl on mixing performance might have an impact on the device performance. On the other hand, the turbine blades increase the operating pressure by chocking the exit of the combustor.

3. The thermal conductivity of the structure was identified in literature as an important design parameter for sustaining combustion inside a small chamber. Although the CFD model in this work accounted for the variation of the structure thermal conductivity of stainless steel with temperature, future research and development of the device should investigate different types of materials if the manufacturing process is allowed.

4. A constant surface emissivity value of 0.8 was used throughout the optimisation studies herein to calculate the heat loss of a microchamber external wall by means of radiation. A separate case study was carried out on a simple combustor configuration (baseline design) and the results showed that the combustor efficiency improved by 4 % when the surface emissivity was set to 0.3. Therefore, a reduction in the surface emissivity could be achieved by applying a special layer of coating with low emissivity to the surface of a micro-combustor, which was also suggested by Cao and Xu (2007).

5. The heat loss of a microchamber through the internal walls, specifically the lower wall, can be reduced by applying a similar layer of coating suggested above with lower thermal conductivity compared to that of the structure material or considering a hollow wall design within the structure of a device as shown in Figure 8-2.

6. The numerical study conducted in subsection 7.11.2 suggested that the required

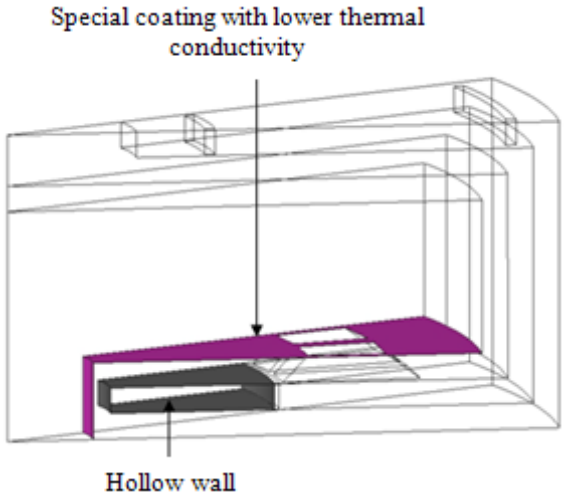

Figure 8-2: Suggested ways to improve heat loss of a chamber

mixing length of the hydrogen fuel with air is short in order to achieve a stable and complete combustion. Also the combustor design configuration found in Figure 6-18 (reactants mixture entering the combustion chamber from the vertical wall) was not suitable for hydrocarbon fuels because of a lengthy reaction time and lower initial enthalpy of the mixture which led to the flame stabilising near the chamber exit. Moreover, it was also found that the design has a lower structure temperature. From the aforementioned, examining a hydrogen-air mixture together with this design configuration and using air injection from the lower wall is a potential candidate for future development.

7. Considering a baffle plate arrangement similar to that studied in Appendix B-(B-3) in the design of a microcombustor for reactants mixture enhancement at low Reynolds number.

8. Redesigning the optimum microthruster configuration for producing a lower level of thrust by considering the following:

- Specify low total mass flow rate range
- Use a cross-sectional area of the inlet-to-chamber that exhibited higher local flow velocity to flame speed. The previous could be implemented as a design parameter and the latter as a design constraint.
- Consider the design suggested in subsection 7.11.2 where the fuel was introduced downstream near to the chamber inlet.

9. Designing a robust ignition device to allow a microcombustor to re-light at different altitudes. The design of this part and the suggestion provided by Mehra (2000) could be used as a starting point in future development.

10. Considering the optimisation of recirculation zones inside the combustion chamber, this may require the inner surfaces of a chamber to be represented by B-spline or similar curves rather than simple linear elements, so that the control points of these curves can be used as additional optimisation design parameters.

11. Deploying a range of thermal expansion and other properties such as the Young's Modulus as optimisation parameters, may potentially result in definition of a unique material for use in the design of a microcombustor.

The author's publications

Saddawi, S.D., Kipouros, T. and Savill, A.M., (2012), *Computational Engineering Design for Micro-Scale Combustors*, Proceedings of ASME Turbo Expo, Copenhagen, Denmark. Paper No. GT2012-69522.

Saddawi, S.D., Kipouros, T. and Savill, A.M., (2013), *Computational Engineering Design for Micro-Scale Combustion Devices: A Thermally Improved Configuration*, Proceedings of ASME Turbo Expo 2013, San Antonio, Texas, USA. GT2013-94599.

D'ammaro, A., Kipouros, T., **Saddawi, S.D**. and Savill, A.M., (2010), *Computational Design for Micro Fluidic Devices Using Lattice Boltzmann and Heuristic Optimisation Algorithms*, Proceedings of Joint OCCAM/ICFD Lattice Boltzmann Workshop, Oxford, UK.

References

Alexeenko, A.A., Levin, D.A., Gimelshein, S.F., Collins, R.J. and Reed, B.D., (2002), *Numerical modeling of axisymmetric and three-dimensional flows in microelectromechanical systems nozzles*, AIAA, Vol. 40, No. 5, 897-904.

Al-Shemmeri, T.T., (1990), *Energy Management*, Module notes, Staffordshire University, England, UK.

Al-Sultan, K.S. and Al-Fawzan, M.A., (1997), *A tabu search Hooke and Jeeves algorithm for unconstrained optimization*, European Journal of Operational Research, Vol. 103, Issue 1, pp. 198-208.

Anderson, J.D., (2004), *Modern compressible flow : with historical perspective*, 3rd. ed., international ed., McGraw-Hill. Boston.

ANSYS Inc., (2009a), *ANSYS CFX 12.1 user manual*.

ANSYS Inc., (2009b), *ANSYS FLUENT 12.1.4 : chemical reactions library*.

Attia, U.M., Marson, S. and Alcock, J.R., (2009), *Micro-injection moulding of polymer microfluidic devices*, Microfluidics and nanofluidics, Vol. 7, Issue 1, pp. 1-28.

Attia, U.M., (2011), *Personal communication*, Cranfield University, England, UK.

Attia, U.M. and Alcock, J.R., (2011), *A review of micro-powder injection moulding as a microfabrication technique*, Journal of Micromechanics and Microengineering 21, art. No 043001.

Attia, U.M. and Alcock, J.R., (2012), *Fabrication of Hollow, 3D, micro-scale metallic structures by micro-powder injection moulding*, Journal of Materials Processing Technology, Vol. 212, Issue 10, pp 2148-2153.

Bäck, T., Fogel, D.B. and Michalewics, Z., (1997), *Handbook of evolutionary computation*, Bristol : Institute of Physics Publishing ; New York ; Oxford : Oxford University Press. ISBN:0750303921.

Baukal, C.E., (2001), *The John Zink Combustion Handbook*, CRC Press, ISBN: 0849323371.

Bayt, R. and Breuer, K., (2001), *Systems Design and Performance of Hot and Cold Supersonic Microjets*, 39th AIAA Aerospace Sciences Meeting and Exhibit. Reno, Nevada. Paper No. AIAA-2001-0721.

Bayt, R.L., Ayon, A.A. and Breuer, K.S., (1997), *A Performance Evaluation of MEMS-based Micronozzles*, AIAA 1997-3169.

Beattie, J.R., Williams, J.D. and Robson, R.R., (1993), *Flight Qualification of an 18-mN Xenon Ion Thruster*, AIAA, AHS, and ASEE, Aerospace Design Conference, Irvine, CA.

Benson, T. (2012), *NASA Glenn Research Center: Compressible Aerodynamics index*, available at: http://www.grc.nasa.gov/WWW/k-12/airplane/shortc.html (accessed 2012/October/14).

Bianchi, L., Dorigo, M., Gambardella, L.M. and Gutjahr, W.J., (2009), *A survey on metaheuristics for stochastic combinatorial optimization*, Natural Computing, Vol. 8, Issue 2, pp 239-287.

Bloor, M.I.G. and Wilson, M.J., (1989), *Generating blend surfaces using partial differential equations*, Journal of Computer-Aided Design, Vol. 21, No. 3, 165-171.

Blum, C. and Roli, A., (2003), *Metaheuristics in Combinatorial Optimization: Overview and Conceptual Comparison*, ACM Computing Surveys, Vol. 35, No. 3, pp. 268–308.

Buche, D., Stoll, P. and Koumoutsakos, P., (2001), *An evolutionary algorithm for multi-objective optimization of combustion processes*, Center for Turbulence Research Annual Research Briefs 2001 pp. 231–239.

Butler, M.S., Moran, C.W., Sunderland, P.B. and Axelbaum, R.L., (2009), *Limits for hydrogen leaks that can support stable flames*, International Journal of Hydrogen Energy, Vol. 34, Issue 12, pp. 5174-5182.

Cao, H.L. and Xu, J.L., (2007), *Thermal performance of a micro-combustor for micro-gas turbine system*, Journal of Energy Conversion and Management. Vol. 48, Issue 5, 1569-1578.

Catalano, L.A., Dadone, A., Manodoro, A. and Saponaro, A., (2006), *Efficient design optimization of duct-burners for combined-cycle and cogenerative plants* , Engineering Optimization, Vol. 38, Issue 7, pp. 801-820.

Cengal, Y.A. and Boles, M.A., (2002), *Thermodynamics: an engineering approach*, 4th ed., McGraw-Hill companies, Inc. New York, US. ISBN: 0-07-1238332-1.

Chelouah, R. and Siarry, P., (2000), *Tabu Search applied to global optimization*, European Journal of Operational Research, Vol. 123, Issue 2, pp. 256–270.

Conner, A.M. and Tilley, D.G., (1998), *A Tabu search method for the optimization of fluid power circuits*, Proceedings of the Institution of Mechanical Engineers, Part I: Journal of Systems and Control Engineering, Vol. 212, No., 5, pp. 373-381.

D'ammaro, A., (2010), *Computational Design for Micro Fluidic Devices Using Lattice Boltzmann and Heuristic Optimisation Algorithms*, MSc Thesis, Cranfield University, England, UK.

D'souza, N.T., (2008), *Design optimisation of helical gear pair in helicopter transmission systems*, M.Sc. Thesis, Cranfield University, UK.

D'ammaro, A., Kipouros, T., Saddawi, S.D. and Savill, A.M., (2010), *Computational Design for Micro Fluidic Devices Using Lattice Boltzmann and Heuristic Optimisation Algorithms*, Proceedings of Joint OCCAM/ICFD Lattice Boltzmann Workshop, Oxford, UK.

Dantzig, G.B. and Thapa, M.N., (1997), *Linear Programming, 1:Introduction*, Springer, ISBN-10: 0387948333.

Daou, J. and Matalon, M., (2002), *Influence of Conductive Heat-Losses on the Propagation of Premixed Flames in Channels*, Combustion and Flame, Vol. 128, Issue 4, pp. 321-339.

Davy, H., (1816), *On the Fire-Damp of Coal Mines, and on Methods of Lighting the Mines So as to Prevent Its Explosion*, Philosophical Transactions of the Royal Society of London , Vol. 106, pp. 1-22.

Davy, H., (1817), *Some Researches on Flame*, Philosophical Transactions of the Royal Society of London , Vol. 107, pp. 45-76.

Dawes, W.N., Kellar, W.P., Harvey, S.A., Dhanasekaran, P.C., Savill, A.M. and Cant, R.S., (2003), *Managing the Geometry is Limiting the Ability of CFD to Manage the Flow*, 33rd AIAA Fluid Dynamic Conference, Orlando, FL, AIAA Paper 2003-3732.

deGroot, W.A., Maloney, T.M. and Vanderaar, M.J., (1998), *Power, Propulsion, and Communications for Microspacecraft Missions*, NASA/CR-1998-206607.

deGroot, W.A., (1998), *Propulsion Options for Primary Thrust and Attitude Control of Microspacecraft*, NASA/CR-1998-206608.

Despierre, A., Stuttaford, P.J. and Rubini, P.A., (1997), *Gas turbine combustor design using genetic algorithms*, Int. Gas Turbine and Aeroengine Congress & Exhibition, Orlando, Florida, ASME Paper 97-GT-72.

Djenidi, L. and Moghtaderi, B., (2006), *Numerical investigation of laminar mixing in a coaxial microreactor*, Journal of Fluid Mechanics, Vol. 568, No. 1, pp. 223-242.

Edwards, K., Edgar, T.F. and Manousiouthakis, V.I., (1998), *Kinetic model reduction using genetic algorithms*, Computers & Chemical Engineering, Vol. 22, Issues 1–2, pp. 239-246.

Epstein, A.H., Senturia, S.D., Al-Midani, Q., Anathasuresh, G., Ayon, A., Breuer, K., Chen, K., Ehrich, F.E., Esteve, E., Frechette, L., Gauba, G., Ghodssi, R., Groshenry, C., Jacobson, S., Kerrebrock, J.L., Lang, J.H., London, A., Lopata, J., Mehra, A., Mur Miranda, J.O., Nagle, S., Orr, D.J., Piekos, E., Schmidt, M.A., Shirley, G., Spearing, S.M., Tan, C.S., Tzeng, Y. and Waitz, I.A., (1997), *Micro-Heat Engines, Gas Turbines, and Rocket Engines –the MIT Microengine Project*, 28th AIAA, Fluid Dynamics Conference.

Fernandez-Pello, A.C., (2002), *Micro-Power Generation Using Combustion: Issues and Approaches*, Proceedings of the Combustion Institute, Vol. 29, Issue 1, pp. 883–899.

Foli, K., Okabe, T., Olhofer, M., Jin, Y. and Sendhoff, B., (2006), *Optimization of micro heat exchanger: CFD, analytical approach and multi-objective evolutionary algorithms*, International Journal of Heat and Mass Transfer, Vol. 49, Issues 5–6, pp. 1090–1099.

Forrester, A., Sobester, A. and Keane, A., (2008), *Engineering Design via Surrogate Modelling: A Practical Guide*, 1st ed., Wiley, ISBN: 0470060689.

Glassman, I., (1987), *Combustion*, 2nd ed., Academic Press Inc, Florida. ISBN: 0-12-285851-4.

Glassman, I., (2008), *Combustion*, 4th ed., Elsevier Inc. ISBN: 978-0-12-088573-2.

Glover, F., (1986), *Future paths for integer programming and links to artificial intelligence*, Computers & Operations Research, Vol. 13, Issue 5, pp. 533-549.

Grisnik, S.P., Smith, T.A. and Saltz, L.E., (1987), *Experimental Study of Low Reynolds Number Nozzles*, 19th AIAA/DGLR/JSASS International Electric Propulsion Conference, Colorado Springs, Colorado. Paper No. AIAA-87-0992.

Groshenry, C., (1995), *Preliminary Design Study of a Micro-Gas Turbine Engine*, S.M. Thesis, , Massachusetts Institute of Technology, USA.

Harvey, S.A., (2002), *The Design Optimisation of Turbomachinery Blade Rows*, Ph.D. Thesis, University of Cambridge, England, UK.

Hedar, A.R. and Fukushima, M., (2004), *Heuristic pattern search and its hybridization with simulated annealing for nonlinear global optimization*, Optimization Methods and Software, Vol. 19, Issue 3-4, 291-308.

Hedar, A.R. and Fukushima, M., (2006), *Tabu Search directed by direct search methods for nonlinear global optimization*, European Journal of Operational Research, Vol. 170, Issue 2, pp. 329-349.

Holman, P.J., (2002), *HEAT TRANSFER*, 9th ed., McGraw-Hill companies, Inc. New York, US. ISBN: 0-07-112230-3.

Hua, J., Wu, M. and Kumar, K., (2005a), *Numerical simulation of the combustion of hydrogen–air mixture in micro-scaled chambers Part II: CFD analysis for a micro-combustor*, Chemical Engineering Science, Vol. 60, Issue 13, pp. 3507–3515.

Hua, J., Wu, M. and Kumar, K., (2005b), *Numerical simulation of the combustion of hydrogen–air mixture in micro-scaled chambers. Part I: Fundamental study*, Chemical Engineering Science, Vol. 60, Issue 13, pp. 3497-3506.

Huang, W.M., Vosen, S.R. and Greif, R., (1986), *Heat Transfer During Laminar Flame Quenching : Effect of Fuels*, Twenty-first Symposium (International) on Combustion/The Combustion Institute, pp. 1853-1860.

Iki, N., Gruber, A. and Yoshida, A., (2008), *A Numerical and an experimental study for optimization of a small annular combustor*, Journal of Power and Energy System, Vol. 2, Issue 3, pp. 921-933.

Isomura, K., Tanaka, S., Togo, S.-. and Kanebako, H., (2005), *Development of Micromachine Gas Turbines at Tohoku University*, Micro Gas Turbines, Educational Notes RTO-EN-AVT-131, pp. 10-1 – 10-34.

Ivanov, M.S., Markelov, G.N., Ketsdever, A.D. and Wadsworth, D.C., (1999), *Numerical Study of Cold Gas Micronozzle Flows*, AIAA 1999-0166.

Jaeggi, D.M., Parks, G.T., Kipouros, T. and Clarkson, P.J., (2005), *A multi-objective tabu search algorithm for constrained optimisation problems*, Evolutionary Multi-Criterion Optimization, LNCS, Vol. 3410, pp. 490-504, Springer Berlin/Heidelberg.

Jaeggi, D.M., Parks, G.T., Kipouros, T. and Clarkson, P.J., (2008), *The development of a multi objective Tabu searchalgorithm for continuous optimization problems*, European Journal of Operational Research, Vol. 185, Issue 3, pp. 1192_1212.

Janiga, G. and Thevenin, D., (2007), *Reducing the CO emissions in a laminar burner using different numerical optimization methods*, Proceedings of the Institution of

Mechanical Engineers, Part A: Journal of Power and Energy, Vol. 221, No. 5, pp. 647-655.

Jejurkar, S.Y. and Mishra, D.P., (2009), *A review of recent patents on micro-combustion and applications*, Recent Patents on Engineering, Kings Norton Library, UK. 3, 194-209.

Jejurkar, S.Y. and Mishra, D.P., (2010), *Numerical characterization of a premixed flame based annular microcombustor*, International Journal of Hydrogen Energy, Vol. 35, Issue 18, pp. 9755-66.

Jejurkar, S.Y. and Mishra, D.P., (2011), *Thermal performance characteristics of a microcombustor for heating and propulsion*, Applied Thermal Engineering, Vol. 31, Issue 4, pp. 521-527.

Jones, M., Curnock, P., Bradbrook, S.J. and Brich, N., (2001), *Evolutions in Aircraft Engine Design and Vision for the Future*, Fifteenth International Symposium on Air Breathing Engines. Bangalore, India. Cited in Rogero (2003).

Ju, Y. and Maruta, K., (2011), *Microscale combustion: Technology development and fundamental research*, Progress in Energy and Combustion Science, Vol. 37, Issue 6, pp. 669-715.

Kaisare, N.S. and Vlachos, D.G., (2007), *Optimal reactor dimensions for homogeneous combustion in small channels*, Catalysis Today, Vol. 120, Issue 1, pp. 96-106.

Kim, S.C., (1994), *Calculations of Low-Reynolds-Number Resistojet Nozzles*, Journal of Spacecraft and Rockets. Vol. 31, No. 2, 259-264.

Kipouros, T., (2006), *Multi-objective Aerodynamic Design Optimisation*, Ph.D. Thesis, University of Cambridge, England, UK.

Kipouros, T., Jaeggi, D.M., Dawes, W.N., Parks, G.T., Savill, A.M. and Clarkson, P.J., (2008), *Biobjective Design Optimization for Axial Compressors Using Tabu Search*, AIAA Journal, Vol. 46, No. 3, pp. 701-711.

Köhler, J., Bejhed, J., Kratz, H., Bruhn, F., Lindberg, U., Hjort, K. and Stenmark, L., (2002), *A hybrid cold gas microthruster system for spacecraft*, Sensors and Actuators A: Physical. Vol. 97-98, 587-598.

Koziel, S. and Yang, X.S., (2011), *Computational Optimization, Methods and Algorithms*, Studies in Computational Intelligence, Vol. 356, ISBN: 9783642208584.

Kundu, P., Bhattacharyya, T.K. and Das, S., (2012), *Design, fabrication and performance evaluation of a vaporizing liquid microthruster*, J. Micromech. Microeng. Vol. 22, No. 2, 025016 (15pp).

Kuo, C.H. and Ronney, P.D., (2007), *Numerical modeling of non-adiabatic heat-recirculating combustors*, Proceedings of the Combustion Institute, Vol. 31, Issue 2, pp. 3277–3284.

Larangot, B., Conédéra, V., Dubreuil, P., Do Conto, T. and Rossi, C., (2002), *Solid Propellant MicroThruster : an alternative propulsion device for nanosatellite*, Presented at Aerospace Energetics Equipment, Avignon (France), 12–14 Nov 2002.

Lefebvre, A.H., (1998), *Gas turbine combustion*, 2nd ed., Taylor & Francis, Philadelphia, PA, pp. 340 cited in Motsamai et al. (2008).

Lefebvre, A.H. and Norster, E.R., (1968), *The Design of Tubular Gas Turbine Combustion Chambers for Optimum Mixing Performance*, Proceedings of the Institution of Mechanical Engineers, Conference Proceedings, Vol. 183, No. 14, pp. 150-155.

Lewis, R.M., Torczon, V. and Trosset, M.W., (2000), *Direct Search Methods:Then and Now*, Journal of Computational and Applied Mathematics, Vol. 124, No. 1, pp. 191–207, Cited in Kipouros et al. (2008).

Li, J., Chou, S.K., Huang, G., Yang, W.M. and Li, Z.W., (2009a), *Study on premixed combustion in cylindrical micro combustors: Transient flame behavior and wall heat flux*, Experimental Thermal and Fluid Science, Vol. 33, Issue 4, pp. 764-773.

Li, J., Chou, S.K., Li, Z.W. and Yang, W.M., (2009b), *Characterization of wall temperature and radiation power through cylindrical dump micro-combustors*, Combustion and Flame, Vol. 156, Issue 8, pp.1587-1593.

Li, J., Chou, S.K., Yang, W.M. and Li, Z.W., (2009c), *A numerical study on premixed micro-combustion of CH4–air mixture: Effects of combustor size, geometry and boundary conditions on flame temperature*, Chemical Engineering Journal, Vol. 150, Issue 1, pp. 213-222.

Lin, C.X. and Gadepalli, V.V.V., (2009), *A computational study of gas flow in a De-Laval micronozzle at different throat diameters*, Int. J. Numer. Meth. Fluids. Vol. 59, Issue 11, 1203–1216.

London, A.P., (2000), *Development and test of a microfabricated bipropellant rocket engine*, Ph.D. Thesis, Massachusetts Institute of Technology, Cambridge, MA, USA.

London, A.P., Ayón, A.A., Epstein, A.H., Spearing, S.M., Harrison, T., Peles, Y. and Kerrebrock, J.L., (2001a), *Microfabrication of a high pressure bipropellant rocket engine*, Sensors and Actuators A: Physical. Vol. 92, issue 1-3, 351-357.

London, A.P., Epstein, A.H. and Kerrebrock, J.L., (2001b), *High-Pressure Bipropellant Microrocket Engine*, Journal of Propulsion and Power, Vol. 17, No. 4, 780-787.

Marcuccio, S., Genovese, A. and Andrenucci, M., (1998), *Experimental Performance of Field Emission Microthrusters*, Journal of Propulsion and Power. Vol. 14, No. 5, 774-781.

Mattingly, J.D., (1996), *Elements of Gas Turbine Propulsion*, McGraw-Hill Inc., U.S.A, cited in Stuttaford (1997).

Maurya, D.K., Das, S. and Lahiri, S.K., (2005), *Silicon MEMS vaporizing liquid microthruster with internal microheater*, J. Micromech. Microeng., Vol. 15, No. 5, 966–970.

Mehra, A., (2000), *Development of a high power density combustion system for a silicon micro gas turbine engine*, Ph.D. Thesis, MIT, Cambridge, USA.

Mehra, A., Ayon, A.A., Waitz, I.A. and Schmidt, M., (1999), *Microfabrication of high-temperature silicon devices using wafer bonding and deep reactive ion etching*, Journal of Microelectromechanical Systems, Vol. 8, Issue 2, 152-160.

Mehra, A., Zhang, X., Ayon, A.A., Waitz, I.A., Schmidt, M.A. and Spadaccini, C.M., (2000), *A Six-Wafer Combustion System for a Silicon Micro Gas Turbine Engine*, Journal of Microelectromechanical System, Vol. 9, No. 9, pp. 517-27.

Moghtaderi, B., Shames, I. and Djenidi, L., (2006), *Microfluidic characteristics of multi-holed baffle plate micro-reactor* , International Journal of Heat and Fluid Flow. Vol. 27, No. 6, pp. 1069-1077.

Morash, D.H. and Stand, L., (1994), *Miniature Propulsion Components for the Pluto Fast Fly by Spacecraft*, 30th AIAA/ASME/SAE/ASEE Joint Propulsion Conference, Indianapolis, IN, USA. Paper No. AIAA 1994-3374.

Motsamai, O.S., Visser, J.A. and Morris, R.M., (2008), *Multi-disciplinary design optimization of a combustor*, Journal of Engineering Optimization, Vol. 40, No. 2, 137–156.

Mueller, J., (1997), *Thruster Options for Microspacecraft: A Review and Evaluation of Existing Hardware and Emerging Technologies*, AIAA 1997-3058.

Mueller, J., Chakraborty, I., Bame, D., Tang, W., Lawton, R. and Wallace, A.P., (1998), *Proof-of-Concept Demonstration of a Vapoizing Liquid Micro-Thruster*, AIAA 1998-3924.

Mueller, J., Marrese, C., Polk, J., Yang, E., Green, A., White, V., Bame, D., Chakraborty, I., Vargo, S. and Reinicke, R., (2001), *An overview of MEMS-based micropropulsion developments at JPL*, IAAA Symposium for Small Satellite for Earth Observation. Berlin, Germany.

Mueller, J., Tang, W.C., Wallace, A.P., Li, W., Bame, D., Chakraborty, I. and Lawton, R., (1997), *Design, Analysis and Fabrication of a Vaporizing Liquid Micro-Thruster*, AIAA 1997-3054.

Murthy, J.N., (1988), *Gas Turbine Combustor Modelling For Design*, Ph.D. Thesis, Cranfield University, England, UK.

Myers, R.H., Montgomery, D.C. and Anderson-Cook, C.M., (2009), *Response Surface Methodology: Process and Product Optimization Using Designed Experiments*, 3rd ed., Wiley-Blackwell, ISBN: 0470174463.

NASA (2010), *The Nano-Satellite Launch Challenge*, available at: http://www.spaceflorida.gov/nano-sat-launch-challenge (accessed 2012/October/14).

NASA Glenn Research Center, (2004), *Pulsed Plasma Thrusters*, NASA Facts Publications. Doc. No. FS–2004–11–023–GRC.

NASA JPL (2012), *DAWN Mission : Ion Propulsion*, available at: http://dawn.jpl.nasa.gov/mission/ion_prop.asp (accessed 2012/October/15).

NASA Science (2012), *Space Technology 5 (ST5)*, available at: http://science.nasa.gov/missions/st5/ (accessed 2012/October/14).

Norton, D.G. and Vlachos, D.G., (2003), *Combustion characteristics and flame stability at the microscale: a CFD study of premixed methane/air mixtures*, Chemical Engineering Science, Vol. 58, Issue 21, pp. 4871–4882.

Norton, D.G. and Vlachos, D.G., (2004), *A CFD study of propane/air microflame stability*, Combustion and Flame, Vol. 138, Issue 1, pp. 97-107.

Ono, S. and Wakuri, Y., (1977), *An Experimental Study on the Quenching of Flame by Narrow Cylindrical Passage*, Bulletin of the JSME, Vol. 20, No. 147, pp. 1191-1198.

Paschereit, C.O., Schuermans, B. and Buche, D., (2003), *Combustion Process Optimisation Using Evolutionary Algorithm*, Proccedings of ASME Turbo Expo, Atalanta, USA.

Polzin, K.A., Raitses, Y., Gayoso, J.C.N. and Fisch, J., (2010), *Comparisons in Performance of Electromagnet and Permanent-Magnet Cylindrical Hall-Effect Thrusters*, 46th AIAA/ASME/SAE/ASEE Joint Propulsion Conference & Exhibit. Nashville, TN. Paper No. AIAA 2010-6695.

prEN1993-1-2, (2003), *Eurocode 3: Design of Steel Structures. Part 1.2:General Rules _ Structural Fire Design*, Commission of European Communities, Brussels. Cited in:

http://www.mace.manchester.ac.uk/project/research/structures/strucfire/materialInFire/Steel/references.htm?p=4|#18.

Raimondeau, S., Norton, D.G., Vlachos, D.G. and Masel, R.I., (2002), *Modeling of High-Temperature Microburners*, Proceedings of the Combustion Institute, Vol. 29, Issue 1, pp. 901-907.

Rao, S.S., (2009), *Engineering optimization : theory and practice*, 4th ed., John Willey & Sons, ISBN: 9781615831791.

Rhee, M.S., Zakrzwski, C.M., Thomas, M.A. and Bauer, F.H., (2000), *Highlights of Nanosatellite Development Program at NASA-Goddard Space Flight Center*, Small Satellites, 14th, Logan, UT, USA. Report/Patent No. SSC00-X-5.

Rinz, A. and Mongia, H.C., (1986), *Gas turbine combustor design methodology*, Proceedings of AIAA conference. Cited in Motsamai et al. (2008).

Robinson, C. and Smith, D.B., (1984), *The auto-ignition temperature of methane*, Journal of Hazardous Materials, Vol. 8, Issue 3, pp.199-203.

Rogero, J.M., (2003), *A genetic algorithms based optimisation tool for the preliminary design of gas turbine combustors* , Ph.D. Thesis, Cranfield University, England, UK.

Ronney, P.D., (2003), *Analysis of non-adiabatic heat-recirculating combustors*, Combustion and Flame, Vol. 135, Issue 4, pp. 421–439.

Rossi, C., (2002), *Micropropulsion for Space –A Survey of MEMS-based Micro Thrusters and their Solid Propellant Technology*, Sensors Update. Vol. 10, Issue 1, 257–292.

Rossi, C., Do Conto, T., Estève, D. and Larangot, B., (2001), *Design, fabrication and modelling of MEMS-based microthrusters for space application*, Smart Mater. Struct., Vol. 10, No. 6, 1156–1162.

Rothe, D.E., (1971), *Electron-Beam Studies of Viscous Flow in Supersonic Nozzles*, AIAA Journal, Vol. 9, Issue 5, 804-811.

Sederberg, T.W. and Parry, S.R., (1986), *Free-form deformation of solid geometric models*, ACM SIGGRAPH Computer Graphics, Vol. 20, Issue. 4, 151-160.

Shabanian, S.R., Rahimi, M., Khoshhal, A. and Alsairafi, A.A., (2010), *CFD Study on Hydrogen-Air Premixed Combustion in a Micro Scale Chamber*, Iran J. Chem. Chem. Eng. Vol. 29, No. 4, pp. 161-172.

Shan, X.C., Wang, Z.F., Jin, Y.F., Wu, M., Hua, J. and Wong, C.K., (2005), *Studies on a micro combustor for gas turbine engines*, Journal of Micromechanics and Microengineering. Vol. 15, issue 9, 215-221.

Singh, R., (2008), *Design Optimisation of Aircraft Turbo cooler System*, MSc Thesis, Cranfield University, England, UK.

Sitzki, L., Borer, K., Schuster, E. and Ronney, P.D., (2001), *Combustion in Microscale Heat-Recirculating Burners*, The Third Asia-Pacific Conference on Combustion, Seoul, Korea.

Sjostrand, M. and D'Angelo, Y., (2011), *Compressible Direct Numerical Simulation of a Mesoscale Combustor*, Proceedings of the European Combustion Meeting, Cardiff, UK.

Spadaccini, C.M., (2004), *Combustion System for Power-MEMS Applications*, Ph.D. Thesis, MIT, Cambridge, USA.

Spadaccini, C.M., Mehra, A. and Zhang, X., (2002a), *High power density silicon combustion system for micro gas turbine engine*, Journal of Engineering for Gas Turbines and Power, Vol. 125, No. 3. 709-719.

Spadaccini, C.M., Mehra, A., Lee, J., Zhang, X., Lukachko, S. and Waitz, I.A., (2002b), *High Power Density Silicon Combustion Systems for Micro Gas Turbine Engines*, Proceedings of ASME TURBO EXPO 2002, Amsterdam, The Netherlands. GT-2002-30082.

Srinivas, N. and Deb, K., (1994), *Multiobjective optimization using non-dominated sorting ingenetic algorithm*, Evolutionary Computing Vol. 2, No. 3, pp. 221–248.

Ströhle, J. and Myhrvold, T., (2007), *An evaluation of detailed reaction mechanisms for hydrogen combustion under gas turbine conditions*, International Journal of Hydrogen Energy. Vol. 32, issue 1, 125 – 135.

Stuttaford, P.J., (1997), *Preliminary Gas Turbine Combustor Design Using a Network Approach*, Ph.D. Thesis, Cranfield University, England, UK.

Takeno, T., Sato, K. and Hase, K., (1981), *A theoretical study on an excess enthalpy flame*, Eighteenth Symposium (International) on Combustion, Vol. 18, Issue 1, pp 465 - 472.

Thevenin, D. and Janiga, G., (2008), *Optimization and Computational Fluid Dynamics*, Springer, ISBN: 978-3-540-72152-9.

Trapani, G., (2009), *Multi-Objective Optimization of 2D High-Lift Airfoil Configurations using TabuSearch*, MSc Thesis, Cranfield University, England, UK.

Trapani, G., Kipouros, T. and Savill, A.M., (2012), *The Design of Multi-Element Airfoils Through Multi-Objective Optimization Techniques*, CMES: Computer Modeling in Engineering & Sciences, Vol. 88, No. 2, pp. 107-140.

Tuccillo, R. and Cameretti, M.C., (2005), *Combustion and Combustors for MGT Applications*, Micro Gas Turbines, Educational Notes RTO-EN-AVT-131, pp. 5-1 – 5-56.

Tzeng, Y.-S., (1997), *An Investigation of Microcombustion Thermal Phenomena*, S.M. Thesis, Massachusetts Institute of Technology, USA.

University of Leeds (2009), *Hydrogen oxidation mechanism, a subset of the Leeds methane mechanism (v. 1.2)*, available at: http://garfield.chem.elte.hu/Combustion/Combustion.html (accessed 2012/October/15).

Vosen, S.R., Greif, R. and Westbrook, C.K., (1984), *Unsteady Heat Transfer During Laminar Flame Quenching*, Twentieth Symposium (International) on Combustion/The Combustion Institute, pp 75-83.

Waitz, I.A., Gautam, G. and Tzeng, Y.-S., (1998), *Combustors for Micro Gas Turbine Engines*, Journal of Fluids Engineering, Vol. 120, Issue 1, 109-117.

Wang, F.Z., Wu, M., Shan, X.C. and Hua, J.S., (2006), *MEMS-based combustor with hairpin-shape design of gas recirculation channel*, Journal of Microsystem Technologies, Vol.12, Issue 10-11, pp. 993-997.

Weinberg, F.J., Rowe, D.M., Min, G. and Ronney, P.D., (2002), *On Thermoelectric Power Conversion from Heat Recirculating Combustion Systems*, Proceedings of the Combustion Institute, Vol. 29, Issue 1, pp. 941–947.

Whalen, M.V., (1987), *Low Reynolds Number Nozzle Flow Study*, NASA Glenn Research Center, NASA-TM-100130.

Winter, C.J., (1990), *Hydrogen Technologies for Future Aircraft*, Air traffic and the Environment-Background, Tendencies, and Potential Global Atmospheric Effects, Proceedings of the DLR International Colloquium, Bonn, Germany, U. Schumann (Editor), Springer-Verlag cited in Tzeng (1997).

Wolpert, D.H. and Macready, W.G., (1997), *No Free Lunch Theorems for Optimisation*, IEEE Transactions on Evolutionary Computation, Vol. 1, No. 1, pp. 67-82.

Woodfield, P.L., Nakabe, K. and Suzuki, K., (2003), *Numerical study for enhancement of laminar flow mixingusing multiple confined jets in a micro-can combustor*, International Journal of Heat and Mass Transfer, Vol. 46, Issue 14, pp. 2655–2663.

Wu, M. and Lin, P., (2010), *Design, fabrication and characterization of a low-temperature co-fired ceramic gaseous bi-propellant microthruster*, J. Micromech. Microeng. Vol. 20, No. 8, 085026 (11pp).

Yahagi, Y., Sekiguti, M. and Suzuki, K., (2007), *Flow structure and Flame Stability in a Micro Can Combustor with a Baffle Plate*, Applied Thermal Engineering, Vol. 27, Issue 4, pp. 788-794.

Yang, X.-S., (2010), *Engineering Optimization: An Introduction with Metaheuristic Applications*, Hoboken, N.J. : Wiley, ISBN: 9780470582466.

Youssef, H., M Sait, S. and Adiche, H., (2001), *Evolutionary algorithms, simulated annealing and tabu search: a comparative study*, Engineering Applications of Artificial Intelligence, Vol. 14, Issue 2, pp. 167-181.

Zamashchikov, V.V., (1995), *Combustion of gases in thin-walled small-diameter tubes*, Combustion, Explosion and Shock Waves, Vol. 31, No. 1, pp. 20-22.

Appendix A

Fabrication of hollow three-dimensional miniaturized structure

This appendix describes briefly the scheme by which a micro metallic architecture with a 3D cavity can be fabricated using micro-powder injection moulding (μ-PIM) - lost-core approach. The anticipated product of 316L type stainless steel with a cavity of 0.729 mm^3 is approximately 25 times smaller in size to the initial microcombustor chamber cavity design configuration. This manufacturing approach has been carried out and reported for the first time at the School of Applied Science - Cranfield University, UK by Attia and Alcock (2012).

A-1 Description of the product

A preliminary product design using a novel technique of a lost-core was represented by a cube with a fully enclosed 3D cavity. The core of the cube was micro-moulded as a 900 μm -side with radii of 150 μm.

A-2 Description of the manufacturing process

The process undertaken to build the product described above can be summarised in four steps as follows:

- **Step 1**

1. Micro-injection moulding is used to produce a Polyoxymethylene polymer (POM) core.

- **Step 2**

2. POM core is positioned inside another mould according to the intended design using four corner features for fixation in the mould.
3. The mould is over-moulded with powder feedstock to produce a partially enclosed core. The powder feedstock is a mixture of metallic powder and POM, typically 50 – 55 % in volume fraction of metallic powder is used (Attia and Alcock, 2011).
4. The partially enclosed POM core is used as an insert in another mould for full encapsulation by powder feedstock.

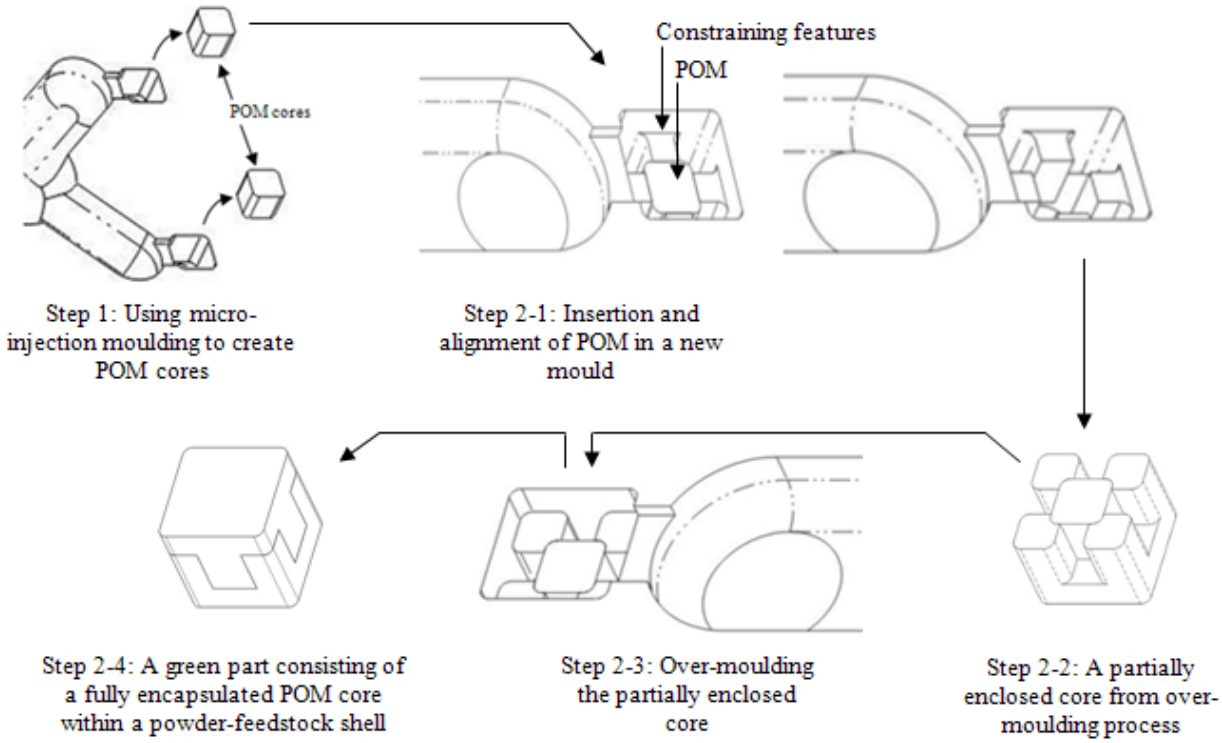

Figure A-1: A schematic of the micro over-moulding process to produce an encapsulated POM core inside a stainless steel shell

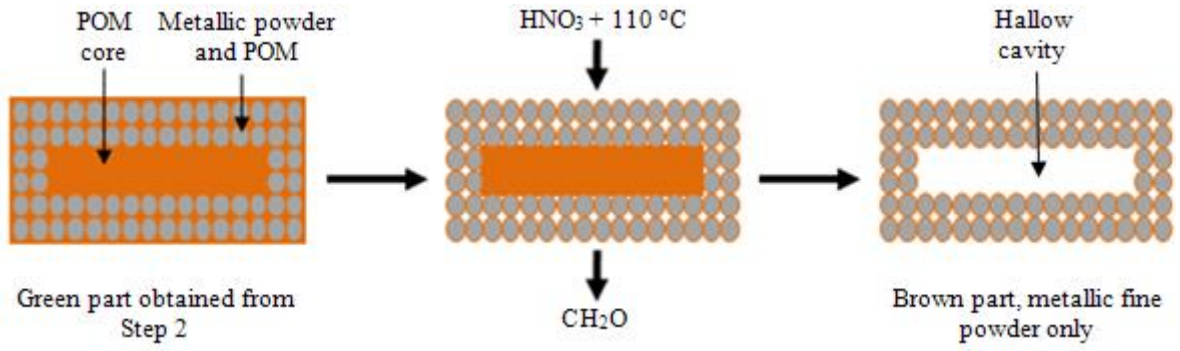

Figure A-2: A schematic of catalytic debinding process

5. The final product of step 2 is a green part consisting of a fully encapsulated POM core within a shell.

The micro over-moulding process undertaken in step 2 is represented schematically in Figure A-1

- **Step 3**

1. In order to remove the POM core and the POM within the encapsulation structure, a catalytic debinding process is deployed. An oven with a temperature of 110 C^o and nitric acid vapor is used. The final product achieved in this step of the process is a brown part which is purely metallic but still in fine powder phase, also the hallow cavity is materialised. A schematic of catalytic debinding is shown in Figure A-2.

- **Step 4**

2. The last stage is sintering which happens in a sintering oven where different elevations of temperatures are used, as illustrated in Table A-1, so that the metallic powder densifies.

The overall micro-powder injection moulding – lost-core approach process in a schematic presentation is shown in Figure A-3.

Table A-1: Sintering schedule

Stage	Schedule
1	From room temperature to 600°C at the rate of 5°C/min
2	Hold at 600°C for 1 h
3	From 600°C to 1250°C at the rate of 3°C/min
4	Hold at 1250°C for 1 h
5	Cooling to room temperature at a rate of 5°C/min

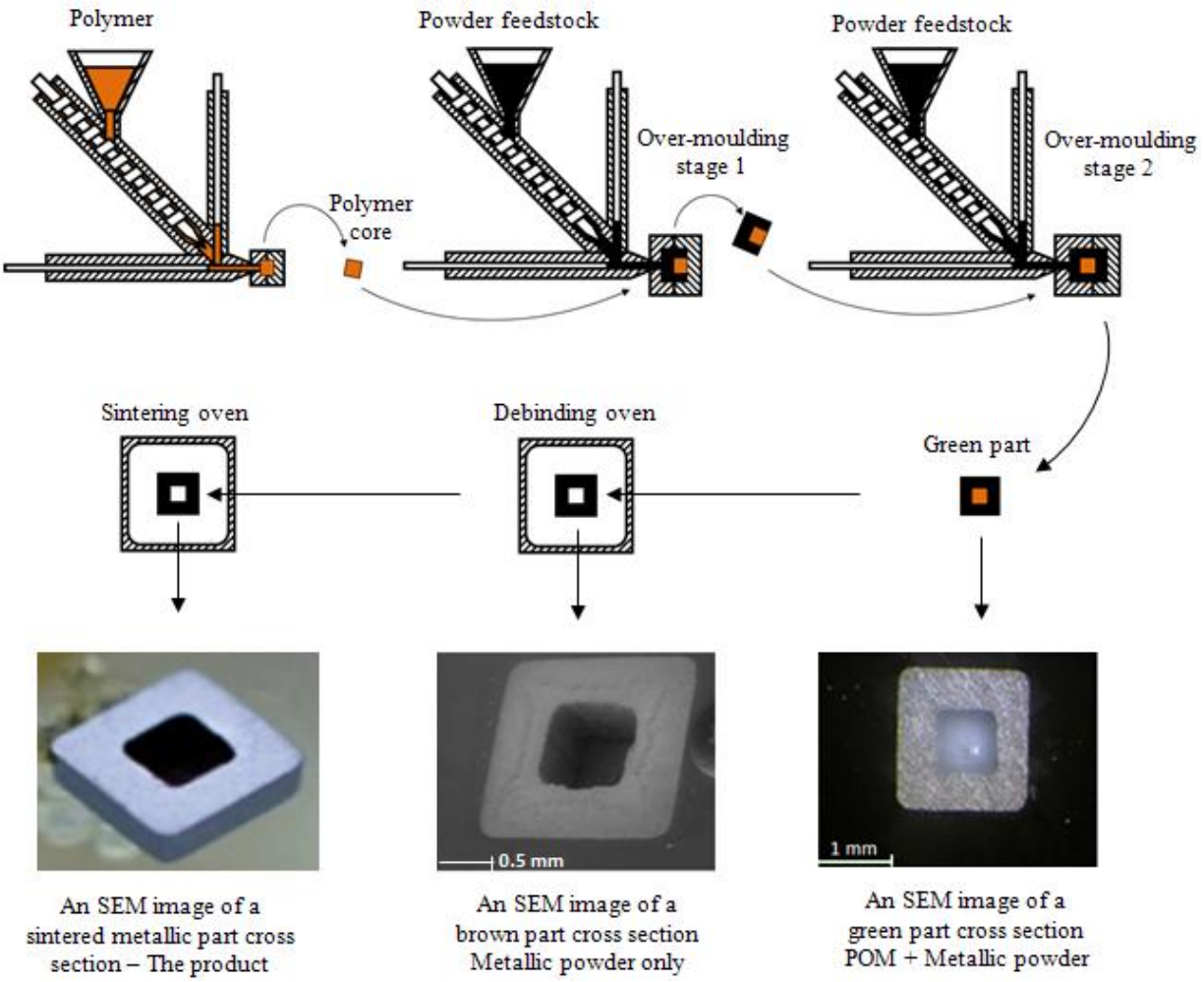

Figure A-3: A schematic of the overall manufacturing process – µPIM - Lost-core approach (Attia, 2011)

A-3 Appendix summary

This appendix described briefly the manufacturing steps by which a micro metallic architecture with 3D cavity was fabricated using micro-powder injection moulding (μPIM) - lost-core approach.

The architecture consisted of a cubic shape with a side 1.9 mm long and a cubical cavity of 900-micron-side. This resulted in a cavity volume which is 25 times smaller in comparison to the initial microcombustor chamber cavity. Therefore, it is feasible to fabricate a stainless steel microcombustor device using this manufacturing approach. In addition, further investigation must be carried out to study the geometry tolerances of the final product at consistent replication accuracy, surface roughness and the possibility of applying an internal and external coating to a microcombustor in order to improve the thermal performance of the device.

Appendix B

Numerical solver validation

This appendix describes the validation of the CFD code integrated within the optimisation system. The performance of the CFD code will be judged based on a results comparison with another well-known CFD solver of ANSYS FLUENT in two case studies and with the experiment results as well as CFD solver of LBM (Lattice Boltzmann Method) in the final case study, where different problems and boundary conditions are considered.

The first case tests the conduction and convection mechanisms capability between the fluid and the solid domains i.e. "*Conjugate Heat Transfer problem"*, where an electronic chip which represents a constant heat generation source is mounted on a flat circuit board. A laminar air stream flows in a confined space over the chip and the board acting as a coolant, thus reducing the temperature of the solid parts. This thermal problem was chosen because of the thermal mechanisms' similarities with a microcombustor device, where the heat source (electronic chip) represents the flame and the air flows inside the duct and the solid parts are similar to the fluid and solid domains found in a microcombustor.

The second case consists of three parts. In part 1, an adiabatic external wall boundary with only the fluid domain of the problem is investigated. Part 2 is similar to part 1 but a convective heat loss to the surroundings is considered. However, in part 3, a convective heat loss from the external wall of the device with both the fluid and the solid domains are numerically investigated.

The last case examines the performance of the CFD code in a laminar mixing in a coaxial jets micro-reactor using a baffle plate problem with diameters as small as 60 μm.

B-1 Test case 1 - Solving a conjugate heat transfer problem

B-1.1 Problem description

Figure B-1 presents the schematic modelling of the problem. This test case and the corresponding numerical solutions can be found at ANSYS FLUENT tutorial guide (ANSYS Inc., 2009b). An electronic chip with a total heat dissipation of 2 W and a

thermal conductivity of 1.0 W/m.K, is mounted on a circuit board which is externally cooled with a heat transfer coefficient of 1.5 W/m^2.K and a thermal conductivity of 0.1 W/m.K. Air used as a coolant with a velocity of 0.5 m/s and 298 K, flows over the board and the chip in a confined space. This resulted in an inlet Reynolds number of 870 approximately thus the flow is treated as laminar. The duct upper wall is externally cooled with a heat transfer coefficient of 1.5 W/m^2.K. Benefiting from the symmetrical configuration of the problem, only one half of the numerical grid was modelled. A structured mesh of 3D hexahedral elements was used to represent the grid which consisted of 87 x 19 x 7 nodes in each direction (x, y and z). The numerical grid is shown in Figure B-2.

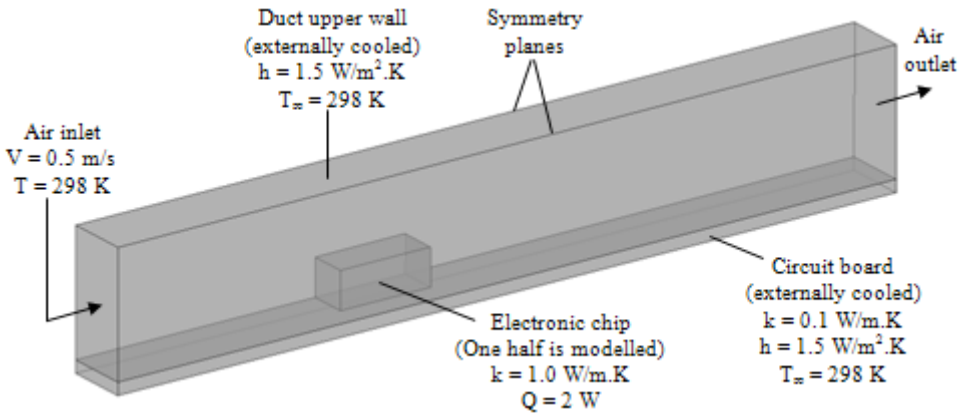

Figure B-1: Schematic of the conjugate heat transfer chip-on-board problem

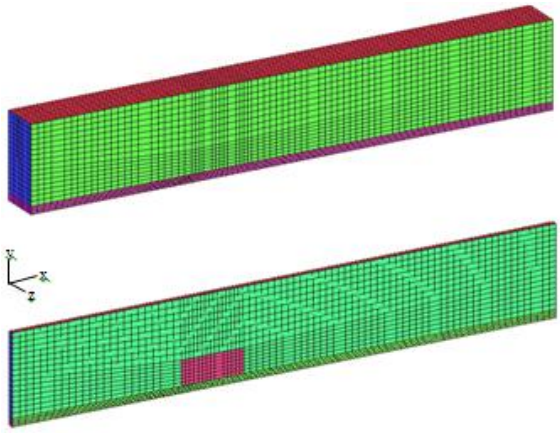

Figure B-2: Test case 1 - The numerical grid. Iso view – Top and x-y section through the chip – Bottom

B-1.2 Results and discussions

The numerical results obtained from the laminar CFD calculations from both CFD codes represented by the temperature, velocity and pressure contours are shown in Figure B-3. The CFX solver results agreed with their counterparts from FLUENT by comparing these results along the flow path. Furthermore, the average flow velocity and temperature, the mass flow rate and total heat transfer calculated at the outlet plane are listed in Table B-1. Again the sets of results agreed well with each other. Further improvement in the calculated value of the heat transfer at the outlet plane can be achieved by increasing the numerical grid size of the problem.

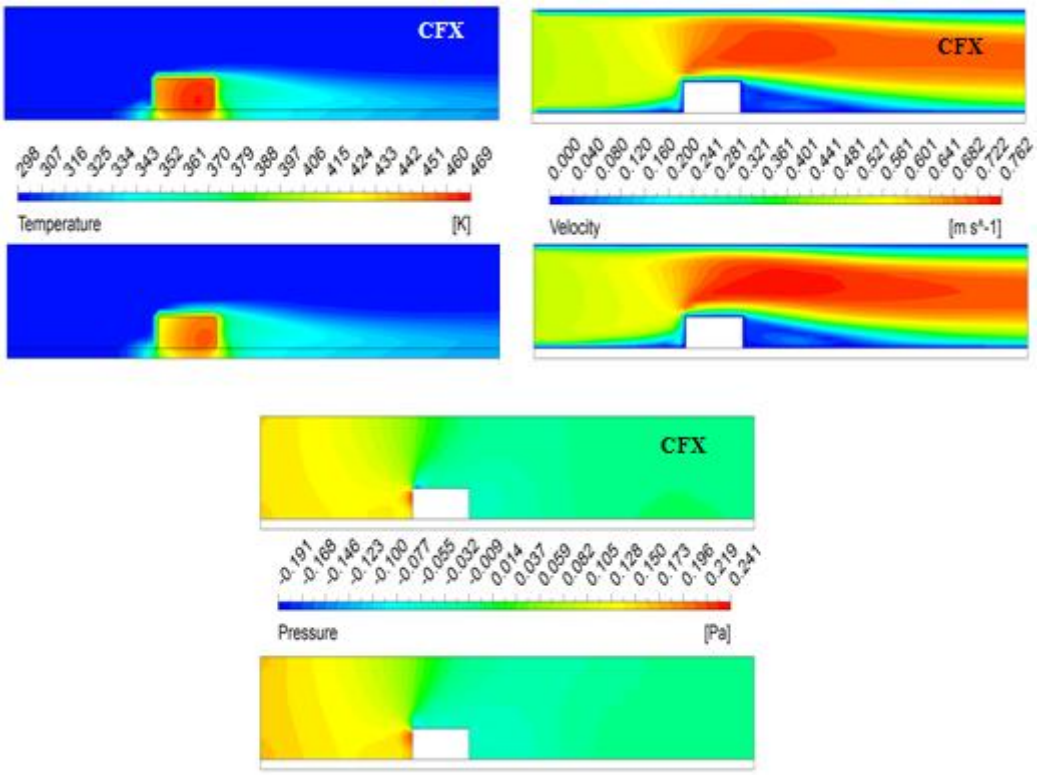

Figure B-3: Numerical results comparisons. Temperature (Top-left), velocity (Top-right) and pressure distribution (Bottom). CFX – Top and FLUENT – Bottom

Table B-1: Results comparison at the outlet plane, CFX vs. FLUENT

Flow metrics of interest at the outlet plane	CFX	FLUENT
Average fluid temperature (K)	302.4	302.5
Average fluid velocity (m/s)	0.601	0.607
Total heat transfer (W)	0.81	0.85
Mass flow rate (g/s)	0.191	0.191

B-2 Test case 2 – Microcombustor baseline design configuration

B-2.1 Problem description

The microcombustor initial design configuration was used in all three parts of this test case, depending on the applied boundary conditions and the numerical domain used. In part one and two, only the fluid domain was implemented, once with an adiabatic external wall and the other with a convective wall of 5 $W/m^2.K$, whereas in the last part both the fluid and the solid with a heat loss from the external wall were used.

3D CFD analysis is carried out using only a 22.5 degree section which represents the main design features. The numerical simulation is executed using the finite rate chemistry (FRC) laminar combustion modelling code and the Eddy dissipation model (EDM) in some parts of the test case. These codes also account for the coupling of heat transfer and fluid dynamics, using a single step hydrogen-air combustion reaction described previously in 6.2.1.2. A hybrid type numerical grid with a total number of elements of 60E+03 for the fluid domain and an unstructured tetrahedral element-type grid for the solid with approximately 92E+03 elements are used. Pre-mixed lean reactants mixture with a total mass flow rate of 2.5E-7 kg/s at a temperature of 300 K and an equivalence ratio of 0.6 is applied at the inlet boundary of the combustor. An outlet type boundary is used to model the combustor exit and the numerical calculations are referenced to a pressure of 1 atm. Moreover, the solid domain of the problem is modelled using the data for a steel material with a density of 8030 kg/m^3, specific heat capacity of 502.48 J/kg.K and a thermal conductivity of 16.27 W/m.K.

B-2.2 Results and discussions

B-2.2.1 Part 1 – Fluid domain with an adiabatic external wall boundary

The temperature results obtained from the CFD evaluations of the CFX and FLUENT codes along the fluid streamlines from the combustor inlet to the outlet are shown in Figure B-4. The prediction of the temperature values from these codes at 92 % of the streamlines were almost the same. A sharp rise in temperature was recorded at the combustion zone by FLUENT compared to CFX of approximately 90 K. On the other hand, the temperature difference between the predicted results of the average flow at the combustor outlet was 2 K.

B-2.2.2 Part 2 – Fluid domain with a convective external wall boundary

The combustor's initial design configuration using the fluid domain with a convective external wall boundary was modelled in this part. The CFX – FRC and EDM combustion model results were compared with their FLUENT counterparts, where the temperature distribution along the fluid path from the inlet to the combustor outlet represented by the streamlines is shown Figure B-5. Again, the numerical results predicted by the CFD codes along 88 % of the streamlines after the combustion zone are within 10 K and importantly the temperature difference is 3 K approximately between the CFX–FRC and FLUENT-FRC models.

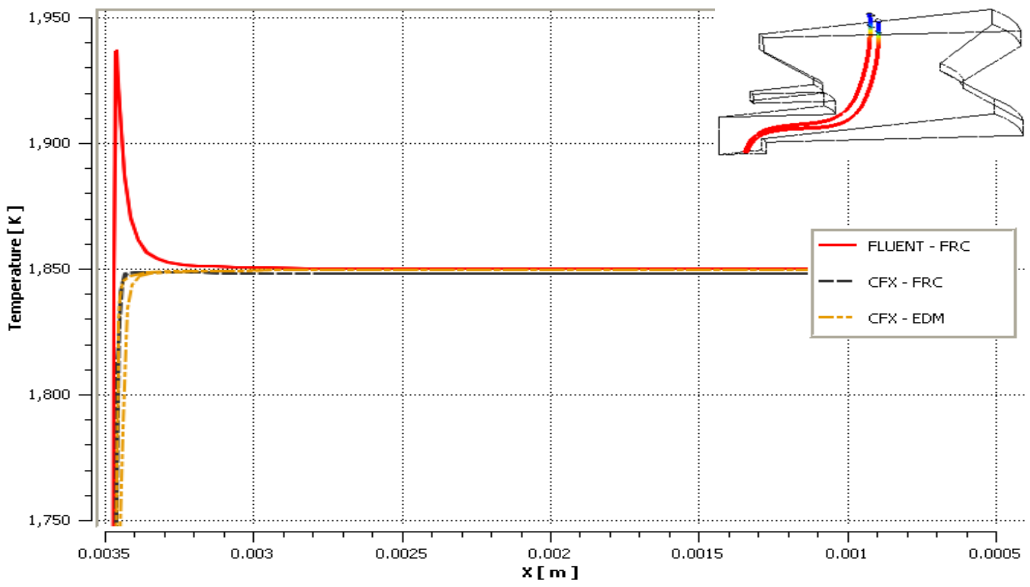

Figure B-4: Part 1 results comparison of the fluid domain with an adiabatic chamber wall boundary

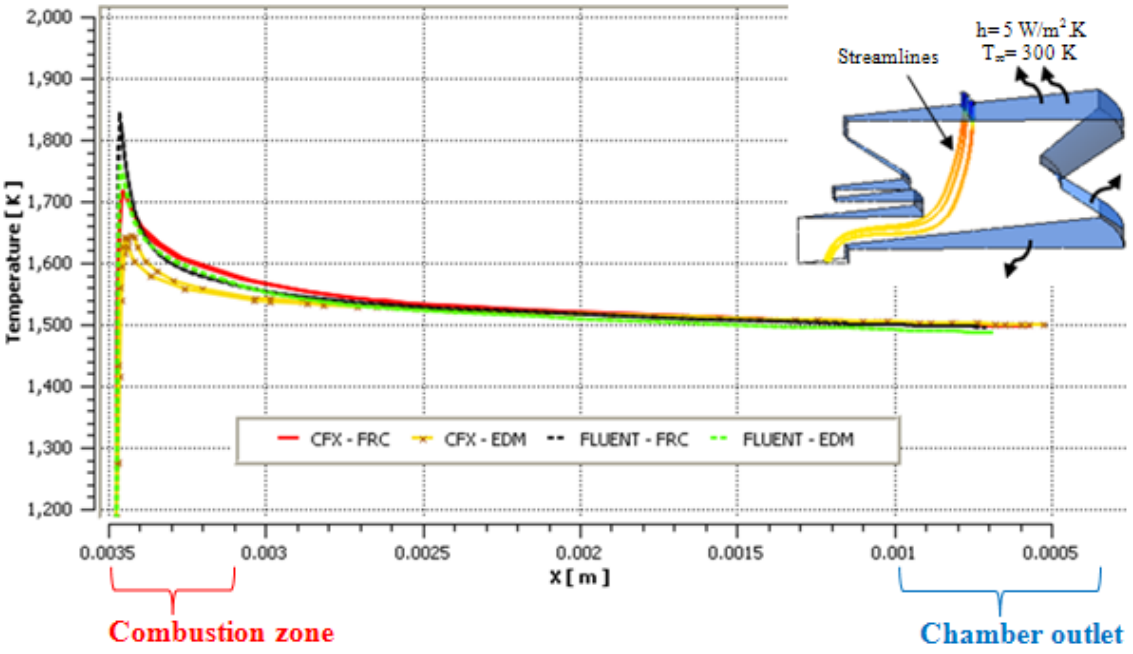

Figure B-5: Part 2 results comparison of the fluid domain with a convective chamber wall boundary

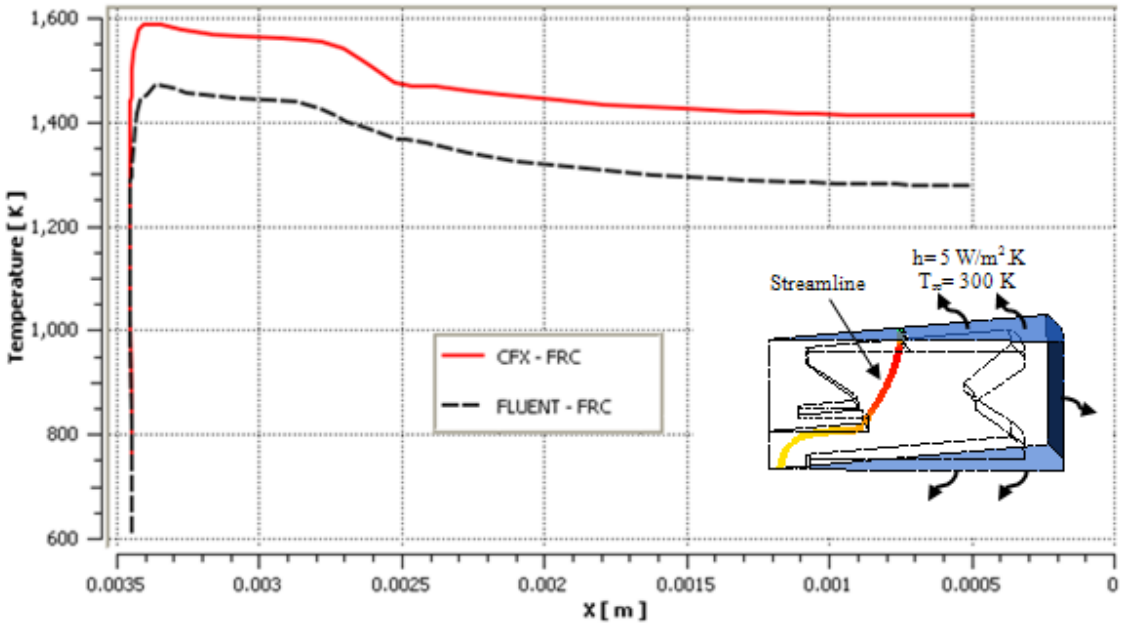

Figure B-6: Part 3 results comparison of the fluid and solid domains with a convective chamber wall boundary

B-2.2.3 Part 3 – Fluid and solid domains with a convective external wall boundary

The results obtained from the numerical simulation using CFX-FRC and FLUENT-FRC combustion models utilising both the fluid and the solid domains with a convective heat loss from the external wall boundary along the streamlines are plotted in Figure B-6. The results comparison of the temperature patterns along those lines for both models is the same. Moreover, the difference in temperature of approximately 80 K was observed when the maximum flame and the fluid flow average exit temperatures from the CFX code were compared with their counterparts of the other solver model. Also, the calculated difference in the convective heat loss from the external wall was 0.013 W which is equivalent to 0.21 W at 360 degree model (full combustor geometry). The latter heat loss value represents 2.1 % of the total heat generated by the fuel during the combustion process.

Further investigation of the difference in results obtained above is carried out through a cylindrical cross-sectional tube with a constant velocity and temperature inlets of water at 3 m/s and 1500 K respectively and an external wall convective heat transfer coefficient of 40 $W/m^2.K$. The aim is to validate the convective heat transfer between the fluid and the solid domains as well as the heat loss from the external wall. The problem specification and the numerical grid configuration used of ~327500 elements are shown in Figure B-7.

The numerical results of the temperature distribution at the external wall of the tube obtained from both CFD codes are plotted in Figure B-8. The results show that the maximum temperature difference of 1.7 K is located above the inlet of the tube, and also show the predicted heat loss from the external wall of 2.095 and 2.097 W by the CFX and FLUENT codes respectively. These results and in particular the heat loss demonstrated that both CFD solvers are able to predict the same flow physics. Based on this finding, the difference in results obtained in part 3 above even though were marginal, refining the numerical grid could reduce those differences.

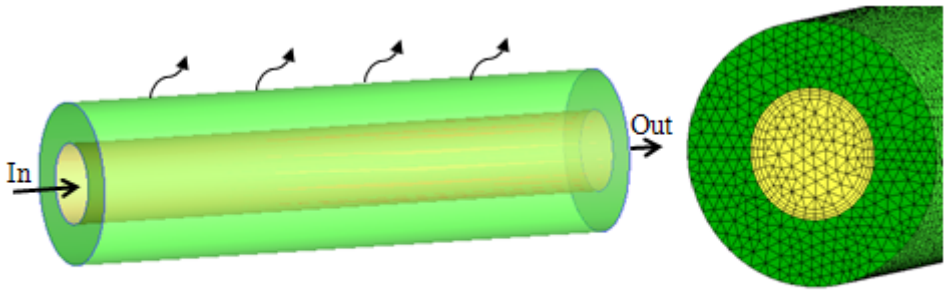

Design parameter	Description/Value
Length	7 mm
Inner and outer diameters	0.5 and 1.0 mm
Structure material	Steel
Fluid flow	Water
Inlet velocity and temperature	3 m/s at 1500 K
Convective heat transfer coefficient (external wall)	40 W/m^2.K
Ambient temperature	300 K

Figure B-7: Problem specification of a convective heat transfer from a steel tube and grid configuration

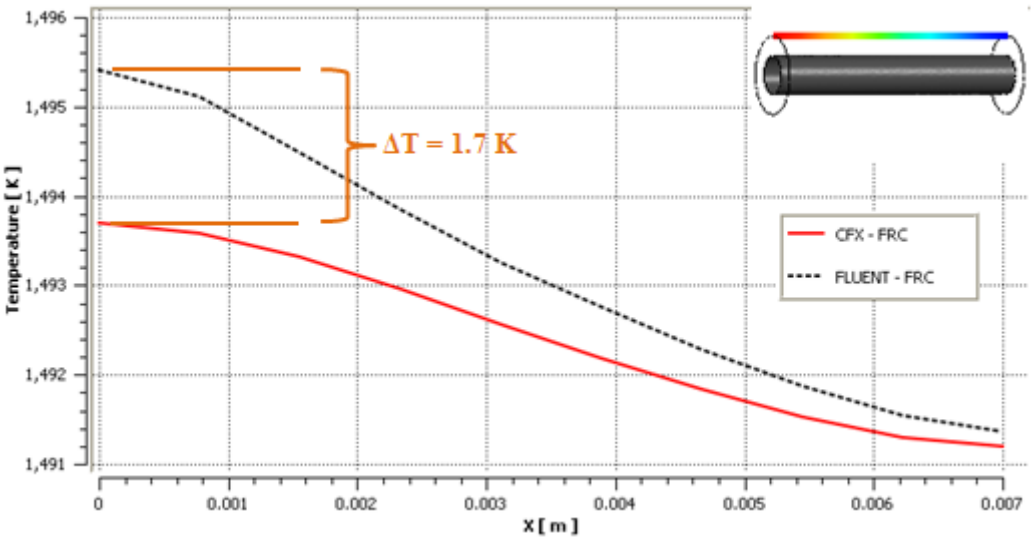

Figure B-8Figure B-7: Results comparison of the external wall temperature distribution CFX vs. FLUENT

B-3 Test case 3 – Laminar mixing in a coaxial jets micro-reactor using a baffle plate

B-3.1 The aim

This case study describes a method to enhance a laminar mixing of coaxial jets at low Reynolds number with the aim to validate the flow results achieved from ANSYS CFX code by comparing them with their counterparts obtained experimentally and numerically using a code of LBM (Lattice Boltzmann method).

B-3.2 Problem description – Part A

Figure B-9 presents a schematic of the micro-reactor under investigation. The reactor has a chamber length of 30 mm and a diameter of 0.3 mm. A baffle plate is used to improve fluid mixing in laminar flow regime. The plate consists of a central nozzle and six other nozzles distributed radially at 0.1157 mm from the reactor centreline, all with diameters of 0.06 mm. For approximation, only water at 298 K is numerically modelled as working fluid whereas a mixture of 98% water and 2% glycerine is applied experimentally. Two different flow velocities are applied at the inlets, 0.356 m/s at the central nozzle and 0.294 m/s for the other nozzles.

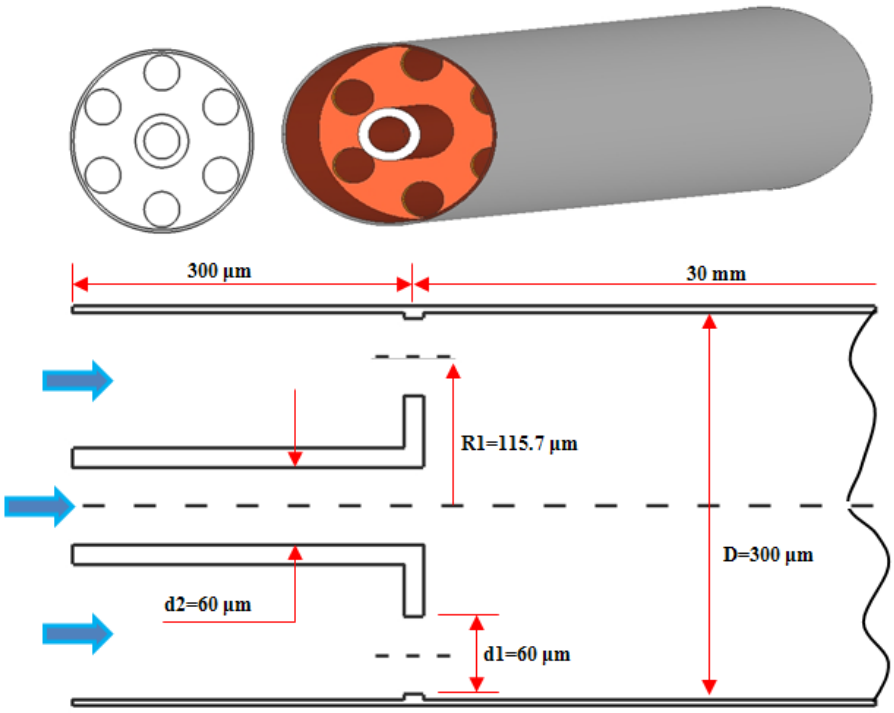

Figure B-9 Schematic presentation of the micro-reactor problem

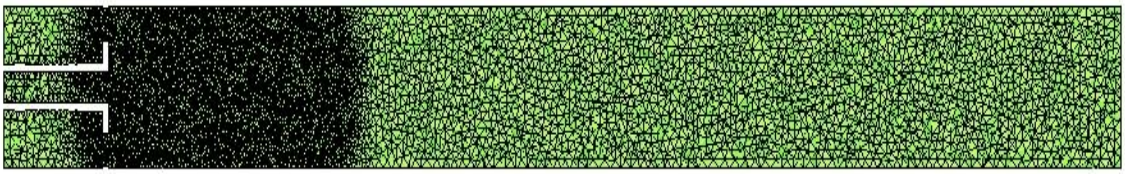

Figure B-10: Numerical grid of the reactor at midplane consists of ~one-million elements

Three-dimensional numerical grid is used to describe the problem with a total number of approximately 1-million tetrahedral elements with fine mesh applied in the mixing zone of the reactor. A cross section of the grid at midplane is shown in Figure B-10.

B-3.2.1 Results and discussion

The laminar flow numerical results of the velocity contours and velocity vector plot are shown in Figure B-11. The CFX results were also compared with the experiment (Djenidi and Moghtaderi, 2006) and LBM code (Moghtaderi et al., 2006) for the same problem and are found to agree well with both in capturing the flow behaviour – flow separation inside the micro-reactor as shown in Figure B-12.

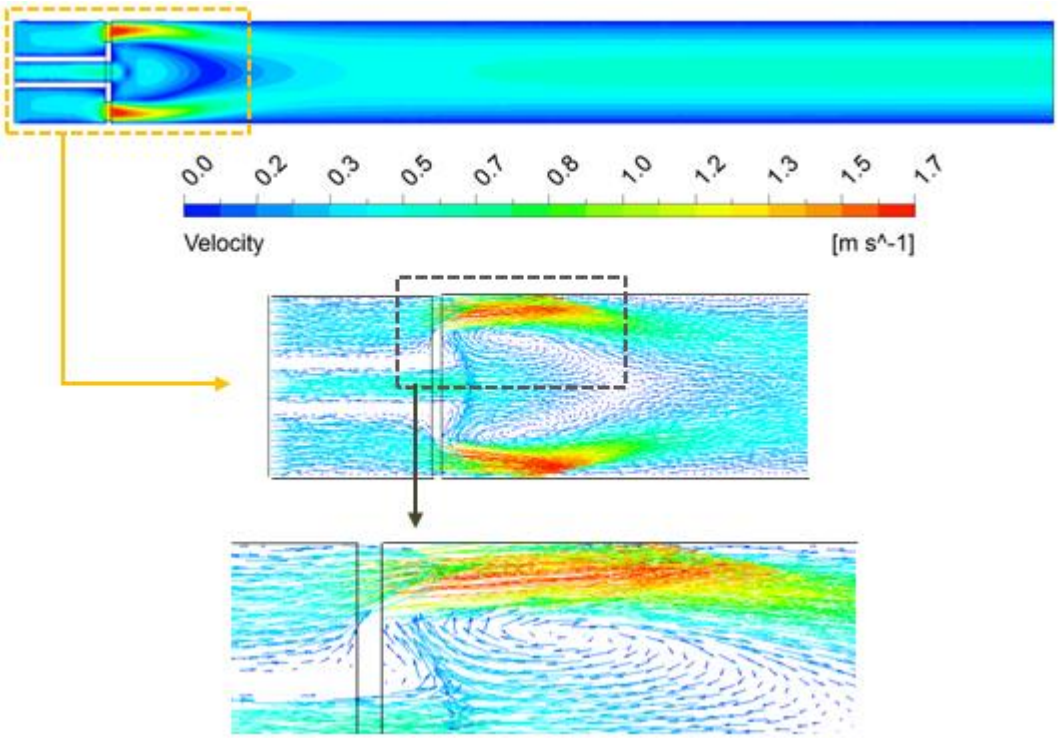

Figure B-11: CFX numerical results. Velocity contours (Top), velocity vector plot (midle) and velocity vector plot close-up view (botom)

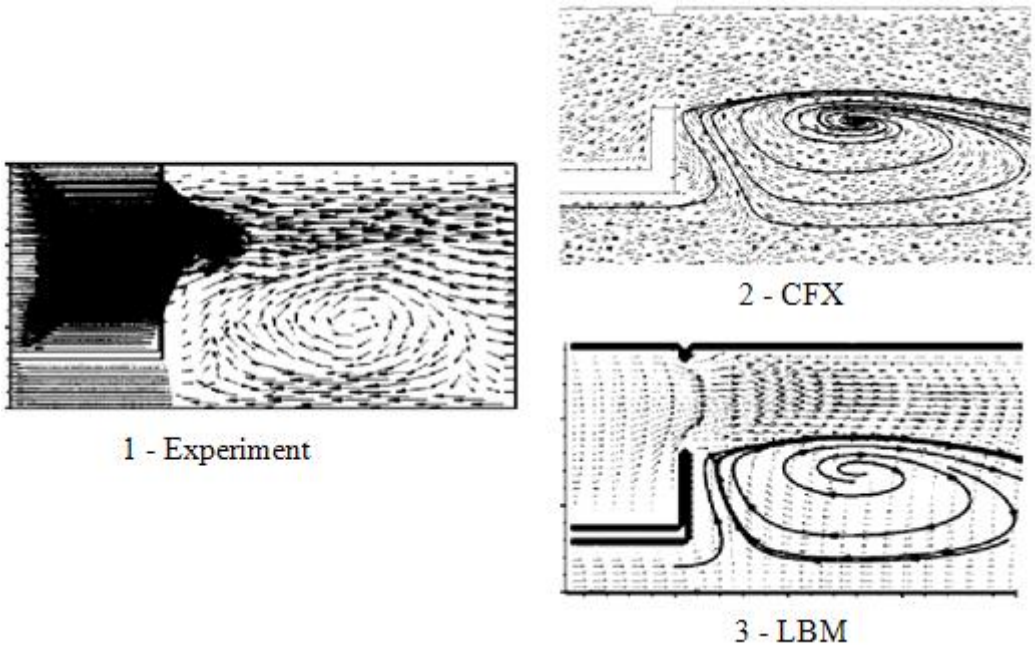

Figure B-12: Velocity contours of design – A. 1-Experiment (Moghtaderi et al., 2006) , 2-CFX code and 3-LBM code (Djenidi and Moghtaderi, 2006)

B-3.3 Problem description – Part B

In this part, the redial nozzles of the baffle plate are positioned inward closer to the central nozzle, precisely at a radius of 78 μm from the device centreline. A schematic of the new baffle plate configuration is represented in Figure B-13. Same numerical grid size and boundary conditions to that of Part A are applied.

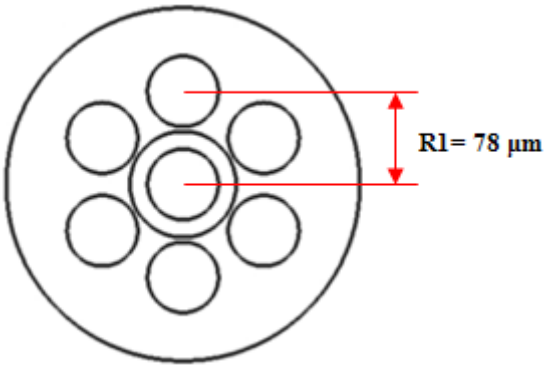

Figure B-13: Schematic illustration of the baffle plate used in Part B

B-3.3.1 Results and discussion

The results of the CFX are represented by the velocity distribution inside the micro-reactor with a new baffle plate configuration are shown in Figure B-14. Also, the results of the CFX and LBM in capturing the flow separation near the reactor wall compare favourably. Furthermore, the results of the modified version of the LBM code (D'ammaro et al., 2010) which was implemented in an optimisation case investigation to optimise the micro-reactor mixing performance agreed with their opposite of the CFX.

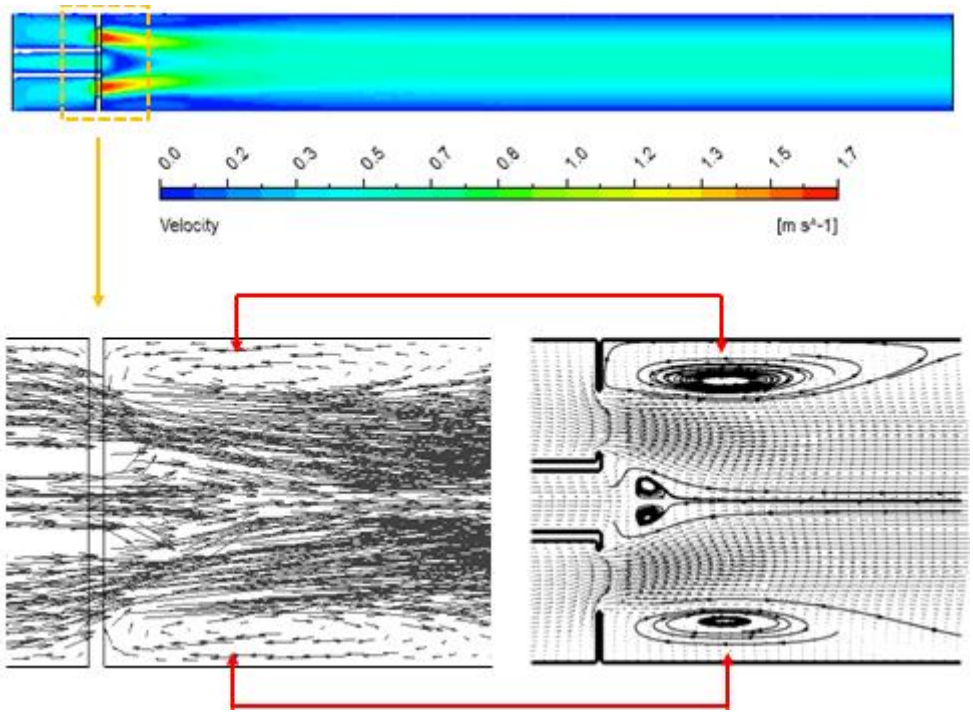

Figure B-14: Velocity contours of the flow field obtained from CFX (Top). CFX velocity vector plot (bottom left) and LBM velocity vector plot by (Djenidi and Moghtaderi, 2006) (bottom right)

B-4 Appendix summary

This appendix described the validation of the CFD code integrated within the optimisation system. The performance of the CFD code was judged based on results comparison with another well-known CFD solver, considering two case studies with different boundary conditions applied.

Test case 1, where the conduction and convection mechanisms' capability between the fluid and the solid domains were tested and the numerical results obtained from the CFX code were a good match with another well-known CFD solver.

Test case 2 consisted of three different parts in which the initial microcombustor design configuration was used. In part one and two, an adiabatic and a convective external wall boundary were used respectively and in both scenarios only the fluid domain was modelled. Again, the numerical results obtained from the tested CFD code compared well with the other code. However, a marginal difference was observed in part 3 when the fluid and the solid domains were modelled with an external heat loss. After further investigation by modelling a cylindrical tube in a separate case, utilising similar domains and boundary conditions, it was revealed that the numerical results achieved from the CFD solver of interest compare favourably with their counterpart solver results. Also, it was suggested that the grid density might be the cause of the results discrepancy in part 3 and not the CFD solver code.

Finally, test case 3 examined the results achieved from the CFX code in modelling a laminar flow mixing in a coaxial jets micro-reactor. Two baffle plate configurations were used in comparison to the results obtained from the experiment and original and modified versions of LBM code which was developed specifically to investigate the low Reynolds flow mixing inside a micro-reactor.

In conclusion, the CFD solver of ANSYS CFX 12.1 or the ANSYS FLUENT 12.1 can be used within the multi-objective optimisation system with the purpose of optimising a micro-scale combustion device with confidence.

Appendix C

Hydrogen oxidation mechanism

```
!
!  This is a hydrogen oxidation mechanism,
!  a subset of the Leeds methane mechanism (v. 1.2)
!  This subset has been created by program MECHMOD.
!
!
ELEMENTS  H  O  N  AR  END
SPECIES
H2     O2   H2O   H2O2   H   O   OH   HO2   AR   N2
END
THERMO ALL
   300.000  1000.000  5000.000
H2                      H   2    0    0    0G    300.00   5000.00 1000.00    0 1
 2.99142300E+00 7.00064400E-04-5.63382900E-08-9.23157800E-12 1.58275200E-15    2
-8.35034000E+02-1.35511000E+00 3.29812400E+00 8.24944200E-04-8.14301500E-07    3
-9.47543400E-11 4.13487200E-13-1.01252100E+03-3.29409400E+00                   4
O2                      O   2    0    0    0G    300.00   5000.00 1000.00    0 1
 3.69757800E+00 6.13519700E-04-1.25884200E-07 1.77528100E-11-1.13643500E-15    2
-1.23393000E+03 3.18916600E+00 3.21293600E+00 1.12748600E-03-5.75615000E-07    3
 1.31387700E-09-8.76855400E-13-1.00524900E+03 6.03473800E+00                   4
H2O                     H   2O   1    0    0G    300.00   5000.00 1000.00    0 1
 2.67214600E+00 3.05629300E-03-8.73026000E-07 1.20099600E-10-6.39161800E-15    2
-2.98992100E+04 6.86281700E+00 3.38684200E+00 3.47498200E-03-6.35469600E-06    3
 6.96858100E-09-2.50658800E-12-3.02081100E+04 2.59023300E+00                   4
H2O2                    H   2O   2    0    0G    300.00   5000.00 1000.00    0 1
 4.57316700E+00 4.33613600E-03-1.47468900E-06 2.34890400E-10-1.43165400E-14    2
-1.80069600E+04 5.01137000E-01 3.38875400E+00 6.56922600E-03-1.48501300E-07    3
-4.62580600E-09 2.47151500E-12-1.76631500E+04 6.78536300E+00                   4
H                       H   1    0    0    0G    300.00   5000.00 1000.00    0 1
 2.50000000E+00 0.00000000E+00 0.00000000E+00 0.00000000E+00 0.00000000E+00    2
 2.54716300E+04-4.60117600E-01 2.50000000E+00 0.00000000E+00 0.00000000E+00    3
 0.00000000E+00 0.00000000E+00 2.54716300E+04-4.60117600E-01                   4
O                       O   1    0    0    0G    300.00   5000.00 1000.00    0 1
 2.54206000E+00-2.75506200E-05-3.10280300E-09 4.55106700E-12-4.36805200E-16    2
 2.92308000E+04 4.92030800E+00 2.94642900E+00-1.63816600E-03 2.42103200E-06    3
-1.60284300E-09 3.89069600E-13 2.91476400E+04 2.96399500E+00                   4
OH                      H   1O   1    0    0G    300.00   5000.00 1000.00    0 1
 2.88273000E+00 1.01397400E-03-2.27687700E-07 2.17468400E-11-5.12630500E-16    2
 3.88688800E+03 5.59571200E+00 3.63726600E+00 1.85091000E-04-1.67616500E-06    3
 2.38720300E-09-8.43144200E-13 3.60678200E+03 1.35886000E+00                   4
HO2                     H   1O   2    0    0G    300.00   5000.00 1000.00    0 1
 4.07219100E+00 2.13129600E-03-5.30814500E-07 6.11226900E-11-2.84116500E-15    2
-1.57972700E+02 3.47602900E+00 2.97996300E+00 4.99669700E-03-3.79099700E-06    3
 2.35419200E-09-8.08902400E-13 1.76227400E+02 9.22272400E+00                   4
N2                      N   2    0    0    0G    300.00   5000.00 1000.00    0 1
 2.92664000E+00 1.48797700E-03-5.68476100E-07 1.00970400E-10-6.75335100E-15    2
-9.22797700E+02 5.98052800E+00 3.29867700E+00 1.40824000E-03-3.96322200E-06    3
 5.64151500E-09-2.44485500E-12-1.02090000E+03 3.95037200E+00                   4
AR                      AR  1    0    0    0G    300.00   5000.00 1000.00    0 1
 2.50000000E+00 0.00000000E+00 0.00000000E+00 0.00000000E+00 0.00000000E+00    2
-7.45375000E+02 4.36600100E+00 2.50000000E+00 0.00000000E+00 0.00000000E+00    3
 0.00000000E+00 0.00000000E+00-7.45375000E+02 4.36600100E+00                   4
END
REACTIONS   MOLES  KJOULES/MOLE
!
!     1
H2+O                    => OH+H               5.120E+04   2.67      26.27
!
!     2
```

```
OH+H                    => H2+O               3.534E+04   2.62      18.95
!
!     3
H2+OH                   => H2O+H              1.020E+08   1.60      13.80
!
!     4
H2O+H                   => H2+OH              4.520E+08   1.60      77.08
!
!     5
O2+H+M                  => HO2+M              2.100E+18   -.80        .00
 N2/0.67/ O2/0.4/ H2O/0./ AR/0.28/
!
!     6
HO2+M                   => O2+H+M             1.159E+20  -1.26     211.41
 N2/0.67/ O2/0.4/ H2O/0./ AR/0.28/
!
!     7
O2+H+H2O                => HO2+H2O            6.890E+15    .00      -8.73
!
!     8
HO2+H2O                 => O2+H+H2O           3.801E+17   -.46     202.68
!
!     9
O2+H                    => OH+O               9.756E+13    .00      62.11
!
!    10
OH+O                    => O2+H               1.450E+13    .00       2.94
!
!    11
H2O2+H                  => HO2+H2             1.690E+12    .00      15.71
!
!    12
HO2+H2                  => H2O2+H             1.507E+09    .78      83.91
!
!    13
H2O2+H                  => OH+H2O             1.020E+13    .00      14.97
!
!    14
OH+H2O                  => H2O2+H             6.724E+07   1.28     295.88
!
!    15
H2O2+O                  => OH+HO2             6.620E+11    .00      16.63
!
!    16
OH+HO2                  => H2O2+O             4.073E+08    .72      77.51
!
!    17
H2O2+OH                 => H2O+HO2            7.830E+12    .00       5.57
!
!    18
H2O+HO2                 => H2O2+OH            4.744E+11    .45     140.59
!
!    19
H2O2(+M)                => 2OH(+M)            3.000E+14    .00     202.87
 N2/0.4/ O2/0.4/ H2O/6.5/ AR/0.35/
    LOW /  3.000E+17    .00     190.40 /
    TROE /     1.0000      1.00      1.00   1040.00 /
!
!    20
2OH(+M)                 => H2O2(+M)           7.230E+13   -.37        .00
 N2/0.4/ O2/0.4/ H2O/6.5/ AR/0.35/
    LOW /  5.530E+19   -.76        .00 /
    TROE /     1.0000      1.00      1.00   1040.00 /
!
!    21
2H+M                    => H2+M               1.870E+18  -1.00        .00
 N2/0.4/ O2/0.4/ H2O/6.5/ H2/0./ AR/0.35/
!
!    22
```

```
H2+M                    => 2H+M               6.269E+18   -.98     436.51
 N2/0.4/ O2/0.4/ H2O/6.5/ H2/0./ AR/0.35/
!
!    23
2H+H2                   => 2H2                9.790E+16   -.60        .00
!
!    24
2H2                     => 2H+H2              3.282E+17   -.58     436.51
!
!    25
H+O+M                   => OH+M               1.180E+19  -1.00        .00
 N2/0.4/ O2/0.4/ H2O/6.5/ AR/0.35/
!
!    26
OH+M                    => H+O+M              2.730E+19  -1.03     429.20
 N2/0.4/ O2/0.4/ H2O/6.5/ AR/0.35/
!
!    27
H+OH+M                  => H2O+M              5.530E+22  -2.00        .00
 N2/0.4/ O2/0.4/ H2O/2.54/ AR/0.15/
!
!    28
H2O+M                   => H+OH+M             1.260E+25  -2.30     503.33
 N2/0.4/ O2/0.4/ H2O/2.54/ AR/0.15/
!
!    29
H+HO2                   => H2+O2              4.280E+13    .00       5.90
!
!    30
H2+O2                   => H+HO2              2.600E+12    .48     231.01
!
!    31
H+HO2                   => 2OH                1.690E+14    .00       3.66
!
!    32
2OH                     => H+HO2              1.839E+10    .83     149.54
!
!    33
H+HO2                   => H2O+O              3.010E+13    .00       7.20
!
!    34
H2O+O                   => H+HO2              3.225E+11    .56     227.22
!
!    35
2O+M                    => O2+M               5.400E+13    .00      -7.48
 N2/0.4/ O2/0.4/ H2O/6.5/ AR/0.35/
!
!    36
O2+M                    => 2O+M               4.816E+16   -.43     493.62
 N2/0.4/ O2/0.4/ H2O/6.5/ AR/0.35/
!
!    37
O+HO2                   => O2+OH              3.190E+13    .00        .00
!
!    38
O2+OH                   => O+HO2              1.338E+12    .43     217.79
!
!    39
2OH                     => O+H2O              1.510E+09   1.14        .42
!
!    40
O+H2O                   => 2OH                1.487E+11    .87      74.56
!
!    41
OH+HO2                  => H2O+O2             2.890E+13    .00      -2.08
!
!    42
H2O+O2                  => OH+HO2             1.193E+14    .16     289.85
!
```

```
!    43
2HO2                    => H2O2+O2            4.220E+14    .00      50.14
DUPLICATE
!
!    44
H2O2+O2                 => 2HO2               2.876E+16   -.29     207.05
DUPLICATE
!
!    45
2HO2                    => H2O2+O2            1.320E+11    .00      -6.82
DUPLICATE
!
!    46
H2O2+O2                 => 2HO2               8.997E+12   -.29     150.09
DUPLICATE

END
```